NONLOCAL TRANSPORT IN FUSION-RELEVANT PLASMAS

Jonathan Peter Brodrick

PhD

University of York
Physics

February 2019

ABSTRACT

Trying to accurately predict results of fusion experiments by means of computer simulations has long been a formidable challenge in both inertial and magnetic confinement approaches. This thesis evaluates and builds on three different models suggested for approximating 'nonlocal' corrections to electron heat transport that arise due to presence of steep temperature gradients: Schurtz, Nicolaï and Busquet's multigroup diffusion model (SNB), Ji and Held's moment based approach (EIC), and the non-Fourier Landau-fluid model of Dimits, Joseph and Umansky (NFLF). It is found that, while the EIC and NFLF models are most successful in matching fully kinetic behaviour for small relative temperature perturbations to high degrees of nonlocality, they overestimate the peak heat flow by as much as 35% and fail to predict preheat in more realistic test problems where relative temperature differences are large. Instead, the popular SNB model proves to be more reliable in such situations with the caveat that its optimal implementation is found to differ significantly in its predictions from that typically used in rad-hydro codes. These conclusions are supported by a number of test problems benchmarked against Vlasov-Fokker-Planck simulations as well as a thorough mathematical analysis of the damping of low-amplitude temperature sinusoids. The majority of test problems presented will be more relevant to indirect drive inertial fusion, but consequences of modelling nonlocality in tokamak heat exhausts shall also be briefly considered. Furthermore, the consequence of incorporating the identified optimal implementation of the SNB model in the LLNL code HYDRA is considered. Finally, a simple method to incorporate nonlocal effects on the Nernst advection of magnetic fields down steep temperature gradients is presented, based on the assumption that the relationship between the Nernst velocity and the heat flow velocity is unaffected by nonlocality. The effectiveness of this method is demonstrated in a number of inertial fusion scenarios.

CONTENTS

LIST OF TABLES

LIST OF FIGURES

To James and Liora,
May the world you grow up into become a better place than the one in which you were born.

"All models are wrong, but only some are useful"

—George Box

ACKNOWLEDGMENTS

This thesis has been a long time in the making and I certainly couldn't have done it without the support, encouragement and advice received from my collaborators, colleagues and family. Over the course of my studies, I have had the much relished opportunity to converse and work with inspirational individuals in the field of fusion research and it is appropriate that I now take the time to express my deep gratitude to everyone involved. I should also make sure to express my gratitude to the funding bodies—EPSRC, the IOP and EUROFUSION—that enabled valuable academic travel and made sure I didn't go hungry.

Being able to twice visit LLNL, the world centre of inertial fusion research was certainly the highlight of my time in plasma physics and the enthusiasm of the staff in spite of the seemingly insurmountable task facing them was certainly refreshing and infectious. Of these, I would first and foremost like to thank Marty Marinak who helped orchestrate my visits and kindly involved me in many stimulating discussions on nonlocal models. Mehul Patel additionally proved to be an early wise and reliable source on the workings of the SNB model in HYDRA, and his cooperation with Gary Kerbel in assessing and implementing my suggested changes into HYDRA made my labour feel worthwhile. Another source of motivation was Dave Strozzi who really helped me reach a more relevant audience by participating in the LLNL Club Med transport meetings and promoting the highly enjoyable and memorable Anomalous Absorption Conference in Florence, Oregon. Furthermore, I would like to thank Will Farmer for all his encouragement and for kindly sharing his microdot simulation data. And finally, Mark Sherlock, the Brit who infiltrated the ranks of the Livermore transport team, I am greatly appreciative of your mentorship, wisdom and time. Although I am sincerely hopeful that our paths may cross again one day, I would like to make one last expression of my gratitude for all the hospitality at LLNL: So long, and thanks for all the burritos!

A significant chunk of this PhD concerning computational modeling of thermal and magnetised transport was spent learning and using numerous plasma simulation codes. Thus I am eternally grateful to the attentive and rapid assistance I've received from the developers of these codes. To the ever considerate Robert Kingham for help in understanding the wonderful IMPACT code and also for sharing his expertise in analysing fusion simulations and writing clear scientific papers. To Alex Chankin for kindly hosting me at IPP Garching and helping me

get to grips with the KIPP VFP code. The dedicated support provided by John Omotani and Ben Dudson in working the EIC nonlocal model in the BOUT++ code was hugely enabling, particularly in realising many of the results in chapter 4. I would also like to thank Maxim Umansky for providing the implementation for the NFLF nonlocal model and allowing me to further develop it, as well as for inviting me to present to his team at LLNL leading to many valued and memorable conversations with his colleagues Andris Dimits, Ilon Joseph and Lynda LoDestro. Thank you, Martin Read and John Bissell for providing access to and sharing your expertise with the CTC transport code. Lastly, I am most grateful to Archis Joglekar and Ben Winjum of UCLA for motivating discussions and their ever helpful assistance in taming the elusive OSHUN code.

Of course, none of this work or these collaborations would have happened were it not for my supervisor, Christopher Ridgers. A constant source of encouragement and ideas, Chris helped me to get to grips with the more obscure terminology involved in inertial fusion research and set me on the path to push the field of nonlocal modelling just that little bit further. Down the supervisory line, a meticulous approach of double, triple or even quadruple checking results was passed down to ensure that no stone was left out of place. It was also Chris who acted as the central network point for setting up all the aforementioned collaborations that have had a tremendous impact on my work. Needless to say, I will always be appreciative of your understanding and patience, particularly regarding the challenges of balancing academic research with family life. Additionally, I would like to share my appreciation for the camaraderie and inspiration of the 'team Ridgers' transport wing: Martin, Dario and Michael.

Finally, I would like to thank all my family who were the true source of support in writing this thesis: My parents, in-laws and grandparents who were all heroically there to expedite our move up to Scotland before write-up was completed. And thank you again to my parents who equipped me with the work ethic and dedication to see this PhD through and did whatever they could to pick up the slack when things got tough. It was certainly the inspiration of my beautiful children James and Liora to push this thesis to completion, partly invoking my desperation to finally get some proper sleep! But it was my darling wife, Lucy, who was the one ever present companion there to lean on through all the turbulence. Thank you for your unending love, support and patience.

DECLARATION

As a result of the aforementioned multitude of collaborations I participated in as part of my doctoral program, it is important to distinguish the work that I personally did myself. The major reliance on previous work present in this thesis is that on various plasma simulation codes. The only codes that I wrote from scratch were a simple local heat flow model, the in-house SNB model and the simplified Fourier-space VFP code DILL. I additionally designed a mesh refinement and smoothing method to deal with coarsely grained data as detailed in section 3.6. As I was unable to obtain access to any advanced radiation-hydronamic code for my thesis, simulations with these were performed on my behalf by collaborators: I utilised test problems performed by LLNL's Marty Marinak and Will Farmer as well as my supervisor Chris Ridgers at the University of York with the NIF HYDRA code, while benchmarks of the French fusion code CHIC were carried out by Jean-Luc Feugeas and Philippe Nicolaï at CELIA. All simulations with other codes were performed individually by myself unless clearly specified. The original implementers of these codes and any contributions I made to them are detailed below.

- The VFP code IMPACT was originally implemented by Robert Kingham (Imperial College London) with some later extensions provided by Christopher Ridgers. I made a small modification that enabled the code to correctly apply the collision fix to simulations with spatially varying ionisations and made some minor modifications to the laser heating routines.
- Alex Chankin and David Coster wrote the 1D2V VFP code KIPP, I helped diagnose a few minor errors in the code and assist with extensions to higher ionisation.
- Mark Sherlock (LLNL) wrote the K2 code.
- Michail Tzoufras originally wrote the OSHUN which is now being maintained and extended by researchers at UCLA including Archis Joglekar and Ben Winjum.
- Maxim Umansky provided the original Fortran implementation of the NFLF model which I have significantly extended to allow for automatic recalculation of optimal fitting coefficients based on user specifications using the variable projection algorithm (see section 3.4).
- The EIC model was originally coded into BOUT++ by John Omotani (Chalmers Institute of Technology) and Ben Dudson (University of York), I updated the

code by adapting to normalised units and calculating more combinations of coefficients in the various bases.

- Finally, the CTC code was designed and implemented by John Bissell (University of Warwick) with later add-ons provided by Martin Read. I extended this code to take account of inhomogeneous ionisations by using the collision fix.

An attempt to continually clarify any sharing of responsibilities will be made throughout this thesis. Some of the work in this thesis has been published previously (sometimes verbatim), some of the results presented in chapters 4 and 5 was first seen in

- J P Brodrick et al. (2017) 'Testing nonlocal models of electron thermal conduction for magnetic and inertial confinement fusion applications' *Phys. Plasmas* **24** (9), p. 092309

And most of chapter 7 comes from

- J P Brodrick et al. (2018) 'Incorporating kinetic effects on nernst advection in inertial fusion simulations' *Plasma Phys. Control. Fusion* **60** (8), p. 084009

Another paper that I was involved in that encouraged further thought about the role of the electric field in the SNB model was,

- M Sherlock, J P Brodrick and C P Ridgers (2017) 'A comparison of non-local electron transport models for laser-plasmas relevant to inertial confinement fusion' *Phys. Plasmas* **24** (8), p. 082706

I declare that this thesis is a presentation of original work and I am the sole author. This work has not previously been presented for an award at this, or any other, University. All sources are acknowledged as References.

York, February 2019

Jonathan Peter Brodrick

1

INTRODUCTION

Global energy consumption is expected to rise approximately 28% between 2015 and 2040 with no sign of slowing; this is mostly as a result of continuing economic growth in non-OECD Asian countries including China and India (Energy Information Administration 2017). Encouragingly, the use of dangerously polluting coal is predicted to peak in the mid-2020's, with the demand for liquid fuels also anticipated to grow more slowly than that from other sources. However, a more substantial long-term reduction of the relative contribution of fossil fuels to the global energy mix is thought to be necessary to avert potentially catastrophic environmental consequences, such as eventual average temperature rises exceeding 3 °C (Cox et al. 2018).

With almost 50% of the world's oil consumption currently being used by non-air transport, (Energy Information Administration 2017), a key player on the route to decarbonification will undoubtedly be widespread adoption of the electric automobile. This process is being expedited by countries such as Norway and France aiming to abolish the sale of non-hybrid petrol and diesel cars by 2025 and 2040 respectively (*The Guardian* 7th July 2017). However, without the correct infrastructure in place such a revolutionary transition could feasibly be limited to a geographical restructuring of carbon emissions (Drax 2017). While falling unit costs should lead to intermittent renewables like solar and wind forming a greater part of our electricity supply (Coren 2017), nuclear power could still play

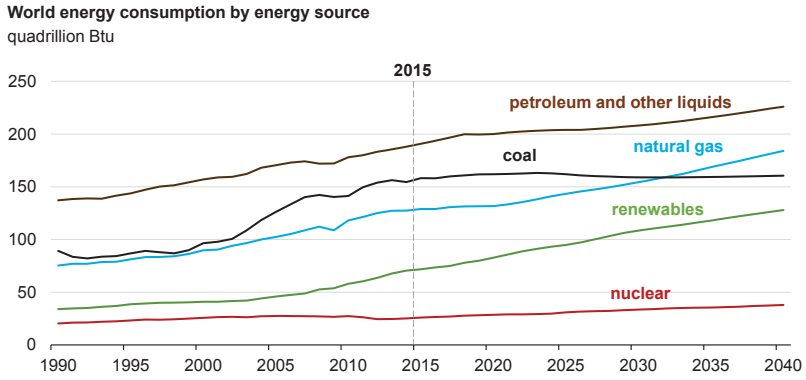

FIGURE 1.1: Historical and projected global energy demand by energy source, reproduced from International Energy Outlook (Energy Information Administration 2017).

a vital role in load balancing a low-carbon economy, especially if users decide to charge their cars at peak times (such as the early evening) (Brown 2018).

Despite nuclear fission as a whole being far safer for both the environment and humanity than all other non-renewables (The International Energy Administration 2002), it has been increasingly falling out of favour since the earthquake at Fukushima. Furthermore, some of the radioactive waste produced by fission has extremely long half-lives (up to many thousands of years) and are becoming ever more expensive to store. An alternative source of nuclear power is to harness the power of the stars through nuclear fusion: producing energy through the combination of isotopes of the universe's lightest and most common element, hydrogen, to form more stable nuclei such as helium.

The most feasible fusion reaction is that between deuterium and tritium, ${}^{2}_{1}\mathrm{D} + {}^{3}_{1}\mathrm{T} \longrightarrow {}^{4}_{2}\mathrm{He} + {}^{1}_{0}\mathrm{n} + 17.65\,\mathrm{MeV}$, due to its high cross section and reaction energy (Boyd and Sanderson 2003, Chap. 1 pp. 2–3). The two fuels are relatively abundant and a commonly quoted elucidation is that one bathtub of sea water (typically consisting of 156 ppm deuterium, Hornberger n.d.) combined with the lithium (used to breed tritium) in a standard laptop battery would provide enough energy for one human's lifetime energy needs. More importantly, a careful choice of reactor first wall and structural materials could limit the radioactive waste created by reactions with escaping neutrons to a small volume that could be safely recycled on the order of decades (Ongena and Oost 2012) and there is no risk of a nuclear meltdown.

While JET may have come close with its record-breaking attempts in 1997, the elusive goal of net energy gain has not yet been achieved. This is largely due to the difficulty in meeting the restrictive conditions on fuel density n_{DT} and confinement time τ required for ignition known as the Lawson criterion: $n_{\mathrm{DT}}\tau \gtrapprox 10^{20}\ \mathrm{s\,m^{-3}}$ (Boyd and Sanderson 2003, Chap. 1, pp. 3–4). There are currently two mainstream routes for meeting this requirement: magnetic confinement fusion (MCF) using donut-shaped devices known as tokamaks which contain the plasma on timescales of up to a minute or more with strong magnetic fields at relatively low densities of $10^{19\text{–}20}\ \mathrm{m^{-3}}$, and inertial confinement fusion (ICF) which instead relies on reaching extremely high densities exceeding $1 \times 10^{26}\ \mathrm{m^{-3}}$ by compressing small millimetre-scale capsules using lasers. These lasers can shine either directly on to the capsule surface or onto a surrounding metal cylinder called a hohlraum which then radiates x-rays back on to the capsule through the helium gas-fill (see fig. 1.2); it is the latter of these that shall be the main (but not only) focus of this thesis.

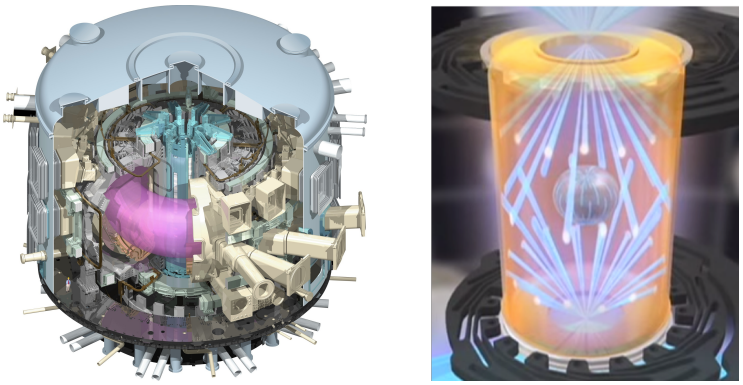

FIGURE 1.2: The ITER tokamak (left) is currently under construction in Cadarache, France (image reproduced from `www.iter.org/news/galleries`). An alternative approach being explored at NIF at LLNL in California is indirect drive ICF (right) (image reproduced from `lasers.llnl.gov/media/video-gallery/ride-the-beamline`).

Due to the high, kilo-electronvolt temperatures necessary for fusion to be viable, it is inevitable that very large temperature differences will be realised in fusion experiments. These can often occur on scalelengths that are comparable to the mean free path for perpendicular scattering (mfp) of more energetic electrons with ions

$$\lambda_{ei} = \frac{(\epsilon/\mathrm{keV})^2}{Z \log \Lambda_{ei} n_e / 10^{20}\ \mathrm{m}^{-3}} \times 1.5 \times 10^3\ \mathrm{m} \tag{1.0.1}$$

where $\epsilon = \frac{1}{2} m_e v^2$ is the energy of the electron, Z is the ionisation of the plasma, $\log \Lambda_{ei}$ is the Coulomb logarithm (introduced in section 2.1 and typically taking values around 5–15) and n_e is the electron density. As a result, energetic electrons can escape hot regions for cold ones with minimal collisions, causing the plasma to drift out of local equilibrium (meaning the distribution of electron velocities would no longer be Gaussian) and invalidating many of the assumptions governing 'classical' heat transport.

The most dominant contribution to the classical electron heat flux $\vec{Q}$ is from electrons travelling at about 2.6 times the thermal velocity $v_{2T} = \sqrt{2 k_B T_e / m_e}$. Due to the v^4 scaling of the appropriate mfp's, these suprathermals can travel almost fifty times further than thermal electrons enabling excess heat to be deposited beyond the steepest part of the temperature profile (often referred to as 'preheat' in the literature—Epperlein and Short 1991) as shown in fig. 1.3. A reduced population of suprathermals is left behind in the region of steep temperature gradient, contributing to a reduction in the heat flux. These 'nonlocal' effects

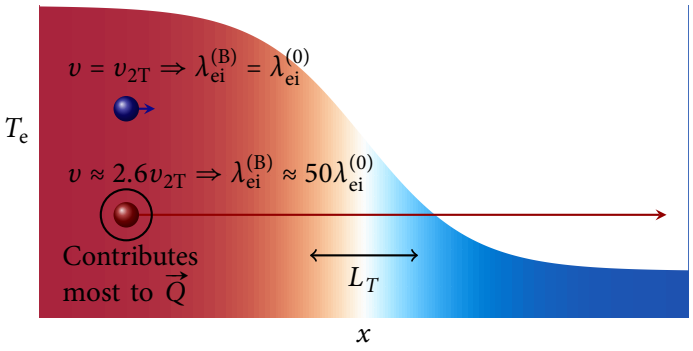

FIGURE 1.3: Suprathermal electrons travelling at $2.6v_{2T}$ can escape steep temperature gradients before thermalising due to their mean free paths being almost 50 times that of thermal electrons. The resultant displacement of suprathermal electrons leads to 'preheat' at the foot of the temperature gradient along with a reduction of the peak heat flux. (Colors are simply to indicate warmer and cooler regions.)

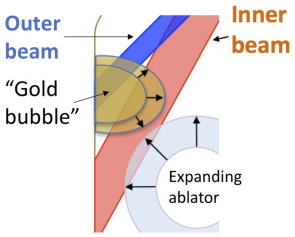

FIGURE 1.4: *The expansion of the gold bubble caused by the outer beams can block the pathway of the inner beams and affect implosion symmetry. (Image reproduced from Callahan et al. 2018).*

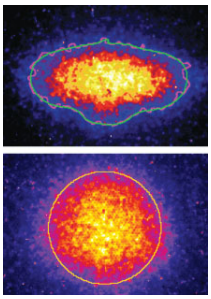

FIGURE 1.5: *Weakened inner beams can lead to 'pancaking' of the capsule implosion. A recalibration of the beams can restore the symmetry (below). (Image reproduced from* `str.llnl.gov/AprMay10/damkroger.html`*.)*

can become important even for temperature scalelengths as long as ~100 thermal mfp's (Schurtz et al. 2000).

While the short, sub-millimetre scalelengths involved in inertial fusion make the importance of nonlocal transport self-evident (and this has been known for a long time), the low densities present in tokamaks, particularly along the scrape-off layer where excess heat is exhausted, means that nonlocality can also play a role in MCF. The way this interplay of flux reduction and preheat plays out within these two conventional fusion routes is detailed in the next two sections. Following this, an outline of the research that will be presented in this thesis is provided.

1.1 NONLOCAL EFFECTS IN INERTIAL FUSION

For the case of indirect-drive inertial fusion, steep temperature gradients of less than 100 µm (corresponding to values of $\lambda_{ei}^{(B)}/L_T \gtrsim 10$–$20\%$ (Schurtz et al. 2000)) can be set up near the surface of the gold bubble ablated by outer beams. As illustrated in fig. 1.4, the expansion of the gold bubble can impede the course of the inner beams (Callahan et al. 2018) which balance the symmetry of the implosion. With the electron temperature greatly affecting the inverse bremsstrahlung absorption mechanism inside the gold bubble, it is critical to model thermal transport accurately.

A simple, popular method to account for the flux reduction aspect of nonlocality is the flux-limiter approach (detailed in section 2.3.1). However, there is no universally optimal value for such a flux-limiter f_Q; it needs to be tuned to experiments. Use of what appeared to be an overly restrictive flux-limiter of $f_Q = 0.05$ in the NIF radiation-hydrodynamics code HYDRA led to predictions of a very hot > 5 keV gold bubble. Optimising the experimental set up according to the restrictive model, however, resulted in an undesirable 'pancaked' implosion better matched by a higher flux-limiter of $f_Q = 0.15$ that would allow for increased cooling, and thus increased ability to impede the inner beams, of the gold bubble (Rosen et al. 2011). This was not the last time the recommended flux-limiter was changed: in order to eliminate previously necessary ad hoc multipliers on the radiation drive (which would otherwise be overestimated by 30%) that arose after multiple to changes to the atomic physics model in HYDRA the flux-limiter was lowered again, this time to 0.03 (Jones et al. 2016).

Magnetised liner inertial fusion or MagLIF *is an alternative approach to* ICF *that essentially involves running a sub-microsecond pulse of high current (10–70 MA) through a thin hohlraum containing heated fusion fuel. The aximuthal fields generated by the current creates a compressional 'Z-pinch' effect which could achieve the Lawson criterion at lower densities than typical* ICF *by providing longer confinement times (Slutz and Vesey 2012).*

Nonlocality can also play a role in magnetised transport, which is important in a variety of ICF scenarios: Self-generated fields in the megagauss (~100 tesla) range have been observed to occur near laser hotspots on direct-drive capsule shells (Séguin et al. 2012; Igumenshchev et al. 2014), and hohlraum walls (Li et al. 2009). These fields have the ability to inhibit thermal transport and raise plasma temperatures (Stamper 1991; Farmer et al. 2017). Furthermore, the potential of an externally-imposed field to improve performance and potentially cross the ignition barrier has been demonstrated in magnetised liner inertial fusion (MagLIF, see margin) (Slutz et al. 2010; Slutz and Vesey 2012; Sefkow et al. 2014; Gomez et al. 2014), plasma-liner-driven magneto-inertial fusion (MIF) (Knapp and Kirkpatrick 2014; Ryzhkov 2014; Hsu et al. 2017), direct-drive ICF (Gotchev et al. 2008; Chang et al. 2011; Hohenberger et al. 2012) and indirect-drive ICF (Montgomery et al. 2015; Strozzi et al. 2015; Perkins et al. 2017).

Over thirty years ago, Brackbill and Goldman (1983) were the first to demonstrate that the flux-limiting of *all* transport coefficents more accurately captured features predicted by a kinetic code. Much later, Davies et al. (2015) found that flux-limiting corrections to the classical Nernst velocity, which concerns the advection of magnetic field down steep temperature gradients, are necessary for matching simulated yield and ion temperature to a direct-drive experiment with an externally imposed field. This explanation is supported in a recent work by Hill and Kingham (2017), where a significant reduction of the peak Nernst velocity compared to the Braginskii prediction is observed in a 2D kinetic simulation of a non-uniformly irradiated CH-foil. Additionally, the authors observed an *enhancement* of the Nernst velocity inside the foil where the temperature

gradient is relatively flat. Similar to the phenomena of nonlocal preheat which is important in directly-driven ICF capsules, such an effect could not be captured by flux-limiters.

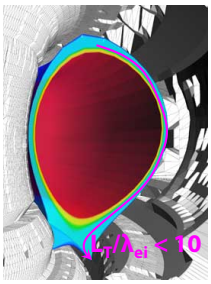

FIGURE 1.6: *Due to low densities, parallel heat transport in the scrape-off layer can be very nonlocal. (Image modified from* `euro-fusion.org`*.)*

1.2 NONLOCAL EFFECTS IN THE SCRAPE-OFF LAYER

In tokamaks, the dominant transport mechanism occurs perpendicular to field lines, where the electrons are almost completely relocalised by the short Larmor radius. However, parallel transport becomes important in the scrape-off layer (SOL), which exhausts energy from the core plasma to the 'divertor' depicted in fig. 1.6 (Chodura 1990). Thermal electrons entering the SOL at the separatrix have mfp's ranging from 1% (C-Mod) to 20% (DIII-D/Tokamak de Varennes (TdeV)) of the distance to the divertor target (connection length). For ITER this is estimated to be 8%. In fact, the ratio of λ_{ei} to the local temperature scalelength $L_T = 1/\nabla_\parallel \log T_e$ tends to vary along the SOL from approximately 1 (TdeV) or 0.1 (DIII-D) at the separatrix, to 0.01 near the colder divertor (Batishchev et al. 1997). These ratios are almost two orders of magnitude higher for suprathermal electrons, rendering the heat transport inherently nonlocal. Furthermore, transient events, such as edge localised modes (ELM's), disruptions and filaments, can create even higher temperatures and steeper gradients, with which the associated suprathermals would be almost collisionless (Omotani and Dudson 2013).

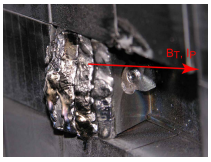

FIGURE 1.7: *High heat loads on the divertor plates can lead to significant material damage. (Image reproduced from Lipschultz et al. 2012)*

Current state of the art codes, such as SOLPS (Schneider et al. 1992; Reiter 1992) and UEDGE (Rognlien et al. 1994), have been shown to significantly underestimate the outer divertor target electron temperature and overestimate its density compared to experiment in existing tokamaks, which in turn affects other plasma parameters. Chankin and Coster (2009) have suggested that nonlocal effects in addition to inadequate treatment of neutrals (which was largely ruled out by a sensitivity analysis) and inappropriate use of time-averaging could explain this discrepancy. The plausibility of this hypothesis is supported by recent gyrokinetic simulations performed by Churchill et al. (2016). Another important factor is the effect of the enhanced suprathermal population on Langmuir probe characteristics(Horacek et al. 2003; Jaworski et al. 2012, 2013; Izacard 2016): Ďuran et al. (2015) have shown that a more sophisticated interpretation of probe results can reduce but not eliminate the discrepancy. Resolution of this discrepancy is critical as excessive heat loads could erode and severely limit the lifetimes of the divertor target plates (Turnyanskiy et al. 2015) as shown in Fig. 1.7.

1.3 THESIS OUTLINE

Due to the important uncertainties laid out above concerning the accuracy of standard heat transport modelling tools there is demand for a more complete approach that is not too computationally intensive. These sophisticated alternatives are referred to as reduced nonlocal models with one of the most popular being the 'SNB' multigroup diffusion model (Schurtz et al. 2000). Validation and improvement of such models shall be the main focus of this thesis.

A detailed description of various relevant nonlocal models is provided in the next chapter, particularly of the SNB, eigenvector integral closure (EIC) (Ji et al. 2009) and non-Fourier Landau-fluid (NFLF) (Dimits et al. 2014) models which shall be explored in detail throughout the remainder of the thesis. First principles (i.e. kinetic) approaches such as Vlasov-Fokker-Planck that will be used as valuable benchmarks for the nonlocal models will also be described in this chapter along with its relation to the standard classical transport formulation for fluid-based plasma simulation. Following this the exact numerical implementation of the codes and models used in this thesis will be outlined in chapter 3.

Testing of the nonlocal models in unmagnetised regimes shall be presented in chapters 4 to 6. Firstly, the performance of the models in predicting the damping of a low-amplitude temperature sinusoid (often referred to as the Epperlein Short test), where valuable analytical progress can be made, shall be evaluated in great detail in chapter 4. While this is far from the first time such a study has taken place, a number of new insights are unveiled through the step-by-step process that is taken, such as how to tune some of the nonlocal models to capture limiting behaviour more accurately. More relevant test problems with large relative temperature differences will then be presented in chapter 5. The finding here will be that, given that care is taken with implementation, the SNB model is the most successful at replicating kinetic results. However, it will be shown that the model still has some failings such as overestimating both thermal conduction in the low density hohlraum gas fill and preheat. Chapter 6 then shows the impact of incorporating the implementation suggested by this thesis in a number of important inertial fusion code.

Finally, Chapter 7 explores the crossover between nonlocality and magnetised transport by studying fully-kinetic magnetised Vlasov-Fokker-Planck (VFP) simulations. The SNB model will again be investigated as a potentially accurate and efficient way to account for nonlocal modifications to the 'Nernst' advection of magnetic fields down temperature gradients.

Conclusions will be presented in chapter 8, with appendices to follow. The first of these, appendix A, will contain suggested coefficients for the NFLF model while the seconds consists of various derivations and proofs that were too lengthy or distracting to provide in the main body. Definitions of various symbols, terms and abbreviations can be found beyond this, while bibliographic references are provided at the very end.

2

THEORETICAL BACKGROUND

The long-range nature of the Coulomb interaction between charged particles, means that plasmas are inherently a complex state of matter to model. Things get even more complicated if an attempt is made to actually predict the various ionisation and energy states of the ions, which generally requires sophisticated reduced models based on quantum mechanics. Fortunately, the defining ability of a plasma to screen out localised charge imbalances over the scale of the Debye length provides some degree of simplification. The Debye length is defined as

$$\lambda_{\mathrm{D}} = \sqrt{\frac{\varepsilon_0 k_{\mathrm{B}} T_{\mathrm{e}}}{n_{\mathrm{e}} e^2}} \tag{2.0.1}$$

and is usually much smaller than length scales of interest. This 'Debye screening' is possible if the number of electrons within a Debye sphere $n_{\mathrm{e}}\lambda_{\mathrm{D}}^3 \gg 1$ and allows long-range collective interactions to be treated separately from short-range 'collisional' interactions within the Debye sphere.

As the focus of this thesis concerns the interplay of electron heat transport with magnetic fields, the ionisation, density and Coulomb logarithm profiles shall generally be imposed and kept constant rather than simulated. For this reason, equations for ion motion and transport shall be neglected, except in some simulations performed by collaborators at LLNL with the HYDRA code. Furthermore, all forms of plasma-neutral interaction are neglected in this thesis.

Of course it is unfeasible to simulate individual particles, as even in tokamaks electron number densities can exceed 10^{13} cm^{-3} (Boyd and Sanderson 2003, p. 10, fig 1.4). There are therefore two main levels of simplification used in modelling plasmas: kinetic and hydrodynamic. Kinetic approaches takes into account some of the fine-scale features of the plasma at different points in space, most importantly the distinct behaviour of electrons with different velocities at a single spatial location, while the hydrodynamic assumes a local equilibrium and thus expects each species to follow a Maxwell-Boltzmann distribution. The method most applicable to accurately predicting the evolution of the electron distribution function directly for the moderately collisional transport problems of interest in this thesis is the Vlasov-Fokker-Planck (VFP) approach .

Another method of modelling plasmas kinetically is offered by particle-in-cell (PIC) codes, which simulate a large number of macroparticles (typically between

10^4 and 10^6) in each cell of a spatial grid. The net electric charge and current in each cell is calculated and used to obtain macroscopic electromagnetic fields by solving Maxwell's equations. Acceleration of the particles is then provided by these fields. Particle-in-cell codes are particularly effective on extremely short timescales where local collisions are not so important and provide a natural way of modelling laser-plasma interactions. However, incorporating an accurate collisional model to capture the interactions between particles in the same cell that lead to equilibration can be very challenging. One popular solution is to use Monte Carlo collisions by only sampling a limited number of interactions per cell (Takizuka and Abe 1977). Nevertheless, this significantly increases computational time and place more stringent requirements on the number of particles per cell required to provide accurate statistics.

2.1 THE VLASOV-FOKKER-PLANCK EQUATION

The Vlasov-Fokker-Planck equation takes a less memory intensive continuum approach that instead considers the evolution of the (one-particle) electron velocity distribution function (EDF) f_e representing the number density of electrons with a given velocity at each spatial location. This is much more efficient at capturing the important physics associated with more energetic electrons that is so important to heat transport. The evolution of the EDF is given by

$$\frac{\partial f_e}{\partial t} + \vec{v} \cdot \vec{\nabla} f_e - \frac{e}{m_e}\left(\vec{E} + \vec{v} \times \vec{B}\right) \cdot \frac{\partial f_e}{\partial \vec{v}} = C_e(f_e), \tag{2.1.1}$$

where $C_e = C_{ee} + C_{ei}$ is the collision operator describing both electron-electron and electron-ion collisions (Boyd and Sanderson 2003, chap. 8) . An intuitive understanding of the VFP equation is formed by viewing it as a continuity equation (such as typical fluid equations) in seven dimensions; specifically, the quantity of electrons with a given velocity at a single spatial location increases when the number of electrons with that velocity travelling into that cell is greater than the amount travelling out of it, or when more electrons are being accelerated towards that velocity than away from it. The collision operator makes sure that the EDF will relax towards a Maxwellian over time and always preserves number density; desirably, collisions with like particles additionally preserve total energy and momentum. The Trubnikov-Rosenbluth (Trubnikov 1965; Rosenbluth et al. 1957) expression for the collision operator can be derived by considering the net

'One-particle' here refers to the neglection of simultaneous multi-particle interactions giving rise to lasting correlations between the involved particles. As long as the collision frequency is sufficiently slower than the plasma frequency $\omega_{pe} = v_{1T}/\lambda_D$ these should not be important and the plasma can be treated as Markovian (Boyd and Sanderson 2003, chap. 12).

effect of the Coulomb collisions between the EDF and a test particle and is given by

$$C_{e\beta}(f_e, f_\beta) = -\Gamma_{e\beta}\frac{\partial}{\partial v_i}\left(\frac{m_e}{m_\beta}f_e\frac{\partial}{\partial v_i}\int\frac{f_\beta}{|\vec{v}-\vec{u}|}\,\mathrm{d}^3\vec{u} - \frac{1}{2}\frac{\partial f_e}{\partial v_j}\frac{\partial^2}{\partial v_i \partial v_j}\int f_\beta|\vec{v}-\vec{u}|\,\mathrm{d}^3\vec{u}\right) \tag{2.1.2}$$

(applying standard Einstein summation over repeated indices). Here we have defined

$$\Gamma_{e\beta} = 4\pi\left(\frac{Z_e Z_\beta e^2}{4\pi m_e \varepsilon_0}\right)^2 \log\Lambda_{e\beta}, \tag{2.1.3}$$

where $Z_i = Z$ is the average ionisation and $Z_e = -1$, along with m_i the ion mass.

The Coulomb logarithm is a measure of the importance of small-angle collisions over large-angle and is often given as the logarithmic ratio of the Debye length to impact parameter for perpendicular deflection $b_{90} = |Z_e Z_i e^2/4\pi\varepsilon_0 m_{e\beta} v_{1T}^2|$ (where $m_{e\beta} = m_e m_\beta/(m_e m_\beta)$). Strictly speaking, $\log\Lambda$ should be velocity dependent (Cooper and Herman 1973) but this feature is not considered in the derivation of most transport and always neglected in the VFP codes used in this thesis. Many texts provide different expressions for the Coulomb logarithm often taking into account that use of the de Broglie wavelength $\lambda_B = \hbar/2m_{e\beta}v_{1T}$ is necessary in place of the impact parameter for fast moving electrons (with energy $\epsilon \gtrapprox 10Z^2$ eV), and four examples (for cold ions $T_i < m_e T_e/m_i$) are provided here for comparison,

$$\log\Lambda_{e\beta} = \log(\lambda_D/b_{90}), \qquad \text{(Boyd and Sanderson 2003)}$$

$$\log\Lambda_{ei} = \log(3\lambda_D/\max(b_{90}, \lambda_B)), \qquad \text{(NRL, Huba 2016)}$$

$$\log\Lambda_{ei} = \log(\lambda_D/2\sqrt{2\pi}\lambda_B) + \tfrac{1}{2}(\log(16\pi) - \gamma_E - 1), \qquad \text{(BPS, Brown et al. 2005)}$$

$$\log\Lambda_{ei} = \frac{1}{2}\log\left(1 + \sqrt{\frac{\lambda_D^2 + R_i^2}{\lambda_B^2 + b_{90}^2}}\right). \qquad \text{(GMS, Gericke et al. 2002)}$$

where $\gamma_E = 0.5772\ldots$ is the Euler-Mascheroni constant and $R_i = \sqrt[3]{3/4\pi n_i}$ is the effective ion radius. A brief scan of the literature (Ma et al. 2014; Kodanova et al. 2014; Zhao 2017) seems to suggest that it is still inconclusive whether the BPS or GMS formula is more accurate. For a more involved approach also see Mulser et al. 2014. However, deliberations on the Coulomb logarithm are not relevant to the conclusions of this thesis as a constant Coulomb logarithm is generally imposed and calibrated for comparison tests.

In VFP codes, the associated ion distribution function f_i is typically assumed to be Maxwellian, and all codes used in this thesis, except for KIPP, assume a cold ion population and neglect terms of order $m_\mathrm{e}/m_\mathrm{i}$ (eliminating electron-ion energy equilibration), simplifying the electron-ion collision operator to:

$$C_\mathrm{ei}(f_\mathrm{e}, n_\mathrm{i}\delta(v)) = n_\mathrm{i}\Gamma_\mathrm{ei}\frac{\partial}{\partial v_i}\left(\cancel{\frac{m_\mathrm{e}}{m_\mathrm{i}}\frac{v_i}{v^3}f_\mathrm{e}} + \overbrace{\frac{v^2\delta_{ij} - v_i v_j}{2v^3}\frac{\partial f_\mathrm{e}}{\partial v_j}}^{0}\right), \tag{2.1.4}$$

where $\delta(v)$ is the Dirac delta function and δ_{ij} is the Kronecker delta tensor. Note that if there are multiple ion species with a combined density n_i then the total effect on electrons colliding with each species can be obtained by replacing Z_i with the root mean square ionisation $Z_* = \sqrt{\langle Z^2\rangle}$. Throughout this thesis, Z will simply be used as a shorthand for Z_* in cases when multiple ionisation states are present.

The collision operator only considers small-angle scattering, which is valid as long as the Coulomb logarithm is sufficiently greater than unity. As a rule of thumb, the VFP approach is only accurate to within $1/\log\Lambda$, but so are all methods derived from it, such as hydrodynamics. Plasmas with small Coulomb logarithms are typically high temperature or low density and referred to as strongly coupled. Examples relevant to ICF include the cooler part of the partially ionised hohlraum wall or the stagnation phase of capsule implosions. In such situations quantum effects such as degeneracy often come into play and therefore require more novel modelling approaches (Sijoy et al. 2017).

In retaining details of fine scale structure and predicting deviations from a Maxwellian, the EDF is a very powerful tool that allows many macroscopic features of interest to be calculated directly by taking moments in velocity space—for example, the electron number density $n_\mathrm{e} = \int f_\mathrm{e}\,\mathrm{d}^3v$, the electric current density $\vec{j} = -e\int \vec{v} f_\mathrm{e}\,\mathrm{d}^3v$ (as the ions are assumed to be stationary in this thesis), the electron pressure $P_\mathrm{e} = \frac{1}{3}m_\mathrm{e}\int v^2 f_\mathrm{e}\,\mathrm{d}^3v$ and the electron heat flow $\vec{Q} = \frac{1}{2}m_\mathrm{e}\int v^2\vec{v} f_\mathrm{e}\,\mathrm{d}^3v$. The calculation of the magnetic and electric fields appearing in the VFP equation can be determined through Faraday's law and the Ampère-Maxwell law respectively. For the latter case, the displacement current is often removed to eliminate transient features occurring at the plasma frequency, greatly increasing the minimum viable timestep for explicit codes. Nevertheless, Ampère's law still provides a sufficient closure for obtaining the electric field through an integral constraint on the electric current $\vec{j} = -e\int v f_\mathrm{e}\,\mathrm{d}^3v = \vec{\nabla}\times\vec{B}/\mu_0$ which can be applied to the VFP equation itself.

2.1.1 *Gyro-averaging*

Due to the high dimensionality of the VFP equation it is often not computationally tractable to solve without some simplification, often through taking advantage of symmetry. For the case where variations only occur along magnetic field lines, symmetry in the perpendicular direction allows for elimination of the magnetic field by 'gyro-averaging' (integrating azimuthally around the $v_\parallel$ axis, this process is still valid even in the absence of magnetic fields by instead using the axis parallel to gradients in macroscopic plasma parameters such as density and temperature; this yields the 1D2V (one-dimensional in space, two-dimensional in velocity) 'drift kinetic equation' (DKE)

$$\frac{\partial f_\mathrm{e}}{\partial t} + v_\parallel \frac{\partial f_\mathrm{e}}{\partial s_\parallel} - \frac{eE_\parallel}{m_\mathrm{e}} \frac{\partial f_\mathrm{e}}{\partial v_\parallel} = C_\mathrm{e}(f), \tag{2.1.5}$$

where f_e and C_e now represent their gyro-averaged forms, and $\parallel$ denotes components of vectors parallel to the magnetic field. While the gyro-averaged collision operator can be derived quite straightforwardly from eq. (2.1.2) by using cylindrical coordinates and assuming azimuthal symmetry, its exact form is fairly cumbersome and the reader is referred to (Xiong et al. 2008; Chankin et al. 2012) for more details.

2.1.2 *Cartesian Tensor/Spherical Harmonics expansion*

Sometimes the strong symmetry appropriate for gyro-averaging is broken by spatial gradients perpendicular to the magnetic field, or in more than one direction in the absence of magnetic field. Furthermore, even the use of two velocity dimensions can be restrictive, mainly because a Cartesian grid does not capture the more egg-shaped nature typical of the EDF at higher collisionalities. An alternative way to reduce the dimensionality of the VFP equation is to perform an expansion in increasing degrees of anisotropy, this is convenient for problems of high and moderate collisionality as collisions reduce the degree of anisotropy. Two different bases that take advantage of the structure of the electron-ion collision operator have been used to perform this expansion—Cartesian tensors

$$f_\mathrm{e}(\vec{v}) = f_0(v) + \frac{v_i}{v} f_{1i}(v) + \frac{v_i v_j}{v^2} f_{2ij}(v) + \ldots \tag{2.1.6}$$

and (unnormalised) spherical harmonics.

$$f_\mathrm{e}(\vec{v}) = \sum_l \sum_{m=-l}^{l} f_m^l(v)\mathrm{P}_l^m(\cos\theta)\mathrm{e}^{im\phi}, \tag{2.1.7}$$

in spherical coordinates where P_l^m are the associated Legendre polynomials. Both conventions lead to a reduction of the number of velocity dimensions to one and have been shown to be essentially equivalent to each other by Johnston (1960). The first few terms in the expansion can be quite easily understood by analogy with a more familiar fluid treatment—the isotropic part of the EDF corresponds to field quantities and can be used to calculate the macroscopic variables

$$n_\mathrm{e} = 4\pi \int_0^\infty v^2 f_0 \,\mathrm{d}v, \quad P_\mathrm{e}^{(\mathrm{Isotropic})} = \frac{4\pi}{3}\int_0^\infty m_\mathrm{e} v^4 f_0 \,\mathrm{d}v, \tag{2.1.8}$$

while the first order anisotropy $\vec{f}_1$ pertains to flow quantities

$$\vec{j} = \frac{4\pi}{3}\int_0^\infty \vec{f}_1 \,\mathrm{d}v, \quad \vec{Q} = \frac{4\pi}{3}\int_0^\infty m_\mathrm{e} v^2 \vec{f}_1 \,\mathrm{d}v. \tag{2.1.9}$$

As a final example, the second order anisotropy plays a role in determining the anisotropic pressure tensor

$$P_{\mathrm{e}ij}^{(\mathrm{Anisotropic})} = \tfrac{1}{3} m_\mathrm{e} \int_0^\infty v_i v_j f_\mathrm{e} \,\mathrm{d}^3 v = \frac{4\pi}{3}\int_0^\infty m_\mathrm{e} v^4 \left(\frac{\delta_{ij}}{3} f_0 + \frac{2}{5} f_{2ij}\right) \mathrm{d}v \tag{2.1.10}$$

by invoking the fact that $\overleftrightarrow{f}_2$ is traceless.

The equations for the evolution of the first three terms are given by

$$\frac{\partial f_0}{\partial t} + \frac{v}{3}\vec{\nabla}\cdot\vec{f}_1 - \frac{e\vec{E}}{3m_\mathrm{e}v^2}\cdot\frac{\partial v^2 \vec{f}_1}{\partial v} = C_0 \tag{2.1.11}$$

$$\frac{\partial \vec{f}_1}{\partial t} + v\vec{\nabla} f_0 + \frac{2}{5} v\vec{\nabla}\cdot\overleftrightarrow{f}_2 - \frac{e\vec{E}}{m_\mathrm{e}}\frac{\partial f_0}{\partial v} - \frac{e\vec{E}}{3m_\mathrm{e}v^3}\cdot\frac{\partial v^3 \overleftrightarrow{f}_2}{\partial v} - \frac{e}{m_\mathrm{e}}(\vec{B}\times\vec{f}_1) = C_1 \tag{2.1.12}$$

$$\frac{\partial \overleftrightarrow{f}_2}{\partial t} + v\overleftarrow{\nabla}\vec{f}_1 - \frac{v}{3}\vec{\nabla}\cdot\vec{f}_1 - \frac{ve}{m_\mathrm{e}}\frac{\partial}{\partial v}\left(\frac{\overleftarrow{E}\vec{f}_1 - \frac{1}{3}\vec{E}\cdot\vec{f}_1\overleftrightarrow{I}}{v}\right) - \frac{e}{m_\mathrm{e}}(\vec{B}\times\overleftrightarrow{f}_2) = C_2 \tag{2.1.13}$$

and so on (Thomas et al. 2012), where $\overleftrightarrow{I}$ is the identity tensor, $(\vec{B}\times\overleftrightarrow{f}_2)_{ij} = B_k(\epsilon_{ikn}f_{2jn} + \epsilon_{jkn}f_{2in})$ and $(\overleftarrow{A}\vec{B})_{ij} = (A_iB_j + A_jB_i)/2$. Additionally, the contribution of the third order anisotropy f_{3ijk} to the $\overleftrightarrow{f}_2$ equation (2.1.13) has been neglected. This truncation of the expansion beyond the desired degree of anisotropy is generally referred to as a 'polynomial' closure, and the equation set presented here corresponds to what is called a P2 closure.

While the isotropic part of the distribution function is only directly affected by electron-electron collisions,

$$C_0 = C_{ee0} = \frac{4\pi\Gamma_{ee}}{v^2}\frac{\partial}{\partial v}\left(\int_0^v f_0 u^2\,\mathrm{d}u f_0 + \frac{1}{v}\int_0^v u^2\int_u^\infty f_0 w\,\mathrm{d}w\,\mathrm{d}u\frac{\partial f_0}{\partial v}\right) \tag{2.1.14}$$

both electron-electron and electron-ion collisions contribute at higher orders of anisotropy

$$C_n = -\frac{n(n+1)}{2}\nu_{ei} f_n + C_{een} \tag{2.1.15}$$

to zeroth order in the electron-ion mass ratio, where

$$\nu_{ei} = \frac{n_i\Gamma_{ei}}{v^3} = \left(\frac{e^2}{m_e\varepsilon_0}\right)^2\frac{Zn_e\log\Lambda_{ei}}{4\pi v^3} \tag{2.1.16}$$

is the velocity-dependent electron-ion collision frequency.

2.1.3 *The Collision Fix*

The operators describing the consequence of electron-electron collisions on higher order anisotropies, C_{een}, are unfortunately quite cumbersome to represent, and can be very challenging to solve in implicit VFP codes such as IMPACT. As e-e collisions are a factor of Z less frequent than e-i, their effect at very high ionisation charges (i.e. the Lorentz limit where $Z \gg 1$) can be neglected. At moderate collisions their effect is often approximated by simply modifying the e-i frequency to $\nu_{ei}^* = \nu_{ei}/\xi$, where the collision fix ξ is often used to recover the correct ionisation dependence of the parallel thermal conductivity in the local limit. A popular choice for the collision fix is $\xi_{ES} = (Z+0.24)/(Z+4.2)$ (Epperlein and Short 1991). One particular issue with this approach that is explored in more detail in section 2.4, is that it can sometimes get other transport coefficients wrong; of significance to the work in this thesis, Nernst advection (formalised below in section 2.2.2) in low-Z plasmas can be overestimated by factor exceeding two when using the naïve collision fix approach. Therefore, simulating magnetised transport effects at low ionisations it is imperative to use the full electron-electron collision operators C_{een}.

2.1.4 *An 'Entropic' Closure*

One particular issue with both the Cartesian tensor and spherical harmonic expansion, is that truncation at a finite order allows for parts of the distribution to be negative, typically at higher velocities. As this is clearly unphysical an alternative method of expansion, denoted by MN (e.g. M1, M2, etc.), which guarantees positive-definiteness has been suggested and is given by

$$f_\mathrm{e} = \exp\left(\alpha_0 + \frac{v_i}{v}\alpha_{1i} + \frac{v_i v_j}{v^2}\alpha_{2ij} + \dots\right). \tag{2.1.17}$$

This conveniently coincides with the form for the EDF obtained by maximising the local angular entropy given the first $N+1$ moments

$$H_v[f_\mathrm{e}] = -\int f_\mathrm{e}\log f_\mathrm{e} - f_\mathrm{e}\,\mathrm{d}^2\Omega, \tag{2.1.18}$$

where integration is performed over all solid angle for a given speed v. For the case of truncation after the first-order anisotropy, i.e. an MN expansion, the alpha coefficients (which are in fact Lagrange multipliers) fortunately do not need to be solved for directly and the Cartesian tensor eqs. (2.1.11) and (2.1.12) can still be used with the new 'entropic' approach merely providing a new closure for

$$\overleftrightarrow{f}_2 \approx \frac{15}{4}\varsigma^2(1+\varsigma^2)\left(\frac{\overleftarrow{f}_1\overrightarrow{f}_1}{\left|\overrightarrow{f}_1\right|^2} - \frac{\overleftrightarrow{I}}{3}\right), \tag{2.1.19}$$

where $\varsigma = |\overrightarrow{f}_1/f_0|$. (For more details on the MN approach see Dubroca et al. 2010; Del Sorbo et al. 2015; Del Sorbo 2015; Touati et al. 2014).

2.2 CLASSICAL TRANSPORT THEORY

A much simpler approach to modelling quasineutral plasmas is to treat them as electrically conducting fluids. For a cold stationary ion background, continuity equations charge density $\rho = e(n_\mathrm{i} - n_\mathrm{e})$, electric current and electron pressure can be obtained by taking moments of VFP equation.

$$\frac{\partial\rho}{\partial t} + \overrightarrow{\nabla}\cdot\overrightarrow{j} = 0 \tag{2.2.1}$$

$$\frac{\partial\overrightarrow{j}}{\partial t} - \frac{e}{m_\mathrm{e}}\overrightarrow{\nabla}P_\mathrm{e} = \frac{e}{m_\mathrm{e}}\left(n_\mathrm{e}e\overrightarrow{E} - \overrightarrow{j}\times\overrightarrow{B} - \overrightarrow{R}_\mathrm{ei}\right) \tag{2.2.2}$$

$$\frac{3}{2}\frac{\partial P_\mathrm{e}}{\partial t} + \overrightarrow{\nabla}\cdot\overrightarrow{Q} - \overrightarrow{E}\cdot\overrightarrow{j} = 0 \tag{2.2.3}$$

where $\vec{R}_{\mathrm{ei}}$ is a dissipative friction term arising from electron-ion collisions, $\vec{Q}$ is the heat flow and $\vec{E} \cdot \vec{j}$ term is known as Joule heating. The electron pressure has here been assumed isotropic by enforcing the P1 closure, and the mean electron flow velocity $\vec{u}_{\mathrm{e}} = -\vec{j}/en_{\mathrm{e}}$ is assumed to be much smaller than the thermal velocity $v_{2\mathrm{T}} = \sqrt{2k_{\mathrm{B}}T_{\mathrm{e}}/m_{\mathrm{e}}}$ so that it does not contribute significantly to the pressure moment. To further simplify the fluid model the electron inertia term ($\frac{\partial \vec{j}}{\partial t}$) is often neglected along with the displacement current in the Ampère-Maxwell law, this is justified for cases when the electric field varies on a similar timescale to the macroscopic plasma parameters but relinquishes the ability of directly capturing the effect of electromagnetic waves on the plasma. Consequently, the electric current adapts instantaneously to changes in the electric and magnetic fields according to

$$\vec{j} = \frac{\vec{\nabla} \times \vec{B}}{\mu_0}. \tag{2.2.4}$$

As the electric current is now guaranteed to be divergence free, it is impossible for charge imbalance to arise and eq. (2.2.1) can be neglected. Therefore, it is only the evolution of the electron temperature along with the magnetic field that remain as true evolution equations of interest. (Ohm's law is still relevant but should no longer be considered an 'evolution' equation due to the neglection of electron inertia and is now a simple equality.)

$$\frac{\partial T_{\mathrm{e}}}{\partial t} = \frac{2}{3n_{\mathrm{e}}k_{\mathrm{B}}}(-\vec{\nabla} \cdot \vec{Q} + \vec{E} \cdot \vec{j}), \tag{2.2.5}$$

$$\frac{\partial \vec{B}}{\partial t} = -\vec{\nabla} \times \vec{E}. \tag{2.2.6}$$

2.2.1 *The Chapman-Enskog approach to deriving transport coefficients*

While an evolution equation for the heat flow could of course be obtained by taking the appropriate moment of the VFP equation, this would again correspond to an even higher moment of the EDF. This hierarchy of equations needs to be closed somewhere, and the classical approach chooses to do so by finding an expression for $\vec{Q}$ (and $\vec{R}_{\mathrm{ei}}$) in terms of lower order moments (n_{e}, $\vec{j}$, T_{e}). The method used to obtain this 'closure' is the Chapman-Enskog expansion (Chapman et al. 1953).

Central to the Chapman-Enskog method is the idea that, in the limit of high collisionality, the distribution function can be expanded about a Maxwellian in

increasing degrees of nonlocality (indicated by the Knudsen number $\mathrm{Kn}{\sim}\lambda_{\mathrm{ei}}^{(\mathrm{B})}/L_T$) based solely on its macroscopic parameters

$$f_\mathrm{e} = f_\mathrm{e}^{(\mathrm{mb})} + \mathrm{Kn} f_\mathrm{e}^{(1)} + \mathrm{Kn}^2 f_\mathrm{e}^{(2)} + \ldots \tag{2.2.7}$$

The expansion is performed sequentially by substituting the n-th order expansion into the left-hand side of the VFP equation, to obtain to the $n+1$-th term by inverting the collision operator. The nature of $f_\mathrm{e}^{(1)}$ is best understood by considering the Cartesian tensor (or spherical harmonic) expansion of the VFP equation laid out in eqs. (2.1.11) to (2.1.13); the base Maxwellian term will clearly contribute on the left-hand side of the $\vec{f}_1$ equation (2.1.12) meaning that the first correction $f_\mathrm{e}^{(1)}$ will contain an anisotropic component related to $\vec{f}_1$. The only other place where an isotropic Maxwellian would contribute is through the $\frac{\partial f_0}{\partial t}$ term in eq. (2.1.11), but as this is second order in Kn we can conclude that $f_\mathrm{e}^{(1)}$ *only* contributes towards the first-order anisotropy $\vec{f}_1$. Labelling the anisotropy and electric field arising with this first correction as $\vec{f}_1^{(\mathrm{mb})}$ and respectively $\vec{E}^{(\mathrm{mb})}$, the equation that must be solved is

$$\frac{e}{m_\mathrm{e}}(\vec{B} \times \vec{f}_1^{(\mathrm{mb})}) - \nu_{\mathrm{ei}} \vec{f}_1^{(\mathrm{mb})} + C_{\mathrm{eel}}\left[f_\mathrm{e}^{(\mathrm{mb})}, \vec{f}_1^{(\mathrm{mb})}\right] = v\vec{\nabla} f_\mathrm{e}^{(\mathrm{mb})} - \frac{e\vec{E}^{(\mathrm{mb})}}{m_\mathrm{e}} \frac{\partial f_\mathrm{e}^{(\mathrm{mb})}}{\partial v}. \tag{2.2.8}$$

A number of methods have been used to solve this equation, Spitzer and Härm (1953) tackled the zero magnetisation limit using finite differencing, while many other authors, including Braginskii (1965), used a polynomial expansion for $\vec{f}_1$ to incorporate magnetic field effects. Epperlein and Haines (1986) provide a thorough review of the different approaches in the introduction to their paper, which provides significant accuracy improvements upon Braginskii by using a finite differencing method. As an illustration of how various transport effects arise, Epperlein (1984) provided an analytic derivation in the Lorentz limit (where C_{eel} can be removed). This is summarised here for the case where spatial gradients are perpendicular to the magnetic field and begins by inverting combination of collision operate on the left-hand side giving

$$\vec{f}_1^{(\mathrm{mb})} = -\frac{\nu_{\mathrm{ei}} + \vec{\omega}_{\mathrm{ce}}\times}{{\nu_{\mathrm{ei}}}^2 + \omega_{\mathrm{ce}}^2}\left(\frac{\vec{\nabla} n_\mathrm{e}}{n_\mathrm{e}} + \left(\frac{m_\mathrm{e} v^2}{2k_\mathrm{B}T_\mathrm{e}} - \frac{3}{2}\right)\frac{\vec{\nabla} T_\mathrm{e}}{T_\mathrm{e}} + \frac{e\vec{E}^{(\mathrm{mb})}}{k_\mathrm{B}T_\mathrm{e}}\right) v f_\mathrm{e}^{(\mathrm{mb})}, \tag{2.2.9}$$

where $\vec{\omega}_{ce} = e\vec{B}/m_e$ is the cyclotron frequency directed in the direction of the magnetic field. Expressions for the electric current and heat flow can be found by taking the appropriate moment,

$$\frac{\Gamma_{ei}\vec{j}}{en_e} = \frac{\langle v^5\rangle}{3}\frac{\vec{\nabla}P_e}{P_e} + \frac{5\langle v^5\rangle - m_e\langle v^7\rangle/k_BT_e}{6}\frac{\vec{\nabla}T_e}{T_e} + \frac{\langle v^5\rangle}{3}\frac{e\vec{E}^{(mb)}}{k_BT_e} \tag{2.2.10}$$
$$+ \frac{\vec{\Omega}}{v_{2T}^3}\times\left(\frac{\langle v^8\rangle}{3}\frac{\vec{\nabla}P_e}{P_e} + \frac{5\langle v^8\rangle - m_e\langle v^{10}\rangle/k_BT_e}{6}\frac{\vec{\nabla}T_e}{T_e} + \frac{\langle v^8\rangle}{3}\frac{e\vec{E}^{(mb)}}{k_BT_e}\right)$$
$$\frac{\Gamma_{ei}\vec{Q}}{n_e} = -\frac{\langle v^7\rangle}{6}\frac{\vec{\nabla}P_e}{P_e} - \frac{5\langle v^7\rangle - m_e\langle v^9\rangle/k_BT_e}{12}\frac{\vec{\nabla}T_e}{T_e} - \frac{\langle v^7\rangle}{6}\frac{e\vec{E}^{(mb)}}{k_BT_e} \tag{2.2.11}$$
$$- \frac{\vec{\Omega}}{v_{2T}^3}\times\left(\frac{\langle v^{10}\rangle}{3}\frac{\vec{\nabla}P_e}{P_e} + \frac{5\langle v^{10}\rangle - m_e\langle v^{12}\rangle/k_BT_e}{6}\frac{\vec{\nabla}T_e}{T_e} + \frac{\langle v^{10}\rangle}{3}\frac{e\vec{E}^{(mb)}}{k_BT_e}\right)$$

where $\vec{\Omega} = \vec{\omega}_{ce}/\nu_{ei}^{(0)}$ (with $\nu_{ei}^{(0)} = \nu_{ei}(v_{2T})$) and $\langle v^n\rangle = 4\pi\int_0^\infty v^{n+2}f_e^{(mb)}\,dv/n_e$. The final step is to rearrange eq. (2.2.10) for the electric field and then substitute into eq. (2.2.11) resulting in

$$\vec{Q} = -\overleftrightarrow{\kappa}\cdot\vec{\nabla}k_BT_e - \frac{k_BT_e}{e}\overleftrightarrow{\beta}\cdot\vec{j}, \tag{2.2.12}$$
$$en_e\vec{E} = -\vec{\nabla}P_e - n_e\overleftrightarrow{\beta}\cdot\vec{\nabla}k_BT_e + \frac{\overleftrightarrow{\alpha}}{en_e}\cdot\vec{j} + \vec{j}\times\vec{B} \tag{2.2.13}$$
$$\vec{R}_{ei} = -n_e\overleftrightarrow{\beta}\cdot\vec{\nabla}k_BT_e + \frac{\overleftrightarrow{\alpha}}{en_e}\cdot\vec{j}, \tag{2.2.14}$$

where $\overleftrightarrow{\kappa}$, $\overleftrightarrow{\beta}$, $\overleftrightarrow{\alpha}$ are the thermal conductivity, thermoelectric and resistivity tensors respectively. These tensors are best understood using a basis aligned to the magnetic field and the driving force (either the temperature gradient or current density, denoted generally by $\vec{s}$) consisting of the parallel direction '$\parallel$' pointing in the direction of the magnetic field, the perpendicular direction '$\perp$' corresponding to the component of driving force that is perpendicular to the magnetic field, and the wedge direction '$\wedge$' perpendicular to both (i.e. parallel to $\vec{B}\times\vec{s}$). In this basis, the action of a transport coefficient on the parallel component of the driving force is a simple scaling but an additional rotation towards the $\wedge$ direction is provided when acting on the perpendicular component . This can be understood by representing the transport coefficients $\overleftrightarrow{\kappa}$, $\overleftrightarrow{\beta}$, $\overleftrightarrow{\alpha}$ generically by

$$\overleftrightarrow{A} = \begin{pmatrix} A_\parallel & 0 & 0 \\ 0 & A_\perp & 0 \\ 0 & A_\wedge & 0, \end{pmatrix} \tag{2.2.15}$$

although it doesn't really makes sense to assign values to the third column as the third component of the driving force is always zero by definition. In the absence of magnetic fields this formulation can still be applied as long by freely choosing a 'direction' for the zero magnetic field (thus breaking the symmetry) as all 'wedge' transport coefficients tend to zero and the parallel and perpendicular coefficient equalise;

The transport coefficients depend on a number of macroscopic plasma parameters. However, the transport coefficients can be conveniently separated into dimensional and dimensionless parts. Using the notation of Epperlein and Haines (1986), the latter is generally denoted by the subscript $_c$ depending only on ionisation Z and the magnetisation $\chi = \omega_{ce}\tau_{ei}^{(B)}$ and

$$\tau_{ei}^{(B)} = 3\sqrt{\frac{\pi}{2}}\left(\frac{4\pi\varepsilon_0}{e^2}\right)^2 \frac{\sqrt{m_e}T_e^{3/2}}{4\pi Z n_e \log\Lambda_{ei}} \tag{2.2.16}$$

is the Braginskii electron-ion collision time (Braginskii 1965). While the thermoelectric tensor $\overleftrightarrow{\beta}$ is already in dimensionless form, the other two transport coefficients can be represented as

$$\overleftrightarrow{\kappa} = \frac{n_e T_e \tau_{ei}^{(B)}}{m_e}\overleftrightarrow{\kappa}_c, \quad \overleftrightarrow{\alpha} = \frac{m_e n_e}{\tau_{ei}^{(B)}}\overleftrightarrow{\alpha}_c. \tag{2.2.17}$$

With respect to dependence on magnetisation, the parallel component always equals the perpendicular in the absence of any magnetic fields. As χ increases both the perpendicular thermal conductivity $\kappa_\perp$ and thermoelectric coefficient $\beta_\perp$ decrease as a result of the desirable thermal insulating properties of magnetic fields, while the resistivity tensor instead increases. On the other hand the wedge components are zero in the limit of no magnetic field and then increase up to a moderate magnetisation (between 0.1 and 10) before decreasing again. See fig. 1 of (Epperlein and Haines 1986) for a nice illustration of this.

A numerical approximation for the variation of the dimensionless coefficients with ionisation and magnetisation can be found in (Epperlein and Haines 1986). Integral expressions for three transport coefficients relevant to this thesis are reproduced here in the Lorentz and low magnetisation limit from (Epperlein 1984),

$$\kappa_\perp^c = \frac{8}{9\sqrt{\pi}}\left(\langle V^9\rangle - \frac{\langle V^7\rangle^2}{\langle V^5\rangle}\right), \tag{2.2.18}$$

$$\kappa_\wedge^c = \frac{8}{9\sqrt{\pi}}\Omega\left(\langle V^{12}\rangle - 2\frac{\langle V^{10}\rangle\langle V^7\rangle}{\langle V^5\rangle} - \frac{\langle V^7\rangle^2\langle V^8\rangle}{\langle V^5\rangle^2}\right), \tag{2.2.19}$$

$$\beta_\wedge^c = \Omega\Big(\frac{\langle V^{10}\rangle}{\langle V^5\rangle} - \frac{\langle V^8\rangle\langle V^7\rangle}{\langle V^5\rangle^2}\Big), \tag{2.2.20}$$

where the use of capital $V = v/v_{2\mathrm{T}}$ now denotes $\langle V^n\rangle = 4\pi\int_0^\infty v_{2\mathrm{T}}^3 V^{n+2} f_\mathrm{e}^{(\mathrm{mb})}\,\mathrm{d}V/n_\mathrm{e}$.

2.2.2 *Common Names for Specific Transport Phenomena*

While the tensor formulation above for the closure of the heat flux and electric fields encapsulates a number of phenomena in a very compact and convenient manner, physicists, being physicists, have taken to naming most of the individual effects that arise from these equations. The given names are detailed below (heat flux effects first followed by electric field effects) and usually originate from historical experimental discoveries concerning thermoelectric materials other than plasmas. Due to the MCF part of this thesis being focussed purely on parallel transport, the relevance of the various transport phenomena discussed here will only be considered for inertial fusion. The most relevant term for this thesis is the Nernst effect, for which nonlocal effects are investigated in detail in chapter 7.

Ettingshausen Effect

A rather interesting phenomenon involving the transport of heat towards region of greater magnetic fields is the Ettingshausen effect. This stems from the contribution of the $\beta_\wedge$ coefficient to the perpendicular heat flow

$$Q^{(\mathrm{Ettingshausen})}_{\vec{B}\times\vec{j}} = \frac{k_\mathrm{B}T_\mathrm{e}}{e}\beta_\wedge j. \tag{2.2.21}$$

This term only becomes comparable to thermal conduction when either magnetisation or the magnetic field gradients become very large and is not important in conventional inertial fusion. However, one scenario where Ettingshausen could become significant is magnetised liner inertial fusion (García-Rubio and Sanz 2018) where strong magnetic fields could help insulate the hot spot.

Righi-Leduc Heat Flow

The Righi-Leduc heat flow simply refers to the heat flux perpendicular to both the magnetic field and the temperature gradient. This can be thought of as the partial deflection of the heat flux due to the magnetic field and is given by

$$Q^{(\mathrm{RL})}_{\vec{B}\times\vec{\nabla}T_\mathrm{e}} = -\kappa_\wedge \nabla_\perp k_\mathrm{B}T_\mathrm{e} \tag{2.2.22}$$

The potential of the Righi-Leduc heat flow to inconveniently reduce hot spot temperatures in indirect drive implosions was demonstrated recently by Walsh et al. (2017).

Peltier Effect

The heat flow associated with the electric current is termed the Peltier effect

$$Q_{\vec{j}}^{(\text{Peltier})} = \frac{k_\text{B} T_\text{e}}{e} \beta_\perp j, \tag{2.2.23}$$

and can also be considered a deflection of the Ettingshausen heat flow.

Seebeck Effect

Perhaps the most simple of the thermoelectric effects, the Seebeck effect corresponds to the potential difference set up along a temperature gradient. This of course has two separate contributions given by

$$E_{\nabla_\parallel T_\text{e}}^{(\text{Seebeck})} = -\frac{1+\beta_\parallel}{e} \nabla_\parallel T_\text{e}, \quad E_{\nabla_\perp T_\text{e}}^{(\text{Seebeck})} = -\frac{1+\beta_\perp}{e} \nabla_\perp T_\text{e}. \tag{2.2.24}$$

The parallel electric field will only affect the evolution of the magnetic field if ionisation varies perpendicular to the magnetic field, potentially causing a very slight deflection of the electric field. On the other hand the contribution of the perpendicular Seebeck effect to Faraday's law will exist if the ionisation or magnetisation vary in either the wedge direction or along the magnetic field.

Biermann Battery

Magnetic fields can be created from non-parallel temperature and density gradient by the Biermann battery effect,

$$E_{\vec{\nabla} n_\text{e}} = -\frac{k_\text{B} T_\text{e}}{e n_\text{e}} \vec{\nabla} n_\text{e} \implies \frac{\partial B}{\partial t}^{(\text{Biermann})} = \frac{\vec{\nabla} T_\text{e} \times \vec{\nabla} n_\text{e}}{e n_\text{e}}. \tag{2.2.25}$$

This has proven to be important in both conventional approaches to inertial fusion due to lasers causing temperature gradients that are somewhat normal to the laser beam, while the ablation of the heat material (either the hohlraum wall or the capsule surface) results in density gradients that are almost entirely parallel to the beam. Consequently, magnetic fields azimuthal to the laser beam are generated and have been experimentally observed to reach the megagauss regime (i.e. on the order of ~100 tesla) on both the capsule surface Séguin et al.

2012; Igumenshchev et al. 2014, and hohlraum walls Li et al. 2009. Notably, when plasmas drift out of local equilibrium (i.e. become non-Maxwellian) magnetic fields can be generated even in the absence of density gradients (Kingham and Bell 2002) this is due to the pressure gradient term in the generalised Ohm's law being a simplification of the moment of the electron velocity distribution function that arises from a kinetic approach (see previous section).

Nernst Effect

One of the most important terms affecting the evolution of the magnetic field in the presence of significant temperature gradient is the Nernst effect,

$$E^{(\text{Nernst})}_{\vec{\nabla} T_\text{e} \times \vec{B}} = -n_\text{e} \beta_\wedge \nabla_\perp k_\text{B} T_\text{e} \tag{2.2.26}$$

The dependence of both the Nernst and Ettingshausen effects on the coefficient $\beta_\wedge$ arises from what is known as the Onsager symmetry (Onsager 1931).; however, this can break down for non-Maxwellian plasmas.

The Nernst effect manifests itself as the advection of magnetic field down temperature gradients at the Nernst velocity $v_\text{N} = (-)\beta_\wedge \nabla_\perp k_\text{B} T_\text{e}/eB$. For the case of laser-plasmas v_N typically lies between the ion sound speed and the electron thermal velocity (Willingale et al. 2010), resulting in the build-up of magnetic field at the foot of the temperature gradient, a process known as convective amplification (Nishiguchi et al. 1984). The consequent cavitation of the magnetic field in hot regions of the plasma degrades its desirable insulating properties (Ridgers et al. 2008a); recent indirect-drive simulations have demonstrated that neglecting the effect of Nernst advection on self-generated fields can lead to a 1.5 keV overestimation of the plasma temperature (Farmer et al. 2017).

Resistive Diffusion

The effect of the resistivity tensor is to relax steep magnetic field gradients, as

$$E^{(\text{Resistive Diffusion})}_{\vec{j}} = \frac{\alpha_\perp}{e^2 {n_\text{e}}^2} j \tag{2.2.27}$$

$$\implies \frac{\partial \vec{B}}{\partial t}^{(\text{Resistive Diffusion})} = -\vec{\nabla} \times \left(\frac{\alpha_\perp}{e^2 {n_\text{e}}^2 \mu_0} \vec{\nabla} \times \vec{B} \right). \tag{2.2.28}$$

For the special case where all spatial gradients occur in a single spatial dimension perpendicular to the direction of the magnetic field, this simplifies to a standard

diffusion equation. Using z for the direction of the magnetic fields and x for the direction of spatial gradients we obtain

$$\frac{\partial B_z}{\partial t} = \frac{\partial}{\partial x}\left(\frac{\alpha_\perp}{e^2 {n_\mathrm{e}}^2 \mu_0}\frac{\partial}{\partial x}B_z\right). \tag{2.2.29}$$

On the other hand the wedge component of the resistivity tensor will deflect the diffusion, allowing steep magnetic field gradients to generate magnetic fields in a different direction.

Hall Effect

The final term in eq. (2.2.14) is the Hall effect, $\vec{j} \times \vec{B}$, setting up a potential difference perpendicular to the electric current and the magnetic field. Using vector identities this can be rewritten in terms of the magnetic pressure gradient and the variation of the magnetic field along field lines only, $\vec{j} \times \vec{B} = -\nabla^2 B^2/2\mu_0 + (\vec{B}\cdot\vec{\nabla})\vec{B}/\mu_0$. It is only the latter which contributes to the evolution of the magnetic field and corresponds to the relaxation of magnetic tension. Clearly this term only contributes when the magnetic curvature is very high and was calculated to be negligible for the case of self-generated indirect drive ICF (Farmer et al. 2017) but is of central importance in MAGLIF (Slutz et al. 2010; Slutz and Vesey 2012; Sefkow et al. 2014; Gomez et al. 2014).

2.2.3 *Incorporating Radiation*

One final element relevant to thermal transport is the heating of plasmas by laser light. Electromagnetic waves are able to travel almost unimpeded through a plasma until its electron density exceeds the critical density (where the plasma frequency equals the laser frequency). Beyond this point the plasma is heated through the excitation of resonant waves and the laser energy that is not reflected is completely absorbed over the skin depth c/ω_{pe}. Despite the relative transparency of the underdense plasma, substantial heating can still occur before the critical surface is reached and the dominant process for this is inverse bremsstrahlung.

Only inverse bremsstrahlung (IB) absorption shall be considered in this thesis. It is the oscillation of electron in the laser's electric field followed by thermalising electron-ion collisions that drives IB heating at a rate

$$\frac{3}{2}\frac{\partial P_\mathrm{e}}{\partial t}^{(\mathrm{IB})} = \frac{2\pi n_\mathrm{i} \Gamma_{\mathrm{ei}} m_\mathrm{e} v_{\mathrm{osc}}^2}{3} f_0(v=0), \text{ where } \frac{v_{\mathrm{osc}}}{c} = \sqrt{\frac{I\lambda^2}{1.4\times 10^{18}\,\mathrm{W\,\mu m^2/cm^2}}}$$

is the maximum quiver velocity corresponding to a laser with intensity I and wavelength λ. As the energy gain from quivering is most pronounced among slower electrons, the EDF can actually become distorted towards a super-Gaussian, $e^{-(v/\alpha v_{2T})^m}$ (where $m > 2$ and α is an energy conserving parameter) and therefore reduce the heating rate compared to what would be expected from a Maxwellian (Langdon 1980; Dum 1978b,a). While useful fit functions to approximate this effect have been provided by Matte et al. (1988) and significant modification to transport coefficients are observed when m is high (Ridgers et al. 2008b; Ridgers 2008), the EDF distortion due to IB is often neglected and will also be in this thesis to avoid the possibility of confounding the effect with nonlocal transport. Sensitivity tests have been performed to ensure that such a neglection does not greatly change observed physics. Instead, all fluid codes will assume that f_0 is a Maxwellian when simulating laser heating effects

$$\frac{3}{2}\frac{\partial P_e}{\partial t}^{(MH)} = \frac{\frac{1}{2} n_e m_e v_{osc}^2}{\tau_{ei}^{(B)}} \tag{2.2.30}$$

The definition of the Braginskii collision time $\tau_{ei}^{(B)}$ can be found in eq. (2.2.16) as well as in the List of Symbols.

while kinetic codes will use the 'Maxwellian heating operator', so named for ensuring the EDF remains a Maxwellian in the OD case (, on the right-hand side of eq. (2.1.11)

$$\frac{\partial f_0}{\partial t}^{(MH)} = \frac{v_{osc}^2}{6\tau_{ei}^{(B)} v^2}\frac{\partial}{\partial v}\left(v^2 \frac{\partial f_0}{\partial v}\right) \tag{2.2.31}$$

2.3 NONLOCAL TRANSPORT

In the derivation of the transport coefficients in the previous section the whole method hinged on the assumption that the isotropic part of the distribution function was Maxwellian and the Knudsen number was small. However, as we have seen, this is not always true in fusion plasmas. When the temperature gradients are steep, suprathermal electrons can find themselves in very different plasma conditions before they are scattered or thermalised. As a consequence the EDF becomes distorted, with a deficit of suprathermals at the steepest part of the temperature gradient leading to a reduction in heat flux and a surplus of suprathermals at the foot of the temperature allowing heat flow.

Such distortions in the EDF are ideally captured by careful simulation with VFP codes but of course these are computationally intensive; even in the diffusion approximation the need to keep track of the contribution of electrons of very different velocities in multiple spatial dimensions is memory intensive and

working out how these couple to other 'multiphysics' effects such as radiation, material interaction or equation of state is not usually straightforward. A particular challenge is posed by the rapidity of the plasma oscillation relative to most other timescales of interest, requiring either a time step that resolves the plasma frequency or an implicit approach. Both options greatly increase computational demands, although the explicit treatment can be sped up somewhat by placing artificial multipliers on the plasma permittivity. Furthermore, in ICF the extreme conditions created by the high-energy lasers require a sophisticated mix of Lagrangian and Eulerian gridding systems (known as Adaptive Lagrangian Eulerian or ALE) that are even considerably challenging to implement for hydrodynamical approaches. Therefore it is desirable to consider an alternative approach; one that requires less computational effort than solving the VFP equations but provides a fairly reliable improvement on the local treatment. Such alternative approaches are more generally known as 'reduced nonlocal models' and we shall start with one of the oldest methods of accounting for some of the effects of nonlocality.

2.3.1 *Flux-limiters*

The simplest approach to including the flux-reducing aspect of nonlocal transport is the use of flux-limiters. First incorporated in laser-plasma codes no later than 1975 (Book et al. 1975), the current use of the flux-limiter is as an artificial, numerical upper bound on the heat flux to some proportion f_Q of the free-streaming limit $Q_{\mathrm{fs}} = P_{\mathrm{e}} v_{1\mathrm{T}}$. It is often argued that it is physically impossible for this limit to be exceeded, but this can be countered by the simple example of a heat flux driven by very energetic electrons represented with a distribution function of

$$f_{\mathrm{e}} = \frac{n_{\mathrm{e}} - n_{\mathrm{hot}}}{\pi^{3/2}} \exp\left(- \frac{m_{\mathrm{e}}(\vec{v} + \vec{v}_{\mathrm{return}})^2}{2k_{\mathrm{B}} T_{\mathrm{cold}}} \right) + n_{\mathrm{hot}} \delta(\vec{v} - \vec{v}_{\mathrm{hot}}) \tag{2.3.1}$$

where δ denotes a delta function and the return velocity of the bulk electrons $\vec{v}_{\mathrm{return}} = -n_{\mathrm{hot}} \vec{v}_{\mathrm{hot}} / (n_{\mathrm{e}} - n_{\mathrm{hot}})$ ensures that there is no net current. The total (isotropic) pressure of this system would be

$$P_{\mathrm{e}} = (n_{\mathrm{e}} - n_{\mathrm{hot}})(k_{\mathrm{B}} T_{\mathrm{cold}} + \tfrac{1}{3} m_{\mathrm{e}} v_{\mathrm{return}}^2) + \tfrac{1}{3} m_{\mathrm{e}} n_{\mathrm{hot}} v_{\mathrm{hot}}^2, \tag{2.3.2}$$

giving the heat flow as

$$\vec{Q} = (n_{\mathrm{e}} - n_{\mathrm{hot}})(\tfrac{5}{2} k_{\mathrm{B}} T_{\mathrm{cold}} + \tfrac{1}{2} m_{\mathrm{e}} v_{\mathrm{return}}^2) \vec{v}_{\mathrm{return}} + \tfrac{1}{2} m_{\mathrm{e}} n_{\mathrm{hot}} v_{\mathrm{hot}}^2 \vec{v}_{\mathrm{hot}}, \tag{2.3.3}$$

which would have magnitude greater than Q_{fs} for $v_{\mathrm{hot}} \gg v_{\mathrm{IT}}$ as long as n_{hot} is not too large. Of course such a situation is quite contrived and would probably be short-lived due to the effect of collisions, but this example illustrates that the free-streaming limit is not some unbreakable law of physics and reminds us that we should not immediately discount any theory that predicts heat exceeding the free-streaming limit.

Nevertheless, the practicality of the flux-limiter approach has enabled rapid advancement in plasma simulation capabilities: Firstly, it provides a freely tunable parameter by which to match fluid codes to experimental results or kinetic simulations. Furthermore, the guarantee of a maximum heat flux also allows for tractable timesteps when using explicit time-differencing due to conversion of the asymptotic behaviour of the CFL condition from quadratic to linear $\Delta t < 2\Delta x Q_{\mathrm{fs}}/3P_{\mathrm{e}}$. (Without flux-limitation the heat flow velocity $v_Q = 2\vec{Q}/3P_{\mathrm{e}}$ is unbounded and the diffusive form of the heat equation leads to $\Delta t \propto \Delta x^2$.) However, the arbitrary and unpredictive nature of the flux-limiter is rather unsatisfactory and values for $\mathfrak{f}_Q$ ranging from 0.03 (Jones et al. 2016) to 0.15 (Rosen et al. 2011) have been suggested for use in NIF design codes and up to 3 for SOL modelling (Fundamenski 2005). Furthermore, the inability of this approach to account for preheat is a severe handicap.

While popular ICF hydro codes (e.g. HYDRA, LASNEX, LASNEX, LILAC and DRACO) often limit the heat flow to the minimum of the free-streaming and local heat flows (Rosen et al. 2011; Davies et al. 2015), in this thesis the smoother 'harmonic' implementation of the flux-limiter is used

$$\vec{Q}^{(\mathrm{fl})} = \frac{\vec{Q}^{(\mathrm{B})}}{1 + |\vec{Q}^{(\mathrm{B})}/\mathfrak{f}_Q Q_{\mathrm{fs}}|}. \tag{2.3.4}$$

In the classical transport code CTC summarised in section 3.2 this is achieved for the perpendicular component of the heat flow (as CTC considers a simulation plane perpendicular to the field the parallell component is not considered) by multiplying the perpendicular thermal conductivity by the flux-limiting factor (not an actual flux-limiter)

$$\theta_\alpha = \left(1 + \frac{\kappa_\perp^{(\mathrm{B})}}{f_\alpha Q_{\mathrm{fs}}} \left| \frac{\partial T_{\mathrm{e}}}{\partial x} \right| \right)^{-1}. \tag{2.3.5}$$

This technique is extended also to the Nernst and Righi-Leduc coefficients ($\beta_\wedge$, $\kappa_\wedge$) with independent flux-limiters $\mathfrak{f}_{\mathrm{N}}$, $\mathfrak{f}_{\mathrm{RL}}$. There are applied by multiplying the transport coefficients by the appropriate flux-limiting factor θ. However,

the perpendicular thermal conductivity $\kappa_\perp$ is used in obtaining all flux-limiting factors θ_α for consistency (Bissell 2012), i.e.

$$\beta_\wedge^{(\mathrm{fl})} = \frac{\beta_\wedge{}^{(\mathrm{B})}}{1+|\vec{Q}_\perp^{(\mathrm{B})}/\mathrm{f_N}Q_{\mathrm{fs}}|}, \kappa_\wedge^{(\mathrm{fl})} = \frac{\kappa_\wedge{}^{(\mathrm{B})}}{1+|\vec{Q}_\perp^{(\mathrm{B})}/\mathrm{f_{RL}}Q_{\mathrm{fs}}|}, . \tag{2.3.6}$$

Note that this method used by CTC actually allows for the total magnitude of the heat flow to potentially exceed the free-streaming but such considerations are only relevant when magnetised transport is discussed in chapter 7.

2.3.2 *Convolution Models*

Due to the failings of the flux-limiter approach at providing a truly predictive description of nonlocal transport, more sophistical models are necessary. One such alternative is based on the idea that the heat flux at one location depends on contributions from surrounding regions (see fig. 2.1). The distance at which nearby electrons could contribute to the heat flow would surely be on the order of their mean free path, with the contribution decreasing with distance. Such an effect could be expressed as convolution of the classical heat flux, $\vec{Q}^{(\mathrm{B})}$ with some kernel $W(x,x')$ representing the probability of an electron carrying its energy from x' to x without colliding:

$$\vec{Q}^{(\mathrm{conv})} = \int W(x,x')\vec{Q}^{(\mathrm{B})}(x')\,\mathrm{d}x'. \tag{2.3.7}$$

The great advantage of such an approach is that it has the ability to predict preheat from high-energy electrons arriving into cooler areas with flatter temperature gradients, while also guaranteeing that the local heat flow will be recovered when the MFP becomes much shorter than the scalelength.

The majority of convolution models that have been put forward are one-dimensional. This is for good reason: such an approach is firstly quite awkward to formulate in multiple dimensions and also computationally intensive to solve as the integration scales quadratically with total number of cells (unless a Monte Carlo approach is used). One of the earliest and most well-received convolution models due to its simple intuitive form was that of LMV, Luciani, Mora and Virmont (1983)

$$W^{(\mathrm{LMV})}(x,x') = \frac{1}{2a\lambda_{\mathrm{e}}^{(\mathrm{T})}(x')}\exp\left(-\frac{|\int_x^{x'} n_{\mathrm{e}}(x'')\,\mathrm{d}x''|}{2an_{\mathrm{e}}(x')\lambda_{\mathrm{e}}^{(\mathrm{T})}(x')}\right) \tag{2.3.8}$$

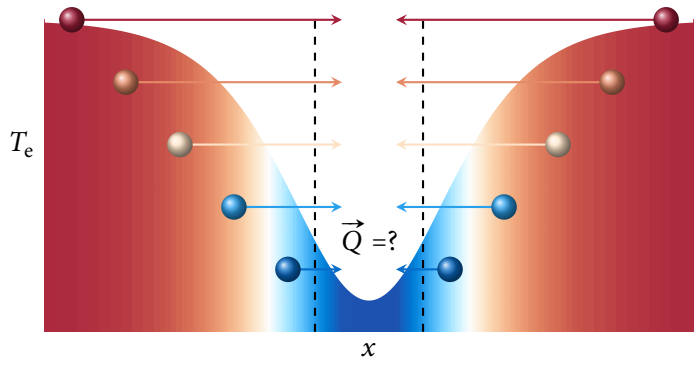

FIGURE 2.1: Convolution models are based on the idea that the heat flux at one point can be affected by electrons some distance away.

where $a = 32$ was determined by comparison with VFP codes and $\lambda_e^{(T)} = \sqrt{Z+1}\lambda_{ei}(v_{1T})$ is essentially a geometric average of electron-ion and electron-electron thermal MFPs. Other more complex kernels were calculated either from using a simplified collision operator (Albritton et al. 1986) or from a Fourier analysis (see section 2.3.6).

2.3.3 *Multigroup Diffusion (SNB)*

Probably the most important and widely used nonlocal model is the multigroup diffusion or 'SNB' model named after the original authors Schurtz, Nicolaï and Busquet (Schurtz et al. 2000). Implemented in inertial fusion codes such as Lawrence Livermore National Laboratory's HYDRA (Rosen et al. 2011), CELIA laboratory's CHIC (Breil and Maire 2007) , the University of Rochester Laboratory for Laser Energetics' (LLE) DRACO (Cao et al. 2015) and the University of Rome's DUED (Marocchino et al. 2013), the model originated as a multi-dimensional extension of the aforementioned LMV convolution approach. In order to achieve this satisfactorily, slight modifications to the 1D kernel were necessary corresponding to

$$W^{(SNB)}(x,x') = \int_0^\infty \frac{\beta^4 e^{-\beta}}{24} \frac{\sqrt{3}}{\sqrt{Z+1}\lambda_{ei}(x',\beta)} \exp\left(-\sqrt{3}\left|\int_x^{x'} \frac{2}{\sqrt{Z+1}\lambda_{ei}(x'',\beta)}\,dx''\right|\right) d\beta, \tag{2.3.9}$$

where the integrand is considered to represent the contribution from electrons with different energies (i.e. $\beta = \frac{1}{2} m_e v^2 / k_B T_e$) and $\lambda_{ei} = v/\nu_{ei}$ is the energy-dependent electron-ion MFP arising from the definition of ν_{ei} given in eq. (2.1.16).

The real insight behind the SNB model is that the above kernel can be identified as the weighted integral of Green functions $G(x, x', \beta)$ over electron energy,

$$W^{(\mathrm{SNB})}(x, x') = \int_0^\infty \frac{\beta^4 \mathrm{e}^{-\beta}}{24} \frac{2G(x, x', \beta)}{\sqrt{Z+1}\lambda_{ei}(x', \beta)} \mathrm{d}\beta \tag{2.3.10}$$

$$\implies G(x, x', \beta) = \frac{\sqrt{3}}{2} \exp\left(-\sqrt{3} \left| \int_x^{x'} \frac{2}{\sqrt{Z+1}\lambda_{ei}(x'', \beta)} \mathrm{d}x'' \right| \right). \tag{2.3.11}$$

These Green functions are the solutions to a continuum of second-order PDE's, to which Schurtz et al. suggested a valuable multi-dimensional generalisation as

$$\left[\frac{2}{\sqrt{Z+1}\lambda_{ei}} - \vec{\nabla} \cdot \frac{\sqrt{Z+1}}{6} \lambda_{ei} \vec{\nabla} \right] G(\vec{x}, \vec{x}', \beta) = \delta(\vec{x} - \vec{x}). \tag{2.3.12}$$

Working this into the convolution equation for the heat flow we obtain

$$\vec{Q}^{(\mathrm{SNB})} = \int \int_0^\infty \frac{\beta^4 \mathrm{e}^{-\beta}}{24} \vec{Q}^{(\mathrm{B})} \left(\delta(x - x') + \vec{\nabla} \cdot \frac{\sqrt{Z+1}}{6} \lambda_{ei} \vec{\nabla} G \right) \mathrm{d}\beta \, \mathrm{d}\vec{x}' \tag{2.3.13}$$

$$= \vec{Q}^{(\mathrm{B})} - \int \int_0^\infty \left(\vec{\nabla} \cdot \frac{\beta^4 \mathrm{e}^{-\beta}}{24} \vec{Q}^{(\mathrm{B})} \right) \frac{\sqrt{Z+1}}{6} \lambda_{ei} \vec{\nabla} G \, \mathrm{d}\beta \, \mathrm{d}\vec{x}' \tag{2.3.14}$$

$$= \vec{Q}^{(\mathrm{B})} - \int_0^\infty \frac{\sqrt{Z+1}}{6} \lambda_{ei} \vec{\nabla} H_\beta \tag{2.3.15}$$

using integration by parts, where H_β is the solution to the inhomogeneous PDE

$$\left[\frac{2}{\sqrt{Z+1}\lambda_{ei}} - \vec{\nabla} \cdot \frac{\sqrt{Z+1}}{6} \lambda_{ei} \vec{\nabla} \right] H_\beta = -\vec{\nabla} \cdot \frac{\beta^4 \mathrm{e}^{-\beta}}{24} \vec{Q}^{(\mathrm{B})} \, \mathrm{d}\beta. \tag{2.3.16}$$

The above equation is said to represent a 'multigroup diffusion of electrons with different energies and is the key one to be solved for obtaining the SNB heat flow. Note that the subscript indicates that H_β is an (infinitesimal) distribution over the energy parameter β (H could also be a distribution over velocity and is used as such later in this thesis, but we will usually not insist upon the formality of the subscript).

The solution of eq. (2.3.16) typically consists of breaking H_β up into N discrete energy groups denoted by H_g bounded below by $\beta_{g-\frac{1}{2}}$ and above by $\beta_{g+\frac{1}{2}}$ with a characteristic velocity v_g which lies within these bounds (see section 3.3 for more

details). This can give acceptable convergence for as few as $N = 25$ groups. The MFP associated with a particular group and defined in eq. (23) of the SNB paper (Schurtz et al. 2000) can be related to the velocity-dependent electron-ion MFP as

$$\lambda_g = \frac{\sqrt{Z+1}}{2}\lambda_{\mathrm{ei}}(v_g). \tag{2.3.17}$$

One particular issue with LMV-type kernels is their asymptotic behaviour at low degrees of collisionality; such models typically predict the heat flow to approach zero as the temperature scalelength decreases while kinetic approaches reveal that it should reach a constant value proportional to the free-streaming heat flow and the amplitude of the perturbation (see section 4.4). Underestimation of the heat flux in such regimes could lead to an inability to damp high resolution features or numerical noise. A novel approach to somewhat circumvent this in the SNB model was suggested by Schurtz et al. (2000); this involves limiting the diffusive MFP according to the strength of the electric field

$$\frac{1}{\lambda_g^{(E)}} = \frac{1}{\lambda_g} + \frac{|e\vec{E}^{(\mathrm{SH})}|}{\frac{1}{2}m_\mathrm{e}v^2}, \text{ where } en_\mathrm{e}\vec{E}^{(\mathrm{SH})} = -\vec{\nabla}P_\mathrm{e} - n_\mathrm{e}\beta_\parallel^{(\mathrm{SH})}\vec{\nabla}k_\mathrm{B}T_\mathrm{e} \tag{2.3.18}$$

is the local Spitzer-Härm electric field.

Thus, the final equation (set) to be solved is

$$\left[\frac{1}{\lambda_g} - \vec{\nabla}\cdot\frac{\lambda_g^{(E)}}{3}\vec{\nabla}\right]H_g = -\vec{\nabla}\cdot\int_{\beta_{g-\frac{1}{2}}}^{\beta_{g+\frac{1}{2}}}\frac{\beta^4\mathrm{e}^{-\beta}}{24}\,\mathrm{d}\beta\;\vec{Q}^{(\mathrm{B})} \tag{2.3.19}$$

with the nonlocal heat flow now being obtained by a sum

$$\vec{Q}^{(\mathrm{SNB})} = \vec{Q}^{(\mathrm{B})} - \sum_g \frac{\lambda_g^{(E)}}{3}\vec{\nabla}H. \tag{2.3.20}$$

Standard PDE numerical algorithms such as alternate-direction implicit (ADI) are typically used for solving eq. (2.3.19), see section 3.3 for the methodology used in this thesis for the 1D case.

Schurtz et al. (2000) suggest approximating the ionisation-dependence of the thermo-electric transport coefficient as $\beta_\parallel^{(SH)} = \frac{1}{2}(Z + 0.477)/(Z + 2.15)$, but the accuracy of this is questionable compared to the Epperlein and Haines (1986) numerical coefficients.

Rederiving from the kinetic equations

Despite having roots in the more phenomenological convolution approach, the developers of the SNB model managed to illustrate a link to the VFP equations under a number of simplifications. Starting from the P1 Cartesian tensor expansion, neglecting time-derivatives (in order to achieve a stationary model)

and approximating the effect of electron-electron collisions on the anisotropic part of the EDF by incorporating the collision fix into the electron-ion collision frequency ν_{ei}, we obtain

$$\frac{v}{3}\vec{\nabla}\cdot\vec{f}_1 - \frac{e\vec{E}}{3m_e v^2}\cdot\frac{\partial v^2\vec{f}_1}{\partial v} = C_{ee0}\left[f_0\right], \tag{2.3.21}$$

$$v\vec{\nabla}f_0 - \frac{e\vec{E}}{m_e}\frac{\partial f_0}{\partial v} = -\nu_{ei}^*\vec{f}_1. \tag{2.3.22}$$

The authors proceed to perform an expansion about the local form of the distribution function $f_e^{(mb)} + \vec{V}\cdot\vec{f}_1^{(mb)}/v$. However, they replace the anisotropic contribution

$$\vec{f}_1^{(mb)} = \lambda_{ei}^*\left(\frac{m_e v^2}{2k_B T_e} - 4\right) f_e^{(mb)}\frac{\vec{\nabla}T_e}{T_e}, \text{ with} \tag{2.3.23}$$

$$\vec{g}_1^{(mb)} = -\lambda_{ei}^* f_e^{(mb)}\frac{\vec{\nabla}T_e}{T_e} \tag{2.3.24}$$

where $\lambda_{ei}^* = \xi\lambda_{ei} = v/\nu_{ei}^*$. This modification achieves positive-definiteness without affecting the integral used to calculate the heat flow, and is argued to be compensated by the further assumption of neglecting the electric fields (Schurtz et al. 2000). At this point the model now renders as

$$\frac{C_{ee0}\left[\delta f_0\right]}{v} + \vec{\nabla}\cdot\frac{\lambda_{ei}{}^{(E)}}{3}\vec{\nabla}\delta f_0 = \frac{\nabla\cdot\vec{g}_1^{(mb)}}{3}, \tag{2.3.25}$$

where $\delta f_0 = f_0 - f_e^{(mb)}$, with the deviation from the local heat flow given as

$$\delta\vec{Q} = \frac{2\pi m_e}{3}\int_0^\infty \delta\vec{f}_1 v^5\,\mathrm{d}v = -\frac{2\pi m_e}{3}\int_0^\infty v^5\lambda_{ei}^*\vec{\nabla}\delta f_0\,\mathrm{d}v, \tag{2.3.26}$$

where $\delta\vec{f}_1 = \vec{f}_1 - \vec{f}_1^{(mb)}$. Note that here the electron-ion MFP λ_{ei} appears separately from what is essentially the electron-electron MFP $\lambda_{ee}{\sim}v/C_{ee0}$, and the use of the geometrically averaged MFP $\lambda_g{\sim}\sqrt{\lambda_{ee}\lambda_{ei}}$ used by Schurtz et al. (2000) is only appropriate if the ionisation Z is assumed constant. In chapter 5 it shall be seen that the 'separated' and 'averaged' implementations make considerably different predictions when ionisation gradients are large. To properly recover the previously given form of the SNB model eqs. (2.3.15) and (2.3.16) the phenomenological limitation of the MFP due to the electric field must be included, $H = 2\pi m_e v^5\delta f_0\,\mathrm{d}v$ identified and the electron-electron collision operator replaced with a velocity-dependent Krook frequency (BGK) $C_{ee0}^{(BGK)}[\delta f_0] = -4\nu_{ei}\delta f_0/Z$.

Note that the incorporation of the collision fix was not suggested until a later paper (Nicolaï et al. 2006).

Issues with the kinetic link

We shall now take the time to consider the assumptions that have been made in arriving at the SNB from the kinetic equations. To the author of this thesis, one of the most confusing assumptions is the stationary assumption; for if this were the *only* assumption made, then a simple moment-based analysis of the VFP equations predicts that the heat flow should be divergence free (i.e. a constant if spatial gradients only occur in one dimension). However, this is clearly not always the case as proportionality between the heat flux and the temperature gradient should be recovered in the local limit. The introduction of the other assumptions into the SNB model, most prominently that of a model collision operator, desirably allows for spatial variation in the heat flow to be predicted, even in 1D.

Additionally, it is important to understand that the electric field in no way comes from the VFP equation and is only added on with a 'physics' justification that conveniently overcomes inherent numerical issues with stationary nonlocal models. However, the 'physics' justification should be digested with some hesitancy as in reality the electric field only limits the MFP of electrons travelling in the same direction as it, but enhances that of electrons travelling perpendicularly or in the opposite direction. The SNB model does not take the direction of the electrons into account and instead reduces it in all directions. (This criticism was originally provided by Manheimer et al. 2012)

A final consideration about the mean free paths used in the model is the appropriateness of geometrically averaging the electron-electron and electron-ion mfp's to obtain a single group mfp λ_g. Such an approach would only be valid in the case of homogeneous ionisation. This seems to have been remedied by employing distinct electron-electron and electron-ion mfp's in a later paper (Nicolaï et al. 2006) but no comment was made at the time as to whether this turned out to be an important change or not. In section 5.4 we shall see that separating the mfp's provides a marked improvement in predicting the heat flow in ICF relevant scenarios possessing steep ionisation gradients.

Alternative Collision Models

Recall that the derivation of the SNB model from the kinetic equation requires that the collision operator in eq. (2.3.25) is modeled as $C_{ee0}[\delta f_0] = -4\nu_{ei}\delta f_0/Z$, which

is often referred to as a velocity-dependent Krook (BGK) model collision operator. However, alternative model collision operator are possible and are investigated in chapter 4 of this thesis such as that suggested by Albritton, Williams, Bernstein and Swartz (AWBS) (Albritton et al. 1986):

$$C_{ee0}^{(\mathrm{AWBS})}[\,\cdot\,] = \frac{\nu_{ei}}{Z} v \frac{\partial}{\partial v}[\,\cdot\,], \tag{2.3.27}$$

which attempts to incorporate the slowing down of electrons as a result of collisions, or scaled versions of the BGK operator

$$C_{ee0}^{(\mathrm{BGK})}[\,\cdot\,] = -r\frac{\nu_{ei}}{Z} \times \cdot \tag{2.3.28}$$

Note that the original SNB implementation corresponds to $r = 4$. However, when the link to the kinetic equations is presented in the original paper (Schurtz et al. 2000) (III F) as well as in section II of a later publication (Nicolaï et al. 2006) a simple multiple of $r = 1$ is indicated. In this thesis it shall be argued that using the BGK collision operator with a different value ($r = 2$) along with the Epperlein-Short collision fix $\xi_{ES} = (Z + 2.4)/(Z + 0.42)$ gives very good agreement with VFP simulation across a wide range of problems (and ionisation values).

As for the AWBS operator, in spite of its differential formulation its use does not actually require a significant increase in computational time unless an attempt to parallelise over energy groups is being made. This is because the velocity-space first-order differential equation is simply closed from above with the boundary condition $\delta f_0(v = \infty) = 0$.

Validation Status of the SNB Model

Until now, there have only been a few instances where the SNB model is compared directly to VFP simulations. In the original paper (Schurtz et al. 2000) the damping rate of temperature sinusoids was shown to compare favourably to kinetic predictions for scalelengths no steeper than $\sqrt{Z}k\lambda_{ei} = 1$ and specifically for the case of $Z = 4$. Schurtz et al. further observed that the SNB model was able to predict qualitatively similar temperature contours to Epperlein et al.'s VFP code SPARK (1988a) for a 2D problem that concerned laser heating of a planar beryllium target (Epperlein et al. 1988b).

Another important work in evaluating the success of the SNB model is that of Marocchino et al. (2013), who compared the implementation of the model in the University of Rome hydro code DUED to VFP simulations carried out with OSHUN (Tzoufras et al. 2011; Tzoufras et al. 2013). Again, damping of

temperature sinusoids was investigated, but this produced the peculiar result that the agreement between SNB and VFP seemed to be very good for $Z = 1$ and then became progressively worse as the ionisation increased. Attempting to replicate such findings (presented in section 6.2 of this thesis), it was concluded that the implementation of the SNB model used by Marocchino et al. corresponded to a multiplier of $r = 16$ on the electron-electron mfp coupled with a neglection of any correction to angular scattering as a result of electron-electron collisions (i.e. ξ is set to one) (Brodrick et al. 2017). The second problem investigated by Marocchino et al. involved the relaxation of initially Gaussian temperature profiles. And while the rapid rate at which the temperature gradient evanesced limited the degree of nonlocality that could be observed upon reaching a quasistationary state, such a setup proved quite motivational in assessing preferable benchmarks of the SNB model for this thesis such as by extending the region of hot plasma.

Due to the variety of implementations outlined here and the potential for these to give materially different predictions for heat flow that could have significant ramifications for the way a simulated ICF experiment could evolve, it is imperative that a more thorough exploration of these implementation choices with comparison to VFP codes be carried out in hope of identifying the 'optimal implementation' of the SNB.

Magnetised Extension

Of all the models studied in this thesis, the SNB is the only one that has been extended to magnetised regimes (Nicolaï et al. 2006). The authors achieved this largely through modifications to the mfp and introducing a deflection term, both stemming from a simplified VFP analysis. Specifically, the equation set solved is

$$\frac{C_{\mathrm{ee0}}^{(\mathrm{BGK})}\left[\delta f_0\right]}{v} + \vec{\nabla} \cdot \frac{{\lambda_{\mathrm{ei}}}^{(E)}}{3} \frac{1 + V^3 \vec{\Omega}\times}{1 + V^6 \Omega^2} \vec{\nabla} f_0 = \frac{\nabla \cdot \vec{g}_1^{(\mathrm{mb})}}{3}, \tag{2.3.29}$$

where $V = v/v_{2\mathrm{T}}$, $\Omega = \omega_{\mathrm{ce}}/\nu_{\mathrm{ei}}^{(0)}$. The same source term $\vec{g}_1^{(\mathrm{mb})}$ is used here as in the unmagnetised model but the magnetised Braginskii electric field is used in limiting the electron-ion mfp and the correction to the anisotropic part of the EDF

$$\delta \vec{f}_1 = -\frac{{\lambda_{\mathrm{ei}}}^{(E)}}{3} \frac{1 + V^3 \vec{\Omega}\times}{1 + V^6 \Omega^2} \vec{\nabla} f_0 \tag{2.3.30}$$

is instead applied to a Maxwellian part $\vec{f}_1^{(\mathrm{mb})}$ more appropriate for magnetised conditions (see eq. 22 in Nicolaï et al. 2006). Due to difficulties of implementation

as well as the importance of first validating the unmagnetised model this was also not attempted in this thesis. One alternative nonlocal model that also includes magnetic fields is the 'MN model'.

2.3.4 *The 'M1 Model'*

Inspired by the SNB approach, Del Sorbo et al. formulated a stationary model based on the VFP equations able to deal with magnetic fields self-consistently but with considerably fewer assumptions; the only assumptions made were the neglection of time derivatives and the use of the AWBS operators to approximate isotropic electron-electron collisions. (Recall that, in addition to being more computationally intensive to solve, if the exact collision operator were used the model would predict an unrealistic divergence free heat flow due to the neglection of the time derivative.) Finally, the authors suggested that the MN closure be used to ensure that reconstruction of the EDF is positive-definite making it a stronger candidate than the SNB for assessing the impact of nonlocality on parametric instabilities that depend on velocity gradients of the EDF.

Named quite simply the 'MN model' it is summarised by the following equation set (note that this differs from that presented by Del Sorbo et al. as we are using Cartesian tensors rather than spherical harmonics):

$$\frac{v}{3}\vec{\nabla}\cdot\vec{f}_1 - \frac{e\vec{E}}{3m_e v^2}\cdot\frac{\partial v^2\vec{f}_1}{\partial v} = C_{ee0}^{(\mathrm{AWBS})}[\delta f_0] \tag{2.3.31}$$

$$v\vec{\nabla}f_0 + \frac{2}{5}v\vec{\nabla}\cdot\overleftrightarrow{f}_2 - \frac{e\vec{E}}{m_e}\frac{\partial f_0}{\partial v} - \frac{e\vec{E}}{3m_e v^3}\cdot\frac{\partial v^3\overleftrightarrow{f}_2}{\partial v} - \frac{e}{m_e}(\vec{B}\times\vec{f}_1) = C_{ee0}^{(\mathrm{AWBS})}[\vec{f}_1] - \nu_{ei}\vec{f}_1, \tag{2.3.32}$$

with $\overleftrightarrow{f}_2$ given by the closure in eq. (2.1.19). Additionally, the electric field is obtained by

$$\vec{E} = -\frac{m_e}{6e}\frac{1+\beta^{(\mathrm{SH})}(Z)}{2.5}\frac{\int_0^\infty \vec{\nabla}f_0 v^7\,\mathrm{d}v}{\int_0^\infty f_0 v^5\,\mathrm{d}v}, \tag{2.3.33}$$

which is the ambipolar form resulting from using ν_{ei}^* on the right-hand side of eq. (2.3.32) (at least when relative temperature gradients are much steep than relative density gradients). While this model has been shown to perform tangibly differently to the SNB, especially in the magnetised regimes (Del Sorbo et al. 2016), it has not been benchmarked against fully kinetic (i.e. VFP or PIC) simulations.

Therefore, it is impossible to be sure which model is performing better. However, due to being discovered at a later date and requiring a non-trivial implementation, the MN model is not explored further in this thesis.

2.3.5 *The CMG velocity-dependent Krook model*

Also investigated by Marocchino et al. is the velocity-dependent Krook method of Colombant, Manheimer and Goncharov (Manheimer et al. 2008; Colombant and Manheimer 2008), referred to as both the CMG and the VDK model. This model is somewhat complex and difficult to describe compactly, but stems from a replacement of all collision operators with velocity-dependent functions and then treating electron with velocities above a characteristic velocity as nonlocal. Furthermore it has a more thorough treatment of the electric field than the SNB model using integrals of the approximated EDF to ensure zero current (or alternatively pressure balance). Similarly to the SNB model it manifests as a convolution approach with a kernel that is an integral over velocity, but now with a lower bound. As the model appears quite cumbersome to implement, especially in more than one dimension (Manheimer et al. 2012), and more importantly exhibits a curious kink corresponding to the somewhat arbitrary choice of characteristic velocity (see fig. 1 of Marocchino et al. 2013) this model will not be studied in this thesis.

2.3.6 *Landau Fluid*

Another kind of convolution model arises from a linearised analysis, i.e. where all perturbations are small enough to be independent and can be separated out into sinusoids of specific wavelengths through a Fourier transform. In Fourier space the VFP equation is greatly simplified and some analytical progress can be made. While a detailed exploration of this is left until the next chapter, the qualitative behaviour of the thermal conductivity is to decrease from its local value monotonically. There is a large variety of analytic approximations for the relative reduction of the thermal conductivity (which is independent of spatial

location for a given wavelength) provided in the literature, a few are outlined here:

$$\kappa_\parallel = \tfrac{3}{2}\chi_1 n_e v_{2T} k_B/k, \qquad \text{(Hammett and Perkins 1990)}$$

$$\frac{\kappa_\parallel}{\kappa_\parallel^{(B)}} = \frac{1}{1+50\sqrt{Z\xi_{ES}}k\lambda_{ei}^{(T)}} \qquad \text{(Epperlein and Short 1991)}$$

$$\frac{\kappa_\parallel}{\kappa_\parallel^{(B)}} = \left(ak\lambda_{ei}^{(B)} + \frac{1+b_Q Zk^2\lambda_{ei}^{(B)2}}{1+b_Q Zk^2\lambda_{ei}^{(B)2}/ac_1(k\lambda_{ei}^{(B)})^{1-\eta}}\right)^{-1}, \qquad \text{(Bychenkov et al. 1994)}$$

where $k = 2\pi/\lambda_T$ is the wavenumber associated with the temperature perturbation and other coefficients will be defined in chapter 4. Epperlein and Short suggested that such closures could be used to construct convolution models by providing a convolving kernel that is the inverse Fourier transform of the above expressions, i.e.

$$W(x,x') = \frac{1}{2\pi}\int_{-\infty}^{\infty}\frac{\kappa_\parallel(k)}{\kappa_\parallel^{(B)}}e^{ik(x-x')}\,dk. \tag{2.3.34}$$

However, the validity of this approach only holds for the case of relatively small-amplitude temperature perturbations, considerable relative gradients in temperature or density would introduce nonlinearities into the mfp's, and it is not self-evident how to manage this. For example the mfp could be taken as a constant over the entire domain, or it could be averaged over each distinct interval $[x, x']$.

Ji and Held (2014) take the opposite approach to Epperlein and Short, providing an analytic expression for the kernel in configuration space

$$W(s-=,s') = \frac{m_e T_e(s)^{3/2}}{\sqrt{2}k_B T_e(s')^{5/2}\kappa_{\parallel c}^{(B)}}(d+a\exp(-b|s-s'|^c)\log(1-\alpha\exp(-\beta|s-s'|^\gamma)), \tag{2.3.35}$$

where $s(x) = \int_0^x dx'/\sqrt{2}\lambda_{ei}^{(B)}(x')$ is an integrated distance in mean free paths, $\kappa_{\parallel c} = m_e\kappa_\parallel^{(B)}/n_e k_B T_e \tau_{ei}^{(B)}$ is the dimensionless thermal conductivity and the numerical coefficients $a, b, c, d, \alpha, \beta, \gamma$ for hydrogen ($Z = 1$) are given in Table I of Ji and Held 2014. From this we can obtain the dimensionless thermal conductivity in Fourier space

$$\kappa_{\parallel c} = 2\int_0^\infty (d + a\exp(-b|s'|^c)\log(1-\alpha\exp(-\beta|s'|^\gamma))\cos(\sqrt{2}k\lambda_{ei}^{(B)}s')\,ds'. \tag{2.3.36}$$

The validity of some of the fits presented here will be assessed in section 4.6.1.

Another method of incorporating the above closures for the thermal conductivity is to actually perform simulations in Fourier space. This is what is usually meant by the 'Landau fluid' approach and is common in fluid simulations of fluctuations along magnetic field lines within the tokamak core, made convenient by the inbuilt periodic boundary conditions allowing particular resonant modes to arise. Indeed the amplitude of fluctuations can be relatively small in some scenarios such as H-mode. On the other hand, temperature differences between the last-closed flux-surface and the divertor target are always large and the geometry and boundary conditions are much more complex than within the core making a Fourier approach undesirable for simulating SOL transport.

2.3.7 *Non-Fourier Landau-Fluid (NFLF)*

Addressing these issues with a Fourier approach to SOL transport, the innovation by Dimits, Joseph and Umansky (Dimits et al. 2014) was to enable direct calculation of the nonlocal parallel heat flux in configuration space by approximating the Fourier closure as a sum of Lorentzians

$$\frac{\kappa_\parallel(k)}{\kappa_\parallel^{(\mathrm{B})}} \approx \sum_{j=1}^{N} \frac{p_j}{q_j^2 + \left(ak\lambda_{\mathrm{ei}}^{(\mathrm{B})}\right)^2}, \tag{2.3.37}$$

where a is an ionisation-dependent coefficient present in the original papers that parametrises the damping behaviour in the collisionless limit $\kappa_\parallel(k \to \infty) \sim \kappa_\parallel^{(\mathrm{B})}/ak\lambda_{\mathrm{ei}}^{(\mathrm{B})}$, N is the number of Lorentzians chosen for the fit and p_j, q_j are fit parameters. From this, the heat flow can be reconstructed as a sum of 'dummy contributions'

$$\vec{Q}^{(\mathrm{NFLF})} = \sum_{j=1}^{N} \vec{Q}_j \text{ where } \vec{Q}_j = \frac{p_j \vec{Q}^{(\mathrm{B})}}{q_j^2 + \left(ak\lambda_{\mathrm{ei}}^{(\mathrm{B})}\right)^2}. \tag{2.3.38}$$

Rearranging the above equation and taking the inverse Fourier transform gives a set of N second-order ODE's that can be used to calculate the contributions in configuration space.

$$\left[q_j^2 - (a\lambda_{\mathrm{ei}}^{(\mathrm{B})})^2 k^2\right] \vec{Q}_j = p_j \vec{Q}^{(\mathrm{B})} \longrightarrow \left[q_j^2 + (a\lambda_{\mathrm{ei}}^{(\mathrm{B})})^2 \nabla^2\right] \vec{Q}_j = p_j \vec{Q}^{(\mathrm{B})}, \tag{2.3.39}$$

This model is arguably one of the most efficient nonlocal models yet devised (with the exception of flux-limiters): able to provide reasonable agreement with some kinetic simulations with as few as three second-order ODE's—the SNB

model typically requires 25 groups or more. This approach also conveniently avoids the issue of defining the mean free path in reciprocal space. However, the absence of a direct link to the VFP equation could make it difficult to devise ways to improve the model or extend it to varying ionisation or magnetised regimes. Initial validation work showed that the model performed favourably against VFP for simple test problems with a hydrogen plasma, but with some room for improvement. In this thesis significant improvements to the model will be suggested by calibrating the base analytic fit, calculating new sets of coefficients for $Z = 1$ and $Z = 8$ and modifying the nonlinear behaviour.

2.3.8 *Eigenvector Integral Closure*

The last nonlocal model to be studied in this thesis is the 'moment-based' approach, here referred to as the 'Eigenvector Integral Closure' or EIC for short, originally proposed by Ji et al. (2009) and applied to the scrape-off layer by Omotani et al. (2013). Directly derived from simplifications of the VFP equation, the model necessarily neglects the time-derivative term to allow the heat flow to be calculated based on input density and temperature profiles only, rather than the history of the distribution function; this assumption should be reasonable over 'mean' SOL profiles (i.e. averaged over time to eliminate fine-scalelength fluctuations), but could break down for transient events with faster timescales such as filaments and ELMs.

The EIC model expresses the distribution function as $f_e = f_0 + \delta f_e$, where δf_e is a perturbation to an initial, usually Maxwellian, guess f_0. Assuming the perturbation δf_e is small, the nonlinear collision and electric field terms in the VFP equation are linearised, which (for a Maxwellian f_0) yields

$$\frac{\partial \delta f_e}{\partial s_\parallel} - \frac{C^{(\mathrm{L})}(\delta f_e)}{v_\parallel} = \frac{eE_\parallel}{m_e v_\parallel}\frac{\partial f_0}{\partial v_\parallel} - \frac{\partial f_0}{\partial s_\parallel}, \tag{2.3.40}$$

where the linearised collision operator for collisions of electrons with themselves is given by

$$C^{(\mathrm{L})}_{ee0}(f_e) = C_{ee}\left(\widetilde{f}_e, f_e^{(\mathrm{mb})}\right) + C_{ee}\left(f_e^{(\mathrm{mb})}, \widetilde{f}_e\right) \tag{2.3.41}$$

because collisions between two Maxwellians of the same species vanish identically.

The next step is to attempt a separation of variables into $s_\parallel$ and $\vec{v}/v_{2\mathrm{T}}$ by expressing

$$\delta f_\mathrm{e} = \sum_n w_n(s_\parallel) g_n(\vec{v}/v_{2\mathrm{T}}) \text{ such that } \frac{C_L(g_n)}{v_\parallel} = \frac{g_n}{\lambda_n}, \tag{2.3.42}$$

in terms of the eigenfunctions g_n of the operator $C^{(\mathrm{L})}/v_\parallel$, which depends only on $\vec{v}/v_{2\mathrm{T}}$; the corresponding eigenvalues are denoted by $1/\lambda_n$. Substituting (2.3.42) into (2.3.40) and assuming that the dependence of g_n on space through $v_{2\mathrm{T}}$ is negligible (only valid when relative temperature perturbations are small globally) yields

$$\sum_n \left(g_n \frac{\partial w_n}{\partial s_\parallel} + w_n \cancelto{0}{\frac{\partial g_n}{\partial s_\parallel}} + \frac{w_n g_n}{\lambda_n} \right) = \frac{eE_\parallel}{m_\mathrm{e} v_\parallel} \frac{\partial f_0}{\partial v_\parallel} - \frac{\partial f_0}{\partial s_\parallel}. \tag{2.3.43}$$

By similarly decomposing the right-hand side into (orthogonal) eigenfunction contributions, a set of independent first-order ODE's for w_n is formed that can be solved efficiently. Consequently, δf_e can be reconstructed and the nonlocal correction to the heat flux computed through an integral in $v_\parallel$ (hence the nomenclature Eigenvector Integral Closure or EIC).

The advantage of this approach is that it circumvents the need to solve in velocity-space at every timestep (as a VFP code must). The main challenge is identifying a discrete description of the eigenfunctions g_n that converges rapidly for use in a numerical scheme. In practice, this is done by using an orthonormal polynomial moment-basis to express g_n as a vector and the operator $C^{(\mathrm{L})}/v_\parallel$ as a matrix. The original authors (Ji et al. 2009) proposed to use the popular Legendre polynomials P_l to describe the dependence of δf_e on pitch angle $\cos\theta = v_\parallel/v$ and then the Laguerre polynomials $\mathrm{L}_k^{(l+½)}$ for variation with total speed, e.g.

$$\delta f_\mathrm{e} = \sum_{l,k} \delta f_\mathrm{e}^{l,k} \mathrm{P}_l\left(\frac{v_\parallel}{v}\right) \mathrm{L}_k^{(l+½)}\left(\frac{v^2}{v_{2\mathrm{T}}^2}\right) \frac{\mathrm{e}^{-v^2/v_{2\mathrm{T}}^2}}{\pi^{3/2} v_{2\mathrm{T}}^3} \tag{2.3.44}$$

This converges rapidly in the hydrodynamic limit but slowly in the collisionless limit. As an alternative, J T Omotani et al. (2015) proposed a Hermite-Laguerre basis, decoupling parallel and perpendicular velocity components, which allows for easier implementation of sheath boundary conditions (not investigated in this thesis). In this basis the perturbation to the distribution function can be described as

$$\delta f_\mathrm{e} = \sum_{p,j} \delta f_\mathrm{e}^{p,j} \mathrm{He}_p\left(\frac{v_\parallel}{v_{2\mathrm{T}}}\right) \mathrm{L}_j^{(0)}\left(\frac{v_\perp^2}{v_{2\mathrm{T}}^2}\right) \frac{\mathrm{e}^{-v^2/v_{2\mathrm{T}}^2}}{\pi^{3/2} v_{2\mathrm{T}}^3} \tag{2.3.45}$$

2.4 MODELLING NONLOCAL TRANSPORT IN MAGNETIC FIELDS

While the majority of nonlocal models are limited to purely unmagnetised regimes, magnetised extensions have been put forward for both the SNB (Nicolaï et al. 2006) and the MN model (Del Sorbo et al. 2016). These were developed by further pursuing the identified link to the VFP equation resulting in a magnetic modification the SNB mfp. Additionally, Luciani et al. Luciani et al. 1985, developed a convolution model for the Nernst velocity and Righi-Leduc heat flow based on simplifications to the quasistatic VFP equation. However, the accuracy of these have not yet been verified against fully kinetic simulations. Furthermore, the magnetised SNB model does not prescribe any method for calculating nonlocal corrections to the Nernst velocity, which will be the primary focus of the magnetised nonlocal transport studies presented in chapter 7.

One possibility for approximating the effect of nonlocality on Nernst advection would involve relying on the relation between the energy group contribution H_g and the nonlocal perturbation to the isotropic part of the EDF δf_0. This would provide a simple method of calculating corrections to the Nernst coefficient $\beta_\wedge$ by taking moments of the EDF as shown in eq. (2.2.20). However, the accuracy with which H_g approximates δf_0 has been called into question by Sherlock et al. (2017) making such an approach somewhat hazardous. An alternative method for obtaining an approximation of nonlocal Nernst using reduced models designed only for thermal transport has been explored by Lancia et al. (2014) and is used as an inspiration for the investigation in chapter 7. Originating from a proof by Haines (1986a) under the assumption that the electron-ion collision frequency ν_{ei} varies artificially as $1/v^2$ and electron-electron collisions can be neglected, this method involves the assumption that the ratio between the Nernst and heat flow velocities $v_Q \propto Q_\perp/P_e$ is unaffected by nonlocality. In reality ν_{ei} varies as $\log\Lambda_{ei}(v)/v^3$), leading to $\beta_\wedge$ depending on a slightly higher moment than $\kappa_\perp$ (cf. eqs. (2.2.18) and (2.2.20)). But application of this simple approximation in a nonlocal model very similar to the SNB (Riquier 2016; Fuchs 2017) was able to reduce discrepancies between modelling and experiments of a planar laser-solid interaction (Lancia et al. 2014, 2013).

Consequently, a reasonable conclusion would be that both heat flow and Nernst advection should be flux-limited by a similar degree. And this was indeed confirmed by Kho and Haines (1985, 1986) using fully-kinetic VFP simulations, although the Righi-Leduc heat flow was found to require more restrictive limitation,

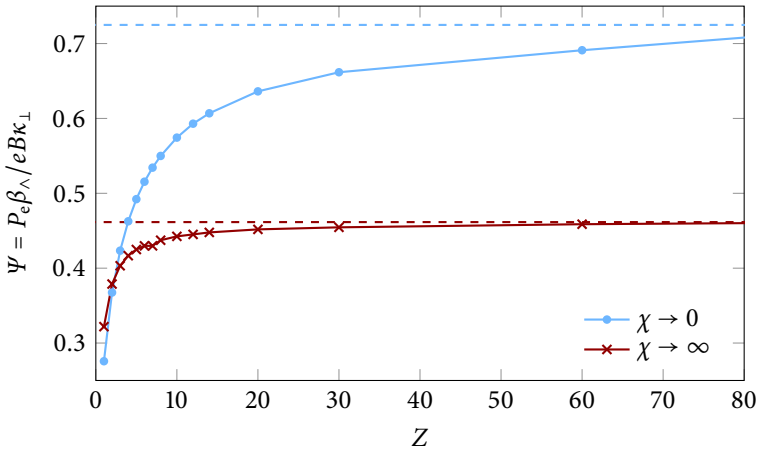

FIGURE 2.2: The local prediction due to Epperlein and Haines (1986) (see eq. (2.4.1)) for the dimensionless quantity $\Psi = P_e\beta_\wedge/eB\kappa_\perp$ in the limit of zero and infinite magnetisation. Dashed lines show the values obtained using the anisotropic collision fix $\xi_{ES} = (Z + 0.24)/(Z+4.2)$ (Epperlein and Short 1991), which turn out to be independent of ionisation.

mosly likely due to it depending on a much higher velocity moment (see eq. 2.2.19). However, they only considered a plasma of moderate and uniform ionisation ($Z = 10$) and neglected anisotropic electron-electron collisions, which can have a significant effect on the Nernst velocity for low-Z plasmas, such as present in the hohlraum gas-fill. Furthermore, they did not compare the time-integrated effect of using a flux-limited hydrodynamic model against VFP simulations on plasma profiles.

We can quantify the ratio between the Nernst velocity and the heat flow velocity by the parameter $\Psi = P_e\beta_\wedge/eB\kappa_\perp$. The value of ψ in the limits of zero and infinite magnetisation can be calculated using the polynomial coefficients calculated by Epperlein and Haines (1986, table III and IV) as

$$\lim_{\chi\to 0}\Psi = \frac{\beta_{0\wedge}}{\gamma_0},\ \lim_{\chi\to\infty}\Psi = \frac{(\beta_1'' = 1.5)}{\gamma_1'}. \tag{2.4.1}$$

If the collision fix is used as an alternative to fully accounting for electron-electron collisions on VFP codes (dashed lines in fig. 2.2) then the value of Ψ in these limits becomes independent of ionisation and equal to its Lorentz limit values (0.46 and 0.73 respectively). This is due to cancellation of ξ in the two places it appears: in the $\tau_{ei}^{(B)}$-dependence of $\kappa_\perp$ and the χ-dependence of $\beta_\wedge$. Consequently, the local Nernst velocity can be greatly overestimated by this approach at low ionisations (by a factor greater than two for a low magnetisation hydrogen plasma).

Two simple, constant approximations for Ψ have been previously suggested and used: Nishiguchi et al. (1984) first suggested that $\Psi \approx \frac{2}{3}$, which obtains the low magnetisation limit to within 10% for $Z > 12$ but overestimates the Nernst velocity at high magnetisation by 40% or more. This was first used by Kho and Haines (1985, 1986) to demonstrate that the link between Nernst advection and perpendicular heat flow was not greatly affected by nonlocality, and more recently by Lancia et al. (2014) who used a reduced nonlocal heat flow model to provide a nonlocal prediction of the Nernst velocity as $v_\mathrm{N} \approx 2\vec{Q}_\perp/3P_\mathrm{e}$. Alternatively, the simplified analysis performed by Haines (1986a) predicted $\Psi = \frac{2}{5}$ even if the isotropic part of the distribution function is far from Maxwellian. This is the approach employed by Davies et al. (2015) in calculating the flux-limited Nernst velocity and works very well for values of Z between 2 and 3, but provides an underestimate of ~15–80% at higher ionisations and low magnetisations.

Mostly due to difficulties in implementation, magnetised extensions of the SNB and MN models have not been investigated in this thesis. However, a detailed assessment of the effectiveness of using the local ratio approach to obtain the nonlocal Nernst effect from the nonlocal heat flow is provided in chapter 7.

3

NUMERICAL IMPLEMENTATION

3.1 VLASOV-FOKKER-PLANCK CODES

Details are here provided of the equation sets and numerical methods employed by the cohort of Vlasov-Fokker-Planck codes used in this thesis. As a brief summary,

- KIPP simulates the EDF in one spatial and two velocity dimensions by assuming azimuthal symmetry and using operator splitting methods. It is very computationally intensive but is ideal for problems where high degrees of anisotropy can be expected (i.e. at low collisionalities).
- IMPACT is a fully-implicit VFP code able to simulate the interaction between magnetic and thermal transport. In order to do so efficiently, a Cartesian tensor expansion of the EDF is truncated after the first-order anisotropy (P1) and the effect of electron-electron collisions on the anisotropic part of the EDF is approximated through dividing the electron-ion collision frequency by the collision fix ξ_{ES}.
- K2 and OSHUN are also able to capture magnetised thermal transport effects but can go up to any order of anisotropy in a spherical harmonic expansion while retaining the full electron-electron collision operator at all orders of anisotropy. To balance against this added complexity, time-differencing is mostly explicit. Testing of these codes in more than one spatial direction is currently somewhat limited.
- DILL is a Fourier-space VFP code produced specifically for this thesis in order to efficiently simulate the damping of temperature sinusoids under the P1 approximation.
- SPRING is a rather ancient Fourier-space VFP code developed by Epperlein and Short (1994) that is able to include arbitrary harmonics.

3.1.1 *KIPP*

The 1D2V KIPP code (Chankin et al. 2012) is designed to solve the DKE derived in eq. (2.1.5) to describe parallel transport in the scrape-off layer. In order to

resolve potentially large temperature gradients near the divertor, non-uniform Cartesian spatial grids as depicted in fig. 3.1 are available; these start with the first cell located at the reflective 'stagnation' point and the exterior boundary of the final cell located at the divertor target/sheath. Note that this setup is significantly different from the other VFP codes we shall explore shortly, where both left and right boundaries are instead treated symmetrically with reflective boundaries typically placed on a cell face rather than a cell centre. Parallelisation of the code is such that there is only one spatial cell allocated to each processor, meaning that the spatial resolution can be limited by the number of cores available on the cluster.

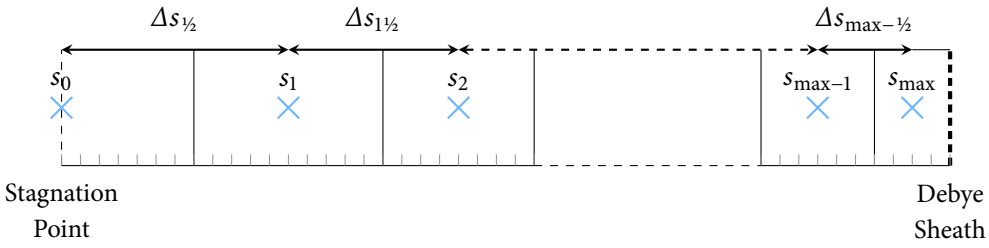

FIGURE 3.1: An example of the nonuniform grid structure used in the KIPP code. The EDF is defined on cell centres denoted by crosses.

Meanwhile, the two-dimensional velocity grid extends from $v_\parallel = -\mathtt{vmax}$ to $v_\parallel = \mathtt{vmax}$ over $2 \times \mathtt{mmax} + 1$ cells in the direction parallel to the simulation axis and from $v_\perp = 0$ to $v_\perp = \mathtt{vmax}$ over $\mathtt{mmax} + 1$ cells (where both vmax and mmax are user defined) in the perpendicular direction. Nonuniformities are also allowed and are parametrised by the variable EPS defining the ratio between adjacent cells; an example with EPS = 1.1 is illustrated in fig. 3.2. For each velocity grid, unique files must be generated containing Green function methods to solve Poisson equations for the Rosenbluth potentials that appear in the collision operator. Unfortunately, the code to generate these functions was lost prior to receiving access to KIPP, and therefore only previously generated files can be used. The highest available velocity grid thus available for use in this thesis is given by the coefficients $\mathtt{vmax} = 7v_{1\mathrm{T}}, \mathtt{mmax} = 256, \mathtt{EPS} = 1.01$.

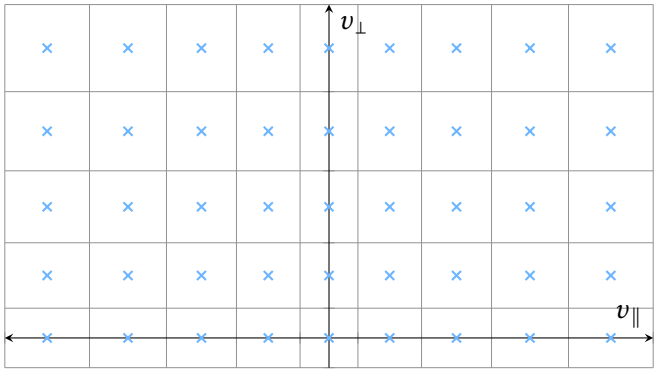

FIGURE 3.2: An example KIPP velocity grid where the ratio between adjacent cell widths is given by the parameter EPS = 1.1. Crosses mark the locations at which the EDF is defined.

The code uses an operator splitting method inspired by Shoucri and Gagne (1978) that separates the electron free-streaming from the electric field and collision operator terms and is summarised as

$$f_e^*(s_\parallel, \vec{v}) = f_e^{(n)}(s_\parallel, \vec{v} + e\vec{E}^{(n)}\Delta t/2m_e), \tag{3.1.1}$$

$$f_e^{**}(s_\parallel, \vec{v}) = f_e^*(s_\parallel - v_\parallel \Delta t, \vec{v}), \tag{3.1.2}$$

$$f_e^\dagger(s_\parallel, \vec{v}) - \Delta t C_e(f_e^\dagger) - \frac{e\vec{E}^{(n)}\Delta t}{m_e}\frac{\partial f_e^\dagger}{\partial v_\parallel} = f_e^{(n)}(s_\parallel, \vec{v}), \tag{3.1.3}$$

$$f_e^{(n+1)}(s_\parallel, \vec{v}) = f_e^{**}(s_\parallel, \vec{v}) + f_e^\dagger(s_\parallel, \vec{v}) - f_e^*(s_\parallel, \vec{v}), \tag{3.1.4}$$

where the number of timesteps is given by the superscript n and intermediate steps are indicated by the asterisks. Note that this scheme does differ somewhat from that suggested by Shoucri and Gagne (namely a half-step of free-streaming, followed by a full step of acceleration due to the electric field and then a final half-step of free-streming) in order to save computational with negligible loss of accuracy.

Differencing of the distribution function for the initial acceleration due to the parallel electric field is performed by a straightforward three-point stencil Lax-Wendroff method,

$$f_e\left(v_{\parallel n} + \frac{eE_\parallel \Delta t}{2m_e}\right) = f_e(v_{\parallel n}) + \frac{e\vec{E}\Delta t}{m_e}\frac{f_e(v_{\parallel n+½}) - f_e(v_{\parallel n-½})}{\Delta v_{\parallel n+½} + \Delta v_{\parallel n-½}} \tag{3.1.5}$$

where the interpolation of the EDF to cell boundaries is given by

$$f_{\mathrm{e}}(v_{\parallel n\pm\frac{1}{2}}) = \frac{(2\Delta v_{\parallel n\pm\frac{1}{2}} - \Delta v_{\parallel n\mp\frac{1}{2}})f_{\mathrm{e}}(v_{\parallel n}) + \Delta v_{\parallel n\mp\frac{1}{2}} f_{\mathrm{e}}(v_{\parallel n\pm 1})}{2\Delta v_{\parallel n\pm\frac{1}{2}}} \pm \frac{e\vec{E}\Delta t}{2m_{\mathrm{e}}} \frac{f_{\mathrm{e}}(v_{\parallel n\pm 1}) - f_{\mathrm{e}}(v_{\parallel n})}{\Delta v_{\parallel n\pm\frac{1}{2}}} \tag{3.1.6}$$

All instances of f_{e} in eqs. (3.1.5) *and* (3.1.6) *are evaluated at the same $s_\parallel$ and $v_\perp$.*

to ensure that the numerical parallel velocity gradient is accurate to second order (although the second derivative is only accurate to first order when the grid is nonuniform). Dirichlet boundary conditions, $f_{\mathrm{e}}(v_\parallel) = 0$, are imposed at $|v_\parallel| = \texttt{vmax}$.

Interpolation from the cell-centres $s_\parallel$ to the off-centred $s_\parallel - v_\parallel \Delta t/2$ during the free-streaming step is instead performed using a sophisticated second-order explicit upwinding scheme. This is given by LeVeque (2004)

$$f_{\mathrm{e}}(s_n - v_\parallel \Delta t, \vec{v}) = f_{\mathrm{e}}(s_{n\mp 1}, \vec{v}) - (\pm(\Delta s_{n\mp\frac{1}{2}}) + v_\parallel \Delta t)\sigma(s_{n\mp 1}), \tag{3.1.7}$$

where '$\mp$' = '$-$' if $v_\parallel > 0$ and '$+$' if $v_\parallel < 0$. The slope $\sigma(s_n)$ is calculated according to a non-uniform version of LeVeque's monotonised central-difference limiter (MC limiter), such an approach provides second-order accuracy whenever possible but also avoids undesirable oscillations that could arise from noisy data or when the timestep is insufficiently small. Formally, the MC limiter, which is preferable to alternatives such as the superbee which has the issue of sometimes artificially steepen smooth slopes (see LeVeque 2004, for more details), defined as

$$\sigma(s_n) = \mathrm{minmod}\left(\frac{f_{\mathrm{e}}(s_{n+1}) - f_{\mathrm{e}}(s_{n-1})}{\Delta s_{n+\frac{1}{2}} + \Delta s_{n-\frac{1}{2}}}, 2\frac{f_{\mathrm{e}}(s_{n+1}) - f_{\mathrm{e}}(s_n)}{\Delta s_{n+\frac{1}{2}}}, 2\frac{f_{\mathrm{e}}(s_n) - f_{\mathrm{e}}(s_{n-1})}{\Delta s_{n-\frac{1}{2}}}\right), \tag{3.1.8}$$

with 'minmod' being a three-argument extension, $\mathrm{minmod}(a, b, c) = \mathrm{minmod}(a, \mathrm{minmod}(b, c))$, of the two-argument function

$$\mathrm{minmod}(a, b) = \begin{cases} a \text{ if } |a| \leqslant |b| \text{ and } ab > 0 \\ b \text{ if } |b| \leqslant |a| \text{ and } ab > 0 \\ 0 \text{ if } ab \leqslant 0 \end{cases} \tag{3.1.9}$$

The above method can be extended quite simply to the stagnation point s_0 by invoking a ghost cell s_{-1} at which the EDF is deemed to be $f_{\mathrm{e}}(s_{-1}, v_\parallel, v_\perp) = f_{\mathrm{e}}(s_1, -v_\parallel, v_\perp)$. On the other hand, achieving an acceptable treatment of the

sheath boundary condition is more challenging. The procedure used by KIPP is to firstly use Lax-Wendroff inspired schemes (LeVeque 2004) to treat electrons with $v_\parallel < 0$ travelling from $s_{\max}$ to $s_{\max-1}$ and those with $v_\parallel > 0$ travelling from $s_{\max}$ to the target by defining the slope

$$\sigma(s_{\max}) = \frac{f_e(s_{\max}) - f_e(s_{\max-1})}{\Delta s_{\max-½}}. \tag{3.1.10}$$

Subsequently, the flux coming back from the target to $s_{\max}$ is obtained by fully reflecting only electrons with energies below the sheath potential drop and absorbing the rest at the target. The sheath potential drop is calculated such that the reflected electron flux balances the ion flux $n_i\sqrt{k_B T_e/m_i}$.

The penultimate step that calculates the combined effect of collisions and the inter-cell acceleration of electrons due to the electric field is performed by treating the Rosenbluth potentials (the integral terms in eq. (2.1.2)) explicitly (i.e. at timestep n) and the transport terms (first/second order velocity derivatives) implicitly. Differencing on the velocity grid is performed using a nine-point stencil of the distribution function and is found to perform with essentially second-order accuracy (Chankin et al. 2012). Both calculation of the Rosenbluth potentials (which requires solving Poisson equations) and the combined application of the Fokker-Planck collisions with the electric field are performed using the MUMPS sparse matrix solver. This is therefore the most computationally demanding step, making the chosen parallelisation scheme highly advantageous in avoiding any unnecessary inter-node communication by dedicating one processor to each spatial cell.

The electric field at each timestep is finally obtained by requiring it to counteract any differences incurred to the net electron flux. Further intricate rebalancing steps also occur to ensure other conservation (e.g. energy) laws are obeyed, but these will not be detailed in this thesis.

3.1.2 *IMPACT*

A simplified approach that is valid in more collisional regimes is the diffusion approximation: This consists of expanding the distribution function in Cartesian tensors and truncating all but the first two terms, reducing the number of velocity-space dimensions to one, and therefore increasing efficiency. The IMPACT code, originally developed by Kingham and Bell (2004) (two-dimensional in space) employs the diffusion approach and makes a further simplification of ignoring angular scattering due to electron-electron collisions, valid in the Lorentz limit.

In order to recover the correct local thermal conductivity for lower-Z plasmas the factor $\xi(Z)$ is used in the electron-ion collision frequency. Comparisons between IMPACT and KIPP suggest that these approximations do not greatly affect the results for unmagnetised thermal ramp relaxation problems studied in section 5.1, but can overestimate Nernst advection at low ionisations when the degree of magnetisation becomes appreciable due to reasons outlined in section 2.4. The equations solved by IMPACT, along with Ampere and Faraday's Law are thus

$$\frac{\partial f_0}{\partial t} + \frac{v}{3}\vec{\nabla}\cdot\vec{f}_1 - \frac{e\vec{E}}{3m_e v^2}\cdot\frac{\partial v^2\vec{f}_1}{\partial v} = C_{ee0}\left[f_0\right], \tag{3.1.11}$$

$$\frac{\partial \vec{f}_1}{\partial t} + v\vec{\nabla}f_0 - \frac{e\vec{E}}{m_e}\frac{\partial f_0}{\partial v} - \frac{e}{m_e}(\vec{B}\times\vec{f}_1) = -\frac{\nu_{ei}}{\xi}\vec{f}_1, \tag{3.1.12}$$

where

$$\nu_{ei} = \frac{4\pi Z n_e e^4 \log\Lambda_{ei}}{v^3} \tag{3.1.13}$$

is the velocity-dependent electron-ion collision frequency in Gaussian units.

The IMPACT code is fully implicit and first-order in time, and uses fixed-point/Picard iterations to handle nonlinear terms. The implicit treatment of the electric field enforces charge conservation at every iteration. Detailed notes on time differencing can be found in Kingham and Bell 2004. Note that the option is offered of retaining or neglecting the electron inertia term $\frac{\partial \vec{f}_1}{\partial t}$.

3.1.3 *K2 & OSHUN*

In order to address the inaccuracies in Nernst advection arising at low ionisations when using IMPACT, the K2 (Sherlock et al. 2017) and OSHUN (Tzoufras et al. 2011; Tzoufras et al. 2013; Joglekar et al. 2018) codes were deployed. Based on the KALOS formalism (Bell et al. 2006), the codes expand the EDF in spherical harmonics and employ a mixture of implicit and explicit time differencing, taking advantage of operator splitting. Both codes use the full anisotropic electron-electron collision operator, as is necessary to achieve acceptable values of $\beta_\wedge$ at low ionisations, even in the local limit. Comparisons showed reasonable agreement between K2 and OSHUN with slight discrepancies attributable to the number of harmonics used and exact implementation of boundary conditions.

A novel approach to increasing the timestep allowed by the restrictive Courant–Friedrichs–Lewy condition for explicit codes is employed by K2; an artificial

multiplier of 100 is applied to the electric permittivity, effectively reducing the plasma frequency by a factor of 10. Allowing for efficient explicit solutions to Maxwell's equations. On the other hand, OSHUN offers a (somewhat computationally intensive) implicit electric field solve as a means for allowing timesteps exceeding the plasma frequency. Both approaches are valid as long as the exact dynamics of plasma fluctuations are not of interest.

3.1.4 *DILL*

In order to efficiently analyse the implications of the diffusion approximation at very short wavelengths in chapter 4, I created a Diffusive Implicit code adapted specifically for Linearised problems in the Lorentz (high-Z) limit (DILL). The need for this code was to avoid numerical instabilities that can occur at high degrees of nonlocality when using codes such as IMPACT as well as enabling a more efficient Fourier formulation that completely reduced the spatial resolution needed for for studying small sinusoidal temperature perturbations from about 500 cells to just one. Results obtained using the DILL code are compared to analytical results in the second part of section 4.4.2 titled Without Electron Inertia and in section 4.5.1.

The code is designed to study small-amplitude sinusoidal perturbations of a single wavelength, λ, where the isotropic part of the EDF takes the form of $f_0(x,v,t) = f_e^{(mb)}(v) + \widetilde{f}_0(v,t)\cos(kx)$, with $k = 2\pi/\lambda$ and $f_e^{(mb)}$ the background Maxwellian with electron density n_0 and electron temperature T_0. Currently, a simplified version of the linearised electron-electron collision operator $C_{ee0}^{(L)}$ that is accurate at low and high velocities (but is only approximate at intermediate velocities) is used; this is equivalent to employing the first term of the iterative form for $C_{ee0}^{(L)}$ presented in section 4.3.1 and appendix B.6. The assumption of no electron inertia (i.e. $\frac{\partial \widetilde{f}_1}{\partial t} = 0$), allows the equation for the anisotropic part of the EDF, $\widetilde{f}_1$, to be easily repackaged into the $\widetilde{f}_0$ equation, giving

$$\frac{\partial \widetilde{f}_0}{\partial t} + \frac{k^2 v^2}{3\nu_{ei}^*}\left(\widetilde{f}_0 - \frac{e\widetilde{\phi}}{k_B T_0} f_e^{(mb)}\right) = \Gamma_{ee}\frac{k_B T_0}{m_e v^2}\frac{\partial}{\partial v}\left\{\frac{I_0(f_e^{(mb)})}{v} f_e^{(mb)}\frac{\partial}{\partial v}\frac{\widetilde{f}_0}{f_e^{(mb)}}\right\}, \tag{3.1.14}$$

as the equation to be solved by DILL along with an additional prescription for the electric potential. Convenient normalisations for this equation are $u =$

$\xi k^2 \lambda_{\mathrm{ei}}^{(0)} v_{2\mathrm{T}} t/3$, $V = v/v_{2\mathrm{T}}$, $F = v_{2\mathrm{T}}^3 \widetilde{f}_0/n_{\mathrm{e}}$ and $\Phi = e\widetilde{\phi}/k_{\mathrm{B}}T_0$, transforming eq. (3.1.14) into

$$\frac{\partial F}{\partial u} + V^5\left(F - \Phi\frac{\mathrm{e}^{-V^2}}{\pi^{3/2}}\right) = \frac{\zeta}{\sqrt{\pi}}\frac{1}{V^2}\frac{\partial}{\partial V}\frac{\gamma(3/2, V^2)}{V}\mathrm{e}^{-V^2}\frac{\partial}{\partial V}F\mathrm{e}^{V^2} \tag{3.1.15}$$

where $\zeta = 3/\xi Z k^2 \lambda_{\mathrm{ei}}^{(0)2}$ is a normalised coefficient used to modify the wavelength of the perturbation.

Performing a uniform cell-centred discretisation in velocity with cell size ΔV and a first-order discretisation in time with timestep Δu and defining the velocity diffusion coefficient $D^* = \gamma(3/2, V^2)\mathrm{e}^{-V^2}/V\sqrt{\pi}$ allows for the the following implicit formulation of the equation set,

$$\left(\frac{1}{\Delta u} + V^5 - \frac{\zeta}{V^2}\frac{\partial}{\partial V}D^*\frac{\partial}{\partial V}\mathrm{e}^{V^2}\right)F^{(n+1)} - \frac{V^5\mathrm{e}^{-V^2}}{\pi^{3/2}}\Phi^{(n+1)} = \frac{F^{(n)}}{\Delta u} \tag{3.1.16}$$

$$\text{along with } \frac{4\pi}{k^2{\lambda_{\mathrm{D}}}^2}\sum_{\{V\}} V^2\Delta V F^{(n+1)} + \Phi^{(n+1)} = 0 \quad \text{(Gauss' Law)}$$

$$\text{or} \quad \pi^{3/2}\sum_{\{V\}} V^7\Delta V F^{(n+1)} + \Phi^{(n+1)} = 0, \quad \text{(Zero Current)}$$

where the superscripts denote timestep. This system can be represented as a matrix equation

$$\left(\begin{array}{c|c} \nwarrow & \uparrow \\ A & B \\ \searrow & \downarrow \\ \hline \leftarrow C \rightarrow & D \end{array}\right)\left(\begin{array}{c} \uparrow \\ F^{(n+1)} \\ \downarrow \\ \hline \phi^{(n+1)} \end{array}\right) = \left(\begin{array}{c} \uparrow \\ F^{(n)}/\Delta u \\ \downarrow \\ \hline 0 \end{array}\right) \tag{3.1.17}$$

with four submatrices: A a tridiagonal matrix, B a column vector, C a row vector and $D = 1$. Right multiplying the top equation by CA^{-1} and then taking the result away from the bottom equation provides a formula for the electric potential at the next timestep $\Phi^{(n+1)}$ in terms of the distribution function at the previous timestep:

$$\Phi^{(n+1)} = P_{\mathrm{Schur}}^{-1} F^{(n)}/\Delta u., \tag{3.1.18}$$

where we have defined the rank zero Schur complement matrix, $P_{\text{Schur}} = D - CA^{-1}B$. Substituting this into eq. (3.1.16) gives the distribution function at the next timestep as

Note that P_{Schur} only needs to be calculated once for each simulation.

$$F^{(n+1)} = A^{-1}(F^{(n)}/\Delta u - B\Phi^{(n+1)}) \tag{3.1.19}$$

The DILL code simply steps forward the electric potential and distribution function by sequentially solving eqs. (3.1.18) and (3.1.19) and using the Thomas algorithm to apply A^{-1}. The advantage of the Schur complement approach used here is that it allows for a very efficient linear velocity-cell scaling while still being fully implicit.

The specific structure of the submatrix A, which captures the evolution of the distribution function due to diffusion in both configuration and velocity space, is given by

$$A_{ij} = \begin{cases} \dfrac{1}{\Delta u} + V_i^5 + \dfrac{\zeta}{V_i^2}\dfrac{(D^*_{i+½} + D^*_{i-½})e^{V_i^2}}{\Delta V^2} & \text{if } j = i \\ -\dfrac{\zeta}{V_i^2}\dfrac{D^*_{i\pm½}e^{V^2_{i\pm1}}}{\Delta V^2}, & \text{if } j = i \pm 1 \\ 0, & \text{otherwise,} \end{cases} \tag{3.1.20}$$

where $D^*_n \equiv D^*(V_n)$. The boundary conditions used are (1) zero gradient of F at $V = 0$, implemented by neglecting any appearance of $D_*(0)$ and (2) an enforced 'straight line' behaviour of F at the upper bound of the velocity grid. For an N-cell velocity grid extending from $V_1 = \Delta V/2$ to $V_N = V_{\max} - \Delta V/2$, the latter boundary condition is summarised as equating the gradient of F at $V = V_{N+½}$ and $V = V_{N-½}$ leading to the following modification of the final two matrix elements

$$A_{N,N-1} = -\frac{\zeta}{V_N^2}\frac{D^*_{N-½}e^{V^2_{N-1}} - D^*_{N+½}e^{V_N^2}}{\Delta V^2} \tag{3.1.21}$$

$$A_{N,N} = \frac{1}{\Delta u} + V_N^5 + \frac{\zeta}{V_N^2}\frac{D^*_{V_{N-½}}e^{V_N^2} - D^*_{V_{N+½}}e^{V^2_{N+1}}}{\Delta V^2}. \tag{3.1.22}$$

A more complete treatment of electron-electron collisions could easily be incorporated in the future by treating the more complicated neglected terms explicitly or iterating within a single timestep as is done with IMPACT.

3.1.5 *SPRING*

Finally, we also include results previously obtained with the SPRING (Epperlein 1994) VFP code which takes a Cartesian expansion to arbitrary order and does not neglect/approximate anisotropic electron-electron collisions. This code uses a linearised approach and 1D geometry, i.e. the spatial gradient operator $\vec{\nabla}$ is replaced by ik, making it advantageous for analysing the small-amplitude sinusoidal temperature perturbations featured in chapter 4, but not problems with large temperature perturbations. No considerations of magnetic fields were included in the code.

3.2 THE CLASSICAL TRANSPORT CODE, CTC

Used mostly in chapter 7 to investigate magnetised transport the Classical Transport Code (CTC) developed by Bissell (2011) provides a fully-implicit solution for the coupled evolution of magnetic field and temperature profiles using the Epperlein and Haines (1986) polynomial fits for the transport coefficients. Originally, the code was only written to simulate nitrogen plasmas ($Z = 7$) but the author of this thesis extended this to uniformly ionised helium plasmas ($Z = 2$) and enabled treatment of inhomogeneous ionisations using the Lorentz limit ($Z = \infty$) transport coefficients with the average collision time $\tau_{\mathrm{ei}}^{(\mathrm{B})}$ multiplied by the Epperlein-Short (1991) collision fix ξ_{ES}. The code also has the potential to deal with hydrodynamics and super-Gaussian transport coefficients arising from inverse bremsstrahlung absorption of laser energy (Ridgers et al. 2008b; Dum 1978b,a), neither of which are investigated in this thesis. Independent Nernst, Righi-Leduc and thermal flux-limiters are available and calculated using the method outlined in section 2.3.1. A number of important works employing this code include Bissell et al. 2010; Bissell 2012; Read et al. 2016.

3.3 THE SNB MODEL

The implementation of the unmagnetised SNB model used in this work is able to solve eqs. (2.3.19) and (2.3.20) with the velocity-dependent Krook operator in 1D on a non-uniform grid. A perhaps overly detailed description of the method used is here provided to facilitate the needs of others who may want to implement the model themselves. However, a condensed summary in the form of a flowchart is presented in fig. 3.4 Additionally, a simple test to demonstrate the accuracy of the nonuniform differencing is presented in section 3.3.2.

3.3.1 *Implementation*

The structure of the non-uniform grid is slightly different from IMPACT. While the field quantities (n_e, T_e, etc.) are still placed on cell nodes denoted by x_n and flow quantities ($\vec{Q}$, $\vec{E}$) on cell faces, the nodes are not in the centre of cells but instead the faces, given by $x_{n+½} = (x_{n+1} + x_n)/2$, are located halfway between cell nodes. External ghost cells are employed to impose boundary conditions; for a grid containing N interior cells the two ghost cells are denoted x_0 and x_{N+1}. This is depicted in fig. 3.3 and allows for second-order accuracy in calculating gradient quantities of scalar fields (denoted generally here by Φ) on cell faces by

$$\vec{\nabla}\Phi(x_{n+½}) \equiv \frac{\Phi(x_{n+1}) - \Phi(x_n)}{\Delta x_{n+½}}\hat{x}, \text{ where } \Delta x_{n+½} = x_{n+1} - x_n \tag{3.3.1}$$

is the node separation and $\hat{x}$ is a unit vector in the x-direction. However, the divergence operator is only accurate to first-order in general and is defined as

$$\vec{\nabla} \cdot \vec{A}(x_n) \equiv \frac{\vec{A}_x(x_{n+½}) - \vec{A}_x(x_{n-½})}{\Delta x_n}, \text{ where } \Delta x_n = x_{n+½} - x_{n-½} \tag{3.3.2}$$

is the distance between cell faces and $\vec{A}_x$ is the x-component of vector field $\vec{A}$. Other components are not considered in the current 1D implementation.

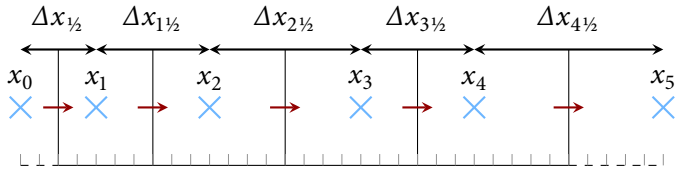

FIGURE 3.3: An example of the nonuniform grid structure used in this work's implementation of the SNB model. Flow quantities (red arrows) are placed on cell faces halfway between cell nodes where field quantities (blue crosses) are placed. The separations between cell nodes is also labelled as Δx.

The inputs required for the model are plasma profiles for field quantities—electron temperature T_e, density n_e, average ionisation Z and the Coulomb logarithms $\log \Lambda_{ei}$ and $\log \Lambda_{ee}$ (which are typically assumed to be constant and equal)—along with a specification for the x-grid. While the profiles can be given in any units or relative to any reference plasma, the current design of the code requires the spatial grid be given relative to the reference mfp

$$\lambda_{ei}^{(0)} = \lambda_{ei}\left(\sqrt{2k_B T_0/m_e}\right) = \left(\frac{4\pi\varepsilon_0}{e^2}\right)^2 \frac{(2k_B T_0)^2}{{m_e}^2 Z_0 n_0 \log \Lambda_0}. \tag{3.3.3}$$

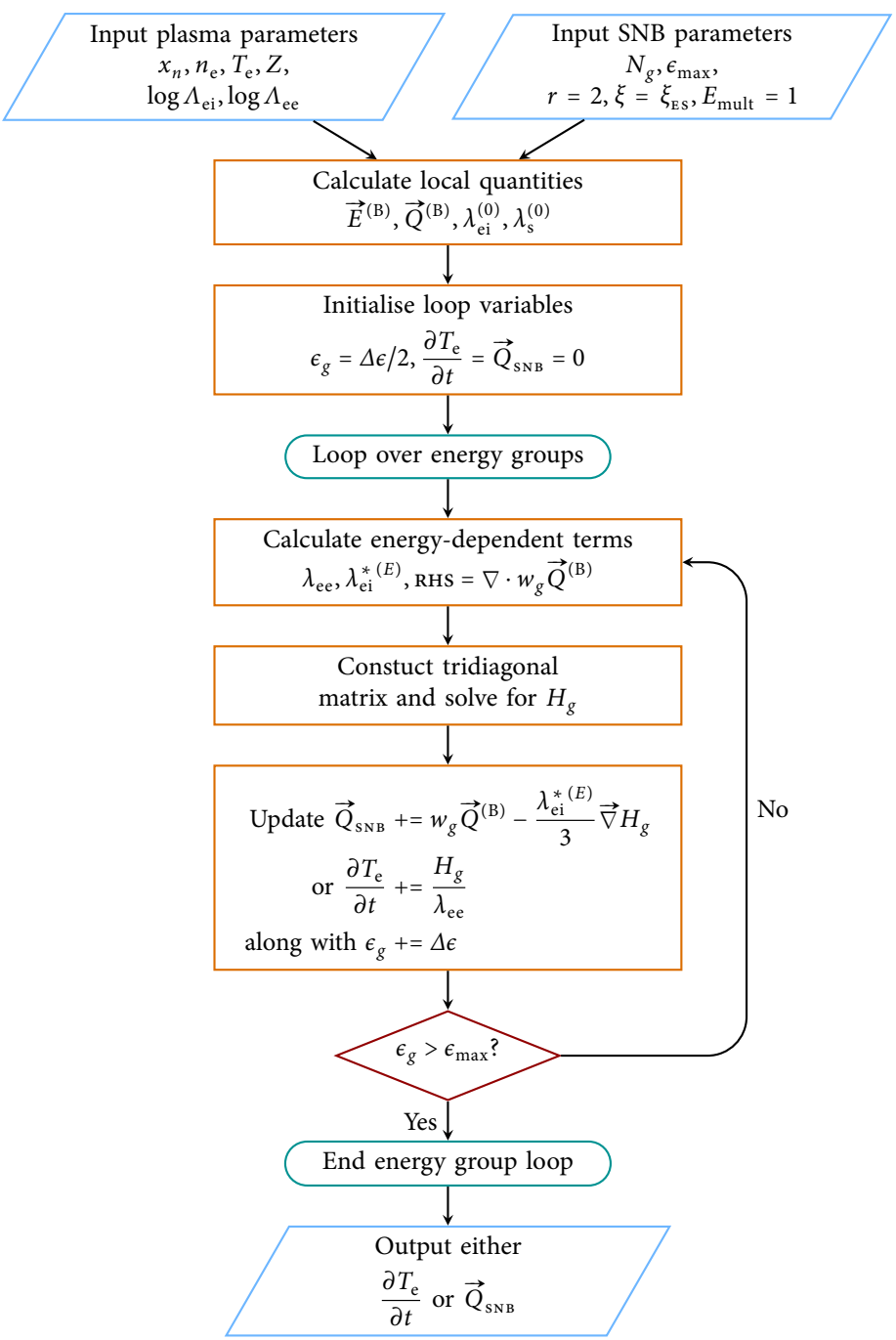

FIGURE 3.4: Flowchart outlining the process used to solve the SNB model equations. Details on normalisations are not included (nor strictly necessary) in this flowchart for reasons of clarity and conciseness.

All profiles are subsequently considered dimensionless relative to the reference plasma when overset by a '~'. These normalised quantities and are related to their dimensional values by

$$\widetilde{T}_\mathrm{e} = \frac{T_\mathrm{e}}{T_0}, \widetilde{n}_\mathrm{e} = \frac{n_\mathrm{e}}{n_0}, \widetilde{Z}_\mathrm{e} = \frac{Z_\mathrm{e}}{Z_0}, \log\widetilde{\Lambda}_\alpha\beta = \frac{\log\Lambda_\alpha\beta}{\log\Lambda_0}, \widetilde{x} = \frac{x}{\lambda_\mathrm{ei}^{(0)}}, \widetilde{t} = \nu_\mathrm{ei}^{(0)}t, \tag{3.3.4}$$

where $_0$ denotes the reference value. Internally computed parameters (including the nonlocal heat flow output by the model) are thus also rendered dimensionless. The dimensional forms for energy, electric field, and heat flow can be recovered using

$$\widetilde{\epsilon} = \frac{\epsilon}{k_\mathrm{B}T_\mathrm{e}}, \widetilde{\vec{E}} = \lambda_\mathrm{ei}^{(0)}\frac{e\vec{E}}{k_\mathrm{B}T_0}, \widetilde{\vec{Q}} = \frac{\vec{Q}}{n_0 m_\mathrm{e}(2k_\mathrm{B}T_0/m_\mathrm{e})^{3/2}}, \tag{3.3.5}$$

respectively. Note that, in contrast to IMPACT, when the dimensional temperature equals the reference temperature the dimensionless temperature $\widetilde{T}_\mathrm{e} = 1$ rather than ½. However, the same normalisation is used for heat flow in this implementation of the SNB model as in IMPACT.

The unnormalised ionisation $Z_\mathrm{e} = Z_0\widetilde{Z}_\mathrm{e}$ is used to approximate the Z-dependence of the parallel thermoelectric coefficient $\beta_\parallel$ (on the cell boundaries) using the expression for γ appearing in equation (34) of the original paper (Schurtz et al. 2000):

$$\beta_\parallel(x_{n+½}) \approx \frac{3}{2} \times \frac{Z(x_{n+½}) + 0.477}{Z(x_{n+½}) + 2.15}, \tag{3.3.6}$$

where Z has been linearly interpolated from cell nodes to faces. Additionally the Z-dependence of the local thermal conductivity, is accounted for on both cell nodes and cell boundaries:

$$\xi(x_n) \approx \frac{Z(x_n) + 0.24}{Z(x_n) + 4.2}, \ \xi(x_{n+½}) \approx \frac{Z(x_{n+½}) + 0.24}{Z(x_{n+½}) + 2.4} \tag{3.3.7}$$

This 'collision fix' is also used to approximate the effects of electron-electron collisions on $\vec{f}_1$ in an identical way to certain VFP codes, such as IMPACT and SPARK, by modifying the SNB electron-ion mfp.

These corrections to the transport coefficients can be used to calculate the stopping distance of a thermal electron travelling antiparallel to the local electric field,

$$\begin{aligned}\frac{1}{\widetilde{\lambda}_{\mathrm{s}}^{(0)}}(x_{n+½}) &= \frac{\widetilde{\vec{E}}^{(\mathrm{B})}}{\widetilde{T}_{\mathrm{e}}}(x_{n+½}) \\ &= \widetilde{\vec{\nabla}}\log\widetilde{n}_{\mathrm{e}}(x_n) + \left(1+\beta_{\parallel}(x_{n+½})\right)\widetilde{\vec{\nabla}}\log\widetilde{T}_{\mathrm{e}}(x_n),\end{aligned} \tag{3.3.8}$$

The positioning of the argument $(x_{n+½})$ on the left-hand side of eq. (3.3.8) indicates that it is the inverse mfp that is calculated in the code (the actual mfp is never used directly). Similar notation is used over the next few pages.

as well as the local heat flow

$$\widetilde{\vec{Q}}^{(\mathrm{B})}(x_{n+½}) = -\frac{8}{\sqrt{\pi}}\frac{\xi(x_{n+½})}{\widetilde{Z}(x_{n+½})}\frac{2}{7}\widetilde{\vec{\nabla}}\widetilde{T}_{\mathrm{e}}^{\,7/2}(x_n) \tag{3.3.9}$$

Following these local calculations the code loops over energy groups, which can be modified by the user selecting the total number of groups N_g and the maximum normalised energy $\widetilde{\epsilon}_{\max}$. From this the grid spacing is simply calculated as $\Delta\widetilde{\epsilon} = \widetilde{\epsilon}_{\max}/N_g$. At this point, only uniformly-spaced energy grids have been investigated. In a similar vein to the spatial grid, each group is denoted $\widetilde{\epsilon}_g$ with upper- and lower-bounds $\widetilde{\epsilon}_{g\pm½}$ such that $\widetilde{\epsilon}_{½} = 0$ and $\widetilde{\epsilon}_{N_g+½} = \widetilde{\epsilon}_{\max}$. The first group-dependent calculation that occurs is that of the crucial variable,

$$\beta_g(x_{n+½}) = \frac{\widetilde{\epsilon}_g}{\widetilde{T}_{\mathrm{e}}(x_{n+½})}, \tag{3.3.10}$$

which is introduced in the original paper as β (Schurtz et al. 2000) and represents the relative energy of a group compared to the thermal energy at that location.

Next the mfp's of each group need to be obtained. However, due to the nature of the model equations it turns out to be more convenient to first calculate the inverse of the mean free paths.

$$\frac{1}{\widetilde{\lambda}_{\mathrm{ei}}^{*}}(x_n,\widetilde{\epsilon}_g) = \frac{\xi(x_n)\widetilde{Z}(x_n)\widetilde{n}_{\mathrm{e}}(x_n)\log\widetilde{\Lambda}_{\mathrm{ei}}(x_n)}{\widetilde{\epsilon}_g^{\,2}}, \text{ and} \tag{3.3.11}$$

$$\frac{1}{\widetilde{\lambda}_{\mathrm{ee}}}(x_n,\widetilde{\epsilon}_g) = \frac{r\widetilde{n}_{\mathrm{e}}(x_n)\log\widetilde{\Lambda}_{\mathrm{ee}}(x_n)}{Z_0\widetilde{\epsilon}_g^{\,2}}, \tag{3.3.12}$$

where r can vary but is typically defined as 2. In the *averaged* version of the SNB model both mfp's are replaced by their geometric average

$$\frac{1}{\widetilde{\lambda}_{\mathrm{e}}^{*}}(x_n,\widetilde{\epsilon}_g) = \sqrt{r\xi(x_n)\log\widetilde{\Lambda}_{\mathrm{ei}}(x_n)\log\widetilde{\Lambda}_{\mathrm{ee}}(x_n)\widetilde{Z}(x_n)/Z_0}\,\frac{\widetilde{n}_{\mathrm{e}}(x_n)}{\widetilde{\epsilon}_g^{\,2}}. \tag{3.3.13}$$

The stopping distance due to the electric field is then incorporated into the limited mfp

$$\widetilde{\lambda}^{*\,(E)}_{\mathrm{ei}}(x_{n+½}, \widetilde{\epsilon}_g) = \frac{1}{\dfrac{1}{\widetilde{\lambda}^{*}_{\mathrm{ei}}}(x_{n+½}, \widetilde{\epsilon}_g) + \dfrac{E_{\mathrm{mult}}}{\beta_g(x_{n+½})} \times \dfrac{1}{\widetilde{\lambda}^{(0)}_{\mathrm{s}}}(x_{n+½})}, \tag{3.3.14}$$

where we have defined the constant E_{mult} (1 by default) to allow for easy investigation of the effect of the electric field and $1/\widetilde{\lambda}^{*}_{\mathrm{ei}}$ has been interpolated on to cell faces. Once again, the implementation of the *averaged* version can be achieved by replacing $_{\mathrm{ei}}$ with $_{\mathrm{e}}$.

The weighting function for each group is calculated using the analytic form of the integral

$$\begin{aligned} w_g(x_{n+½}) &= \int_{\beta_{g-½}(x_{n+½})}^{\beta_{g+½}(x_{n+½})} \frac{\beta^4 \mathrm{e}^{-\beta}}{24} \mathrm{d}\beta \\ &= \left[-\frac{(\beta^4 + 4\beta^3 + 12\beta^2 + 24\beta + 24)}{24} \mathrm{e}^{-\beta} \right]_{\beta_{g-½}(x_{n+½})}^{\beta_{g+½}(x_{n+½})}, \end{aligned} \tag{3.3.15}$$

where the square brackets denote that the difference of the terms inside evaluated at $\beta_{g-½}(x_{n+½})$ and $\beta_{g-½}(x_{n+½})$ is taken. Using w_g the source term for the SNB model can be easily obtained as

$$\mathrm{RHS}(x_n, \widetilde{\epsilon}_g) = -\vec{\widetilde{\nabla}} \cdot \left(w_g(x_{n±½}) \vec{\widetilde{Q}}^{(\mathrm{B})}(x_{n±½}) \right) \tag{3.3.16}$$

All these terms can be combined to form the differential equation that must be solved for the contributions $\widetilde{H}_g$:

$$\left[\frac{1}{\widetilde{\lambda}_{\mathrm{ee}}}(x_n, \widetilde{\epsilon}_g) - \vec{\widetilde{\nabla}} \cdot \frac{\widetilde{\lambda}^{*\,(E)}_{\mathrm{ei}}(x_{n±½}, \widetilde{\epsilon}_g)}{3} \vec{\widetilde{\nabla}} \right] \widetilde{H}_g(x_n) = \mathrm{RHS}(x_n, \widetilde{\epsilon}_g). \tag{3.3.17}$$

The diffusive term in the previous equation is differenced as

$$\begin{aligned} \vec{\widetilde{\nabla}} \cdot \frac{\widetilde{\lambda}^{*\,(E)}_{\mathrm{ei}}}{3} \vec{\widetilde{\nabla}} \widetilde{H}_g &= \frac{\widetilde{\lambda}^{*\,(E)}_{\mathrm{ei}}(x_{n+½}) \vec{\widetilde{\nabla}} \widetilde{H}_g(x_n) - \widetilde{\lambda}^{*\,(E)}_{\mathrm{ei}}(x_{n-½}) \vec{\widetilde{\nabla}} \widetilde{H}_g(x_{n-1})}{3\Delta\widetilde{x}_n} \\ &= \frac{\widetilde{\lambda}^{*\,(E)}_{\mathrm{ei}}(x_{n+½})}{3\Delta\widetilde{x}_n \Delta\widetilde{x}_{n+½}} \left(\widetilde{H}_g(x_{n+1}) - \widetilde{H}_g(x_n) \right) \\ &\quad - \frac{\widetilde{\lambda}^{*\,(E)}_{\mathrm{ei}}(x_{n-½})}{3\Delta\widetilde{x}_n \Delta\widetilde{x}_{n-½}} \left(\widetilde{H}_g(x_n) - \widetilde{H}_g(x_{n-1}) \right), \end{aligned} \tag{3.3.18}$$

where the dependence on $\widetilde{\epsilon}_g$ has been dropped for convenience. Substituting eq. (3.3.18) into (3.3.17) forms the finite difference equation

$$\begin{aligned} & & -\frac{\widetilde{\lambda}_{\mathrm{ei}}^{*(E)}(x_{n-\frac{1}{2}})}{3\Delta\widetilde{x}_n\Delta\widetilde{x}_{n-\frac{1}{2}}} & \quad \widetilde{H}_g(x_{n-1}) \\ +\left(\frac{1}{\widetilde{\lambda}_{\mathrm{ee}}}(x_n) + \frac{\widetilde{\lambda}_{\mathrm{ei}}^{*(E)}(x_{n+\frac{1}{2}})}{3\Delta\widetilde{x}_n\Delta\widetilde{x}_{n+\frac{1}{2}}} + \frac{\widetilde{\lambda}_{\mathrm{ei}}^{*(E)}(x_{n-\frac{1}{2}})}{3\Delta\widetilde{x}_n\Delta\widetilde{x}_{n-\frac{1}{2}}}\right) & \quad \widetilde{H}_g(x_n) & \quad = \mathrm{RHS}(x_n) \\ & & -\frac{\widetilde{\lambda}_{\mathrm{ei}}^{*(E)}(x_{n+\frac{1}{2}})}{3\Delta\widetilde{x}_n\Delta\widetilde{x}_{n+\frac{1}{2}}} & \quad \widetilde{H}_g(x_{n+1}) \end{aligned} \tag{3.3.19}$$

that resembles a tridiagonal matrix, which can be solved with the Thomas algorithm (Conte and Boor 1972).

As $\widetilde{H}_g$ is obtained for each energy group these can be combined to compute either the instantaneous nonlocal heat flow

$$\widetilde{\vec{Q}}_{\mathrm{SNB}}(x_{n+\frac{1}{2}}) = \sum_g w_g(x_{n+\frac{1}{2}})\widetilde{\vec{Q}}^{(\mathrm{B})}(x_{n+\frac{1}{2}}) - \frac{\widetilde{\lambda}_{\mathrm{ei}}^{*(E)}(x_{n+\frac{1}{2}}, \widetilde{\epsilon}_g)}{3}\widetilde{\vec{\nabla}}\widetilde{H}_g(x_n) \tag{3.3.20}$$

or the rate of change of temperature

$$\frac{\partial\widetilde{T}_{\mathrm{e}}}{\partial\widetilde{t}}(x_n) = -\frac{4}{3\widetilde{n}_{\mathrm{e}}}\nabla\cdot\widetilde{\vec{Q}}_{\mathrm{SNB}} = \frac{4}{3\widetilde{n}_{\mathrm{e}}}\sum_g \frac{1}{\widetilde{\lambda}_{\mathrm{ee}}}(x_n, \widetilde{\epsilon}_g)\widetilde{H}_g(x_n). \tag{3.3.21}$$

3.3.2 *Testing*

In order to assess the reliability and accuracy of our treatment of nonuniform grids a simple test case was performed to compare the nonlocal heat flows predicted when using a nonuniform grid to that with a uniform gird. A fully ionised nitrogen plasma ($Z = 7$) of uniform electron density $n_{\mathrm{e}} = 1.5 \times 10^{19}\,\mathrm{cm}^{-3}$ and Coulomb logarithm $\log\Lambda_{\mathrm{ei}} = \log\Lambda_{\mathrm{ee}} = 8.0$ with a Gaussian temperature profile $T_{\mathrm{e}} = 100 + 400\exp(-(x/100\,\mu\mathrm{m})^2)$ eV was analysed over a 500 μm domain. The uniform grid used a spacing of $\Delta x = 4\,\mu$m, while the nonuniform grid chose a uniformly-distributed random value for the grid spacing between 1 μm and 8 μm. As a result of randomisation the nonuniform grid consisted of a slightly different number of cells to the uniform grid (112 internal cells as opposed to 100).

The nonlocal heat flow for both grids, calculated by the SNB model using the default settings, along with the discretisations of the temperature profile is depicted in fig. 3.5. It is observed that both heat flows lie along the same curve with no obvious errors or numerical artefacts; this gives confidence in the nonuniform differencing that is employed here.

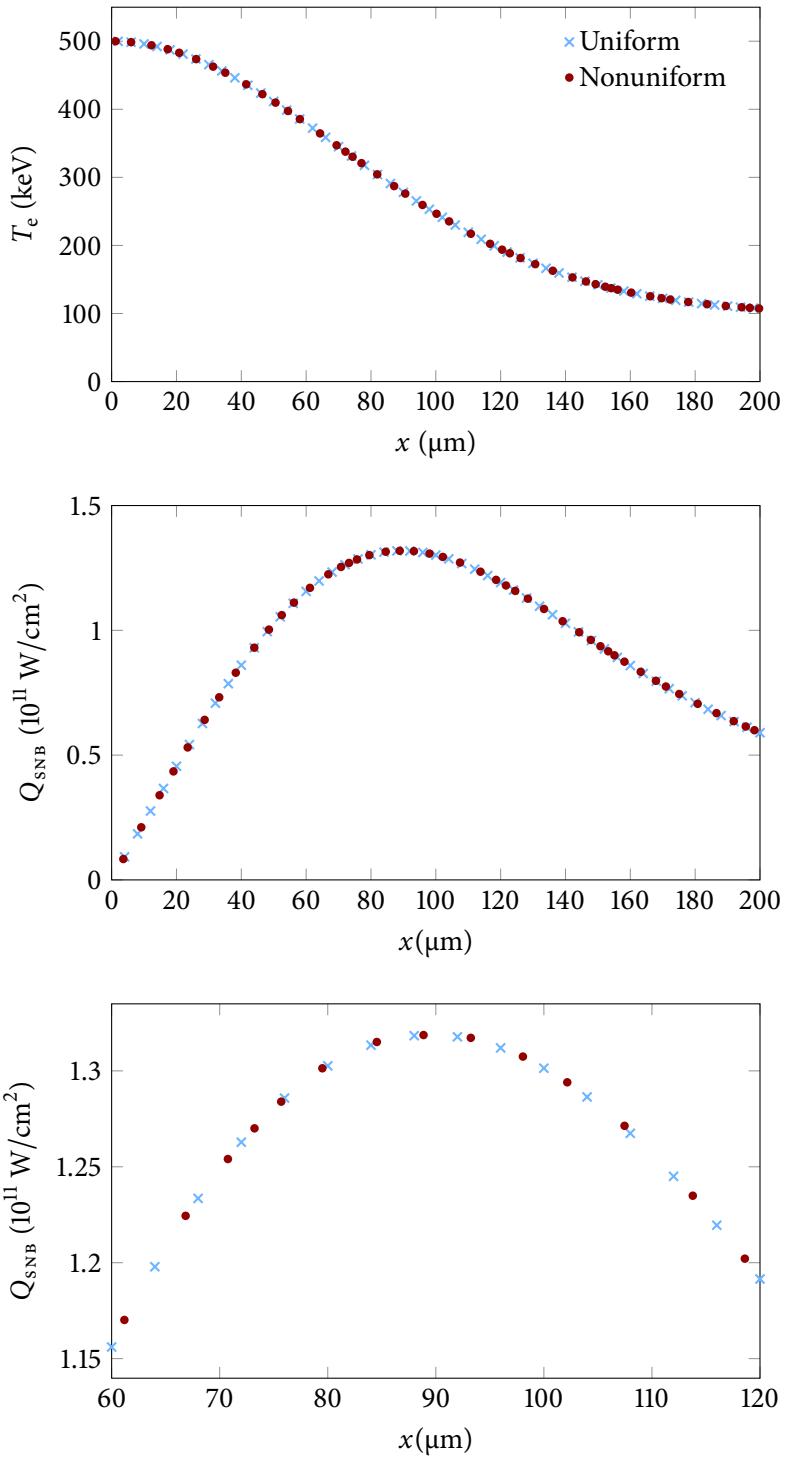

Plasma parameters:
$Z = 7$
$n_e = 1.5 \times 10^{19}$ cm^{-3}
$\log \Lambda_0 = 8$

SNB parameters:
$r = 2$
$\xi = \xi_{ES}$
$E_{mult} = 1$

FIGURE 3.5: The Gaussian temperature profile (top) used to test the finite differencing of the SNB model along with the nonlocal heat flows predicted (middle and bottom) when using a uniform (blue crosses) or nonuniform (red dots) grid. The bottom diagram is simply a zoomed in version of the middle. The simulation domain extends from 0 to 500 μm.

3.4 NON-FOURIER LANDAU-FLUID

The original implementation of the Non-Fourier Landau-Fluid model (NFLF) has been extended beyond solving only three modified Helmholtz equations to a user-defined number of these, N. The code now computes the fitting coefficients p_j, q_j at the beginning of each run of the code, allowing for easy adaptation of the fit function, range and implementation of constraints (see section 3.4.2 and 3.4.4) to fit user requirements.

3.4.1 *Finite differencing*

The contributions $\vec{Q}_j$ to the nonlocal heat flow are obtained by solving the N modified Helmholtz equations

$$\left[q_j^2 D + (a\lambda_{\mathrm{ei}}^{(\mathrm{B})})^2 \vec{\nabla} \cdot D\vec{\nabla}\right] W\vec{Q}_j = p_j D W \vec{Q}^{(\mathrm{B})}, \tag{3.4.1}$$

where a is an ionisation-dependent coefficient present in the original papers (Dimits et al. 2014; Umansky et al. 2015) that parametrises the damping behaviour in the collisionless limit $\kappa_\parallel(k \to \infty) \sim \kappa_\parallel^{(\mathrm{B})}/ak\lambda_{\mathrm{ei}}^{(\mathrm{B})}$, D, W are spatially-dependent weighting profile introduced to explore nonlinear improvements to the model, as they both appear on both sides of the equation they can be of any units ($D = 1/n_{\mathrm{e}}$, $W = {T_{\mathrm{e}}}^4$ provides noticeable improvement over the original model, $D = W = 1$, for low to moderate degrees of nonlocality but can significantly overpredict the preheat in extremely steep temperature gradients, (see section 5.1.1 for more details.) and $\vec{Q}^{(\mathrm{B})}$ is the local heat flow. These contributions are simply combined to obtain the nonlocal heat flow $\vec{Q}_{\mathrm{NFLF}} = \sum_{j=1}^{N} \vec{Q}_j$. Central differencing is applied on a uniform grid such that the field and flow quantities both lie on cell nodes. This transforms eq. (3.4.1) into

$$\begin{aligned}
&-\frac{D(x_{n-½})}{D(x_n)} a^2 \lambda_{\mathrm{ei}}^{(\mathrm{B})}(x_n)^2 \quad W(x_{n-1}) Q_j(x_{n-1}) \\
+ &\left(q_j^2 + \frac{D(x_{n-½}) + D(x_{n+½})}{D(x_n)} a^2 \lambda_{\mathrm{ei}}^{(\mathrm{B})}(x_n)^2\right) W(x_n) \quad Q_j(x_n) \quad = p_j W(x_n) Q^{(\mathrm{B})}(x_n) \\
&-\frac{D(x_{n+½})}{D(x_n)} a^2 \lambda_{\mathrm{ei}}^{(\mathrm{B})}(x_n)^2 \quad W(x_{n+1}) Q_j(x_{n+1})
\end{aligned}$$

where $D_{x+n\pm½}$ refer to evaluation halfway between nodes. The tridiagona system is then solved using the Thomas algorithm (Conte and Boor 1972) with Dirichlet boundary conditions $\vec{Q}_j(x_0) = \vec{Q}_j(x_N) = 0$.

3.4.2 *Calculation of coefficients using separable least squares*

The coefficients p_j, q_j used in the NFLF model are obtained by least squares minimisation such that the sum of Lorentzians

$$\sum_{j=1}^{N} \frac{p_j}{q_j^2 + \left(ak\lambda_{\mathrm{ei}}^{(\mathrm{B})}\right)^2} \approx \frac{\kappa_\parallel(k)}{\kappa_\parallel^{(\mathrm{B})}} \tag{3.4.2}$$

is a good approximation over a specified range in k-space for a given N. Here the right-hand side represents the relative damping rate of a low-amplitude temperature sinusoid compared to that predicted in the local limit. An approximate analytic form for $\kappa_\parallel(k)$ given in eq. (4.6.6) is used in calculating the fit coefficients. The fitting process has been carried out for two ionisations, $Z = 1$ and 8, optimal numerical values for these coefficients are tabulated in appendix A.

Fully-nonlinear fitting routines (e.g. SciPy's `curve_fit`) were found to take a long time to converge as the number of Lorentzians N exceeded about 3 to 6, especially when the initial guess for the coefficients was poor. Fortunately, the fact that the coefficients p_j occur linearly in the model allows the variable projection method for separable nonlinear least squares problems to be used. This method can be applied to any model of the form $\sum_{i=1}^{N} p_j \phi_j(\{q_\alpha\}; k)$ (where ϕ_j can be any functions depending on any number of nonlinear coefficients q_α) used to approximate data $S(k)$. Advantage is taken of the fact that the optimal choice of linear coefficients can be computed exactly for a given set of nonlinear coefficients q_j by solving the matrix equation

$$A_{ij} p_j = \sum_{\{k\}} \phi_i(\{q_\alpha\}) S(k), \text{ where } A_{ij} = \sum_{\{k\}} \phi_i(\{q_\alpha\}) \phi_j(\{q_\alpha\}), \tag{3.4.3}$$

where $\{k\}$ represents the set of points in k-space used for fitting and Einstein summation over repeated indices is implied for this equation only. This allows the linear coefficients p_j to be eliminated so that the model depends purely on the nonlinear coefficients q_j, thereby reducing the dimensionality of the fitting problem by N.

The first publication on the subject of separable least squares was written by Lawton and Sylvestre (1971), based on an unpublished manuscript by Norman E Dahl. However, Golub and Pereyra (1973) suggested a revolutionary improvement to the solution of such problems by providing a way to use analytic derivatives of the nonlinear functions $\frac{\partial \phi_j}{\partial q_k}$ (specified by the user) in constructing the Jacobian for the reformulated problem.

To calculate the NFLF coefficients in this thesis Alan Miller's (2004) Fortran 90 translation of the Stanford implementation of the variable projection algorithm, VARPRO, was used. Originally written by Golub and Pereyra (1972), this version contains a number of optimisations and refinements incorporated by John Bolstad (2007), particularly a major simplification in computing the necessary derivatives provided by Kaufman (1975). The code employs Osborne's modification (1972) of the Levenberg-Marquardt algorithm in the nonlinear minimisation routine. The application of constraints in the fitting procedure that I have added myself shall be outlined in the next subsection. A number of more recent references on the variable projection algorithm include Golub and Pereyra (2003), Björk (2007), Osborne (2007) and O'Leary and Rust (2013).

3.4.3 *Determining fitting region*

The fitting method requires a discrete set of locations $\{k\}$ at which to minimise the least square error. In order to avoid placing too much weight on the collisionless regime, these fitting points were chosen to be uniformly spaced on a logarithmic scale rather than a linear one: Specifically, consecutive values of k were related by a constant ratio of $10^{-0.2}$ when finding coefficient for $Z = 1$ and $10^{-0.1}$ for $Z = 8$. The lowest value of k in this region was chosen to be $2 \times 10^{-3}/\lambda_{\mathrm{ei}}^{(\mathrm{B})}$ for $Z = 1$ and $2 \times 10^{-4}/\lambda_{\mathrm{ei}}^{(\mathrm{B})}$ for $Z = 8$, at which point the thermal conductivity for hydrogen is reduced by less than 0.02% from that in the local limit. However, the upper limit of the fitting region $\max\{k\}$ was varied depending on the number of Lorentzians being used (N) and the desired accuracy.

Typically, as the wavelength shortens the percentage error between the NFLF model and the analytical approximation for $\kappa_\parallel(k)/\kappa_\parallel^{(\mathrm{B})}$ given in eq. 4.6.6 is observed to oscillate with an increasing amplitude (the number of oscillations depends on N) before steeply shooting off to negative 100% as a result of the NFLF asymptote always being proportional to $1/k^2$ regardless of the number of Lorentzians used. Of course, the point at which this difference in asymptote becomes important is later if N is increased. Determination of $\max\{k\}$ for a given N was carried out by first specifying a maximum desired percentage error $\mathrm{p.e.}_{\max}$ and trying to find the largest region in which the error is always less than this. In general, it was found that increasing $\max\{k\}$ until the percentage difference (using optimal coefficients for that region) at the last turning point *just* reaches $\mathrm{p.e.}_{\max}$ optimises the maximum degree of nonlocality at which the desired accuracy is achieved. An illustration of the discussed error oscillation using different fitting regions for the case $N = 3$ is provided in fig. 3.6.

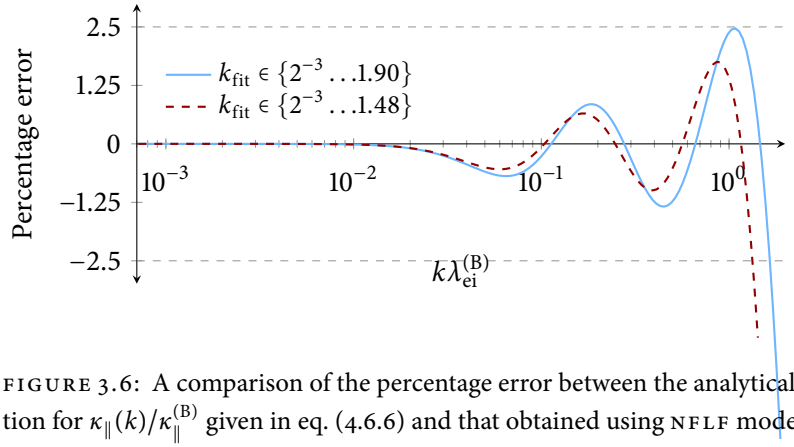

FIGURE 3.6: A comparison of the percentage error between the analytical approximation for $\kappa_\parallel(k)/\kappa_\parallel^{(\text{B})}$ given in eq. (4.6.6) and that obtained using NFLF model with three Lorentzians ($N = 3$) using optimal coefficients obtained from two different fitting regions. Both regions begin at 2×10^{-3} and have a constant ratio of $10^{-0.2}$ between consecutive points. It is shown that extending the fitting region until the final local maximum reaches the desired maximal error of 2.5% optimises the region over which such accuracy is achieved. Both plotted lines extend until the end of their respectibe fitting regions.

Linear coefficients for fitting region $\{2 \times 10^{-3} \ldots 1.48\}$ *are given by*
p_j = 1.736e−3, 5.250e−2, 1.352,
and the nonlinear coefficients are given by
q_j = 9.742e−2, 0.321, 2.099,
while for fitting region $\{2 \times 10^{-3} \ldots 1.90\}$ *they are*
p_j = 2.176e−3, 6.316e−2, 1.682,
q_j = 1.020e−1, 3.513e−1, 2.455.

3.4.4 *Applying constraints*

It is desirable that the limiting behaviour of the thermal conductivity in the hydrodynamic and semicollisional regimes $\kappa_\parallel(k \to 0)/\kappa_\parallel^{(\text{B})} = 1 - b_Q\left(k\lambda_{\text{ei}}^{(\text{B})}\right)^2 + \mathcal{O}\left(k^3\lambda_{\text{ei}}^{(\text{B})3}\right)$ is preserved by the fitting routine. This is achieved by Taylor expanding the left-hand side of eq. (3.4.2) about $k = 0$ and matching coefficients to achieve summation constraints on the fitting parameters

The coefficient b_Q varies with ionisation and is discussed in more detail in the next chapter.

$$\sum_{j=1}^{N} \frac{p_j}{q_j^2} = 1, \sum_{j=1}^{N} \frac{p_j}{q_j^4} = \frac{b_Q}{a^2}. \tag{3.4.4}$$

Each constraint reduces the number of free parameters and can thus be used to eliminate one of the linear coefficents p_j. A demonstration of this for the first constraint is quite simple, by rearranging we obtain

$$p_1 = q_1^2\left(1 - \sum_{j=2}^{N} \frac{p_j}{q_j^2}\right). \tag{3.4.5}$$

Substituting this into eq. (3.4.1) results in a new optimisation problem that does not include p_1

$$\frac{q_1^2}{q_1^2 + k'^2} + \sum_{j=2}^{N} p_j\left(\frac{1}{q_j^2 + k'^2} + \frac{q_1^2}{q_j^2}\frac{1}{q_1^2 + k'^2}\right) = \frac{\kappa_\parallel(k)}{\kappa_\parallel^{(\text{B})}} \tag{3.4.6}$$

Note that the term before the summation is not multiplied by a linear parameter, making it 'purely nonlinear'; the variable projection method is easily able to handle this by incorporating it into the right-hand side (S in eq. (3.4.3)).

The second constraint could be incorporated in a similar manner, this time eliminating p_2, but doing this manually could be prone to errors both in its derivation and its implementation in code form as the fitting functions become quite complex. Additionally, such an approach precludes the possibility of easily introducing new constraints or applying constraints on a different separable nonlinear least squares problem. Therefore, a general, iterative approach to incorporating constraints was implemented. For the moment this only works for nonlinear functions ϕ_j that initially depend on only one nonlinear coefficient q_j. A change of variables $k' = ak\lambda_{\mathrm{ei}}^{(\mathrm{B})}$ is applied in order to adhere to the notation given in the original papers (Dimits et al. 2014; Umansky et al. 2015). The model can then be put in a universal form, where the approximation to be optimised is given by

$$\phi_0 + \sum_{j=1}^{N} p_j \phi_j(q_j; k') \approx S(k'), \tag{3.4.7}$$

where initially $\phi_0 = 0$, $\phi_j = 1/(q_j^2 + k'^2)$ and $S(k') = \kappa_\parallel(k)/\kappa_\parallel^{(\mathrm{B})}$ for the case of the NFLF. In addition to this the analytic form of the derivatives need also be provided, for the NFLF this is simply given by $\partial_j \phi_j = -2q_j/(q_j^2 + k'^2)$, where ∂_j here denotes partial differentiation with respect to nonlinear coefficient q_j. One of the terms $p_j\phi_j$ can then be eliminated for each of the N_c generalised summation constraints denoted by i and expressed as

$$\eta_0^{(i)} + \sum_{j=1}^{N} p_j \eta_j^{(i)}(q_j; k') = 0. \tag{3.4.8}$$

Each constraint is dealt with in turn, starting with $i = 1$. First the fitting functions $\phi_j(q_j)$ are updated along with their derivatives by applying the product and quotient rules for $j = 0$ and $i < j \leqslant N$:

$$\phi_j = \phi_j - \frac{\eta_j^{(i)}}{\eta_i^{(i)}}\phi_i, \tag{3.4.9}$$

$$\partial_j\phi_j = \partial_j\phi_j - \frac{\partial_j\eta_j^{(i)}}{\eta_i^{(i)}}\phi_i, \tag{3.4.10}$$

$$\partial_k\phi_j = \partial_k\phi_j - \frac{\partial_k\eta_j^{(i)}}{\eta_i^{(i)}}\phi_i - \frac{\eta_j^{(i)}}{\eta_i^{(i)}}\partial_k\phi_i + \frac{\eta_j^{(i)}}{\eta_i^{(i)2}}\phi_i\partial_k\eta_j, \qquad k \leqslant i \tag{3.4.11}$$

Note that both the fitting functions and the constraint functions gain an extra dependency (starting with q_1) for each constraint incorporated. Following this ϕ_i is set to 0.

Additionally, the remaining constraint functions denoted by $l > i$ also need to be updated by

$$\eta_j^{(l)} = \eta_j^{(l)} - \frac{\eta_j^{(i)}}{\eta_i^{(i)}}\eta_i^{(l)}, \tag{3.4.12}$$

$$\partial_j\eta_j^{(k)} = \partial_j\eta_j^{(k)} - \frac{\partial_j\eta_j^{(i)}}{\eta_i^{(i)}}\eta_i^{(k)}, \tag{3.4.13}$$

$$\partial_k\eta_j^{(k)} = \partial_j\eta_j^{(k)} - \frac{\partial_k\eta_j^{(i)}}{\eta_i^{(i)}}\eta_i^{(k)} - \frac{\eta_j^{(i)}}{\eta_i^{(i)}}\partial_k\eta_i^{(k)} + \frac{\eta_j^{(i)}}{\eta_i^{(i)2}}\eta_i^{(k)}\partial_k\eta_i^{(i)}. \tag{3.4.14}$$

again for $j = 0$ and $i < j \leqslant N$.

After repeating this entire process for each constraint $i = 2, \ldots, N_c$ the updated fitting functions including the purely nonlinear term ϕ_0 and their derivatives are used as inputs to the variable projection algorithm. The final model used to approximate S is thus given by

$$\phi_0(q_1, \ldots, q_{N_c}) + \sum_{j=N_c}^{N} p_j\phi_j(q_j, q_1, \ldots, q_{N_c}; k') \approx S(k'), \tag{3.4.15}$$

Note that, in practice the iterative incorporation of constraints was coded in a recursive fashion, and it was actually the last linear coefficients $p_N, \ldots, p_{N+1-N_c}$ rather than the first $p_1, \ldots p_{N_c}$ that were eliminated.

Once the coefficients for the rewritten version of the model have been obtained, the values of the eliminated coefficents $p_1, \ldots, p_{N_c}$ need to be calculated. While there are multiple ways of performing this, the method used here was to rearrange

the *original* constraint function to construct a system of linear equations for the eliminated coefficients

$$\sum_{j=1}^{N_c} p_j \eta_j^{(i)} = \eta_0^{(i)} - \sum_{N_c+1}^{N} p_j \eta_j^{(i)}, 1 \leqslant i \leqslant N_c \tag{3.4.16}$$

that can be solved by matrix methods.

3.4.5 *Providing initial guesses*

Even with the variable projection method eliminating all the linear coefficients, it was still possible to experience lack of convergence for N as low as 5. Therefore a robust method of providing initial guesses for the nonlinear coefficients q_j was desired. By looking for patterns in the values of nonlinear coefficients for different values of N, an approximate trend was observed (see fig. 3.7) that could be used as a good starting for calculating q_j for the majority of $N \leqslant 12$ for hydrogen and $N \leqslant 10$ for oxygen:

$$q_j \approx \quad 0.16 \exp(-0.2(N-j) + \quad 0.8(j-1)) \text{ for } Z = 1, \tag{3.4.17}$$

$$q_j \approx 0.065 \exp(-0.2(N-j) + 0.95(j-1)) \text{ for } Z = 8. \tag{3.4.18}$$

One exception was for $N = 6$, where the initial conditions proved unstable for the exact implementation of variable projection used, and the largest nonlinear coefficient drifted off to infinity with each iteration. In this case the initial guesses had to be tweaked manually.

3.5 EIGENVECTOR INTEGRAL CLOSURE

The BOUT++ implementation of J T Omotani et al. (2013; 2015) was used to produce results with the EIC model (the main changes to this implementation made by the author of this thesis were merely choice of units and set up of boundary conditions). The required eigenfunctions and eigenvalues had to first be computed using a Mathematica script, which set up the appropriate collision matrix to solve, however this only needed to be computed once for a given ionisation and particular truncation of moments. Both the original Legendre-Laguerre and the newer Hermite-Laguerre bases are available and periodic/reflective boundary conditions are typically used in this thesis.

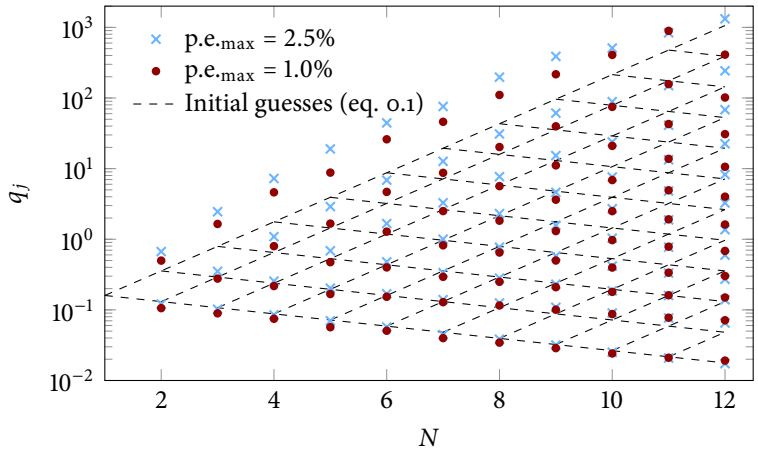

FIGURE 3.7: Intersections of the dashed lines indicate initial guesses for the hydrogen ($Z = 1$) nonlinear coefficients q_j according to eq. (3.4.17).

3.6 SMOOTHING & INTERPOLATION METHODS

There are two places in this thesis where data from 1D HYDRA simulations were used to initialise a VFP simulation: sections 5.4 and 7.4. The IMPACT code was most often used to handle these situations. It was observed that, particularly for the gadolinium hohlraum test in section 5.4, IMPACT had difficulties handling the coarse nonuniform mesh used by HYDRA. While HYDRA is specifically set up to handle large discontinuities over shock fronts by using a Lagrangian mesh, IMPACT is not, and direct use of the HYDRA mesh resulted in a prohibitive amount of nonlinear Picard iterations and eventual convergence failures.

It was found that interpolating (and sometimes also smoothing) the HYDRA data onto a refined mesh not only eliminated these errors but also sped up the IMPACT computation by reducing the number of such iterations needed (even considering the fact that the number of spatial cells has increased). Further computation time was saved by cropping the data to only contain regions of interest where nonlocal transport could occur (i.e. regions with large temperature gradients) and taking care that the electron density did not become overly high. Crop points were often chosen to coincide with locations where many profiles experience either local maxima or a general flattening in gradient. In this section, the methods of mesh refinement, interpolation and smoothing used for the case of one spatial dimension are presented.

3.6.1 *Mesh refinement*

A new refined mesh can be quite simply calculated from a coarse one if a prescription is provided as to how much each cell should be reduced in size. However, it is obtaining an optimal prescription for this that is not completely trivial. While such a prescription was initially provided manually (by trial and error) for the gadolinium hohlraum problem, a slightly less hands-on approach was later developed for use in future comparisons between HYDRA and IMPACT, such as the microdot problem. This new method requires user-defined values for the maximum allowable (1) cell size (2) ratio between any specified plasma quantities (e.g. n_e. T_e, etc.) in neighbouring cells and (3) ratio between neighbouring cell widths to calculate how much each cell should be shrunk by. In order for the mesh refinement not to affect the location of the external boundaries at $x_{½}$ and $x_{N+½}$ and to avoid the difficulty of interpolating near a reflective boundary, the cells denoted by x_0, x_1, x_N, x_{N+1} are not affected by the algorithm.

In the current implementation, specification (2) is only met approximately due to linear interpolation of the profiles (the cubic interpolation outlined in section 3.6.2 below is only used after the new mesh is constructed); this is achieved by reducing the width of each cell by the ratio between the desired and actual percentage differences from its neighbouring cells. If the ratio between the reduced widths of neighbouring cells then exceeds that specified in (3), the width of the larger cell is reduced to be equal to the geometric average of that of its neighbours. Strictly speaking this final operation, which proceeds from left to right, needs to backtrack if it results in a cell becoming significantly smaller than its right neighbour but this possibility is currently not accounted for. Indeed, it is not clear whether specification (3) is at all strictly necessary to obtain a well-behaved mesh, but it is included in the refinement algorithm (with a default maximum width ratio of 20) as a precautionary measure. Finally, if the original width of a cell is not an integer multiple of its reduced width then its width is further reduced to ensure this is the case; this partly makes up for the potential drawbacks mentioned in this paragraph but more importantly increases very slight reductions in cell sizes that could result in incongruously small gaps in which a new cell must be created.

Once all the reduced cell widths have been obtained, additional cell nodes need to be placed between the originals. This is done by first inserting equally spaced boundaries in the newly created gaps such that their spacing is similar to the width of their narrowest neighbour. Specifically, this is achieved by rounding the ratio between is rounded to the nearest integer. As this algorithm was initially

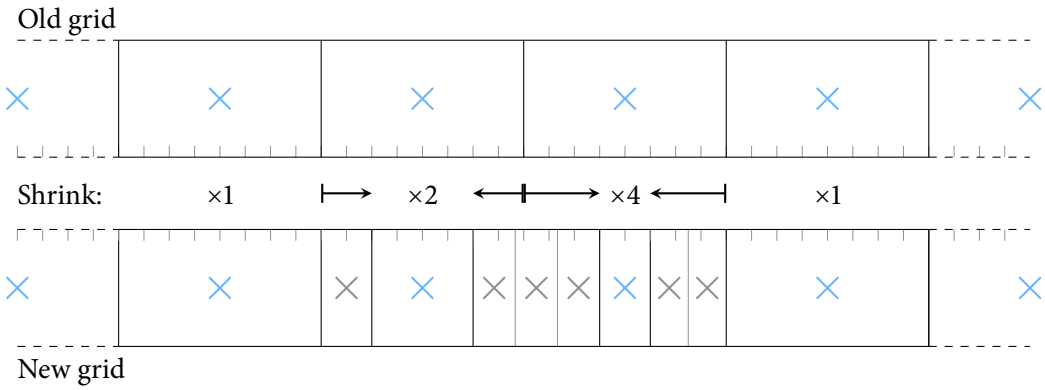

FIGURE 3.8: An illustration of the mesh refinement algorithm used to initialise IMPACT from HYDRA data. A prescription (labelled 'Shrink:') is provided as to how much each cell should be shrunk; cells that touch the external boundary are never affected (their shrinking factor is always one). Each of the resulting gaps is equally divided so that its width is similar to that of its narrowest neighbour. Inserted cells are denoted by grey crosses.

used to create grids for IMPACT the new cell nodes are then simply placed at the centres of these new boundaries. A simple diagram giving an example of this procedure is provided in fig. 3.8.

This method, while certainly not the simplest imaginable, has the convenience of guaranteeing that all nodes originally present on the coarse mesh will also exist on the refined mesh. Conversely, with the exception of the external boundaries, it is not certain that the location of any boundaries on the new grid will coincide with the original boundaries.

3.6.2 *Constrained cubic splines*

Once the refined mesh has been obtained the original HYDRA data needs to be interpolated on to it. However, linear interpolation is not a good candidate for this task due to discontinuities in the first spatial derivative ('kinks'), which tend to either persist or go unstable . Thus, a higher order interpolation method is desired. Unfortunately, the traditional method of cubic spline interpolation is prone to large overshoots resulting from the imposition of a continuous *second* spatial derivative. An alternative method that relaxes this constraint is that of 'constrained cubic splines' (Kruger 2002), which is employed here to achieve satisfactorily smooth data on the interpolated mesh. This method is depicted along with the other mentioned interpolation methods and their problematic

features for the case of the gadolinium hohlraum electron temperature profile in fig. 3.9.

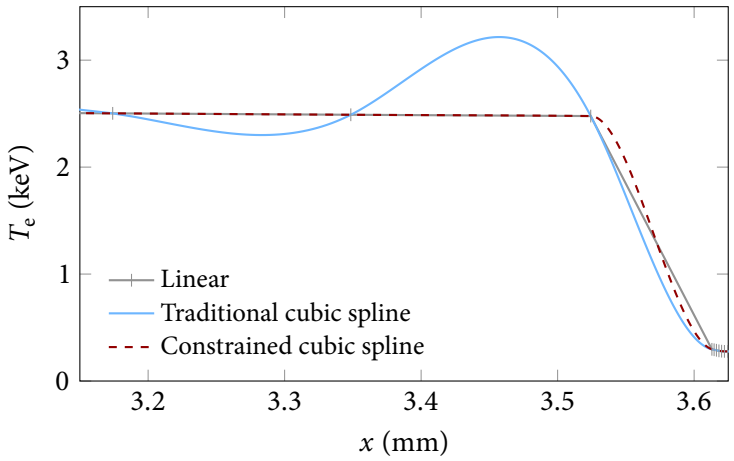

FIGURE 3.9: A comparison of the interpolation methods discussed in section 3.6.2 for the gadolinium hohlraum electron temperature profile (see section 5.4). Gray vertical marks denote the location of the original HYDRA data. It is shown that while traditional cubic spline interpolation is able to resolve the kinks it introduces undesirably large oscillatory overshoots in the interpolated data. By relaxing the constraint that the second order derivative is continuous and providing an alternative method of assigning the gradient at the original node locations, eq. (3.6.3), Kruger's method of constrained cubic splines(2002) manages to overcome both issues.

Any kind of cubic spline interpolation onto a new coordinate x between old cell nodes x_n and x_{n+1} is most conveniently described using a dimensionless parameter

$$x' = \frac{x - x_n}{\Delta x_{n+\frac{1}{2}}}, \text{ for } x_n < x < x_{n+1}, \text{ where, } \Delta x_{n+\frac{1}{2}} = x_{n+1} - x_n \tag{3.6.1}$$

is the node separation. The interpolated value of a field Φ at x can then be calculated as

$$\begin{aligned} \Phi(x) = \; & (1 - x')\Phi_n + x'\Phi_{n+1} \\ & + x'(1 - x')\left((1 - x')\frac{\partial \Phi}{\partial x'}\bigg|_n - x'\frac{\partial \Phi}{\partial x'}\bigg|_{n+1} - (1 - 2x')\Delta\Phi_{n+\frac{1}{2}}\right), \end{aligned} \tag{3.6.2}$$

where $\Phi_n = \Phi(x_n), \Delta\Phi_{n+\frac{1}{2}} = \Phi_n - \Phi_{n+1}$ and $\frac{\partial \Phi}{\partial x'}\Big|_n$ is the spatial derivative of Φ with respect to x' evaluated at x_n. Typically these first order spatial derivatives need to be solved for such that the second order derivatives are continuous.

Instead, the method of constrained cubic splines simply uses the harmonic average of the derivatives at the neighbouring boundaries arising from central differencing:

$$\left.\frac{\partial \Phi}{\partial x'}\right|_n = \frac{1}{2}\left(\frac{\Delta x_{n-½}}{\Delta \Phi_{n-½}} + \frac{\Delta x_{n+½}}{\Delta \Phi_{n+½}}\right)^{-1}. \tag{3.6.3}$$

Additionally, the original paper (Kruger 2002) suggested that if these neighbouring derivatives are of opposite sign then $\left.\frac{\partial \Phi}{\partial x'}\right|_n$ should be set to zero to completely avoid overshoot; however, this is not found to be necessary as the harmonic average alone reduces overshoot to a reasonable level for the received HYDRA data. If interpolation between the ghost and first/last cells were required an alternative definition of the spatial gradient at the ghost cell would be necessary and is indeed provided by Kruger, however this is not needed here.

3.6.3 *Smoothing*

On a final note, some of the profiles analysed experienced a strong degree of noise. This was most notable in the microdot magnetic field profile (see 7.4), which oscillated wildly between positive and negative values near the expanding hohlraum wall, but the electron density profile for the same problem also experienced temporary reverses in gradient as it approached its maximum. There were three reasons why it was deemed appropriate to remove this noise: (1) sharp kinks in the data suggested that the initial grid was insufficiently resolved in the hohlraum wall, (2) IMPACT is known to currently experience issues while dealing with change of sign in the magnetic field, (3) as hydrodynamics was disabled in the IMPACT simulations any kinks that might have washed away in the HYDRA simulation would persist in their initial state indefinitely.

The method of smoothing used for the microdot magnetic field involved first manually selecting the beginning x_L and end x_R of the noisy region by eye. Subsequently, a single cubic equation that matched the profile at the endpoints was fitted to the data in this region by minimising the least-squares error. This approach left two free parameters to be decided by the fitting algorithm. The optimal values for these parameters were then used to define also the gradient of the neighbouring spline(s) at x_L and x_R.

For the case of the electron density profile, a similar technique was used with some additional modifications that required significant subjective choices. Firstly, the electron density in the last five cells of the HYDRA mesh was set equal to that in the sixth last cell (115.3×10^{20} cm^{-3}). This decision was made to accommodate the

reflective boundary conditions employed by IMPACT. Additionally, x_R was free to move along with its associated value of the electron density, but the gradient at this point was enforced to be zero. Consequently, there were three free fitting parameters in this case. Due to the narrow region in which there was problematic noise for this profile, the fitting region was chosen to extend from two cells left of x_L all the way to the last internal cell x_N; cells beyond x_R were all set to the best fit value obtained for the electron density at x_R itself. Not performing this extension of the fitting region led to an undesirable degree of overshoot just to the left of x_L.

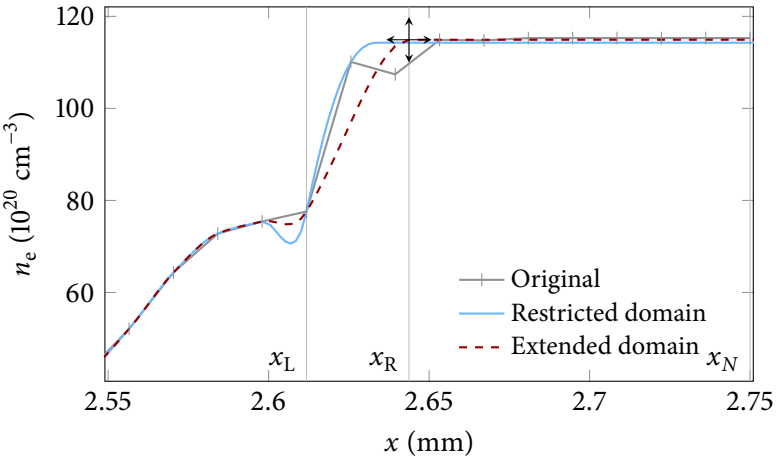

FIGURE 3.10: Smoothing of the HYDRA microdot electron density profile at 4 ns used as an input for IMPACT. Here n_e is capped at 115.3×10^{20} cm^{-3}. The smoothed region is between x_L and x_R. Extending the *fitting* region for obtaining the smoothing coefficients from (x_L, x_N) to $[x_{L-2}, x_N)$ reduces the degree of overshoot towards the left of the smoothed region. Arrows act as a reminder that the location of x_R and the associated electron density are both fitting parameters in addition to the gradient at x_L.

Additionally, it was noted that both the electron density and magnetic field profiles experienced very rapid changes in magnitude and appeared more exponential than polynomial in nature. Therefore, it was the log of the profile that was smoothed and interpolated. The results of this smoothing process, along with the locations of x_L and end x_R are shown for the magnetic field in fig. 3.11 (using both a linear and a log scale) and the electron density in fig. 3.10.

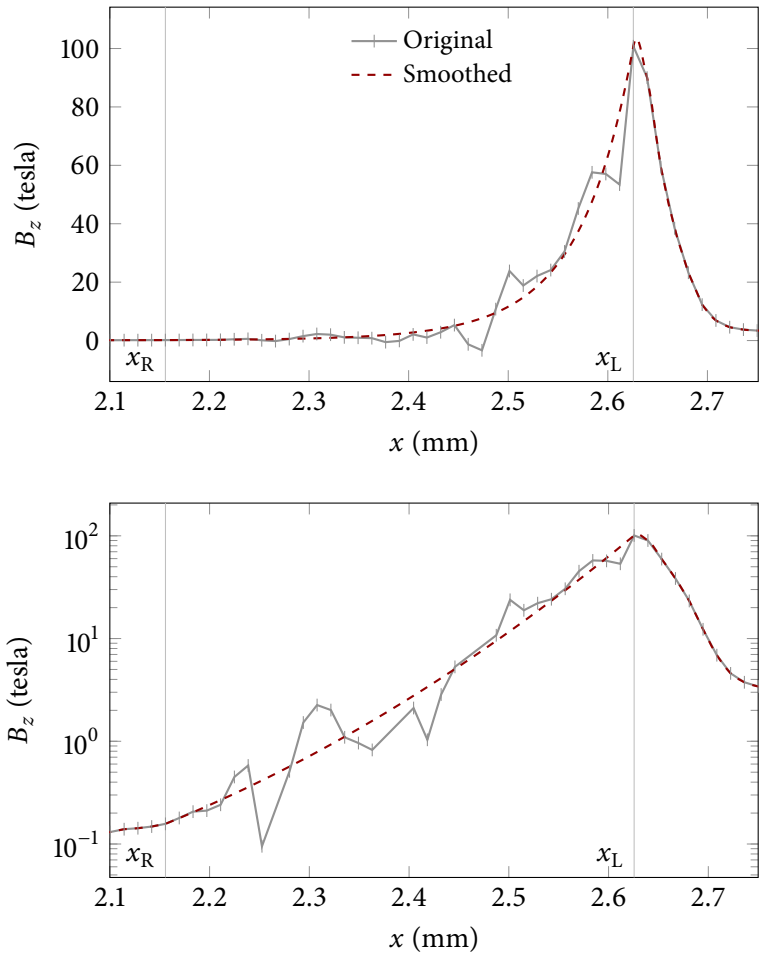

FIGURE 3.11: Smoothing of the HYDRA microdot magnetic field profile at 4 ns used as an input for IMPACT on a linear (top) and logarithmic scale (bottom). The smoothed region is between x_L an x_R.

4

DAMPING OF A LOW-AMPLITUDE TEMPERATURE SINUSOID

One of the most frequently used and insightful methods for assessing the validity of nonlocal models is the 'Epperlein-Short' test. Named after the authors of a seminal paper published in 1991, the test concerns the damping of a sinusoidal temperature profile $T_e = T_0 + \widetilde{T}_e \cos(kx)$, where the temperature perturbation amplitude $\widetilde{T}_e$ is much less than the background temperature T_0, for a plasma with uniform electron density n_e. While such a setup may not be truly representative of the large temperature differences that can arise in fusion experiments, it enables the effect of nonlocality on heat flow to be encapsulated with just one single parameter: the nonlocal reduction of the damping rate γ_D compared to the local Braginskii prediction $\gamma_D^{(B)}$. This relative reduction in damping should be equal to that in both the heat flow and thermal conductivity for a given nonlocality parameter $k\lambda_{ei}^{(B)}$, but the nonlocal reduction in the electric field will take a different value.

Given the amount of literature that already exists on the subject of small sinusoidal perturbations, the level of detail on this subject provided in this chapter may seem surprising. However, such analysis is incredibly powerful in understanding the regimes in which each of the nonlocal models are valid and justifying certain calibrations of the models.

This chapter begins with an explanation of the methodology used to extract values for the nonlocal reduction in peak heat flow and electric field values whether using an analytical framework, the VFP codes IMPACT, KIPP and SPRING or the nonlocal EIC, SNB and NFLF models. (Flux-limiters are not discussed in this chapter as they would not predict any flux reduction whatsoever for an infinitesimal perurbation) Following this is a detailed attempt at characterising the damping behaviour in four specific regimes where analytic progress can be made (in order of decreasing collisionality these regimes are the hydrodynamic regime, the semicollisional regime, the regime of collisionless suprathermals and the collisionless regime) and then making comparisons with the EIC and SNB models. As the regime of collisionless suprathermals is an extension of the collisionless regime it shall be discussed last.

While frequent references will be made to works of earlier authors, especially that of Bychenkov et al. (1994, 1995), additional insight is offered by making comparisons and outlining alternative derivations. For example, Bychenkov et al.

used a polynomial expansion in the majority of their analysis while here we will explore a more direct iterative integral approach for analysing the semicollisional regime. Finally, results from all regimes will be combined to construct a robust analytic fit for the nonlocal thermal conductivity reduction that is acceptably accurate for all $k\lambda_{\mathrm{ei}}^{(\mathrm{B})}$. This will be used to obtain optimal fitting parameters for the NFLF model and be compared to an analytic expression for the performance SNB (using both the BGK and AWBS model electron-electron collision operators) across all collisionalities.

4.1 METHODOLOGY

4.1.1 *Analytical Framework*

A significant advantage of studying small sinusoidal perturbations is that it allows for significant analytical progress to be made through a convenient linearisation procedure. By extending into the complex numbers, the electron distribution function can be written as $f_{\mathrm{e}}(t, x, \vec{v}) = f_{\mathrm{e}}^{(\mathrm{mb})}(v) + \widetilde{f}_{\mathrm{e}}(t, \vec{v})\mathrm{e}^{ikx}$, where $f_{\mathrm{e}}^{(\mathrm{mb})}$ is the EDF for the *background* Maxwellian (with temperature T_0 and density n_{e}) and $\widetilde{f}_{\mathrm{e}}$ is the perturbed distribution function with temperature $\widetilde{T}_{\mathrm{e}}$. Substituting this into the VFP equation, we can obtain an expression for the evolution of the EDF,

$$\frac{\partial \widetilde{f}_{\mathrm{e}}}{\partial t} + ikv_x\widetilde{f}_{\mathrm{e}} + \frac{e\widetilde{E}_x}{k_{\mathrm{B}}T_0}v_x f_{\mathrm{e}}^{(\mathrm{mb})} = C_{\mathrm{ei}}(\widetilde{f}_{\mathrm{e}}, f_{\mathrm{i}}) + C_{\mathrm{ee0}}^{(\mathrm{L})}(\widetilde{f}_{\mathrm{e}}), \tag{4.1.1}$$

where '$\widetilde{\ }$' represents a Fourier-transformed quantity and the linearised collision operator $C_{\mathrm{ee0}}^{(\mathrm{L})}$ defined in section 2.3.8 is appropriate in this limit. The ion distribution function f_{i} will also be assumed to be Maxwellian and shall be treated as a delta function centred at zero in all analysis and with all codes.

The linearised VFP equation can be conveniently translated into an eigenvalue problem by recalling that that the electric field depends linearly on the perturbed EDF $\widetilde{f}_{\mathrm{e}}$ through an integral and rearranging into

$$\frac{\partial \widetilde{f}_{\mathrm{e}}}{\partial t} = -ikv_x\widetilde{f}_{\mathrm{e}} - \frac{e\widetilde{E}_x[\widetilde{f}_{\mathrm{e}}]}{k_{\mathrm{B}}T_0}v_x f_{\mathrm{e}}^{(\mathrm{mb})} + C_{\mathrm{ei}}(\widetilde{f}_{\mathrm{e}}, f_{\mathrm{i}}) + C_{\mathrm{ee0}}^{(\mathrm{L})}(\widetilde{f}_{\mathrm{e}}) \equiv A_k(\widetilde{f}_{\mathrm{e}}), \tag{4.1.2}$$

where we have defined the integro-differential velocity-space operator A_k. Therefore, the evolution of $\widetilde{f}_{\mathrm{e}}$ according to eq. (4.1.2) is as a sum of independently evolving eigenfuctions that oscillate at an angular frequency equal to the imaginary part of the eigenvalue and grow at a rate equal to the real part. For most wavenumbers, k, the real part of the eigenvalue should be negative, correspond-

ing to a damping of the temperature perturbation; otherwise it would persist indefinitely or be unstable unless the corresponding eigenfunction is orthogonal to the initial conditions. The asymptotic damping rate is then given by the slowest damping mode.

A notable exception is in the very short wavelength regime $k\lambda_{\mathrm{ei}}^{(\mathrm{B})} \to \infty$ (i.e. where the contributions from C_{ei} and $C_{\mathrm{ee0}}^{(\mathrm{L})}$ can be neglected), where *all* eigenvalues have zero real part. Surprisingly, damping of density and temperature perturbations can still arise in such a situation despite no individual modes decaying in amplitude. This apparent paradox was resolved by Van Kampen (1955) by analogy with statistical mechanics; perturbations in macroscopic quantities, such as density and temperature, can be thought of as fluctuations away from equilibrium that depend on a contrived amplitude and phase relationship between the various modes (that would occur naturally with vanishing probability), as these 'Van Kampen modes' drift out of phase with each other the macroscopic fluctuations dissipate without any loss of the microscropic information encapsulated in the EDF. To circumvent such complications, a Laplace transform is performed on the time coordinate as opposed to a Fourier transform when analysing the collisionless regime in section 4.4.

4.1.2 *VFP simulations*

IMPACT simulations

Due to the inherently nonstationary nature of VFP codes there is no single unique heat flow for any given density and temperature profile. This is because these profiles do not fully prescribe the underlying distribution function. However, transient features arising from initial conditions can fade on the timescale of a few electron-ion collision times and lead to quasi-steady-states involving what can be considered the 'correct' nonlocal heat flow for a given temperature profile. For the current problem concerning the damping of sinusoidal temperature perturbations, the transient features are namely all eigenfunctions of A_k that damp faster than the slowest decaying mode (SDM). And once their amplitude falls sufficiently below that of the SDM, the asymptotic damping rate mentioned previously can be obtained. Therefore, it was necessary to run integrated VFP simulations starting from sensible initial conditions for long enough to identify the damping rate of the SDM.

IMPACT *parameters summary:*

`nx`	= 500
`vmax`	$= 10v_{2\mathrm{T}}$
`nv`	= 200–500
`dt`	$= 1.0v_{\mathrm{ei}}^{(0)}$
Z	= 7
ξ	= 1
$\widetilde{T}_{\mathrm{e}}/T_0$	$= 10^{-3}$

For the IMPACT simulations, the EDF was initialised as a stationary Maxwellian $f_0(t=0) = n_{\mathrm{e}}\mathrm{e}^{-m_{\mathrm{e}}v^2/2\ kbT_{\mathrm{e}}}/\sqrt{2\pi k_{\mathrm{B}}T_{\mathrm{e}}/m_{\mathrm{e}}}$, $\vec{f}_1 = 0$. The effect of electron

inertia was investigated by running with and without the $\frac{\partial \vec{f}_1}{\partial t}$ term. Most simulations were carried out with an initial relative temperature perturbation amplitude of $\widetilde{T}_e = 0.001 T_0$, to achieve a compromise between avoiding precision errors due to too low an amplitude and nonlinear effects due to too high an amplitude, but there were some simulations carried out with higher amplitudes to investigate any nonlinear amplitude-dependent effects that may arise (such effects were only noticed to have more than a 10% effect on the damping rate when the initial amplitude exceed about 50% of the background, however by the time it was possible to make a reliable prediction of this the amplitude had significantly reduced). A full wavelength was set up and discretised over 500 spatial cells using periodic boundary conditions, while between 200 and 500 uniformly spaced velocity cells were used extending to a maximum velocity of $10 v_{2T}$, where the specific reference thermal velocity used is $v_{2T} = \sqrt{2 k_B \widetilde{T}_e / m_e}$.

While IMPACT enabled a thorough treatment of the high ionisation Lorentz limit due to its neglection of electron-electron collisions in the $\vec{f}_1$ equation, in practice a fully-ionised nitrogen plasma ($Z = 7$) was simulated but without including the collision fix (i.e. $\xi = 1$). Under the diffusion approximation (i.e. without electron inertia) the results could conveniently be translated to any ionisation by multiplying the wavelength by the square root of the relative ionisation. Similarly, the effect of incorporating the collision fix could be obtained by scaling the wavelength by $\sqrt{\xi}$. However, this useful conversion mechanism was not strictly applicable if the electron inertia term was retained.

Values for the dimensionless thermal conductivity were obtained using two methods: (1) by dividing the maximum instantaneous heat flow at each timestep by $7/2 \, n_e \tau_{ei}^{(B)}(T_0) k_B \vec{\nabla} T_e^{7/2} / m_e T_0^{3/2}$ where the gradient term was calculated at the location of the peak heat flow using central differencing, and (2) by directly assessing the asymptotic damping rate of the temperature perturbation amplitude through fitting a straight of $\log(\widetilde{T}_e)$ against time using only the last 5–10 points (see fig. 4.4 for an example with the KIPP code). The thermoelectric conductivity $\beta_\parallel$ was calculated using a similar method to (1) but instead dividing the peak electric field by the temperature gradient $\vec{\nabla} T_e$ and then subtracting 1.

KIPP simulations

In order to fully understand the ramifications of electron-electron collisions for the anisotropic part of the EDF at the low ionisation of $Z = 1$, the 1D2V VFP code KIPP was used. The best velocity grid available was a non-uniform Cartesian grid extending to `vmax` $= 7 v_{1T}$ (where $v_{1T} = \sqrt{k_B \widetilde{T}_e / m_e}$ is an alternative thermal

KIPP *parameters summary:*

`nx` = 127
`vmax` = $7 v_{1T}$
`mmax` = 256
`EPS` = 1.01
$Z = 1$
$\widetilde{T}_e / T_0 = 10^{-3}$

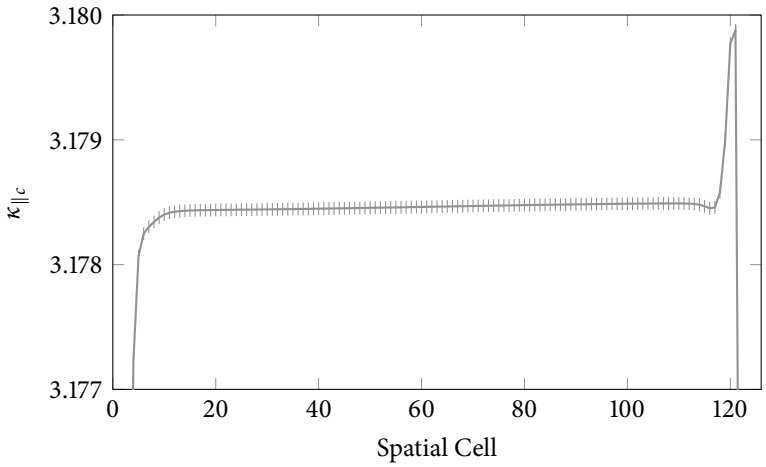

FIGURE 4.1: The KIPP spatial thermal conductivity profile exhibits an unexpected asymmetric spike near the sheath region at the right-hand side. Shown here at the final timestep of a simulation with the parameters $k\lambda_{\mathrm{ei}}^{(\mathrm{T})} = 10^{-3}$, $\mathtt{dt} = 2.5 \times 10^{-4}\tau_{\mathrm{ei}}^{(0)}$

velocity). characterised by the parameters `mmax` = 256, and `EPS` = 1.01 defined in section 3.1.1. The spatial resolution, which was limited by the number of cores available per simulation, was given by 127 cells uniformly spaced cells over a half wavelength, and although this seems a little on the low side it is unlikely to be a convergence bottleneck compared to velocity grid convergence.

Similar methods were used to calculate the transport coefficients as with IMPACT although it was necessary to use forward differencing to calculate the gradient terms due to the upwinding method used to perform the free-streaming step in KIPP (See section 3.1.1). Applying the instantaneous heat flow method at all spatial locations rather than just the peak, unveiled surprising features in the thermal conductivity spatial profile; pictured in fig. 4.1 it is seen that there is an asymmetric spike near the cooler right hand boundary. This seems unexpected and is probably a numerical phenomenon arising from the implementation of the sheath boundary condition. It was found that this artefact persists irrespective of the timestep and velocity grid and is generally on the order of 0.05%. It is the assymmetry of this spike that is most concerning as numerical effects due to lack of spatial convergence or dividing by a very small temperature gradient should be symmetric. Unfortunately, this issue was never fully resolved, and it is hoped that it does not have an appreciable impact on features in the centre of the domain.

A particular issue with the added dimensionality of KIPP was that performing simulations with sufficiently small timestep until only the SDM remained was very computationally expensive and time-consuming (even with 128 cores). Two

solutions were employed to decrease the computational time required (1) an improved method of initialising the EDF so that it more closely resembles that predicted by KIPP and (2) initially using a larger timestep and then restarting with ever smaller timesteps.

Initial KIPP distribution function

One approach to implementing the first method of optimising the initial EDF is to start with the local prediction for the first-order anisotropy $\vec{f}_1$ expected in the absence of nonlocality and use this to reconstruct the EDF along with an isotropic Maxwellian $f_e^{(mb)}$. While IMPACT offers a convenient in-built method to achieve this—by performing the first timestep with the electron inertia term switched off—such an approach is not possible with KIPP due to the Cartesian description of the EDF. Admittedly, it should be possible to instead perform this calculation internally in KIPP using the collisions subroutine with an effectively infinite timestep (to eliminate the time-derivative) before the main loop and first free-streaming step. However, in order to avoid coding complications, a simpler method of identifying the 'steady-state' EDF at a low degree of nonlocality given by $k\lambda_{ei}^{(T)} = 10^{-3}$ and then rescaling was investigated.

Due to the non-uniform Cartesian velocity grid not lending itself amenably to angular integration, the first spherical harmonic $\vec{f}_1$ was estimated by equating it to the part of the total KIPP EDF that was odd in v_x at $v_\perp = 0$ (i.e. $f_{1x} \approx (f_e(v_x, 0) - f_e(v_x, 0))/2$). While the numerical form of $\vec{f}_1$ obtained from this analysis could have been saved as a file for KIPP to use in reconstructing an initial distribution by rescaling and interpolating appropriately, it was more convenient to find a simple analytic approximation for $\vec{f}_1$. This was achieved by expanding

$$\vec{f}_1(V^2) = -V^2 \frac{\lambda_{ei}^{(0)} \vec{\nabla} T_e}{T_e} \sum_{n=0}^{\infty} c_n L_n^{(2)}(V^2) f_e^{(mb)}, \tag{4.1.3}$$

in Laguerre polynomials of order 2, $L_n^{(2)}$, where we have defined the normalised velocity $V = v/v_{2T}$. The order of the Laguerre polynomials, which differs from the choice of ½ made by the EIC model, was chosen because of the direct relationship between the first/second coefficient and electric current/diffusive heat flow respectively. Furthermore , the Spitzer-Härm (1953) expression for the first-order anisotropy of the EDF, $\vec{f}_1^{(sh)} = -(V^2 - 4)V^4 f_e^{(mb)} \lambda_{ei}^{(0)} \vec{\nabla} T_e / T_e$, can be

TABLE 4.1: Coefficients for the Laguerre expansion of the first spherical harmonic of the distribution function for $Z = 1$ obtained from KIPP results and in the analytical Lorentz limit ($Z = \infty$).

Z	c_0	c_1	c_2
1	0	$-4\xi(1)$	$\frac{3}{4}\xi(1)$
∞	0	-4	2

given exactly by only two terms $c_1 = -4, c_2 = 2$. The 'reconstructed' expression for $\vec{f}_1$ that arises from the rounded coefficients (given in table 4.1) is

$$\vec{f}_1^{(\mathrm{rec})} = -(\tfrac{3}{8}V^4 - V^2 - \tfrac{3}{4})V^2 f_\mathrm{e}^{(\mathrm{mb})} \frac{\lambda_\mathrm{ei}^{(0)} \vec{\nabla} \widetilde{T}_\mathrm{e}}{\widetilde{T}_\mathrm{e}}. \tag{4.1.4}$$

The impressive accuracy of this fit is depicted in fig. 4.2.

This simple fit of the first spherical harmonic $\widetilde{f}_1$ was used to initialise the distribution function for KIPP simulations as $f_\mathrm{e}(v_x, v_\perp) = f_\mathrm{e}^{(\mathrm{mb})}(v) + \frac{v_x}{v} f_{1x}^{(\mathrm{rec})}(v)$. Figure 4.3 shows the effect of the new initialisation on convergence of thermal and thermoelectric conductivities with time over the course of a simulation compared to initialising with either a static Maxwellian or the Spitzer-Härm expression $f_\mathrm{e}(v_x, v_\perp) = f_\mathrm{e}^{(\mathrm{mb})}(v) + \frac{v_x}{v}\xi f_{1x}^{(\mathrm{sh})}(v)$ for a simulation with $k\lambda_\mathrm{ei}^{(\mathrm{T})} = 10^{-3}$, $\mathtt{dt} = 0.01\tau_\mathrm{ei}^{(\mathrm{T})}$. While the conductivity encouragingly reaches within 1% of its final value much sooner, the curve still takes a long time to straighten out and converge to a much higher precision. This could be due to the fit being worst in the low velocity region and taking a long time to correct.

Timestep convergence

When using the second method of restarting with smaller and smaller timesteps, the simulation could still take 24–48 hours for the thermal conductivity associated with the slowest damping mode to be accurately ascertained. As timestep convergence itself only scales linearly, an extrapolation technique was used to avoid performing this restart process ad infinitum. This involved plotting the thermal conductivity values predicted by both the peak heat flow and asymptotic damping rate methods against timestep and finding the line of best fit. Figure 4.5 shows that the predicted linear convergence is indeed displayed and that the dimensionless thermal conductivity approaches 3.1779 for $k\lambda_\mathrm{ei}^{(\mathrm{T})} = 10^{-3}$ at zero timestep. This value is significantly lower than predicted using the formula $\kappa_{\|c} = 3.203(1 - b_Q Z k^2 {\lambda_\mathrm{ei}^{(\mathrm{B})}}^2) = 3.20$ provided by Bychenkov et al.'s (1994, 1995)

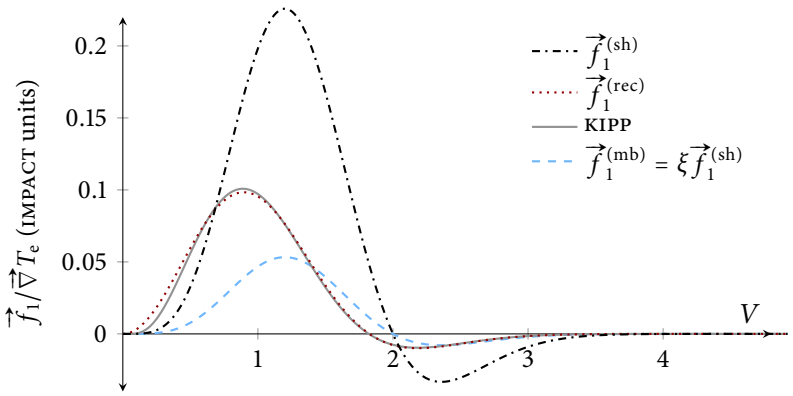

FIGURE 4.2: Using just two Laguerre modes can provide a very accurate reconstruction $\vec{f}_1^{(rec)}$ of the first-order anisotropy of the electron distribution function predicted by KIPP in the local limit (with $k\lambda_{ei}^{(T)} = 10^{-3}$, `dt` $= 2.5 \times 10^{-4}\tau_{ei}^{(0)}$) compared to the standard Spitzer-Härm prediction $\vec{f}_1^{(sh)}$ even when weighted by the collision fix ξ.

with the coefficient $b_Q = 43.5$ introduced in section 4.3. The observed discrepancy probably stems from a lack of convergence in the velocity grid, which was indeed partially confirmed when comparing with a lower resolved velocity grid with `mmax` = 200 predicting an even lower dimensionless thermal conductivity of $\kappa_{\parallel c} = 3.123$ (recall that a higher resolved velocity was unfortunately not available). A similar process was carried out for the thermoelectric conductivity $\beta_\parallel$.

SPRING

Results for the thermal conductivity reduction previously obtained by Epperlein with the SPRING code (1994; 1994) for $Z = 1$ and 8 made available by Bychenkov et al. (1995, Table I) were used to complement the IMPACT and KIPP results. The linearised codes unique use of complex numbers enables directly extraction of the damping rate even when oscillatory features arise at lower collisionalities. Although bear in mind, that the values provided by Bychenkov et al. correspond to the *absolute value* of the thermal conductivity rather than purely the damping portion.

4.1.3 *Nonlocal model analysis*

In contrast to the VFP codes the inherent quasistationarity of the nonlocal models under study (EIC, NFLF and EIC) makes obtaining thermal conductivity predictions much simpler; no integrated simulations needed to take place as the nonlocal heat flow could be calculated instantaneously without waiting for

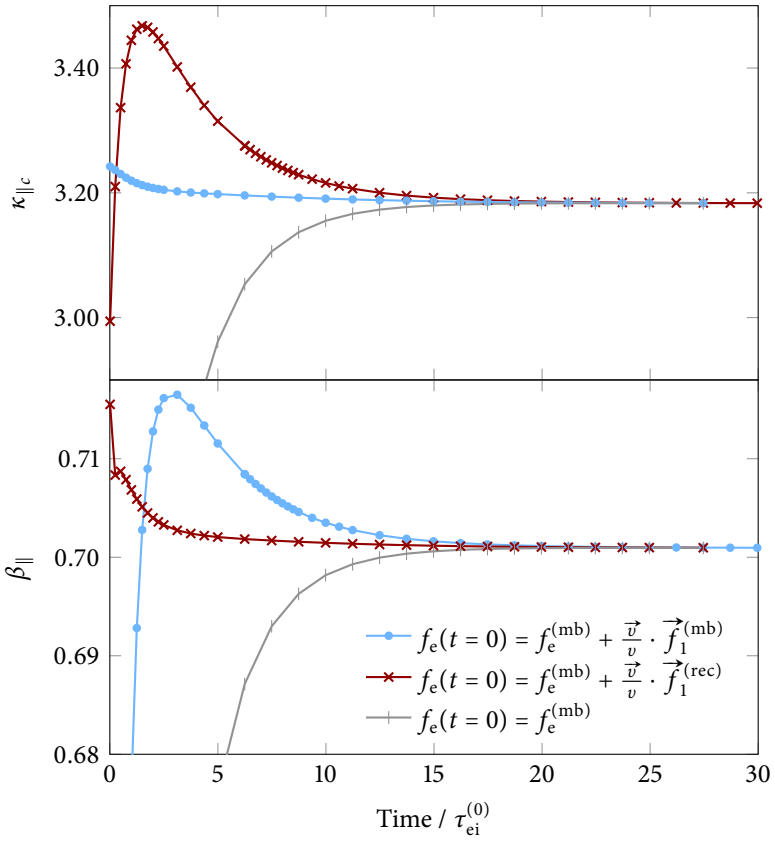

FIGURE 4.3: Imposing the initial EDF $f_\mathrm{e}(t=0) = f_\mathrm{e}^{(\mathrm{mb})} + \frac{\vec{v}}{v} \cdot \vec{f}_1^{(\mathrm{rec})}$ that closely resembles that predicted in the local limit (see fig. 4.2) reduces the KIPP simulation time (shown here for $k\lambda_{\mathrm{ei}}^{(\mathrm{T})} = 10^{-3}$, $\mathtt{dt} = 2.5 \times 10^{-3} \tau_{\mathrm{ei}}^{(0)}$) compared to using just a stationary Maxwellian $f_\mathrm{e}^{(\mathrm{mb})}$ or appending the Spitzer-Härm prediction weighted by the collision fix $\frac{\vec{v}}{v} \xi \vec{f}_1^{(\mathrm{mb})}$.

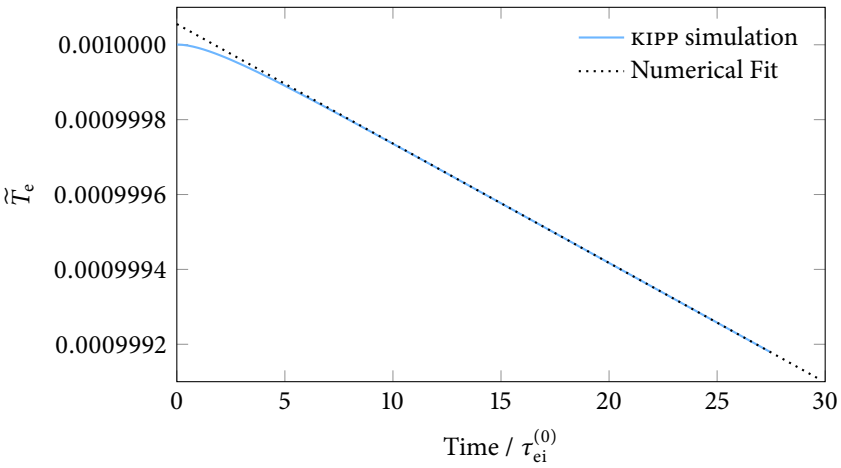

FIGURE 4.4: The evolution of the relative temperature amplitude as predicted by the KIPP VFP with a timestep of $\mathtt{dt} = 2.5 \times 10^{-4} \tau_{ei}^{(0)}$. A constant damping rate is approached within several collision times $\tau_{ei}^{(0)}$ inferring a dimensionless thermal conductivity of 3.1832. Note that the actual damping rate is very large due to the wavelength being $2\pi \times 10^3 \lambda_{ei}^{(T)}$.

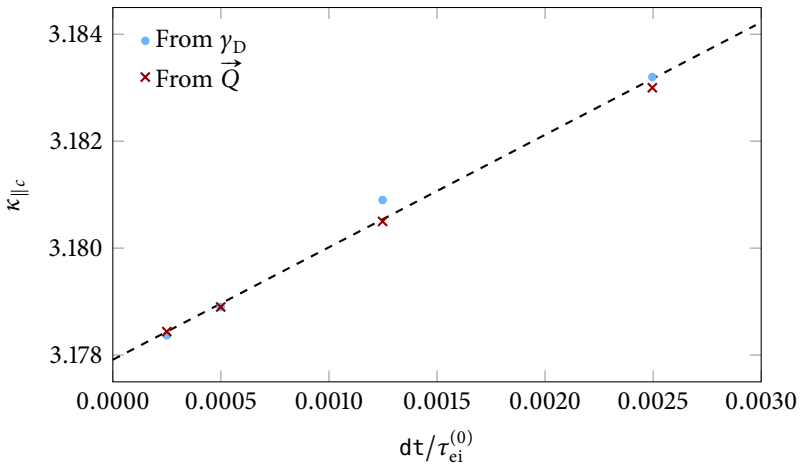

FIGURE 4.5: Fitting a straight line to thermal conductivity calculations using both heat flow/temperature gradient method and the damping rate method confirms a linear scaling of numerical error with timestep. Extrapolation indicates that the thermal conductivity converges to 3.1779 at a high collisionality of $k\lambda_{ei}^{(T)} = 10^{-3}$, which is significantly less than the 3.20 predicted by Bychenkov's formula given in eq. (4.3.1).

transient effects to die out. As a result of not needing to allow the temperature profile itself to damp, it was possible to impose a lower amplitude of $\widetilde{T}_\mathrm{e}/T_0 = 10^{-5}$. Furthermore, the SNB and NFLF models had the added advantage of affording an analytic treatment. (Naturally, this was double-checked using the numerical implementations of the models.)

4.2 HYDRODYNAMIC REGIME

The hydrodynamic regime is concerned with the most collisional of plasmas where typically scalelengths are very large and the isotropic part of the distribution function f_0 can be treated as an exact Maxwellian. This is equivalent to a fluid treatment where the local Braginskii/Spitzer-Härm theory holds. We can obtain the damping rate from the equation for the evolution of the electron temperature:

Recall $v_{2\mathrm{T}} = \sqrt{2k_\mathrm{B}T_0/m_\mathrm{e}}$

$$\frac{3n_\mathrm{e}}{2}\frac{\partial k_\mathrm{B}T_\mathrm{e}}{\partial t} + \vec{\nabla}\cdot\vec{Q}^{(\mathrm{B})} = 0 \tag{4.2.1}$$

$$\implies \frac{\partial \widetilde{T}_\mathrm{e}}{\partial t} = -\frac{2k^2}{3n_\mathrm{e}}\kappa_\parallel^{(\mathrm{B})}\widetilde{T}_\mathrm{e} = -\frac{32}{3\sqrt{\pi}}\xi k^2\lambda_\mathrm{ei}^{(0)}v_{2\mathrm{T}}\widetilde{T}_\mathrm{e}, \tag{4.2.2}$$

Thus the temperature perturbation is exponentially damped at a rate of $\gamma_\mathrm{D} = 32\xi k^2\lambda_\mathrm{ei}^{(0)}v_{2\mathrm{T}}/3\sqrt{\pi}$.

4.3 SEMICOLLISIONAL REGIME

As the wavelength of the temperature perturbation decreases, both the thermal conductivity $\kappa_\parallel$ and the thermoelectric coefficient $\beta_\parallel$ are reduced due to nonlocal effects. Bychenkov et al. (1994, 1995) showed that the lowest order reductions in these coefficients, occurring in what shall be defined here as the semicollisional limit, are given by

$$\frac{\widetilde{Q}_x(k\lambda_\mathrm{ei}^{(\mathrm{B})}\to 0)}{\widetilde{Q}_x^{(\mathrm{B})}} = \frac{\kappa_\parallel(k\lambda_\mathrm{ei}^{(\mathrm{B})}\to 0)}{\kappa_\parallel^{(\mathrm{B})}} = 1 - b_Q Z k^2\lambda_\mathrm{ei}^{(\mathrm{B})2}, \tag{4.3.1}$$

$$\text{and } \frac{\widetilde{E}_x(k\lambda_\mathrm{ei}^{(\mathrm{B})}\to 0)}{\widetilde{E}_x^{(\mathrm{B})}} = \frac{\beta_\parallel(k\lambda_\mathrm{ei}^{(\mathrm{B})}\to 0)}{\beta_\parallel{}^{(\mathrm{B})}} = 1 - b_E Z k^2\lambda_\mathrm{ei}^{(\mathrm{B})2}, \tag{4.3.2}$$

where $b_Q \approx 264$ (see paragraph before eq. 14 in Bychenkov et al. 1994) and $b_E \approx 88$ (from eq. 3.15 in Brantov et al. 1996 using $\beta_\parallel = e\alpha/\sigma$) in the Lorentz limit ($Z = \infty$). The increased relative importance of electron-electron collisions

on the anisotropic part of the EDF at low ionisations will induce an ionisation dependence on b_Q and b_E. Incorporating the collision fix into ν_{ei} to approximate this effect leads to to the prediction that both coefficients will scale as ξ, while Bychenkov et al. instead assumed that they scale as ξ^2. Simulations with the EIC model presented in section 4.3.5 will reveal the true dependence of the coefficients on ionisation.

To gain a deeper insight on the origins of the coefficients b_Q, b_E as well as the nature of the EDF in the semicollisional regime than provided by Bychenkov et al.'s polynomial based approach we shall explore a perturbative approach that is more analytically tractable. Specifically, the Chapman-Enskog process introduced in section 2.2.1 is repeated a further two times to include terms of order $k^3\lambda_{\mathrm{ei}}^{(\mathrm{B})3}$ corresponding to the first nonlocal perturbation to the heat flow. In this limit it is valid to use the Cartesian tensor expansion of the linearised VFP equation keeping only the first three terms:

While f_3 is nonzero at this order it does not affect any terms contributing to transport.

$$\frac{\partial \widetilde{f}_0}{\partial t} + \frac{ikv}{3}\widetilde{f}_{1x} = C_{\mathrm{ee0}}^{(\mathrm{L})}\left(\delta\widetilde{f}_0\right) \tag{4.3.3}$$

$$\frac{\partial \widetilde{f}_{1x}}{\partial t} + ikv\left(\widetilde{f}_0 + \frac{2}{5}\widetilde{f}_{2xx}\right) + \frac{e\widetilde{E}_x v}{k_{\mathrm{B}}T_0} f_{\mathrm{e}}^{(\mathrm{mb})} = C_{\mathrm{ee1}}^{(\mathrm{L})}\left(\widetilde{f}_{1x}\right) - \nu_{\mathrm{ei}}\widetilde{f}_{1x}, \tag{4.3.4}$$

$$\frac{\partial \widetilde{f}_{2xx}}{\partial t} + \frac{2ikv}{3}\widetilde{f}_{1x} = C_{\mathrm{ee2}}^{(\mathrm{L})}\left(\widetilde{f}_{2xx}\right) - 3\nu_{ei}\widetilde{f}_{2xx}, \tag{4.3.5}$$

$$\widetilde{f}_{2yy} = \widetilde{f}_{2zz} = -\frac{1}{2}\widetilde{f}_{2xx}, \tag{4.3.6}$$

where $\delta\widetilde{f}_0 = \widetilde{f}_0 - \widetilde{f}_{\mathrm{e}}^{(\mathrm{mb})}$ is the deviation of the isotropic part of the distribution function from a Maxwellian. Here, the Fourier component of the Maxwellian contribution

$$\widetilde{f}_{\mathrm{e}}^{(\mathrm{mb})} = \left(\frac{m_{\mathrm{e}}v^2}{2k_{\mathrm{B}}T_0} - \frac{3}{2}\right) f_{\mathrm{e}}^{(\mathrm{mb})}(T_0)\frac{\widetilde{T}_{\mathrm{e}}}{T_0} \tag{4.3.7}$$

Reminder: In this chapter $f_{\mathrm{e}}^{(\mathrm{mb})}$ without argument or '$\widetilde{\ }$' always refers to $f_{\mathrm{e}}^{(\mathrm{mb})}(T_0)$ unless explicitly stated otherwise.

Due to the difficulty of treating the electron-electron part of the linearised collision operator analytically this shall be neglected in all equations except the first (4.3.3) and the effect of electron-electron collisions on the anisotropic parts of the distribution function will be approximated by replacing ν_{ei} with $\nu_{\mathrm{ei}}^* = \nu_{\mathrm{ei}}/\xi$. This simplification is completely justified in the Lorentz limit where electron-ion collisions dominate.

For the current problem of a low-amplitude temperature sinusoid the Chapman-Enskog expansion parameter $\mathrm{Kn} = k\lambda_{\mathrm{ei}}^{(\mathrm{B})}$. The expansion of the Fourier-transformed

distribution thus takes the form of $\widetilde{f}_\mathrm{e} = \widetilde{f}_\mathrm{e}^{(\mathrm{mb})} + k\lambda_\mathrm{ei}^{(\mathrm{B})}\widetilde{f}_\mathrm{e}^{(1)} + k^2\lambda_\mathrm{ei}^{(\mathrm{B})2}\widetilde{f}_\mathrm{e}^{(2)} + \ldots$, where we recall that all corrections $f^{(n)}$ only depend on hydrodynamic variables (e.g. $T_\mathrm{e}, n_\mathrm{e}, Z$). As seen in section 2.2.1, the first term can be obtained by substituting $\widetilde{f}_\mathrm{e}^{(\mathrm{mb})}$ into eq. (4.3.4) and enforcing zero current (while correctly assuming that the time-derivative/electron-inertia term can be neglected as it is of higher order):

Remember $\lambda_\mathrm{ei}^* = v/\nu_\mathrm{ei}^*$

$$k\lambda_\mathrm{ei}^{(\mathrm{B})}\widetilde{f}_\mathrm{e}^{(1)} = \frac{v_x}{v}\widetilde{f}_{1x}^{(\mathrm{mb})} = -\frac{v_x}{v}\left(\frac{m_\mathrm{e}v^2}{2k_\mathrm{B}T_0} - 4\right) ik\lambda_\mathrm{ei}^* f_\mathrm{e}^{(\mathrm{mb})}\frac{\widetilde{T}_\mathrm{e}}{T_0}. \tag{4.3.8}$$

4.3.1 *Correction to isotropic part of the EDF*

In order to find the lowest order deviation from the local heat flow, the nonlocal correction to the isotropic part of the distribution function $\delta\widetilde{f}_0$ must first be found by substituting $\widetilde{f}_{1x}^{(\mathrm{mb})}$ into eq. (4.3.3). Due to the temperature amplitude being the only macroscopic parameter that is not constant in time and space, all terms in the Chapman-Enskog expansion will damp at the same rate γ_D. Therefore, as long as $\delta\widetilde{f}_0$ is small only the Maxwellian part of the EDF needs to be considered in the time-derivative term

$$\frac{\partial\widetilde{f}_\mathrm{e}^{(\mathrm{mb})}}{\partial t} = \frac{\partial\log(\widetilde{T}_\mathrm{e})}{\partial t}\widetilde{f}_\mathrm{e}^{(\mathrm{mb})} = -\frac{32}{3\sqrt{\pi}}\xi k^2\lambda_\mathrm{ei}^{(0)}v_{2\mathrm{T}}\widetilde{f}_\mathrm{e}^{(\mathrm{mb})}. \tag{4.3.9}$$

Introducing a relative velocity compared to the background thermal velocity $V = v/v_{2\mathrm{T}}$ the equation that must be solved for $\delta\widetilde{f}_0$ is

$$\underbrace{\left\{-\frac{32}{3\sqrt{\pi}}\left(V^2 - \frac{3}{2}\right)}_{\textit{Nonstationarity}} + \underbrace{\left(V^2 - 4\right)\frac{V^5}{3}}_{\textit{Diffusion}}\right\}\xi k^2\lambda_\mathrm{ei}^{(0)}v_{2\mathrm{T}}f_\mathrm{e}^{(\mathrm{mb})}\frac{\widetilde{T}_\mathrm{e}}{T_0} = C_{\mathrm{ee}0}^{(\mathrm{L})}\left(\delta\widetilde{f}_0\right). \tag{4.3.10}$$

In this thesis, we will use an expression provided by Bychenkov et al. (1994) for the linearised electron-electron collision operator

$$C_{\mathrm{ee}0}^{(\mathrm{L})} = \frac{\nu_\mathrm{ei}^{(0)}}{ZV^2}\frac{\partial}{\partial V}\left(\frac{f_\mathrm{e}^{(\mathrm{mb})}}{2}\hat{L}\left[\frac{\partial\widetilde{\psi}}{\partial V}\right]\right) \tag{4.3.11}$$

$$\text{where } \hat{L}\left[\frac{\partial\widetilde{\psi}}{\partial V}\right] := \frac{2}{\sqrt{\pi}}\frac{\gamma(3/2, V^2)}{V}\frac{\partial\widetilde{\psi}}{\partial V} - \frac{8}{\sqrt{\pi}}\int_0^V U^2\int_U^\infty \mathrm{e}^{-W^2}\frac{\partial\widetilde{\psi}}{\partial W}\,\mathrm{d}W\,\mathrm{d}U, \tag{4.3.12}$$

defining $\nu_\mathrm{ei}^{(0)} = \nu_\mathrm{ei}(v_{2\mathrm{T}})$ and $\widetilde{\psi} = \delta\widetilde{f}_0/f_\mathrm{e}^{(\mathrm{mb})}$ (see appendix B.1 for a derivation). Thus all that remains to find $\delta\widetilde{f}_0$ is to invert $C_{\mathrm{ee}0}^{(\mathrm{L})}$. By multiplying eq. (4.3.10) by

v^2, integrating from ∞ to v (which is consistent with the distribution function vanishing at ∞) and rearranging we can obtain

$$\hat{L}\left[\frac{\partial\widetilde{\psi}}{\partial v}\right] = \Bigg(\underset{\textit{Nonstationarity}}{\frac{32}{3\sqrt{\pi}}V^3} - \underset{\textit{Diffusion}}{\frac{V^8}{3}} \Bigg) \xi Z k^2 \lambda_{\mathrm{ei}}^{(0)2} \frac{\widetilde{T}_{\mathrm{e}}}{T_0} \equiv S(v) \tag{4.3.13}$$

Inverting the operator $\hat{L}$ to obtain $\frac{\partial\widetilde{\psi}}{\partial v}$ (and hence $\delta\widetilde{f}_0$) is a bit more difficult but can be done in a number of ways. Firstly, we can find the exact inverse by recasting $\hat{L}$ into a second-order differential operator and observing that a solution to the homogeneous part is given by $\frac{\partial\widetilde{\psi}_1}{\partial v} = v$. From this we can find an independent solution using the Wronskian and then construct a Green's function that is proven to give the desired inverse in appendix B.4,

$$\hat{L}_*^{-1}[S(V)] = \frac{\sqrt{\pi}}{2}\frac{V\,S(V)}{\gamma(3/2, V^2)} - 2\sqrt{\pi}V\int_*^V \frac{Y^2\int_0^Y S(T)T\mathrm{e}^{-T^2}\,\mathrm{d}T}{\gamma(3/2, Y^2)^2}\,\mathrm{d}Y, \tag{4.3.14}$$

where $*$ is chosen so that $\delta\widetilde{f}_0$ does not affect $\widetilde{T}_{\mathrm{e}}$; i.e. if $V^3\frac{\partial\widetilde{\psi}}{\partial V}\mathrm{e}^{-V^2} = 0$ (see appendix B.2). Practically, this is achieved here by setting $* = 0$ and then adding on a term proportional to V:

$$\hat{L}_*^{-1}[S(V)] = \hat{L}_0^{-1}[S(V)] - \frac{8V}{3\sqrt{\pi}}\int_0^\infty U^3\hat{L}_0^{-1}[S(V)]\mathrm{e}^{-U^2}\,\mathrm{d}U. \tag{4.3.15}$$

In order to gain some understanding of the behaviour of $\frac{\partial\widetilde{\psi}}{\partial v}$ beyond just an integral expression, an iterative form of $\hat{L}_0^{-1}[S(V)]^{\langle N\rangle}$ is employed:

$$\hat{L}_0^{-1}[S(V)]^{\langle N\rangle} = \frac{\sqrt{\pi}}{2}\frac{V\,\bar{S}(V)}{\gamma(3/2, V^2)} - 2\sqrt{\pi}V\sum_{n=1}^{N}\frac{n!I^n\left[\mathrm{e}^{V^2}\int_0^V\bar{S}\,T\mathrm{e}^{-T^2}\,\mathrm{d}T\right]}{\gamma(3/2, V^2)^{n+1}}, \tag{4.3.16}$$

$$\text{where } I[F(V)] = \int_0^V 2U^2\mathrm{e}^{-U^2}F(U)\,\mathrm{d}U \tag{4.3.17}$$

$$\implies \frac{\partial\widetilde{\psi}^{\langle N\rangle}}{\partial V} = \hat{L}_0^{-1}[\bar{S}(V)]^{\langle N\rangle} - \frac{8V}{3\sqrt{\pi}}\int_0^\infty U^3\hat{L}_0^{-1}[\bar{S}(V)]^{\langle N\rangle}\mathrm{e}^{-U^2}\mathrm{d}U, \tag{4.3.18}$$

where $\bar{S}(V)$ is the original source term S with the nonstationarity term removed, as it can be shown explicitly that this term plays no role in determining $\delta\widetilde{f}_0$ (i.e. $\hat{L}_*^{-1}[V^3] = 0$, see appendix B.5). This sequence can proved to converge (see appendix B.6) and is observed to do so rapidly. Unfortunately, the final energy conserving integral needs to be calculated numerically and Mathematica's `NIntegrate` can sometimes get this wrong due to difficulties in treating the denominator $\gamma(3/2, 0)$, which vanishes in the low-velocity limit. In order to avoid

this, a cutoff $V_{\min} = 0.02$ is provided, below which the low-velocity limit of the denominator is integrated analytically. This process is applied to all numerical integrals performed with `NIntegrate`, for example:

$$\begin{aligned}
&\int_0^\infty U^3 \hat{L}_0^{-1}[S(V)]^{\langle N\rangle} \mathrm{e}^{-U^2}\,\mathrm{d}U \\
\approx\ &\int_0^{V_{\min}} \frac{\sqrt{\pi}}{3}\frac{S(V)}{V^2} - 2\sqrt{\pi}V \sum_{n=1}^{N} \frac{n! I^n \left[\mathrm{e}^{V^2}\int_0^V S\, T\mathrm{e}^{-T^2}\,\mathrm{d}T\right]}{\left(\frac{2}{3}V^3\right)^{n+1}}\,\mathrm{d}U \\
+\ &\int_{V_{\min}}^\infty U^3 \hat{L}_0^{-1}[S(V)]^{\langle N\rangle} \mathrm{e}^{-U^2}\,\mathrm{d}U
\end{aligned} \tag{4.3.19}$$

The first two iterations result in the following approximations for $\frac{\partial\widetilde{\psi}}{\partial v}$:

$$\frac{\partial\widetilde{\psi}^{\langle 0\rangle}}{\partial V}\Big/\xi Z k^2 \lambda_{\mathrm{ei}}^{(0)2}\frac{\widetilde{T}_\mathrm{e}}{T_0} = 74.3V - \frac{V^9}{3}\frac{\Gamma(3/2)}{\gamma(3/2, V^2)}, \tag{4.3.20}$$

$$\begin{aligned}
\frac{\partial\widetilde{\psi}^{\langle 1\rangle}}{\partial V}\Big/\xi Z k^2 \lambda_{\mathrm{ei}}^{(0)2}\frac{\widetilde{T}_\mathrm{e}}{T_0} = \\
69.7V - \left(\frac{V^9}{3} + \frac{2}{9}\frac{V^3\gamma(5, V^2) - \gamma(13/2, V^2)}{\gamma(3/2, V^2)}\right)\frac{\Gamma(3/2)}{\gamma(3/2, V^2)},
\end{aligned} \tag{4.3.21}$$

and are plotted against the exact numerical solution in fig. 4.6. The iterative form of $\frac{\partial\widetilde{\psi}}{\partial v}$ is observed to be indistinguishable from the exact form, with the slowest area of convergence being for $v \approx 1.5v_{2\mathrm{T}}$. The ability to satisfactorily approximate $\frac{\partial\psi}{\partial v}$ with a polynomial of degree 9 explains the need noted by Bychenkov et al. (1995) to use a large number of Laguerre polynomials to describe this regime.

Additionally, the iterative convergence of $\widetilde{\psi}$ and $\delta\widetilde{f}_0$ themselves are plotted in figs. 4.7 and 4.8, exhibiting similar behaviour as observed with $\frac{\partial\widetilde{\psi}}{\partial v}$. (The constant of integration used in obtaining $\widetilde{\psi}$ is such that $\delta\widetilde{f}_0$ does not contribute to the electron density.) An illustration of the effect of $\delta\widetilde{f}_0$ on the total isotropic part of the distribution function is provided in fig. 4.9 for a nonlocality parameter of $\xi Z k^2 \lambda_{\mathrm{ei}}^{(0)2}$. As expected, the introduction of nonlocality allows for a deficit of suprathermal electrons ($v \gtrapprox 2.3v_{2\mathrm{T}}$) at the peak of the temperature perturbation which escape to lower temperatures before they have time to collide. Balancing this out is a surplus of thermal electrons $v \approx 1.5v_{2\mathrm{T}}$ to conserve energy and a greatly reduced number of subthermal electrons $v \lessapprox v_{2\mathrm{T}}$ to conserve the total number of electrons. One issue that is just about noticeable is that $\widetilde{f}_0$ is observed to become negative at $v \approx 3.5v_{2\mathrm{T}}$. While the velocity at which this unphysical sign change occurs will of course increase with longer wavelengths, this does reveal an inherent limitation to the Chapman-Enskog expansion (and many forms of asymptotic expansions in general). As we are mainly interested in

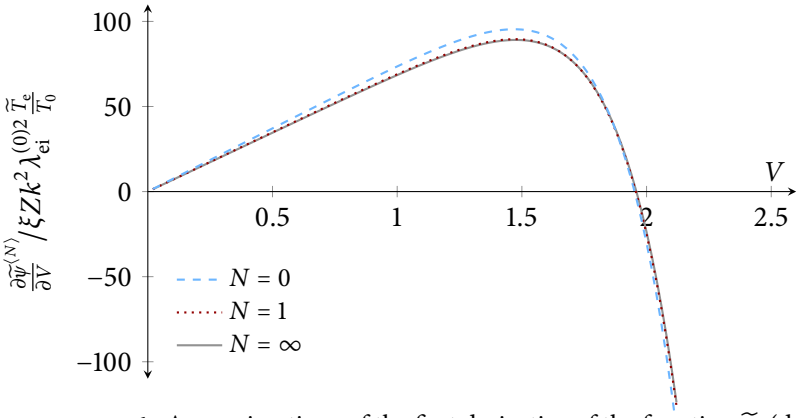

FIGURE 4.6: Approximations of the first derivative of the function $\widetilde{\psi}$, (defined as $\widetilde{\psi} = \delta\widetilde{f}_0 / f_{\mathrm{e}}^{(\mathrm{mb})}$) at the peak of a sinusoidal temperature perturbation. Those obtained using the suggested iterative approach, and given explicitly in eqs. (4.3.20) and (4.3.21) for $N = 0$ and 1, are compared to a numerical integration "$N = \infty$" of eq. (4.3.15) performed by discretising over velocity in steps of $\Delta V = 0.02$.

nonlocal effects on macroscopic observables such as the heat flow rather than the high-velocity behaviour of the EDF, this should not be too much of an issue as long as the unphysical part of $\widetilde{f}_0$ provides a negligible contribution to relevant definite integrals (which it will always do for low enough values of $\xi Z k^2 \lambda_{\mathrm{ei}}^{(0)2}$). An alternative way to avoid this issue would be to use the MN formulation which guarantees positive-definiteness but makes an analytical treatment much more challenging.

4.3.2 *Impact of f_0 on the nonlocal heat flow and electric field*

The nonlocal deviation to the heat flow can be calculated by continuing the Chapman-Enskog expansion on eq. (4.3.4) to obtain the correction to the first-order anisotropy of the distribution function $\delta\widetilde{f}_{1x} = \widetilde{f}_{1x} - \widetilde{f}_{1x}^{(\mathrm{mb})}$. Note that this depends not only on the nonlocal correction to the isotropic part of the distribution function $\delta\widetilde{f}_0$, but also on electron inertia through the term $\frac{\partial \widetilde{f}_{1x}}{\partial t}$ and pressure anisotropy through $\widetilde{f}_{2xx}$. Conveniently, in the semicollisional regime all three terms ($\delta\widetilde{f}_0$, $\frac{\partial \widetilde{f}_{1x}}{\partial t}$ and $\widetilde{f}_{2xx}$) act completely independently and we can investigate in turn the effects of these on the distribution function, heat flow and electric field.

We will concentrate first on the effect of the isotropic part of the distribution function on $\widetilde{f}_1$,

$$\delta\widetilde{f}_{1x}^{(\delta f_0)} = -\lambda_{\mathrm{ei}}^{*}\left(ik\widetilde{\psi} + \frac{e\delta\widetilde{E}_x^{(\delta f_0)}}{k_{\mathrm{B}}T_0}\right) f_{\mathrm{e}}^{(\mathrm{mb})}, \tag{4.3.22}$$

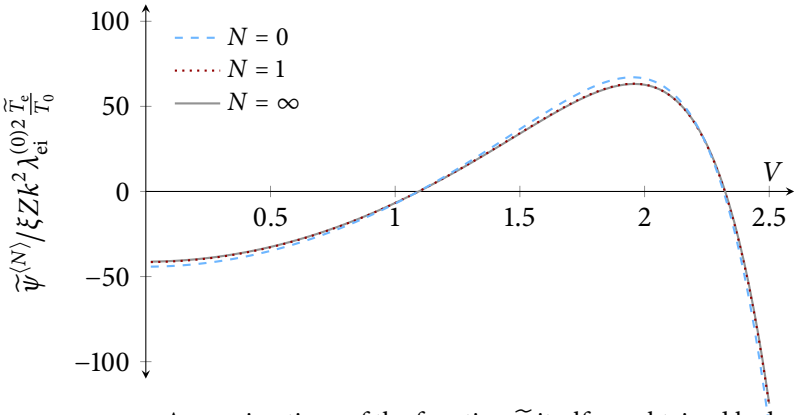

FIGURE 4.7: Approximations of the function $\widetilde{\psi}$ itself are obtained by by numerically integrating the curves plotted in the previous figure, again using a discretisation in steps of $\Delta V = 0.02$. Note that the constant of integration is calculated to ensure that $\delta\widetilde{f}_0$ does not contribute to the plasma density.

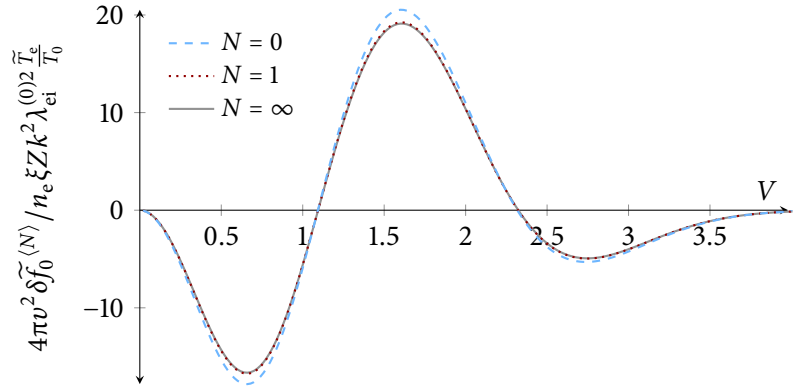

FIGURE 4.8: Approximations for the lowest order perturbation to the density integrand as a result of nonlocality ($4\pi v^2 \delta\widetilde{f}_0 v_{2\mathrm{T}}$) at the peak of a sinusoidal temperature perturbation. These are obtained by simply multiplying the expressions for $\widetilde{\psi}$ plotted in fig. 4.7 by $4v^2 \mathrm{e}^{-V^2}/\sqrt{\pi}$.

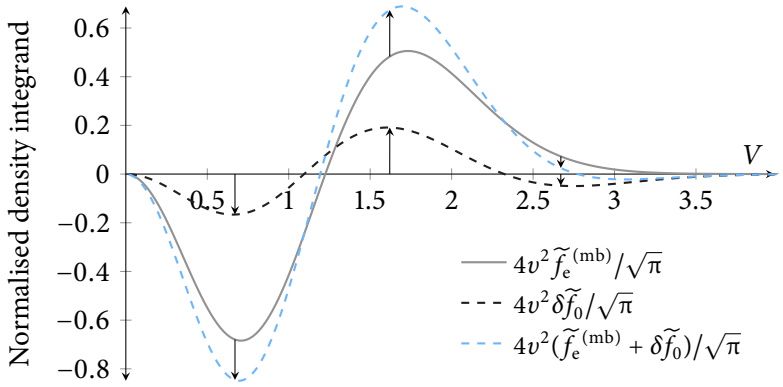

FIGURE 4.9: The relative effect of nonlocality in the semicollisional regime on the density integrand is demonstrated by comparing to the Maxwellian perturbation $\widetilde{f}_e^{(mb)}$ at the peak of a sinusoidal temperature perturbation. A purely numerical calculation of the distribution function (denoted by $N = \infty$ elsewhere) was used to calculate this. Here the modified nonlocality parameter $\xi Z k^2 \lambda_{ei}^{(0)2} = 0.01$ and the relative temperature perturbation $\widetilde{T}_e/T_0$, thermal velocity v_{2T} and electron density n_e have all been normalised to unity.

where the superscript simply denotes that these terms are only due to the contribution of $\delta\widetilde{f}_0$. In fact, it turns out an explicit form for $\delta\widetilde{E}_x^{(\delta f_0)}$ is not required to compute the corresponding perturbation to the heat flow. This can be demonstrated using the fact that the v^3 (curent) moment of $\widetilde{f}_{1x}$ is zero due to the requirement of quasineutrality to rewrite the perturbation to $\widetilde{Q}_x$ due to $\delta\widetilde{f}_0$ as

$$\delta\widetilde{Q}_x^{(\delta f_0)} = \frac{4\pi}{3}\int_0^\infty \frac{1}{2} m_e v^5 \delta\widetilde{f}_{1x}^{(\delta f_0)}\,\mathrm{d}v \tag{4.3.23}$$

$$\equiv \frac{2\pi m_e}{3}\int_0^\infty v^3\left(v^2 - 4{v_{2T}}^2\right)\delta\widetilde{f}_{1x}^{(\delta f_0)}\,\mathrm{d}v. \tag{4.3.24}$$

Integrating by parts eliminates the electric field, allowing the deviation from the nonlocal heat flow to be expressed in terms of the already obtained $\frac{\partial\widetilde{\psi}}{\partial v}$ only:

$$\delta\widetilde{Q}_x^{(\delta f_0)} = \frac{\pi m_e {v_{2T}}^2}{3}\left\{\left[-V^4\widetilde{f}_{1x}^{(\delta f_0)}\right]_0^\infty - \int_0^\infty ikv^4\lambda_{ei}^*\frac{\partial\widetilde{\psi}}{\partial v}f_e^{(mb)}\,\mathrm{d}v\right\} \tag{4.3.25}$$

$$= -\frac{\pi i k m_e {v_{2T}}^2}{3}\int_0^\infty v^4\lambda_{ei}^*\frac{\partial\widetilde{\psi}}{\partial v}f_e^{(mb)}\,\mathrm{d}v \tag{4.3.26}$$

where the first term vanishes as long as $\psi(v = 0)$ is finite. It is useful to express $\delta\widetilde{Q}$ relative to the local heat flow $\widetilde{Q}^{(\mathrm{B})}$ and in terms of the relative velocity V as

$$\frac{\delta\widetilde{Q}_x^{(\delta f_0)}}{\widetilde{Q}_x^{(\mathrm{B})}} = \frac{1}{24}\int_0^\infty V^8 \frac{\partial\widetilde{\psi}}{\partial V} e^{-V^2}\,\mathrm{d}V \Bigg/ \frac{\widetilde{T}_\mathrm{e}}{T_0}. \tag{4.3.27}$$

From the above expression the contribution of $\widetilde{\psi}$ towards the coefficient b_Q defined in eq. (4.3.1) can be easily obtained. Table 4.2 shows that the coefficients obtained from successive iterations of $\frac{\partial\widetilde{\psi}^{\langle N\rangle}}{\partial V}$ converge to the value given by Bychenkov et al. (1994, 1995)—264—giving support for the methodology used here. Additionally, it is shown that using the form of $\frac{\partial\widetilde{\psi}^{\langle N\rangle}}{\partial V}$ prior to enforcing energy conservation (left of arrow) has a small but non-negligible effect decreasing the nonlocal heat flow. (Note that the results corresponding to $N = \infty$ were obtained by performing a numerical integration of eqs. (4.3.15) and (4.3.26) using a velocity discretisation of $\Delta V = 0.02$.)

TABLE 4.2: *Convergence of the parameter $b_Q^{(\delta f_0)}$ with iterations before (left) and after (right) including the energy conserving integral in eq.* (4.3.18).

N	$b_Q^{(\delta f_0)}/\xi$
0	318.6 → 276.5
1	303.9 → 264.5
2	303.2 → 264.0
3	303.1 → 263.9
⋮	⋮
∞	298.5 → 263.9

While we have conveniently eliminated the electric field from the expression for $\delta\widetilde{Q}_x$, one might still be interested in calculating the effect of nonlocality on the electric field itself. To do so, we simply need to enforce zero current on the expression in eq. (4.3.22) and rearrange, giving

$$\frac{e\delta\widetilde{E}_x^{(\delta f_0)}}{k_\mathrm{B}T_0} = \frac{\int_0^\infty -ik\widetilde{\psi}V^7 \mathrm{e}^{-V^2}\,\mathrm{d}V}{\int_0^\infty V^7\mathrm{e}^{-V^2}\,\mathrm{d}V} \tag{4.3.28}$$

$$\implies \quad b_E^{(\delta f_0)} = -\frac{2}{9}\int_0^\infty \widetilde{\psi}V^7\mathrm{e}^{-V^2}\,\mathrm{d}V \Bigg/ \frac{\widetilde{T}_\mathrm{e}}{T_0} Zk^2\lambda_{\mathrm{ei}}^{(0)2} \approx 88.3\xi \tag{4.3.29}$$

TABLE 4.3: *Convergence of the parameter $b_E^{(\delta f_0)}$ with iterations.*

N	$b_E^{(\delta f_0)}/\xi$
0	93.2
1	88.6
2	88.3
⋮	⋮
∞	88.3

in agreement with Brantov et al. (1996). Note that this value is almost exactly three times less than the corresponding coefficient for heat flow, illustrating that nonlocal effects on the electric field are less important in the semicollisional regime. For example to achieve a 10% reduction in the heat flow due to nonlocal perturbations on $\widetilde{f}_0$ would require $k\lambda_{\mathrm{ei}}^{(\mathrm{B})} \approx 0.02/\sqrt{\xi Z}$ but an equivalent reduction in the electric field would only occur at $k\lambda_{\mathrm{ei}}^{(\mathrm{B})} \approx 0.03/\sqrt{\xi Z}$. For the sake of completeness, table 4.3 shows that using the iterative form of $\widetilde{\psi}$ to obtain b_E converges rapidly.

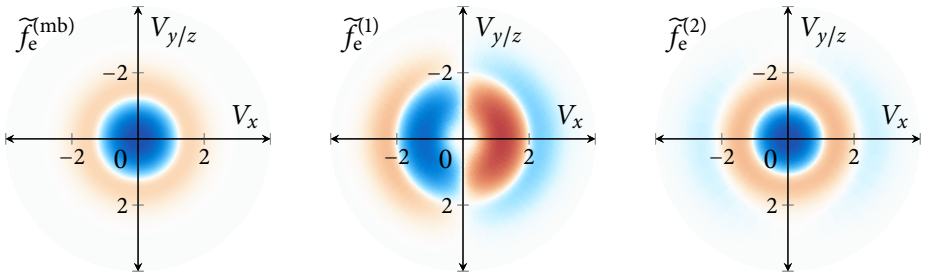

FIGURE 4.10: Density plots illustrating the qualitative effects of the first three terms in the Chapman-Enskog expansion on the EDF for an ionisation of $Z = 1$. (Red denotes positive values and blue denotes negative values.) The first plot refers to the Maxwellian part of the temperature perturbation, the middle plot is simply the local form of $\widetilde{f}_1$, while the last shows the combination of the nonlocal modification to the istotropic part of the EDF $\delta\widetilde{f}_0$ with pressure anisotropy $\overleftrightarrow{f}_2$.

4.3.3 *The role of pressure anisotropy*

Similarly, the effect of the higher order anisotropies encapsulated by $\overleftrightarrow{f}_2$ on the heat flow can be evaluated. Again we can ignore time-derivative to find that

$$\widetilde{f}_{2xx} = -\frac{2}{9} ik\lambda_{ei}^{*} \widetilde{f}_{1x}^{(mb)}, \widetilde{f}_{2yy} = \widetilde{f}_{2zz} = \frac{ik\lambda_{ei}^{*}}{9} \widetilde{f}_{1x}^{(mb)}. \tag{4.3.30}$$

Combining this with $\delta\widetilde{f}_0$ gives

$$\Longrightarrow \widetilde{f}_e^{(2)} = \left(\frac{\widetilde{\psi}}{k^2 \lambda_{ei}^{(B)2}} - \frac{32}{\pi} (3V_x^2 - V^2)(V^2 - 4) V^6 \xi^2 \frac{\widetilde{T}_e}{T_0} \right) f_e^{(mb)} \tag{4.3.31}$$

as the total second-order contribution to the distribution function in Chapman-Enskog theory. It is at lower ionisations that weaker angular scattering allows for more pronounced anisotropies to develop. These anisotropies encourage the reduction of suprathermal electrons already observed at the peak of the temperature perturbation to be stronger for electrons that are travelling mostly along the x-axis as illustrated in fig. 4.10.

The sole contribution of $\overleftrightarrow{f}_2$ to the electric field and heat flow is from $\widetilde{f}_{2xx}$, and can be calculated by substituting into the equation for $\widetilde{f}_{1x}$.

$$\delta\widetilde{f}_{1x}^{(f_2)} = -\lambda_{\mathrm{ei}}^{*}\left(-\frac{4}{45} ik^3\lambda_{\mathrm{ei}}^{*2}(V^2-4) f_{\mathrm{e}}^{(\mathrm{mb})}\frac{\widetilde{T}_{\mathrm{e}}}{T_0} + \frac{e\delta\widetilde{E}_x^{(f_2)}}{k_{\mathrm{B}}T_0}\right) \tag{4.3.32}$$

$$\implies \frac{e\delta\widetilde{E}_x^{(f_2)}}{k_{\mathrm{B}}T_0} = \frac{4}{45}\frac{\int_0^\infty V^{15}(V^2-4)\mathrm{e}^{-V^2}\,\mathrm{d}V}{\int_0^\infty V^7\mathrm{e}^{-V^2}\,\mathrm{d}V} i\xi^2k^3\lambda_{\mathrm{ei}}^{(0)2}\frac{\widetilde{T}_{\mathrm{e}}}{T_0} \tag{4.3.33}$$

$$= \frac{896}{3} i\xi^2k^3\lambda_{\mathrm{ei}}^{(0)2}\frac{\widetilde{T}_{\mathrm{e}}}{T_0}, \tag{4.3.34}$$

which means that the coefficient for reduction of the electric field due to pressure anisotropy is given by $b_E^{(f_2)} = 199.1\xi^2/Z$. Substituting back into eq. (4.3.32)

$$\delta\widetilde{f}_{1x}^{(f_2)} = ik\lambda_{\mathrm{ei}}^{*}\left(V^8(V^2-4)\frac{4}{45} - \frac{896}{3}\right)\xi^2k^2\lambda_{\mathrm{ei}}^{(0)2} f_{\mathrm{e}}^{(\mathrm{mb})}\frac{\widetilde{T}_{\mathrm{e}}}{T_0} \tag{4.3.35}$$

and integrating gives

$$\frac{\delta\widetilde{Q}_x^{(f_2)}}{\widetilde{Q}_x^{(\mathrm{B})}} = \frac{\int_0^\infty V^9\left(V^8(V^2-4)\frac{4}{45} - \frac{896}{3}\right)\mathrm{e}^{-V^2}\,\mathrm{d}V}{\int_0^\infty V^9(V^2-4)\mathrm{e}^{-V^2}\,\mathrm{d}V}\xi^2k^2\lambda_{\mathrm{ei}}^{(0)2} \tag{4.3.36}$$

$$\implies b_Q^{(\mathrm{EI})} = 448\xi^2/Z. \tag{4.3.37}$$

Comparison to M1

These results concerning the form of $\overleftrightarrow{f}_2$ can be compared to those predicted by the MN model. For a low-amplitude temperature perturbation the anisotropy parameter $\vec{\alpha}_1$ used in the MN model is of order $\widetilde{T}_{\mathrm{e}}/T_0$ and can be treated as small such that the distribution function can be expanded as $\widetilde{f}_{\mathrm{e}} = \mathrm{e}^{\alpha_0+\vec{\alpha}_1\cdot\hat{\vec{v}}} = \mathrm{e}^{\alpha_0}(1+\vec{\alpha}_1\cdot\hat{\vec{v}} + \mathcal{O}(\widetilde{T}_{\mathrm{e}}/T_0)^2)$. Therefore, to first-order in the relative temperature amplitude the MN model predicts that $\overleftrightarrow{f}_2 = 0$ and is indistinguishable from the standard P1 approach used in the diffusion approximation. Whether the MN approach to describing the distribution function is an improvement on P1 for a larger amplitude perturbation is unclear from this initial analysis due to the complications of nonlinearities.

4.3.4 *The role of electron inertia*

Also providing a contribution to both the heat flow and electric field at third order in Chapman-Enskog theory is the time-derivative of $\widetilde{f}_1$. This is simply given by

$$\frac{\partial \widetilde{f}_{1x}^{(\mathrm{mb})}}{\partial t} = -\gamma_{\mathrm{D}} \widetilde{f}_{1x}^{(\mathrm{mb})}, \tag{4.3.38}$$

which accordingly reduces $\widetilde{f}_1$ itself through electron inertia,

$$\delta \widetilde{f}_{1x}^{(\mathrm{EI})} = -\lambda_{\mathrm{ei}}^{*} \left(V^3(V^2-4) \frac{32}{3\sqrt{\pi}} \xi^2 i k^3 \lambda_{\mathrm{ei}}^{(0)2} \frac{\widetilde{T}_{\mathrm{e}}}{T_0} + \frac{e\delta \widetilde{E}_x^{(\mathrm{EI})}}{k_{\mathrm{B}} T_0} \right) f_{\mathrm{e}}^{(\mathrm{mb})}. \tag{4.3.39}$$

Enforcing zero-current provides the pertubation to the electric field,

$$\frac{e\delta \widetilde{E}_x^{(\mathrm{EI})}}{k_{\mathrm{B}} T_0} = -\frac{32}{3\sqrt{\pi}} \frac{\int_0^\infty V^{10}(V^2-4)\mathrm{e}^{-V^2}\,\mathrm{d}V}{\int_0^\infty V^7 \mathrm{e}^{-V^2}\,\mathrm{d}V} i\xi^2 k^3 \lambda_{\mathrm{ei}}^{(0)2} \frac{\widetilde{T}_{\mathrm{e}}}{T_0} \tag{4.3.40}$$

$$= -\frac{315}{4} i\xi^2 k^3 \lambda_{\mathrm{ei}}^{(0)2} \frac{\widetilde{T}_{\mathrm{e}}}{T_0}, \tag{4.3.41}$$

resulting in a value for the coefficient $b_E^{(\mathrm{EI})} = -52.5\xi^2/Z$ that is only appreciable at low ionisations. Substituting this back into eq. (4.3.39) results in

$$\delta \widetilde{f}_{1x}^{(\mathrm{EI})} = -ik\lambda_{\mathrm{ei}}^{*} \left(V^3(V^2-4)\frac{32}{3\sqrt{\pi}} - \frac{315}{4} \right) \xi^2 k^2 \lambda_{\mathrm{ei}}^{(0)2} f_{\mathrm{e}}^{(\mathrm{mb})} \frac{\widetilde{T}_{\mathrm{e}}}{T_0}, \tag{4.3.42}$$

which is plotted alongside $\widetilde{f}_{1x}^{(\mathrm{mb})}$ in fig. 4.11. Note that the relative importance of electron inertia increases with velocity due to decreasing collisionality. This can be used to calculate the relative perturbation to the heat flow

$$\frac{\delta \widetilde{Q}_x^{(\mathrm{EI})}}{\widetilde{Q}_x^{(\mathrm{B})}} = \frac{\int_0^\infty V^9 \left(V^3(V^2-4)\frac{32}{3\sqrt{\pi}} - \frac{315}{4} \right) \mathrm{e}^{-V^2}\,\mathrm{d}V}{\int_0^\infty V^9(V^2-4)\mathrm{e}^{-V^2}\,\mathrm{d}V} \xi^2 k^2 \lambda_{\mathrm{ei}}^{(0)2} \tag{4.3.43}$$

$$\implies b_Q^{(\mathrm{EI})} = -\frac{3255}{32}\xi^2/Z = -101.7\xi^2/Z. \tag{4.3.44}$$

Note that the effect of electron inertia is to *increase* both the electric field and heat flow by holding them back to their values at an earlier time when the amplitude of temperature perturbation was larger.

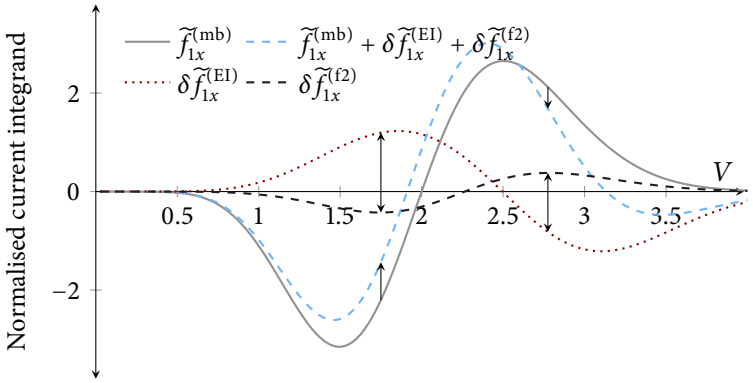

FIGURE 4.11: The relative effect of electron inertia and pressure anisotropy working together on the current integrand. Here the degree of nonlocality is given $\xi^{2/3} k\lambda_{\mathrm{ei}}^{(0)} \approx 0.12$ and the relative temperature perturbation, thermal velocity and electron density have all been normalised to unity.

4.3.5 *Comparison to* EIC

Putting together the previous findings of this section we can summarise the behaviour of the parallel heat flow and electric field in the semicollisional limit as

$$b_Q = 263.9\xi + 448\xi^2/Z - 101.7\xi^2/Z, \tag{4.3.45}$$

$$b_E = \underset{\textit{Diffusion}}{88.3\xi} + \underset{\substack{\textit{Pressure}\\\textit{Anisotropy}}}{199.1\xi^2/Z} - \underset{\substack{\textit{Electron}\\\textit{Inertia}}}{52.5\xi^2/Z}, \tag{4.3.46}$$

where we have labelled the core reduction in transport due to the diffusive modification of $\widetilde{f}_0$ derived in sections 4.3.1 and 4.3.2 along with those occurring due to pressure anisotropy and electron inertia in sections 4.3.3 and 4.3.4. As a result of these latter terms depending inversely on Z, it is only at lower ionisations where they become appreciable. Note that while pressure anisotropy and electron inertia act in opposite directions, the former is almost four times more dominant and increases the nonlocal reduction to the transport.

The most practical tool available to us for testing the accuracy of these findings, particularly at lower ionisations where electron-electron collisions also begin to affect the anisotropic part of the distribution function, is in fact the EIC model whose main assumptions, except for neglection of electron inertia, are valid in this linearised semicollisional regime. While VFP codes such as KIPP, K2 and OSHUN do offer a more complete approach with their ability to evaluate the effect

of electron inertia, their slow (first-order) convergence with timestep means that obtaining high-precision values of heat flow and thermal conductivity is computationally expensive. Such precision is very important in calculating the semicollisional coefficients due to deviations from the quadratic dependence expressed in eq. (4.3.1) becoming noticeable at moderately high collisionalities corresponding to $\sqrt{Z}k\lambda_{\mathrm{ei}}^{(\mathrm{B})} \approx 0.005$; at this point the predicted reduction of heat flow due to nonlocality is less than 1%. Instead, the quasistationary approach employed by the EIC circumvents the need for achieving timestep convergence.

As the implementation of the EIC model used for this thesis does not yet provide values for the nonlocal electric field, only the heat flow coefficient b_Q could be calculated. This was performed by fitting a straight line on a graph of dimensionless thermal conductivity $m_\mathrm{e}\kappa_\parallel/n_\mathrm{e}\widetilde{T}_\mathrm{e}\tau_{\mathrm{ei}}^{(\mathrm{B})}$ against $Zk^2\lambda_{\mathrm{ei}}^{(\mathrm{B})2}$ as illustrated for $Z = 1$ in fig. 4.12. The coefficient b_Q is then given by the ratio between the absolute value of the gradient and the y-intercept of the line of best fit. The fitting range consisted of all long-wavelength simulations performed corresponding to $\sqrt{Z}k\lambda_{\mathrm{ei}}^{(\mathrm{B})} < 10^{-3}$; this always included at least six data points with at least one value of $\sqrt{Z}k\lambda_{\mathrm{ei}}^{(\mathrm{B})}$ below $2 \times 10^{-4}/\sqrt{Z}$. The Legendre-Laguerre basis was employed due to its relatively rapid convergence in the semicollisional regime; only 3 Legendre modes are theoretically needed and we find that 40–50 Laguerre modes are sufficient for obtaining the value of b_Q up to 3 significant figures. Comparing the EIC value of b_Q at $Z = 1$ (43.5) to that obtained with KIPP (42.1) gives a discrepancy of only 4 %; again the KIPP result was considered less accurate due to timestep and velocity grid convergence issues.

TABLE 4.4: *Values for the coefficient b_Q for various values of Z obtained with the* EIC *model using at least 4,40 Legendre-Laguerre moments.*

Z	b_Q
1	43.5
2	73.6
3	96.0
4	113
6	139
8	157
10	170
12	180
14	189
20	206
30	222
500	261

Numerical results for b_Q obtained using the EIC model for a range of ionisations are summarised in table 4.4, in all cases at least 4 Legendre moments/40 Laguerre moments were used. Reassuringly, the value predicted by the EIC model at a high ionisation of $Z = 500$ (261) is close to that predicted by eq. (4.3.45) (262). However, such impressive agreement does not persist at lower ionisations due to the inappropriateness of assuming that the effect of electron-electron collisions on the anisotropic parts of the EDF can be simply approximated by multiplying the electron-ion frequency by the Epperlein-Short (1991) approximation $\xi_{\mathrm{ES}} = (Z + 0.24)/(Z + 4.2)$. This discrepancy is illustrated in fig. 4.13 where the ionisation dependence of the EIC b_Q values is compared to that given by considering only the diffusive and anisotropic terms in eq. (4.3.45) $\xi_{\mathrm{ES}}(1 + 1.7\xi_{\mathrm{ES}})$ (recall that the EIC model neglects electron inertia). Instead we find that a fit of $Z/(Z + 11/2)$ is more appropriate for b_Q, approximating the EIC results to within 7 %. Nevertheless, the implications of this for the validity of using ξ_{ES} in IMPACT and the SNB model are not as serious as they may seem because b_Q only quantifies

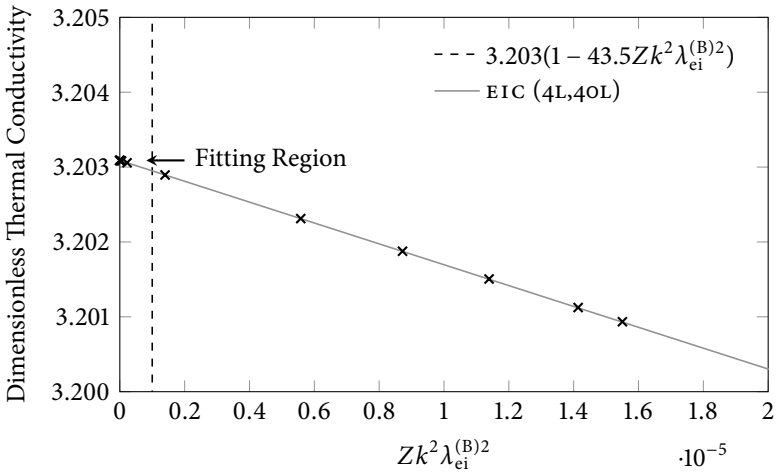

FIGURE 4.12: The coefficients b_Q parametrising the nonlocal reduction of heat flow in the semicollisional regime were calculated from EIC simulations by taking the ratio between the absolute value of the gradient and the y-intercept of the line of best fit for dimensionless thermal conductivity $m_e\kappa_\parallel/n_e\widetilde{T}_e\tau_{ei}^{(B)}$ against $Zk^2\lambda_{ei}^{(B)2}$ (shown here for $Z = 1$) using a fitting region given by $Zk^2\lambda_{ei}^{(B)2} < 10^{-6}$.

the initial *deviation* from the local limit, whereas the *total* heat flux is not very sensitive to marginal errors in b_Q in the semicollisional regime. Additionally, the effect of neglecting pressure anisotropy is also shown in fig. 4.13 by comparing EIC results using just 2 Legendre moments (but still 40+ Laguerre moments) to ξ_{ES} which is the ionisation dependence of the diffusive term in eq. (4.3.45). This confirms our analytical finding that higher-order anisotropies do indeed *increase* the degree of nonlocal heat flow reduction in the semicollisional regime.

4.3.6 *Behaviour of SNB model in the semicollisional regime*

For long wavelength perturbations the diffusive term in the SNB PDE, eq. (2.3.25), can be ignored and thus the distribution function and nonlocal heat flow easily computed in the semicollisional limit. An outline of the derivation is given here, which stems from a continuum treatment of the SNB model as opposed to the usual discretised energy groups. For the original BGK collision operator

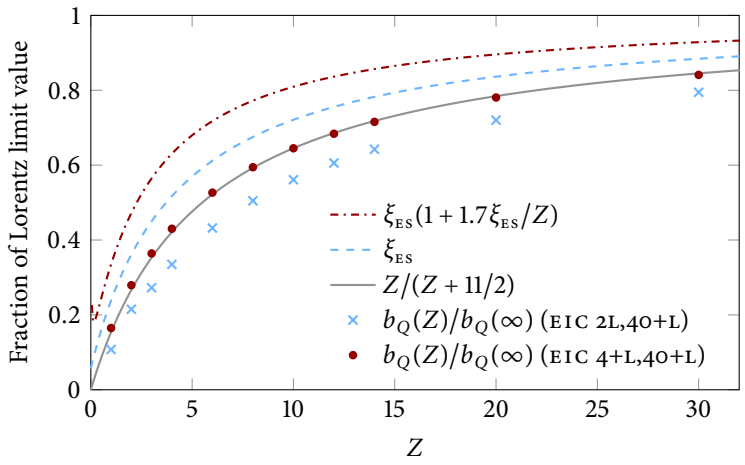

FIGURE 4.13: The red dot-dashed line and crosses represent analytic approximations and EIC predictions for the Z-dependence of the coefficient b_Q including the effects of pressure anisotropy but not electron inertia, while the blue dashed line and crosses neglect both effects. The gray line is simply a new fit found to approximate the EIC results well.

$C_{ee0}^{(BGK)}[f_0] = -rv_{ei}f_0/Z$ used by Schurtz et al. (2000) we can rearrange eq. (2.3.25) to obtain an expression for

$$\widetilde{H}^{(BGK)} \equiv 2\pi m_e v^5 \delta\widetilde{f}_0 \,\mathrm{d}v \tag{4.3.47}$$

$$= -\frac{\mathrm{i}Zk\lambda_{ei}}{12r} V^9\{1, V^2-4\}\mathrm{e}^{-V^2}\widetilde{Q}^{(B)}\,\mathrm{d}V, \tag{4.3.48}$$

again using the contraction $V = v/v_{2T}$. Here the curly brackets distinguish the original source term containing $\vec{f}_1^{(mb)} = -(V^2-4)\lambda_{ei}^* f_e^{(mb)}\vec{\nabla}T_e/T_e$ (right) from the modified source term with $\vec{g}_1^{(mb)} = -\lambda_{ei}^* f_e^{(mb)}\vec{\nabla}T_e/T_e$ (left) used by Schurtz et al. in the standard implementation of the model. Upon integration we then find that the lowest order perturbation to the heat flow is given by

$$\delta\widetilde{Q}_x^{(BGK)} = -\frac{32}{9\pi}\int_0^\infty \frac{V^{17}\{1, V^2-4\}\mathrm{e}^{-V^2}}{36r}\,\mathrm{d}V\,\xi Zk^2\lambda_{ei}^{(B)2}\widetilde{Q}^{(B)}. \tag{4.3.49}$$

(The extra factor of V^8 comes from the velocity dependence of the mfp's in eqs. (2.3.26) and (4.3.49)). If instead the AWBS operator $C_{ee0}^{(AWBS)}[f_0] = \nu_{ei}v\frac{\partial f_0}{\partial v}/Z$ is used we need to integrate to obtain

$$\widetilde{H}^{(AWBS)} = \frac{V^5}{12}\int_\infty^V iZk\lambda_{ei}(U)U^3\{1, U^2-4\}\mathrm{e}^{-U^2}\,\mathrm{d}U\widetilde{Q}^{(B)}\,\mathrm{d}V \tag{4.3.50}$$

TABLE 4.5: Predictions for b_Q made by the SNB model, depending on choice of collision operator (columns) and source term (rows).

	Model collision operator	
RHS	$C_{ee0}^{(BGK)}$	$C_{ee0}^{(AWBS)}$
$\vec{\nabla}\cdot\vec{f}_1^{(mb)}$	$3169\xi/r$	316.9ξ
$\vec{\nabla}\cdot\vec{g}_1^{(mb)}$	$633.8\xi/r$	63.38ξ

by applying the boundary condition $\lim_{V\to\infty}\widetilde{H}=0$. Note that if this integration is performed explicitly on the original source term $\vec{f}_1^{(mb)}$ (second entry in the curly brackets) we obtain the same expression for $\widetilde{H}$ as when using the BGK collision operator and modified source term $\vec{g}_1^{(mb)}$ (eq. 4.3.49, first term in the curly brackets) with the choice of tunable parameter $r=2$. The heat flow can then be obtained using integration by parts:

$$\delta\widetilde{Q}_x^{(AWBS)}=-\frac{32}{9\pi}\int_0^\infty\frac{V^{17}\{1,V^2-4\}e^{-V^2}}{360}\,dV\,\xi Z k^2\lambda_{ei}^{(B)2}\widetilde{Q}^{(B)}. \tag{4.3.51}$$

The numerical results of these calculations are outlined in table 4.5. Our analysis reveals that using the AWBS operator and the kinetic source term $\vec{\nabla}\cdot\vec{f}_1^{(mb)}$ gives a priori the closest value of $b_Q=316.9\xi$ (top right) to within 20% of that predicted analytically in the Lorentz limit (264). This ability of the AWBS collision operator to predict the deviation in the hydrodynamic limit fairly accurately might suggest that it provides an improvement to the original SNB model, however we will later show in section 4.4.3 that coupling it with the original source term $\vec{f}_1^{(mb)}$ leads to unphysical negative values of the thermal conductivities at moderate collisionalities (see section 4.6.3). Nevertheless, this issue does not necessarily imply that the AWBS operator is an inappropriate choice for *other* nonlocal models. For example, the MN model presented by Del Sorbo et al.(2015, 2016) does not appear to exhibit this issue of positive-definitiveness.

Setting $r=2$ exactly in the original implementation of the SNB model (BGK collision operator with the modified source term $\vec{\nabla}\cdot\vec{g}_{1x}^{(mb)}$) gives the same value of $b_Q=316.9\xi$ as with the AWBS operator (bottom-left entry in table 4.5) and the source term $\vec{\nabla}\cdot\vec{f}_{1x}^{(mb)}$ (top-right). However, to match the kinetic results for b_Q, a value of $r=2.4$ is required in the Lorentz limit and $r=3$ for $Z=1$. Matching coefficients to such accuracy does not seem necessary, as using $r=2$

is later found to achieve much better agreement for problems involving large temperature variations in chapter 5.

It is of great interest to evaluate whether the relationship between $\widetilde{H}$ and the isotropic part of the distribution function, $\widetilde{H} \approx 2\pi m_\mathrm{e} v^5 \delta\widetilde{f}_0 \,\mathrm{d}v$, suggested in the original paper is accurate. If this relationship were indeed correct in the high-velocity limit then $\widetilde{f}_0$ would scale as $V^8 \mathrm{e}^{-V^2}$; however, the actual asymptotic behaviour inferred by our previous analysis using the iterative form of the linearised collision operator gives the asymptotic behaviour of $\widetilde{f}_0$ as $V^{10}\mathrm{e}^{-V^2}$ (this can be derived by integrating eq. 4.3.20 or 4.3.21). By comparing eq. (4.3.48) and eq. (4.3.20) we can identify a new relationship between $\widetilde{H}$ and $\widetilde{f}_0$,

$$\widetilde{H} = 2\pi k_\mathrm{B} T_\mathrm{e} v^4 \frac{\partial\widetilde{\psi}}{\partial v} f_\mathrm{e}^{(\mathrm{mb})} \,\mathrm{d}v, \tag{4.3.52}$$

which recovers the correct behaviour of $\widetilde{f}_0$ at high velocities Notably, this interpretation gives rise to exactly the same prediction for the EDF that would arise from using a more realistic model collision operator,

$$C_{\mathrm{ee0}}^{(\mathrm{L})} \approx \frac{k_\mathrm{B} T_\mathrm{e}}{m_\mathrm{e}} \frac{\nu_{\mathrm{ei}}}{Z} v \frac{\partial}{\partial v} \frac{f_\mathrm{e}^{(\mathrm{mb})}}{v} \frac{\partial}{\partial v} \frac{f_0}{f_\mathrm{e}^{(\mathrm{mb})}}, \tag{4.3.53}$$

which is simply just the high-velocity limit of the linearised electron-electron collision operator. Even more impressive is that this interpretation of the EDF justifies the peculiar removal of the return current in the method used by the SNB model to recover the heat flow from H (at least for linearised problems),

$$\delta\vec{Q} = -\int_0^\infty \frac{\lambda_{\mathrm{ei}}^*}{3} \vec{\nabla}\widetilde{H} = -\frac{2\pi k_\mathrm{B} T_\mathrm{e}}{3} \int_0^\infty \frac{\lambda_{\mathrm{ei}}^*}{3} \vec{\nabla} v^4 \frac{\partial\psi}{\partial v} f_\mathrm{e}^{(\mathrm{mb})} \,\mathrm{d}v, \tag{4.3.54}$$

as it is identical to the expression given in eq. (4.3.26), which was derived using integration by parts. This explanation is much more satisfactory than the usual claim of the return current being cancelled out by the purely nonlinear 'Joule-heating' term $\frac{e\vec{E}}{3m_\mathrm{e}v^2} \frac{\partial v^2 \vec{f}_1}{\partial v}$ that usually appears in the f_0 equation.

Figure 4.14 further illustrates the relative success of this new relationship between $\widetilde{H}$ and the isotropic part of the distribution function compared to the old in the semicollisional regime. Additionally, a transformed version of $\widetilde{H}$ that should obey the original relationship

$$H' := \left(\int_0^v \frac{H}{v^4 f_\mathrm{e}^{(\mathrm{mb})}} \,\mathrm{d}v - \int_0^\infty \int_0^u \frac{H}{v^4 f_\mathrm{e}^{(\mathrm{mb})}} \,\mathrm{d}v \, v^2 f_\mathrm{e}^{(\mathrm{mb})} \,\mathrm{d}u \right) \frac{m_\mathrm{e} v^5}{k_\mathrm{B} T_\mathrm{e}} f_\mathrm{e}^{(\mathrm{mb})} \tag{4.3.55}$$

$$\approx 2\pi m_\mathrm{e} v^5 \delta\widetilde{f}_0 \tag{4.3.56}$$

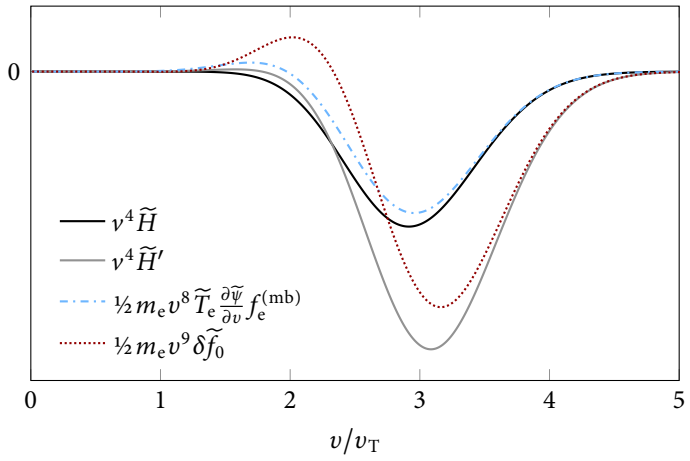

FIGURE 4.14: Comparison of expressions for the nonlocal modification of the EDF at the peak of a low-amplitude temperature sinusoid in the semicollisional regime in arbitrary units. This shows that the SNB term $\widetilde{H}$ (solid back) is better expressed in terms of $\frac{\partial\psi}{\partial v}$ (blue dot-dashed) instead of $\delta\widetilde{f}_0$ directly (red dotted).

is included. Here the double integral is employed to ensure that the nonlocal perturbation to the distribution function does not affect the local electron density. Excellent agreement is observed for velocities greater than approximately $3v_{2T}$; however, notable deviations remain at intermediate velocities near $2v_{2T}$. This suggests that a SNB-like model could be applied to provide corrections for effects that have a high phase-velocity such as SRS or the Landau damping of Langmuir waves, but it might not be appropriate for studying the return current instability (RCI) as this depends on the gradient of the EDF at zero velocity.

4.4 COLLISIONLESS REGIME

When the wavelength of temperature perturbations becomes extremely short, the left-hand side of the VFP equation begins to dominate over collisions on the right. Taken to the extreme limit, collisions can be neglected entirely to describe the evolution of the distribution function by the standard Vlasov equation,

$$\frac{\partial\widetilde{f}_e}{\partial t} + ikv_x\widetilde{f}_e + \frac{e\widetilde{E}_x}{k_B T_0} v_x f_e^{(mb)} = 0. \tag{4.4.1}$$

As there is no explicit dependence on velocities perpendicular to the temperature gradient, it is convenient to integrate over these as well as dividing by the electron density, resulting in

$$\frac{\partial \widetilde{g}}{\partial t} + ikv_x\widetilde{g} - \frac{ike\widetilde{\phi}}{k_\mathrm{B}T_0}\frac{v_x \mathrm{e}^{-m_\mathrm{e}v_x^2/2k_\mathrm{B}T_0}}{\sqrt{2\pi k_\mathrm{B}T_0/m_\mathrm{e}}} = 0, \tag{4.4.2}$$

$$\text{where } \widetilde{g} = \int_{-\infty}^{\infty}\int_{-\infty}^{\infty}\frac{\widetilde{f_\mathrm{e}}}{n_\mathrm{e}}\,\mathrm{d}v_y\,\mathrm{d}v_z, \text{ and } \widetilde{\phi} = \frac{\widetilde{E}}{-ik} \text{ is the electric potential.} \tag{4.4.3}$$

The long-term behaviour of $\widetilde{g}$ is best analysed with the use of a Laplace transform on the time coordinate:

$$(p + ikv_x)\widetilde{g}' - \frac{ike\widetilde{\phi}'}{k_\mathrm{B}T_0}\frac{v_x \mathrm{e}^{-m_\mathrm{e}v_x^2/2k_\mathrm{B}T_0}}{\sqrt{2\pi k_\mathrm{B}T_0/m_\mathrm{e}}} = \widetilde{g}(t=0), \tag{4.4.4}$$

$$\text{where } \widetilde{g}'(p) = \int_0^\infty \widetilde{g}(t)\mathrm{e}^{-pt}\,\mathrm{d}t, \text{ and } \widetilde{\phi}'(p) = \int_0^\infty \widetilde{\phi}(t)\mathrm{e}^{-pt}\,\mathrm{d}t \tag{4.4.5}$$

When deriving the Landau damping of Langmuir waves the standard approach is to relate the electric potential to the distribution function through Gauss' Law (Boyd and Sanderson 2003, pp. 256–258, eq. 7.25), yielding

$$\frac{e\widetilde{\phi}'}{k_\mathrm{B}T_0} = \frac{-1}{k^2\lambda_\mathrm{D}^2 + R\left(\frac{ip}{kv_{2\mathrm{T}}}\right)}\int_{-\infty}^{\infty}\frac{\widetilde{g}(t=0)}{p+ikv_x}\,\mathrm{d}v_x, \tag{4.4.6}$$

$$\text{where } R(\zeta) = \frac{1}{\sqrt{\pi}}\int_{-\infty}^{\infty}\frac{t\mathrm{e}^{-t^2}}{t-\zeta}\,\mathrm{d}t = 1 + \frac{\zeta}{\sqrt{\pi}}\int_{-\infty}^{\infty}\frac{\mathrm{e}^{-t^2}}{t-\zeta}\,\mathrm{d}t \tag{4.4.7}$$

$$= 1 + \sqrt{\pi}\zeta\mathrm{e}^{-\zeta^2}(i - \mathrm{Erfi}(\zeta)) \tag{4.4.8}$$

is the normalised response function given by Hammett and Perkins (1990), $\lambda_\mathrm{D} = v_{1\mathrm{T}}/\omega_\mathrm{pe}$ is the (electron) Debye length and $\mathrm{Erfi}(\zeta) = -i\,\mathrm{Erf}(i\zeta)$ is the imaginary error function. This is calculated by assuming that the imaginary part of ζ is greater than 0 (corresponding to the $\mathrm{Re}(p) > 0$ required by the inverse Laplace transform) and then analytically continuing to the negative imaginary half-plane. The asymptotic behaviour of the electric potential at large times can then be analysed by considering the residues of its Laplace transform

$$\widetilde{\phi}(t) = \sum_j \lim_{p\to p_j}(p-p_j)\widetilde{\phi}'\mathrm{e}^{p_j t}, \tag{4.4.9}$$

where p_j represents the poles of $\widetilde{\phi}'$. More precisely, these poles occur at the zeroes of the denominator $k^2\lambda_\mathrm{D}^2 + R$, and appear symmetrically about the real

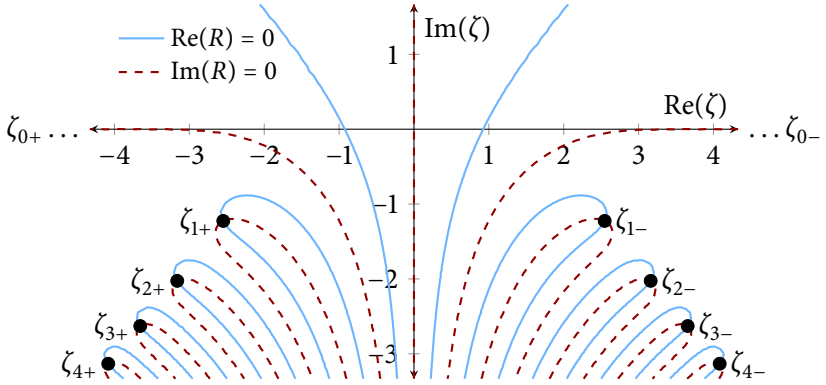

FIGURE 4.15: Zeroes of the response function.

p-axis with a strictly negative imaginary part. In the collisionless yet quasineutral regime that we are interested in (characterised by $k\lambda_D \ll 1 \ll k\lambda_{ei}^{(B)}$) these can be found numerically (or analytically for the case of $p_{0\pm}$):

$$p_{0\pm} = \left(-\sqrt{\tfrac{\pi}{8}} \tfrac{1}{k^3 {\lambda_D}^3} e^{-1/2k^2{\lambda_D}^2} \pm i \right) \omega_{pe}, \tag{4.4.10}$$

$$p_{1\pm} = (-1.22516 \pm 2.54723i) k v_{2T}, \tag{4.4.11}$$

$$p_{2\pm} = (-2.02560 \pm 3.16194i) k v_{2T}, \tag{4.4.12}$$

$$p_{3\pm} = (-2.62887 \pm 3.65597i) k v_{2T}, \tag{4.4.13}$$

$$p_{4\pm} = (-3.13235 \pm 4.08338i) k v_{2T}, \tag{4.4.14}$$

to lowest order in $k\lambda_D$. These can be related to the zeroes of the response function $R(\zeta)$ itself by $\zeta_j = ip_j/kv_{2T}$, which are illustrate in fig. 4.15.

In order to determine the evolution of the temperature perturbation we need to take moments of the distribution function:

$$\frac{\widetilde{T}_e'}{T_0} = 2 \int_{-\infty}^{\infty} \left(\frac{v_x^2}{v_{2T}^2} - \frac{1}{2} \right) \widetilde{g}' \, dv_x \tag{4.4.15}$$

$$= -\left(1 + \frac{2p^2}{k^2 v_{2T}^2} \right) \int_{-\infty}^{\infty} \frac{\widetilde{g}(t=0)}{p + ikv_x} \, dv_x \tag{4.4.16}$$

$$+ \frac{e\widetilde{\phi}'}{k_B T_0} \left(1 - \left(1 + \frac{2p^2}{k^2 v_{2T}^2} \right) R\left(\frac{ip}{kv_{2T}} \right) \right) \tag{4.4.17}$$

$$= -\frac{k^2\lambda_D^2 + 1 + p^2/{\omega_{pe}}^2}{k^2\lambda_D^2 + R\left(\frac{ip}{kv_{2T}}\right)} \int_{-\infty}^{\infty} \frac{\widetilde{g}(t=0)}{p + ikv_x} \, dv_x, \tag{4.4.18}$$

where we have asserted that $\widetilde{f}_e(t = 0)$ has no density or current contribution. The additional terms in the numerator reduce the contribution of the two simple

poles corresponding to weakly damped Langmuir waves by a factor of $\sim k^2 {\lambda_\mathrm{D}}^2$, which essentially removes them in the quasineutral regime we are considering. Therefore, the temperature perturbation is found to die out much quicker than the electric field, and its long-term behaviour is dominated by the two poles next closest to the imaginary p-axis: $p_{1\pm}$. The normalised damping rate (denoted as $\chi_1 = \gamma_\mathrm{D}/k v_{2\mathrm{T}}$) is therefore calculated to be 1.22516 in the collisionless regime, which is a factor $4.91204 \xi k \lambda_\mathrm{ei}^{(0)}$ less than predicted by a local approximation, cf. eq. (4.2.2). Both the imaginary part of the heat flow and the real part of the thermal conductivity are reduced by the same factor meaning that in the collisionless regime they asymptotically approach

$$\mathrm{Im}[\widetilde{Q}_x(k\lambda_\mathrm{ei}^{(\mathrm{B})} \to \infty)] = -\tfrac{3}{2} \chi_1 n_\mathrm{e} v_{2\mathrm{T}} k_\mathrm{B} \widetilde{T}_\mathrm{e}, \tag{4.4.19}$$

$$\mathrm{Re}[\kappa_\parallel(k\lambda_\mathrm{ei}^{(\mathrm{B})} \to \infty)] = \tfrac{3}{2} \chi_1 n_\mathrm{e} v_{2\mathrm{T}} k_\mathrm{B}/k, \tag{4.4.20}$$

respectively, where the extra factor of $\frac{3}{2}$ is included to take into account the difference between the isotropic definition of temperature used here and the anisotropic one used by Hammett and Perkins (1990). Note that the heat flow approaches a constant value while the thermal conductivity decreases with the wavelength of the temperature perturbation.

Our numerically calculated damping rate is slightly (8%) greater than that found by Hammett and Perkins (1990), $2/\sqrt{\pi} = 1.12838$, with a three-pole approximation for the response function. However, Hammett and Perkins' approximation concludes that the corresponding zero lies directly on the real line and thus fails to capture the oscillatory aspect of the temperature evolution present at such low collisionalities.

As for the thermoelectric coefficient, $\beta_\parallel$, this is calculated to be identically zero in the purely collisionless limit and its true asymptotic behaviour can only be understood by introducing some form of weak collisionality.

4.4.1 *Performance of the EIC in the collisionless regime*

While the majority of the simplifications made by the EIC nonlocal model are justified in the linearised regime, the 'quasistationary' assumption that the perturbation to the distribution function $\delta\widetilde{f}_\mathrm{e}$ does not depend on time is not. It is therefore important to understand how this assumption affects the predicted damping rate of our temperature sinusoids. In the collisionless limit, an exact

expression for $\delta\widetilde{f}_\mathrm{e}$ under the quasistationary assumption can be obtained from the DKE:

$$ik v_x \delta\widetilde{f}_\mathrm{e} = -\frac{e\widetilde{E}_x}{k_\mathrm{B}T_0} v_x f_\mathrm{e}^{(\mathrm{mb})} - ikv_x \widetilde{f}_\mathrm{e}^{(\mathrm{mb})} - \frac{\partial \widetilde{f}_\mathrm{e}^{(\mathrm{mb})}}{\partial t} \tag{4.4.21}$$

$$= -\left(\frac{e\widetilde{E}_x}{k_\mathrm{B}T_0} v_x + ik\left(v_x \frac{\widetilde{T}_\mathrm{e}}{T_0} - \frac{2\widetilde{Q}_x}{3n_\mathrm{e}k_\mathrm{B}T_0}\right)\left(\frac{m_\mathrm{e}v^2}{2k_\mathrm{B}T_0} - \frac{3}{2}\right)\right) f_\mathrm{e}^{(\mathrm{mb})}, \tag{4.4.22}$$

We can eliminate $\delta\widetilde{f}_\mathrm{e}$ by recalling that it does not contribute to the temperature moment and consequently calculate the heat flow.

$$\int \left(\tfrac{1}{2} m_\mathrm{e} v^2 - \tfrac{3}{2} k_\mathrm{B} T_0\right) \delta\widetilde{f}_\mathrm{e} \, \mathrm{d}^3\vec{v} = 0 \tag{4.4.23}$$

$$\implies 0 = -\frac{3}{2} n_\mathrm{e} k_\mathrm{B} \widetilde{T}_\mathrm{e} + \frac{2}{3}\widetilde{Q}_x \int \left(\frac{v^2}{v_{2\mathrm{T}}^2} - \frac{3}{2}\right)^2 \frac{\mathrm{e}^{-v^2/v_{2\mathrm{T}}^2}}{v_x \pi^{3/2}} \frac{\mathrm{d}^3\vec{v}}{v_{2\mathrm{T}}^3} \tag{4.4.24}$$

However, the last integral is ill-defined due to the choice of method to integrate (around) the pole at $v_x = 0$. We choose to follow the standard Landau approach of taking πi times the residue at $v_x = 0$. After changing variable to $V_x = v_x/v_{2\mathrm{T}}$, $V_\perp^2 = v_y^2 + v_z^2/v_{2\mathrm{T}}$, $\theta = \arctan2(v_z, v_y)$ and applying orthogonality we obtain

$$\int \frac{(V^2 - \tfrac{3}{2})^2}{V_x} \frac{\mathrm{e}^{-V^2}}{\pi^{3/2}} \mathrm{d}^3\vec{V} = \int_{-\infty}^{\infty} \frac{\mathrm{e}^{-V_x^2}}{V_x\sqrt{\pi}} \mathrm{d}V_x \int_0^{\infty} (V_\perp^2 - 1)^2 \mathrm{e}^{-V_\perp^2} \mathrm{d}V_\perp^2 + \int_{-\infty}^{\infty} \frac{(V_x^2 - \tfrac{1}{2})^2}{V_x} \frac{\mathrm{e}^{-V_x^2}}{\sqrt{\pi}} \mathrm{d}V_x \int_0^{\infty} \mathrm{e}^{-V_\perp^2} \mathrm{d}V_\perp^2 \tag{4.4.25}$$

$$= \frac{5\sqrt{\pi} i}{4} \tag{4.4.26}$$

$$\implies \widetilde{Q}_x = -\frac{9i}{5\sqrt{\pi}} n_\mathrm{e} v_{2\mathrm{T}} k_\mathrm{B} \widetilde{T}_\mathrm{e}, \; \chi_1^{(\mathrm{EIC})} = \frac{1.2}{\sqrt{\pi}}, \tag{4.4.27}$$

which is equal to the Chang and Callen (1992) value cited in the original paper by Ji, Held and Sovinec (2009). Note that this is smaller in magnitude than the standard Hammett-Perkins (1990) value $\left(\chi_1^{(\mathrm{HP})} = \frac{2}{\sqrt{\pi}}\right)$ previously derived without the quasistationary assumption (above) by 40% and also does not include predict any oscillatory behaviour for the temperature perturbation.

The electric field can be calculated in a similar fashion; by instead taking the density moment. The result of this is

$$e\widetilde{E}_x = -\frac{9}{5\sqrt{\pi}} ik k_\mathrm{B} \widetilde{T}_\mathrm{e} \implies \beta_\parallel = \frac{4}{5\sqrt{\pi}}, \tag{4.4.28}$$

which does *not* agree with the correct value of zero derived earlier. This can be thought of as the quasistationary assumption providing a limit below which the thermoelectric coefficient $\beta_\parallel$ can not fall. Fortunately, for most of the problems studied in this thesis an overestimate of $\beta_\parallel$ should not in and of itself affect any observable physics phenomena here such as the damping rates. Furthermore, the quasistationary approach employed by the EIC model ensures that the electron density does not change with time.

Consider now the appropriateness of the Hermite-Laguerre expansion in parallel and perpendicular velocities, which is thought to be more efficient in the collisionless limit than the Legendre-Laguerre expansion in speed and pitch angle. Indeed, only two Laguerre modes are needed to describe the dependence of $\delta\widetilde{f}_e$ on $v_\perp$. However, the Hermite basis is not found to be effective at capturing dependence on v_x, especially at the $v_x = 0$ singularity. In implementing the moment decomposition of the collisionless DKE the odd and even Hermite polynomials are found to decouple from each other completely, with the heat flow only contributing to the odd moments. This is in contradiction with our analysis above where the heat flow *does* contribute to the even density and temperature moments through the Landau treatment of the singularity, and is explained by the removal of these moments from the equation set solved by EIC. Therefore, the description of the distribution function by the EIC is incomplete and the actual value of the heat flow near the collisionless limit depends purely on the small contribution of collisions which recouples the odd and even moments and the method used to close the set of odd Hermite moments from above (usually setting to zero).

To illustrate the extent to which this lack of convergence affects the stability of the Hermite-Laguerre basis, the heat flow predicted by various moment combinations is compared to an accurate fit provided by Ji and Held (2014) in fig. 4.16 (see section 4.6.1 for more details). While maintaining a modest number of four Legendre moments (more than the two that should be needed in the collisionless limit), it is seen that doubling the number of Hermite modes from 40 to 80 leads to significant differences in the heat flow at a range of collisionalities except for a small window given by $400 < k\lambda_{ei}^{(B)} < 700$. However, a second doubling of Hermite modes from 80 to 160 makes very little difference to the predicted heat flow at all wavelengths shown despite the lack of agreement with the analytic fit and the kinks occurring at $k\lambda_{ei}^{(B)} > 1000$ suggesting that convergence has not yet been achieved. Indeed, if instead the number of Laguerre modes are increased from 4 to 20 while maintaining the number of Hermite modes at 80 there is again an appreciable effect on all heat flow values shown, supporting the conclusion

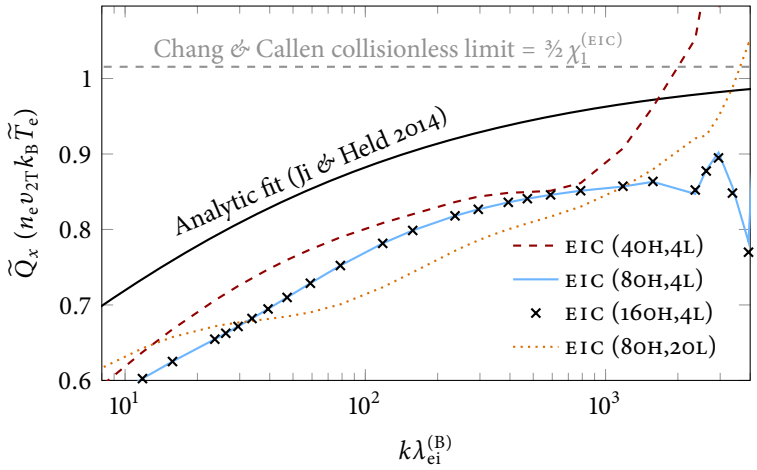

FIGURE 4.16: The slow convergence of the Hermite-Laguerre basis used by the EIC model to the Chang and Callen collisionless limit is shown by comparisons with an analytic fit provided by Ji and Held (2014).

that convergence relies on the recoupling of the odd and even Hermite modes through collisionality, which is only possible when sufficient Laguerre modes are employed. However, we shall see in the next chapter that it is sometimes possible for the Hermite-Laguerre basis to converge faster than the Legendre-Laguerre in regimes with intermediate collisionality and large temperature differences.

4.4.2 *Effect of P1 approximation*

Vlasov-Fokker-Planck codes that expand the EDF according to degrees of anisotropy (e.g. spherical harmonics or Cartesian tensors), such as IMPACT, SPARK, K2 and OSHUN, are not necessarily well suited to capture the fine-scale and highly anisotropic features that arise in the collisionless regime. Certainly, a mere P1 or MN would not be sufficient and would never be wisely chosen to accurately simulate problems of extremely high degrees of nonlocality. Nevertheless, it is an enlightening, albeit academic, exercise to consider the nature of the errors that would occur when employing such an early truncation of the Cartesian tensor expansion.

With electron inertia

The relevant equation to consider here is

$$p\widetilde{f}_0{}' + \frac{ikv}{3}\widetilde{f}_{1x}' = \widetilde{f}_0(t=0) \tag{4.4.29}$$

$$\text{EI}\,p\widetilde{f}_{1x}' + ikv\widetilde{f}_0{}' + \frac{e\widetilde{E}_x'}{k_\text{B}T_0}vf_\text{e}^{(\text{mb})} = \text{EI}\,\widetilde{f}_{1x}(t=0) - \nu_\text{ei}^*\widetilde{f}_{1x}' \tag{4.4.30}$$

where the boolean variable EI takes the value 1 if electron inertia is included in the code's equation set and 0 if it is neglected. While the electron-ion collision term has been retained as it is relatively easy to treat and additionally allows the equation set to still be solved when electron inertia is neglected, consideration of the effect of the electron-electron collision operator is left until the next section. If the EDF is assumed to be initially isotropic, i.e. $\widetilde{f}_{1x}(t=0)=0$, then a convenient rearrangement finds

$$p\widetilde{f}_0{}' + \frac{k^2v^2}{3}\frac{\widetilde{f}_0{}' - \frac{e\widetilde{\phi}'}{k_\text{B}T_0}f_\text{e}^{(\text{mb})}}{\text{EI}\,p + \nu_\text{ei}^*} = \widetilde{f}_0(t=0) \tag{4.4.31}$$

Gauss' law can be used to calculate the electric potential

$$\frac{e\widetilde{\phi}'}{k_\text{B}T_0} = -\frac{e^2\widetilde{n}_\text{e}'}{k^2\varepsilon_0 k_\text{B}T_0} \tag{4.4.32}$$

$$= -\frac{4\pi}{n_\text{e}k^2\lambda_\text{D}^2}\int_0^\infty \frac{(\text{EI}\,p+\nu_\text{ei}^*)v^2\widetilde{f}_0(t=0) + \frac{k^2v^4}{3}\frac{e\widetilde{\phi}'}{k_\text{B}T_0}f_\text{e}^{(\text{mb})}}{p(\text{EI}\,p+\nu_\text{ei}^*)+\frac{k^2v^2}{3}}\,\mathrm{d}v \tag{4.4.33}$$

$$= \frac{-4\pi}{k^2\lambda_\text{D}^2 + R_\text{P1}\left(\frac{ip}{kv_{2\text{T}}}\right)}\int_0^\infty \frac{(\text{EI}\,p+\nu_\text{ei}^*)\widetilde{f}_0(t=0)/n_\text{e}}{p(\text{EI}\,p+\nu_\text{ei}^*)+\frac{k^2v^2}{3}}\,\mathrm{d}v, \tag{4.4.34}$$

where the P1 response function

$$R_\text{P1}(\zeta) = \frac{4}{3\sqrt{\pi}}\int_0^\infty \frac{t^4\mathrm{e}^{-t^2}}{\frac{t^2}{3} - \zeta\left(\text{EI}\,\zeta + \frac{i}{t^3\xi k\lambda_\text{ei}^{(0)}}\right)}\,\mathrm{d}t \tag{4.4.35}$$

$$= 1 + 6\zeta^2 R(\sqrt{3}\zeta) \tag{4.4.36}$$

in terms of the original response function introduced in eqs. (4.4.7) and (4.4.8). In the collisionless limit electron inertia dominates over the electron-ion collisions

meaning that it is acceptable to neglect the latter. The zeroes of the denominator $k^2\lambda_D^2 + R$ in the absence of absence of electron-ion collisions are then given by

$$p_{0\pm} = \left(-3\sqrt{\tfrac{3\pi}{8}}\tfrac{1}{k^5{\lambda_D}^5}\mathrm{e}^{-3/2k^2{\lambda_D}^2} \pm i\right)\omega_{pe}, \tag{4.4.37}$$

$$p_1 = -0.26080kv_{2T}, \tag{4.4.38}$$

$$p_{2\pm} = (-1.12910 \pm 2.02122i)kv_{2T}, \tag{4.4.39}$$

$$p_{3\pm} = (-1.47146 \pm 2.29265i)kv_{2T}, \tag{4.4.40}$$

$$p_{4\pm} = (-1.75897 \pm 2.52866i)kv_{2T}, \tag{4.4.41}$$

showing that the P1 expansion leads a signicantly larger Landau damping decrement than is observed in the fully anisotropic limit for small values of $k\lambda_D$.

Without Electron Inertia

In the absence of electron inertia the differential equation describing the distribution function becomes simpler, but finding the asymptotic behaviour by means of a Laplace transform is less straightforward. The difficulty stems from the presence of fractional poles in $\widetilde{\phi}'(p)$ (the term in the denominator becomes $p\nu_{ei}^{(0)} + k^2v^5/v_{2T}^3$ which induces singularities at five points in the complex plain given by $v = \sqrt[5]{p\nu_{ei}^{(0)}glsv2T[^3]/k^2}$, only one of which is real), leading to an inverse power law decay of the temperature perturbation with time as opposed to an exponential one. Direct analytic treatment of this would require an in-depth understanding of generalised hypergeometric functions. Instead, we can use a more direct approach employing an integrating factor; starting from the Vlasov equation under the diffusive approximation we can rearrange to obtain

$$\frac{\partial}{\partial t}\left(\widetilde{f}_0\mathrm{e}^{k^2v^2t/3\nu_{ei}^*}\right) = \frac{k^2v^2}{3\nu_{ei}^*}\mathrm{e}^{k^2v^2t/3\nu_{ei}^*}\frac{e\widetilde{\phi}}{k_BT_0}f_e^{(mb)} \tag{4.4.42}$$

$$\implies \qquad \mathrm{e}^{V^5u}F(u) = F(u=0) + \frac{V^5\mathrm{e}^{-V^2}}{\pi^{3/2}}\int_0^u \mathrm{e}^{V^5u'}\frac{e\widetilde{\phi}(u')}{k_BT_0}\,\mathrm{d}u', \tag{4.4.43}$$

where we have substituted the dimensionless variables $u = \xi k^2\lambda_{ei}^{(0)}v_{2T}t/3$, $V = v/v_{2T}$, $F = v_{2T}^3\widetilde{f}_0/n_e$. In order to obtain the asymptotic behaviour of the electric potential we can make the ansatz that its asymptotic expansion at $u = \infty$ is given by $\frac{e\widetilde{\phi}}{k_BT_0} = \theta(t-1)\sum_{\{\alpha\}}\frac{c_\alpha}{u^\alpha} + \mathcal{O}(u^\gamma)$ where the Heaviside step function θ is used to avoid singularities at $t = 0$ when evaluating integrals, $\gamma > \max\{\alpha\}$, and the countable set of positive real numbers $\{\alpha\}$ is to be determined; while this ansatz may seem like putting the cart before the horse, it is not only backed

up by considering the Laplace transform of ϕ, but also with simulations using a purpose-built code DILL (see below). Pursuing this route we can calculate the contribution of each term in the asymptotic series to the indefinite integral in eq. (4.4.43) using integration by parts:

$$\mathrm{e}^{-V^5 u}\int_1^u \frac{\mathrm{e}^{V^5 u'}}{u^\alpha}\,\mathrm{d}u = \frac{1}{V^5 u^\alpha}\left(1+\frac{\alpha}{V^5 u}+\frac{\alpha(\alpha+1)}{V^{10}u^2}+\dots\right) \tag{4.4.44}$$

Note that the lower limit of integration was changed from 0 to 1 to account for the initial step function $\theta(t-1)$. Unfortunately, this series is divergent and more problematically introduces singularities in the distribution at $V = 0$. Consequently, we truncate the series after the first term and accept that this only enables calculation of c_α for values of α between $\min\{\alpha\}$ and $\min\{\alpha\}+1$. The density moment of the resulting expression for the distribution function can be substituted into Gauss' law:

$$\frac{e\widetilde{\phi}'}{k_\mathrm{B}T_0} = -\frac{e^2\widetilde{n}_\mathrm{e}'}{k^2\varepsilon_0 k_\mathrm{B}T_0} \tag{4.4.45}$$

$$\implies \sum_{\{\alpha\}}\frac{c_\alpha}{u^\alpha} = -\frac{4\pi}{k^2\lambda_\mathrm{D}^2}\int_0^\infty V^2\mathrm{e}^{-V^5 u}F(u=0)\,\mathrm{d}V \tag{4.4.46}$$

$$-\frac{4}{\sqrt{\pi}k^2\lambda_\mathrm{D}^2}\sum_{\{\alpha\}}\frac{c_\alpha}{u^\alpha}\int_0^\infty V^2\mathrm{e}^{-V^2}\,\mathrm{d}V + \mathcal{O}\left(u^{-\min\{\alpha\}-1}\right) \tag{4.4.47}$$

$$= -\frac{4\pi}{1+k^2\lambda_\mathrm{D}^2}\int_0^\infty V^2\mathrm{e}^{-V^5 u}F(u=0)\,\mathrm{d}V + \mathcal{O}\left(u^{-\min\{\alpha\}-1}\right). \tag{4.4.48}$$

All that is needed now is to calculate the asymptotic expansion of the final integral (this can be done using Watson's Lemma and is detailed in appendix B.7) and then equate coefficients. For an initial Maxwellian perturbation $F(u=0) = (V^2-\tfrac{3}{2})\mathrm{e}^{-V^2}\pi^{-3/2}\widetilde{T}_\mathrm{e}(u=0)/T_0$ we find

$$\frac{e\widetilde{\phi}'}{k_\mathrm{B}T_0} = \frac{1}{1+k^2\lambda_\mathrm{D}^2}\frac{4}{5\sqrt{\pi}}\left(\frac{3\Gamma[\frac{3}{5}]}{2u^{3/5}}+\sum_{m=1}^{4}\frac{(-1)^m}{m!}(m+\tfrac{3}{2})\frac{\Gamma\left[\frac{3+2m}{5}\right]}{u^{(3+2m)/5}}\right)\frac{\widetilde{T}_\mathrm{e}(u=0)}{T_0} + \mathcal{O}(u^{-8/5}). \tag{4.4.49}$$

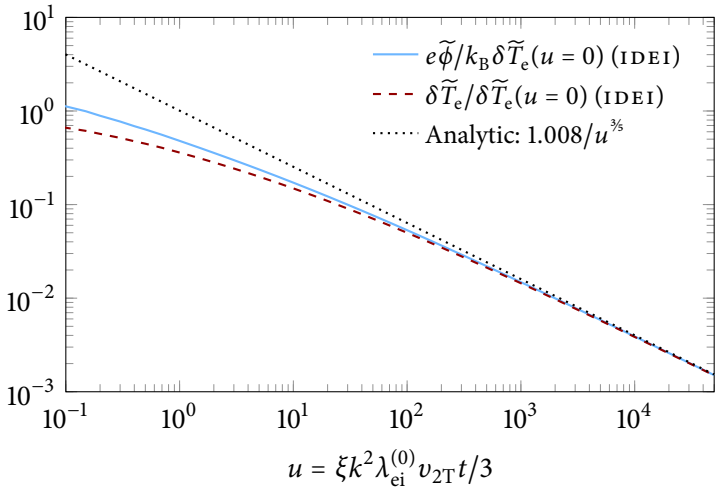

FIGURE 4.17: Simulated electric potential and temperature perturbation amplitudes predicted by the DILL code compared to the analytic asymptotic expansion for an initially Maxwellian perturbation $F = (V^2 - \tfrac{3}{2})e^{-V^2}\pi^{-3/2}\widetilde{T}_e(u=0)/T_0$. The coefficient $1.008 \approx 6\Gamma(\tfrac{5}{2})/5\sqrt{\pi}$.

Similarly, we can also calculate the evolution of the temperature perturbation

$$\widetilde{T}_e = \frac{8\pi}{3}\int_0^\infty V^2(V^2-\tfrac{3}{2})F\,\mathrm{d}V\ T_0 \tag{4.4.50}$$

$$= \frac{8}{3\sqrt{\pi}}\int_0^\infty V^2(V^2-\tfrac{3}{2})^2 e^{-V^2-V^5 u}\,\mathrm{d}V\ \widetilde{T}_e(u=0) + \mathcal{O}(u^{-8/5}) \tag{4.4.51}$$

$$= \frac{4}{5\sqrt{\pi}}\left(\frac{3\Gamma[\tfrac{3}{5}]}{2u^{3/5}} - \frac{7}{2u} + \dots \right.$$
$$\left. \dots \sum_{m=2}^{4}\frac{(-1)^m}{m!}(\tfrac{2}{3}m(m+1)+2m+\tfrac{3}{2})\frac{\Gamma\left[\frac{3+2m}{5}\right]}{u^{(3+2m)/5}}\right)\widetilde{T}_e(u=0)$$
$$+ \mathcal{O}(u^{-8/5}). \tag{4.4.52}$$

Thus, for an initially Maxwellian temperature perturbation both the normalised electric potential and temperature perturbation amplitude damp asymptotically at the same rate $1.008/u^{3/5}$. This is supported by simulations using the DILL code with the collision term neglected (i.e. $\zeta = 0$), which is purpose-built to test the diffusion approximation at very short-wavelengths (see section 3.1.4). The simulated electric potential and temperature perturbation amplitudes are compared to the derived expression in fig. 4.17; showing that this indeed describes the asymptotic behaviour.

For this simulation the DILL *code used Gauss' law to calculate the electric potential with a normalised Debye length of* $k\lambda_D = 0.04$*, and employed a 500 cell velocity grid extending to* $10v_{2T}$ *with a normalised timestep* $\Delta u = 0.01$.

Note that the slowest damping term depends purely on the initial distribution function. Specifically, if the lowest order term in polynomial in front of the

Gaussian term e^{-V^2} scales as V^n then the corresponding asymptotic would be proporional to $1/u^{(3+n)/5}$. Irrespective of the initial distribution function, we observe that this inverse power law behaviour means that both the damping rate $\gamma = -\frac{1}{\widetilde{T}_\mathrm{e}}\frac{\partial \widetilde{T}_\mathrm{e}}{\partial t}$ and the heat flow relative to the temperature amplitude $\widetilde{Q}_x/\widetilde{T}_\mathrm{e}$ decrease to zero over time as $1/u$, in contrast to the correct collisionless limit where these values approach constants respectively (with the damping rate being proportional to k).

In conclusion, we have shown that intrinsic to the diffusive approximation are *qualitative* implications on the behaviour of temperature sinusoids that make it inappropriate and unreliable in the purely collisionless limit. As we have shown that exponential damping still occurs both when electron inertia is retained under a P1 expansion and when it is neglected while accounting for higher degrees of anisotropy (as shown for the EIC model in section 4.4.1), it is therefore understood that only a *combination* of these assumptions results in the non-physical inverse power law damping derived here. Furthermore, we shall see in section 4.5.1 that even including the smallest amount of electron-electron collisions will also restore the expected exponential damping (with a consequent asymptotic dependence of the heat flow on the nonlocality parameter as $\widetilde{Q}_x \sim (k\lambda_\mathrm{ei}^{(\mathrm{B})})^{-1/5}$); this is due to diffusion in velocity space allowing the zero velocity electrons to respond to modifications of the distribution function.

4.4.3 *Behaviour of SNB model in the collisionless regime*

The absence of time derivatives in the SNB equation eq. (2.3.25) makes analysis of its behaviour in the collisionless regime a lot simpler. In this limit the collisional 'screening' term can be neglected rendering the equation as

$$\vec{\nabla}\cdot\frac{\lambda_\mathrm{ei}^{*(E)}}{3}\vec{\nabla}\delta f_0 = \frac{\vec{\nabla}\cdot\{f_1^{(\mathrm{mb})}, g_1^{(\mathrm{mb})}\}}{3}, \tag{4.4.53}$$

giving the nonlocal contribution to the heat flow as

$$\delta\widetilde{Q}_x = -\frac{2\pi m_\mathrm{e}}{3}\int_0^\infty v^5\{f_1^{(\mathrm{mb})}, g_1^{(\mathrm{mb})}\}\,\mathrm{d}v = -\widetilde{Q}^{(\mathrm{B})}. \tag{4.4.54}$$

Therefore the heat flow predicted by the SNB model in the truly collisionless limit is identically zero rather than a constant that is proportional to the amplitude of the temperature sinusoid. This can be thought of as stemming naturally from the diffusive approximation upon which the SNB model is based and can not be avoided in a physical way without either introducing terms with higher-order

anisotropies or taking into account electron inertia in some way. It turns out that as nonlocality increases the heat flow decreases as ~$1/k$ (similarly the thermal conductivity decreases proportional to $1/k^2$), this is in contradiction to claims made by Schurtz et al. (2000) that the nonlinear electric field modification to the electron-ion mfp corrects for this. The derivation of this is left until section 4.6.3.

4.5 REGIME OF COLLISIONLESS SUPRATHERMALS

The rate at which the heat flow approaches the wavelength-independent value derived in the previous section (eq. 4.4.19, eq. 4.4.27) with decreasing wavelength is remarkably slow; even at $k\lambda_{\mathrm{ei}}^{(\mathrm{B})} \approx 100$ the percentage difference predicted by the EIC model is still greater than 10%. A good approximation for the dependence of the absolute heat flow on the nonlocality parameter $k\lambda_{\mathrm{ei}}^{(\mathrm{B})}$ in the collisionless regime, suggested by Bychenkov et al. (1994), is given by

$$|\widetilde{Q}_x(k\lambda_{\mathrm{ei}}^{(\mathrm{B})} \to \infty)| = \tfrac{3}{2}\chi_1 n_{\mathrm{e}} v_{2\mathrm{T}} k_{\mathrm{B}} \widetilde{T}_{\mathrm{e}}(1 - c_\infty/(k\lambda_{\mathrm{ei}}^{(\mathrm{B})})^\eta), \tag{4.5.1}$$

where the parameters $\eta = \tfrac{3}{7}$, $c_\infty = 9\sqrt{Z^{1-\eta}/2\pi} \approx 3.6Z^{\frac{2}{7}}$ were calculated analytically for the Lorentz limit in a previous work by Maksimov and Silin (1993, 1994), while Bychenkov et al. found that substituting c_∞ with $c_1 = 1.8Z^{\frac{2}{7}}$ gave a better fit to SPRING simulations performed by Epperlein (1994).

The method used by Bychenkov et al. to derive the above expression involves retaining a purely differential approximation for the originally integro-differential linearised electron-electron collision operator $C_{\mathrm{ee0}}^{(\mathrm{L})}$ that is valid at low velocities

$$C_{\mathrm{ee0}}^{(\mathrm{L})}(\delta\widetilde{f}_0)/f_{\mathrm{e}}^{(\mathrm{mb})} \approx \frac{2}{3\sqrt{\pi}} \frac{\Gamma_{\mathrm{ee}}}{n_{\mathrm{e}} v_{2\mathrm{T}}} \frac{1}{v^2} \frac{\partial}{\partial v} v^2 \frac{\partial \widetilde{\psi}}{\partial v}, \tag{4.5.2}$$

where $\widetilde{\psi} = \widetilde{f}_0/f_{\mathrm{e}}^{(\mathrm{mb})}$. This is to take into account of the fact that $C_{\mathrm{ee0}}^{(\mathrm{L})}$ experiences a divergence at $v = 0$. Therefore, slow moving electrons will still experience appreciable collisions even at very low degrees of average collisionality where the faster suprathermal electrons are essentially collisionless. Additionally, Bychenkov et al. employed the diffusion approximation to simplify the analysis, but replaced the corrected electron-ion collision frequency ν_{ei}^* appearing in the $\vec{f}_1$ equation with $\nu_1^* = \nu_{\mathrm{ei}}^* H(kv/\nu_{\mathrm{ei}}^*)$, where $H(x) = \sqrt{1 + (\pi x/6)^2}$, to take into account the effect of higher order anisotropies. (The approach used by Maksimov and Silin (1993, 1994) is much more thorough but provides the same final result.) Consequently, the

equation solved by Bychenkov et al. in this regime where only the suprathermal electrons are considered collisionless is given by

$$\frac{\partial\widetilde{\psi}}{\partial t}+\frac{k^2v^2}{3\nu_1^*}\left(\widetilde{\psi}-\frac{e\widetilde{\phi}}{k_\mathrm{B}T_0}\right)=\frac{2}{3\sqrt{\pi}}\frac{n_\mathrm{e}\Gamma_{\mathrm{ee}}}{v_{2\mathrm{T}}}\frac{1}{v^2}\frac{\partial}{\partial v}v^2\frac{\partial\widetilde{\psi}}{\partial v}. \tag{4.5.3}$$

The characteristic velocity beyond which the collision term becomes negligible is given by $v_* = v_{2\mathrm{T}}(2/\sqrt{\pi}Z\xi k^2\lambda_{\mathrm{ei}}^{(0)2})^{1/7}$. Making the substitution $w = v/v_*$ and rearranging we obtain,

$$\frac{\partial}{\partial w}w^2\frac{\partial\widetilde{\psi}}{\partial w}-\frac{w^7}{H(kv/\nu_{\mathrm{ei}}^*)}\left(\widetilde{\psi}-\frac{e\widetilde{\phi}}{k_\mathrm{B}T_0}\right)=-\frac{3\sqrt{\pi}}{2}\frac{Z}{\nu_{\mathrm{ei}}^{(0)}}V_*^2w^2\frac{\partial\widetilde{\psi}}{\partial t}, \tag{4.5.4}$$

where $V_* = v_*/v_{2\mathrm{T}}$.

4.5.1 *Neglecting the anisotropic correction*

As the term approximating the collisions ($\frac{\partial}{\partial w}w^2\frac{\partial}{\partial w}$) only contributes at lower velocities, it is appropriate to first solve the second-order ODE neglecting the high-velocity anisotropic correction (i.e. assuming $H = 1$). Under this simplification the ODE can be converted into a modified Bessel equation of order ½, from which an expression for $\widetilde{\psi}' = \widetilde{\psi} - \frac{e\widetilde{\phi}}{k_\mathrm{B}T_0}$ can be obtained using a Green's function approach:

$$\begin{aligned}\widetilde{\psi}'(w)=\frac{3\sqrt{\pi}}{7\sqrt{w}}\frac{Z}{\nu_{\mathrm{ei}}^{(0)}}V_*^2\Bigg(&K_{1/2}^{(\mathrm{B})}(\tfrac{2}{7}w^{7/2})\int_0^w w'^{3/2}I_{1/2}^{(\mathrm{B})}(\tfrac{2}{7}w'^{7/2})\frac{\partial\widetilde{\psi}'}{\partial t}(w')\,\mathrm{d}w'\\&+I_{1/2}^{(\mathrm{B})}(\tfrac{2}{7}w^{7/2})\int_w^\infty w'^{3/2}K_{1/2}^{(\mathrm{B})}(\tfrac{2}{7}w'^{7/2})\frac{\partial\widetilde{\psi}'}{\partial t}(w')\,\mathrm{d}w'\Bigg).\end{aligned} \tag{4.5.5}$$

In order to obtain a more intuitive feel for the collisionless suprathermals without having to deal with integrals of Bessel functions (which had already been done by Maksimov and Silin), Bychenkov et al. used an approximate form for $\widetilde{\psi}'$ that has identical asymptotic behaviour in the low and high-velocity limits as that above. As Bychenkov et al. were focussing on ion-acoustic waves, they only considered a source term corresponding to an oscillating Maxwellian density perturbation

$$\frac{\partial\widetilde{\psi}'_N}{\partial t}=-i\omega\implies\widetilde{\psi}'_N\approx\frac{3\sqrt{\pi}}{2}\frac{i\omega Z}{\nu_{\mathrm{ei}}^{(0)}}V_*^2\frac{c_\psi}{1+c_\psi w^5}, \tag{4.5.6}$$

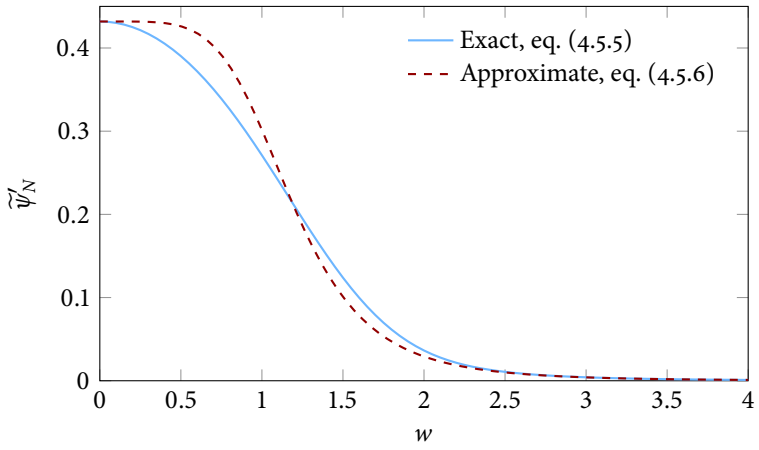

FIGURE 4.18: Comparison of Bychenkov et al.'s approximate expression for the EDF in the collisionless suprathermals given a Maxwellian density perturbation with assumed imaginary angular frequency $\omega = -2iv_{\mathrm{ei}}^{(0)}v_{2\mathrm{T}}^2/3\sqrt{\pi}Zv_x^2$, $\widetilde{\psi}'_N \approx c_\psi/(1 + c_\psi w^5)$ with the exact analytic solution given in terms of modified Bessel function form in eq. (4.5.5).

where $c_\psi = \Gamma(3/7)\Gamma(2/7)/7^{3/7}\Gamma(1/7)$ in terms of gamma functions or 0.432 numerically. The success of this approximation compared to the exact solution is shown in fig. 4.18.

However, we are instead interested in the decay of temperature perturbations and it is therefore more appropriate to use the form given by the EIC model's quasistationary assumption

$$\frac{\partial\widetilde{\psi}_T}{\partial t} = -\left(\frac{v^2}{v_{2\mathrm{T}}^2} - \frac{3}{2}\right)\frac{2ik\widetilde{Q}_x}{3n_\mathrm{e}k_\mathrm{B}T_0}. \tag{4.5.7}$$

For sufficiently small $v_* \ll v_{2\mathrm{T}}$ the quadratic term only contributes at higher velocities and therefore a similar approximation for

$$\widetilde{\psi}'_T \approx ikZ\lambda_{\mathrm{ei}}^{(0)}\frac{3\sqrt{\pi}}{2}\frac{c_\psi(w^2V_*^2 - 3/2)V_*^2}{1 + c_\psi w^5}\frac{2\widetilde{Q}_x}{3n_\mathrm{e}v_{2\mathrm{T}}k_\mathrm{B}T_0}, \tag{4.5.8}$$

turns out to be valid. The heat flow can be obtained by taking the temperature moment compared to the background

$$\frac{\widetilde{T}_\mathrm{e}}{T_0} = \frac{8\pi}{3n_\mathrm{e}}\int_0^\infty v^2(m_\mathrm{e}v^2/2k_\mathrm{B}T_0 - 3/2)\widetilde{\psi}'_T f_\mathrm{e}^{(\mathrm{mb})}\,\mathrm{d}v \tag{4.5.9}$$

$$= \frac{8V_*^3}{3\sqrt{\pi}}\int_0^\infty w^2(w^2V_*^2 - 3/2)\widetilde{\psi}'_T \mathrm{e}^{-w^2V_*^2}\,\mathrm{d}w \tag{4.5.10}$$

$$\approx 8/3\, ikZ\lambda_\mathrm{ei}^{(0)}V_*^5\int_0^\infty \frac{c_\psi(w^2V_*^2 - 3/2)^2w^2}{1+c_\psi w^5}\mathrm{e}^{-w^2V_*^2}\,\mathrm{d}w\frac{\widetilde{Q}_x}{n_\mathrm{e}v_{2\mathrm{T}}k_\mathrm{B}T_0}. \tag{4.5.11}$$

In order to evaluate the behaviour of the heat flow as the collisionless regime is approached, the asymptotic behaviour of the above expression for small V_* must be computed. Unfortunately, naïvely Taylor expanding $\mathrm{e}^{-w^2V_*^2} = 1 - w^2V_*^2\ldots$ and evaluating each integral in turn does not reveal the exact nature of the infinities that occur. A more careful analysis using the Mellin transform and Oosthuizen's (Oosthuizen 2011) converse mapping theorem presented in appendix B.8 reveals that the asymptotic behaviour of the integrals of concern at $V_* = 0$ is given by

$$\int_0^\infty \frac{w^2}{1+c_\psi w^5}\mathrm{e}^{-w^2V_*^2}\,\mathrm{d}w = \frac{\pi}{5c_\psi^{3/5}\sin(3\pi/5)} + \mathcal{O}(V_*^2\log(V_*)), \tag{4.5.12}$$

$$\int_0^\infty \frac{w^4}{1+c_\psi w^5}\mathrm{e}^{-w^2V_*^2}\,\mathrm{d}w = \frac{1}{c_\psi}\big(-\log(V_*) - \gamma_\mathrm{E}/2\big) + \mathcal{O}(V_*^2), \tag{4.5.13}$$

$$\text{and}\quad \int_0^\infty \frac{w^6}{1+c_\psi w^5}\mathrm{e}^{-w^2V_*^2}\,\mathrm{d}w = \frac{1}{c_\psi^{7/5}}\Big(-\frac{1}{2V_*^2} - \frac{\pi}{5\sin(7\pi/5)}\Big) + \mathcal{O}(V_*^2). \tag{4.5.14}$$

This confirms that only the first integral is necessary in determining the asymptotic behaviour in the short-wavelength limit giving

$$\frac{\widetilde{T}_\mathrm{e}}{T_0} \approx \frac{6\pi}{5}c_\psi^{2/5}\,\mathrm{cosec}(3\pi/5)ikZ\lambda_\mathrm{ei}^{(0)}V_*^5\frac{\widetilde{Q}_x}{n_\mathrm{e}v_{2\mathrm{T}}k_\mathrm{B}T_0} + \mathcal{O}(V_*^7\log(V_*)) \tag{4.5.15}$$

$$\approx 2.83ikZ\lambda_\mathrm{ei}^{(0)}V_*^5\frac{\widetilde{Q}_x}{n_\mathrm{e}v_{2\mathrm{T}}k_\mathrm{B}T_0} + \mathcal{O}(V_*^7\log(V_*)) \tag{4.5.16}$$

Substituting V_* with its definition and rearranging obtains the heat flow and thermal conductivity to be

$$\widetilde{Q}_x \approx -0.324\frac{i\xi^{5/7}k^{3/7}\lambda_\mathrm{ei}^{(0)3/7}}{Z^{3/7}}n_\mathrm{e}v_{2\mathrm{T}}k_\mathrm{B}\widetilde{T}_\mathrm{e},\ \kappa_\parallel \approx 0.324\frac{\xi^{5/7}\lambda_\mathrm{ei}^{(0)3/7}}{Z^{3/7}k^{4/7}}n_\mathrm{e}v_{2\mathrm{T}}k_\mathrm{B}. \tag{4.5.17}$$

Before better accounting for higher-order anisotropies let us first compare this analysis with corresponding results produced by the EIC model using only 2

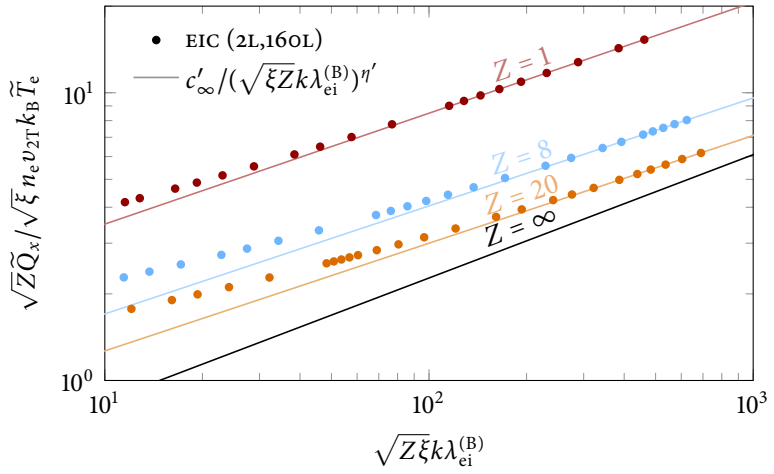

FIGURE 4.19: Under the quasistationary assumption and diffusion approximation the heat flow increases unboundedly at high degrees of nonlocality as a power law; best fit coefficients for the asymptotic behaviour observed when using 2L,160L EIC moments are given in table 4.6.

TABLE 4.6: *Coefficients describing the asymptotic short-wavelength behaviour of the heat flow under the quasistationary assumption when only two Legendre moments are used to describe the* EDF. *Results with finite Z were obtained with the* EIC *code using 2L,160L moments, while those in the Lorentz limit were derived analytically.*

Z	η'	c'_∞
1	0.385	1.439
8	0.375	0.718
20	0.374	0.535
∞	0.429	0.316

Legendre moments (i.e. P1). Figure 4.19 shows that the EIC heat flow takes on a power law behaviour at very high degrees of nonlocality ($\sqrt{\xi Z}k\lambda_{ei}^{(B)} > 100$) for ionisations of $Z = 1, 8, 20$ with an index that is not too far below the predicted $3/7$. For sake of comparison with the above equation modified fitting coefficients (denoted by a prime, and given in table 4.6) have been defined to describe this asymptotic behaviour;

$$\sqrt{Z/\xi}\widetilde{Q}_x = c'_\infty(\sqrt{\xi Z k\lambda_{ei}^{(B)}})^\eta n_e v_{2T} k_B \widetilde{T}_e. \tag{4.5.18}$$

The observed similarity between the EIC results and eq. (4.5.17) adds confidence in the validity of our analysis even at low ionisations where the effect of electron-electron collisions on the anisotropic part of the EDF is not significantly overpowered by electron-ion collisions.

It may seem surprising that the current analysis predicts that the heat flow grows unboundedly with decreasing wavelength, contradicting earlier findings presented in section 4.4.2 that the heat flow in the purely collisionless regime under the diffusive approximation should be zero. The source of this contradiction is the quasistationary assumption made here; at high degrees of nonlocality the time-derivative term $\frac{\partial\widetilde{\psi}}{\partial t}$ will look very different to that assumed by the EIC model.

To better understand the effect of low-velocity electron-electron collisions while properly including the time-derivative in the diffusion approximation,

simplified electron-electron collisions were incorporated in the DILL code (see section 3.1.4 for more details). This revealed that, while nonstationarity plays a negligible role for low and intermediate values of $k\lambda_{\mathrm{ei}}^{(\mathrm{B})}$, it becomes increasingly important at shorter wavelengths leading to an asymptotic damping rate of $\gamma_{\mathrm{D}} \sim \frac{4}{5}$.

4.5.2 *Effect of the anisotropic correction*

We can go a step further and properly include the effects of higher-order anisotropies, which are crucial in the collisionless limit, by reintroducing the correction H. The relationship between the temperature perturbation and the heat flow can be split up into two integrals the diffusive part studied above and the anisotropic correction.

$$\frac{\widetilde{T}_{\mathrm{e}}}{T_0} \approx \frac{8}{3} V_*^5 \int_0^\infty \frac{H(k\lambda_{\mathrm{ei}}^*)(w^2 V_*^2 - \frac{3}{2})^2 w^2}{1/c_\psi + w^5} \mathrm{e}^{-w^2 V_*^2} \,\mathrm{d}w \frac{iZk\lambda_{\mathrm{ei}}^{(0)} \widetilde{Q}_x}{n_{\mathrm{e}} v_{2\mathrm{T}} k_{\mathrm{B}} T_0} \tag{4.5.19}$$

$$\begin{aligned} &\approx \frac{8}{3} V_*^5 \Bigg(\int_0^\infty \frac{\left(\sqrt{1 + (\pi\xi k\lambda_{\mathrm{ei}}^{(0)} w^4 V_*^4/6)^2} - 1\right)(w^2 V_*^2 - \frac{3}{2})^2}{w^3} \mathrm{e}^{-w^2 V_*^2} \,\mathrm{d}w \\ &\qquad + \int_0^\infty \frac{c_\psi (w^2 V_*^2 - \frac{3}{2})^2 w^2}{1 + c_\psi w^5} \mathrm{e}^{-w^2 V_*^2} \,\mathrm{d}w \Bigg) \frac{iZk\lambda_{\mathrm{ei}}^{(0)} \widetilde{Q}_x}{n_{\mathrm{e}} v_{2\mathrm{T}} k_{\mathrm{B}} T_0}. \end{aligned} \tag{4.5.20}$$

The first term in the asymptotic expansion as $k\lambda_{\mathrm{ei}}^{(0)} \to \infty$ arising from the new integral can be quite simply calculated by taking the high-velocity limit for the square root and turns out to be proportional to $(k\lambda_{\mathrm{ei}}^{(0)})^{\frac{3}{5}}$. The subsequent terms are slightly more complicated to derive (again requiring a Mellin transform approach) but, fortunately, these all decrease with $k\lambda_{\mathrm{ei}}^{(0)}$ rather than increase or stay constant, and can therefore be neglected when only interested in the first two terms.

$$\therefore \frac{\widetilde{T}_{\mathrm{e}}}{T_0} \approx \left(\frac{5\pi}{18} \xi k\lambda_{\mathrm{ei}}^{(0)} V_*^7 + 2.83 V_*^5\right) \frac{iZk\lambda_{\mathrm{ei}}^{(0)} \widetilde{Q}_x}{n_{\mathrm{e}} v_{2\mathrm{T}} k_{\mathrm{B}} T_0} \tag{4.5.21}$$

$$\implies \widetilde{Q}_x \approx \frac{-\frac{3}{2} i \chi_1^{(\mathrm{EIC})} n_{\mathrm{e}} m_{\mathrm{e}} v_{2\mathrm{T}} k_{\mathrm{B}} \widetilde{T}_{\mathrm{e}}}{1 + 3.05 Z^{\frac{2}{5}}/\xi^{\frac{5}{5}} k^{\frac{3}{5}} \lambda_{\mathrm{ei}}^{(0)\frac{3}{5}}}. \tag{4.5.22}$$

The factor 3.05 appearing in the final expression above turns out to be between the analytic 3.6 and SPRING-fitted 1.8 given by Bychenkov et al. in eq. 13 of their 1994 paper.

4.5.3 *Comparison to VFP*

To explore the accuracy of this analysis, particularly at lower ionisations, we can compare with VFP simulations . While, it was not possible to obtain meaningful results at such low collisionalities with KIPP or IMPACT due to the oscillatory behaviour (intrinsic to this system due to the increasing role of electron inertia at low collisionalities) obscuring the analysis of the damping rate, Epperlein's SPRING results conveniently provided by Bychenkov et al. are fortunately valid at very short wavelength as the code can distinguish between real and imaginary contributions to the heat flow. However, note that the SPRING thermal conductivity reduction given in the paper are absolute values, while we have mostly focussed on the real part. Furthermore, the EIC model was used as an additional comparison using at least 40,40 Legendre-Laguerre moment due to the slow convergence of the Hermite-Laguerre basis explained in section 4.4.1.

Values for η and c_∞ were obtained by plotting the relative difference between the actual heat flow and that predicted in the purely collisionless limit ($-\frac{3}{2} i \chi_1^{\text{EIC}} n_e v_{2T} k_B \widetilde{T}_e$ for the EIC model) against nonlocality parameter $k\lambda_{ei}^{(B)}$ on a log-log axis and fitting a straight line (shown in fig. 4.20). The alternative coefficient c_1 used to reduce errors when fitting over a wide range of collisionalities was obtained using nonlinear fitting. All coefficents calculated are summarised in table 4.7 for $Z = 1, 2, 4, 6, 8$ (achieving convergence at high degrees of nonlocality with EIC at higher ionisations than $Z = 8$ requires a prohibitive number of moments). Both the index η and the coefficient c_∞ were found to vary weakly with Z and have similar orders of magnitude to those predicted by Bychenkov et al. However, the value of η obtained from EIC data does not seem to be approaching the value, $\frac{3}{7}$, predicted by Bychenkov et al. with increasing Z but rather something less than half this value. There are two possible reasons for this; (1) we have not performed the fitting process in the correct range but need to go to lower collisionalities that are beyond the region of convergence for the number of moments used, or (2) the anisotropic correction H is not sufficient in accounting for all higher-order anisotropic effects. The limited numerical results available from the assumingly exact SPRING code infer a value for η at $Z = 1, 8$ within 0.5–1% of the EIC prediction, but the values for c_∞ are about twice as big.

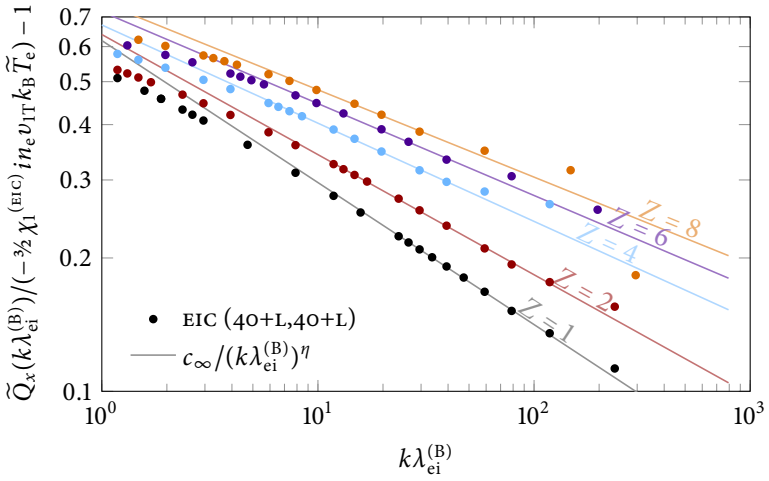

FIGURE 4.20: At high degrees of nonlocality the percentage difference between the EIC heat flow and its value in the collisionless limit, $\widetilde{Q}_x(k\lambda_{ei}^{(B)} \to \infty) = -3\!/\!2\,\chi_1{}^{(EIC)} i n_e v_{1T} k_B \widetilde{T}_e$, can be well approximated by a power-law dependence on $k\lambda_{ei}^{(B)}$. All EIC values were obtained using at least 40 Legendre and 40 Laguerre modes.

TABLE 4.7: Values for coefficients appearing in equations eq. (4.5.1) and eq. (4.6.6) obtained with EIC model (using at least 40,40 Legendre-Laguerre moments) and available SPRING data provided in Bychenkov et al. 1994 (in parentheses), the latter is presumed to be more accurate.

Z	η	c_∞	c_1
1	0.32(0.32)	0.62(1.4)	0.83(1.5)
2	0.27	0.64	1.0
4	0.22	0.67	1.3
6	0.21	0.72	1.5
8	0.20(0.20)	0.75(0.92)	1.7(2.8)

4.6 MODEL COMPARISON AT ARBITRARY COLLISIONALITY

4.6.1 *Optimal fitting functions*

So far, we have derived and quantified the wavelength dependence of the thermal conductivity/heat flow and thermoelectric coefficient/electric field close to the local limit to be

$$\frac{\widetilde{Q}_x(k\lambda_{\mathrm{ei}}^{(\mathrm{B})}\to 0)}{\widetilde{Q}_x^{(\mathrm{B})}} = \frac{\kappa_\parallel(k\lambda_{\mathrm{ei}}^{(\mathrm{B})}\to 0)}{\kappa_\parallel^{(\mathrm{B})}} = 1 - b_Q(Z)Zk^2\lambda_{\mathrm{ei}}^{(\mathrm{B})2}, \tag{4.6.1}$$

$$\text{and } \frac{\widetilde{E}_x(k\lambda_{\mathrm{ei}}^{(\mathrm{B})}\to 0)}{\widetilde{E}_x^{(\mathrm{B})}} = \frac{\beta_\parallel(k\lambda_{\mathrm{ei}}^{(\mathrm{B})}\to 0)}{\beta_\parallel{}^{(\mathrm{B})}} = 1 - b_E(Z)Zk^2\lambda_{\mathrm{ei}}^{(\mathrm{B})2}, \tag{4.6.2}$$

while in the collisionless limit the heat flow was shown to vary as

$$|\widetilde{Q}_x(k\lambda_{\mathrm{ei}}^{(\mathrm{B})}\to\infty)| = \tfrac{3}{2}\chi_1 n_{\mathrm{e}} v_{2\mathrm{T}} k_{\mathrm{B}} \widetilde{T}_{\mathrm{e}}(1 - c_\infty/(k\lambda_{\mathrm{ei}}^{(\mathrm{B})})^\eta), \tag{4.6.3}$$

Once again, it was the unfortunate absence of values for the thermoelectric coefficient from the SPRING and EIC codes that restricted the study of the electric field at very short wavelengths. Additionally, the contributions of various different terms such as those related to electron inertia and higher-order anisotropies have also been analysed.

One analytic fit designed to combine these two limits suggested by Bychenkov et al. (1994 eq. 14, 1995 eq. 57), is given by

$$\frac{\kappa_\parallel^{(\mathrm{Bychenkov})}}{\kappa_\parallel^{(\mathrm{B})}} = \left(ak\lambda_{\mathrm{ei}}^{(\mathrm{B})} + \frac{1 + b_Q Zk^2\lambda_{\mathrm{ei}}^{(\mathrm{B})2}}{1 + b_Q Zk^2\lambda_{\mathrm{ei}}^{(\mathrm{B})2}/ac_1(k\lambda_{\mathrm{ei}}^{(\mathrm{B})})^{1-\eta}}\right)^{-1}, \tag{4.6.4}$$

where Bychenkov et al. suggested $c_1 = 2.1Z^{2/5}\xi^{4/5}$ and we have incorporated the convenient contraction $a = \kappa_{\parallel c}^{(\mathrm{B})}/(\tfrac{3}{2}\sqrt{2}\chi_1)$. While reproducing the correct behaviour in the asymptotic limit this expression unfortunately does not follow the correct dependence on the nonlocality parameter in the semicollisional regime and instead gives

$$\frac{\kappa_\parallel{}^{(\mathrm{Bychenkov})}(k\lambda_{\mathrm{ei}}^{(\mathrm{B})}\to 0)}{\kappa_\parallel^{(\mathrm{B})}} = 1 - ak\lambda_{\mathrm{ei}}^{(\mathrm{B})} + \frac{b_Q Z}{ac_1}k^{2-\eta}\lambda_{\mathrm{ei}}^{(\mathrm{B})2-\eta} - (b_Q Z - a^2)k^2\lambda_{\mathrm{ei}}^{(\mathrm{B})2}\ldots \tag{4.6.5}$$

It was therefore desirable to come up with an alternative interpolation between the collisional and collisionless regimes that guarantees correct asymptotic behaviour. One such possibility is

$$\frac{\kappa_{\parallel}^{(\mathrm{Brodrick})}}{\kappa_{\parallel}^{(\mathrm{B})}} = \left(1 + \left(\frac{1}{b_Q Z k^2 \lambda_{\mathrm{ei}}^{(\mathrm{B})2}} + \frac{1}{ak\lambda_{\mathrm{ei}}^{(\mathrm{B})}(1 + c_1(k\lambda_{\mathrm{ei}}^{(\mathrm{B})})^{-\eta})}\right)^{-1}\right)^{-1}, \tag{4.6.6}$$

using the values of c_1 given in table 4.7, which were obtained by optimising the fit for $k\lambda_{\mathrm{ei}}^{(\mathrm{B})} < 1$. This additionally ensures that the relative thermal conductivity always falls below both unity and the purely collisionless limit, while always being above the expressions (4.6.1) and (4.6.2) given at the beginning of this section.

A different approach was suggested by Ji and Held (2014); this involved providing a closure for the thermal conductivity in configuration space

$$K_{hh}(s) = -(d + a\exp(-b|s|^c))\log(1 - \alpha\exp(-\beta|s|^\gamma)), \tag{4.6.7}$$

where $s(x) = \int_0^x \mathrm{d}x'/\sqrt{2}\lambda_{\mathrm{ei}}^{(\mathrm{B})}(x')$ is an integrated distance in mean free paths and the numerical coefficients $a, b, c, d, \alpha, \beta, \gamma$ for hydrogen ($Z = 1$) are given in Table I of Ji and Held 2014. The heat flow can then be found by a convolution

$$Q_x(x) = -\frac{v_{2\mathrm{T}} k_{\mathrm{B}} T_{\mathrm{e}}}{2} \int_{-\infty}^{\infty} K_{hh}(s - s') n_{\mathrm{e}}(s') \frac{\partial \log(T_{\mathrm{e}}(s'))}{\partial s'} \,\mathrm{d}s' \tag{4.6.8}$$

or in our specific case of a temperature sinusoid, by means of a Fourier cosine transform

$$\widetilde{Q}_x = -\frac{ik\lambda_{\mathrm{ei}}^{(\mathrm{B})} n_{\mathrm{e}} v_{2\mathrm{T}} k_{\mathrm{B}} \widetilde{T}_{\mathrm{e}}}{\sqrt{2}} \int_{-\infty}^{\infty} K_{hh}(s') \cos(\sqrt{2}k\lambda_{\mathrm{ei}}^{(\mathrm{B})} s') \,\mathrm{d}s'. \tag{4.6.9}$$

This gives the dimensionless thermal conductivity to be

$$\kappa_{\parallel c} = 2\int_0^{\infty} K_{hh}(s') \cos(\sqrt{2}k\lambda_{\mathrm{ei}}^{(\mathrm{B})} s') \,\mathrm{d}s'. \tag{4.6.10}$$

Ji and Held's configuration space fit for hydrogen does very well at reproducing the asymptotic behaviour described at the beginning of this section; substituting $\cos(\sqrt{2}k\lambda_{\mathrm{ei}}^{(\mathrm{B})} s')$ with the first two terms of its Taylor series gives $\kappa_{\parallel}^{(\mathrm{B})} = 3.205$ and $b_Q = 50.1$, which is not too far from the value calculated by the EIC model appearing in table 4.4 ($b_Q = 43.5$). Behaviour in the collisionless regime can be assessed using analytical methods suggested by Wong and Lin (1978) and Dai and Naylor (1992); this essentially involves first computing the asymptotic series for $K_{hh}(s)$ near the origin, changing variables to $t = -is$ and finally applying

Watson's Lemma (Watson 1916). Further details are given in appendix B.10 and identifies $\chi_1 = \pi(d+a)\gamma/3 \approx \chi_1^{(\text{EIC})}$ to the initial precision of three significant figures, $\eta = \gamma = 0.417$ which is very close to the predicted $5/12 \approx 0.429$, and $c_1 = \beta \sin(\pi\gamma/2)\Gamma(\gamma)/2^{\gamma/2}\pi = 0.721$.

Recall that the major difference between the two codes is the quasistationary assumption made by the EIC model.

Let us now compare the success of the three fit functions introduced above, along with the simpler $\kappa_\parallel/\kappa_\parallel^{(\text{B})} = 1/(1 + ak\lambda_{\text{ei}}^{(\text{B})})$ (suggested for use with the NFLF model by Dimits et al. (2014)) to actual data from SPRING simulations and the EIC model for ionisations of $Z = 1$ (fig. 4.21) and $Z = 8$ (fig. 4.22). It is demonstrated that, depending on choice of coefficients, our new fit given in eq. (4.6.6) is able to accurately capture the behaviour of either SPRING or EIC data; thermal conductivity reductions predicted by the EIC fit are within just 1% of simulated values for $k\lambda_{\text{ei}}^{(\text{B})} < 6$ (hydrogen) and $k\lambda_{\text{ei}}^{(\text{B})} < 2$ (oxygen). Even up to the limit of convergence for the number of Legendre-Laguerre moments used, just beyond $k\lambda_{\text{ei}}^{(\text{B})} = 100$, the error does not exceed 3% anywhere for hydrogen, while for oxygen the maximum relative error observed was 13%. When instead fitting to SPRING data, larger relative errors of 9% for $Z = 1$ and up to 25% for $Z = 8$, perhaps these errors could be reduced by tuning the index η.

Considering the Ji-Held fit for hydrogen (unfortunately, Ji and Held did not compute coefficients for ionisations greater than 1), it is found to be almost indistinguishable from our new fit to EIC with the Ji-Held fit being ever so slightly more accurate at lower collisionalities. At both ionisations, the fit provided by Bychenkov et al. (1995) is seen to perform significantly worse at low to moderate wavenumbers than our new fit or that of Ji and Held. Curiously, the unphysical increase in thermal conductivity observed here was not apparent in Figure 4 of the 1995 paper, suggesting that perhaps there was an error in transcribing equation (57) in the paper. Finally, while the simplistic fit $1/(1 + ak\lambda_{\text{ei}}^{(\text{B})})$ does not have the same issues of nonphysicality as the Bychenkov fit, it was still found to be especially poor at moderate collisionalities predicting relative errors in excess of 50% for hydrogen and 150% for oxygen in the region of $k\lambda_{\text{ei}}^{(\text{B})} \approx 1$.

4.6.2 *Using the new fit in the NFLF model*

Previously, the NFLF model used the $1/(1 + ak\lambda_{\text{ei}}^{(\text{B})})$ fit to calculate the necessary coefficients. But we have just shown that this fit leads to errors exceeding 50%, even at moderate collisionalities due to it only aiming to fit the special cases of local and collisionless heat flow with no regard to intermediate regimes. Therefore, employing the much improved 'Brodrick' fit to obtain coefficents should increase the accuracy of the model.

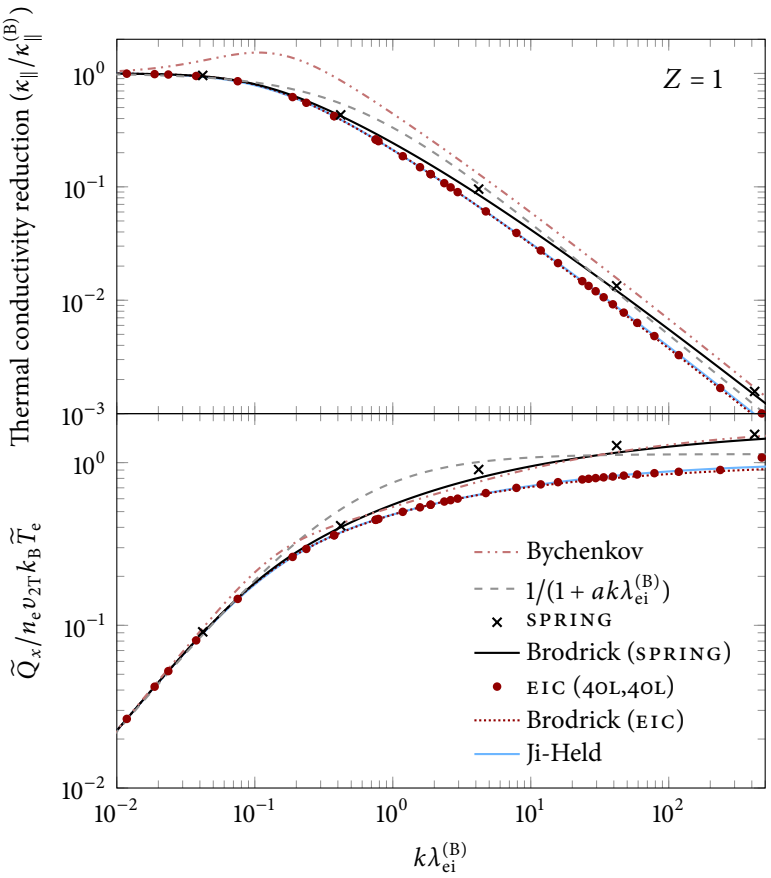

FIGURE 4.21: Comparison of the analytic fits given in eqs. (4.6.4), (4.6.6) and (4.6.10) to SPRING and EIC data for hydrogen ($Z = 1$). The two versions of the new 'Brodrick' fit employ different coefficients (all given in table 4.7) to recover the trends arising from the assumptions of each code.

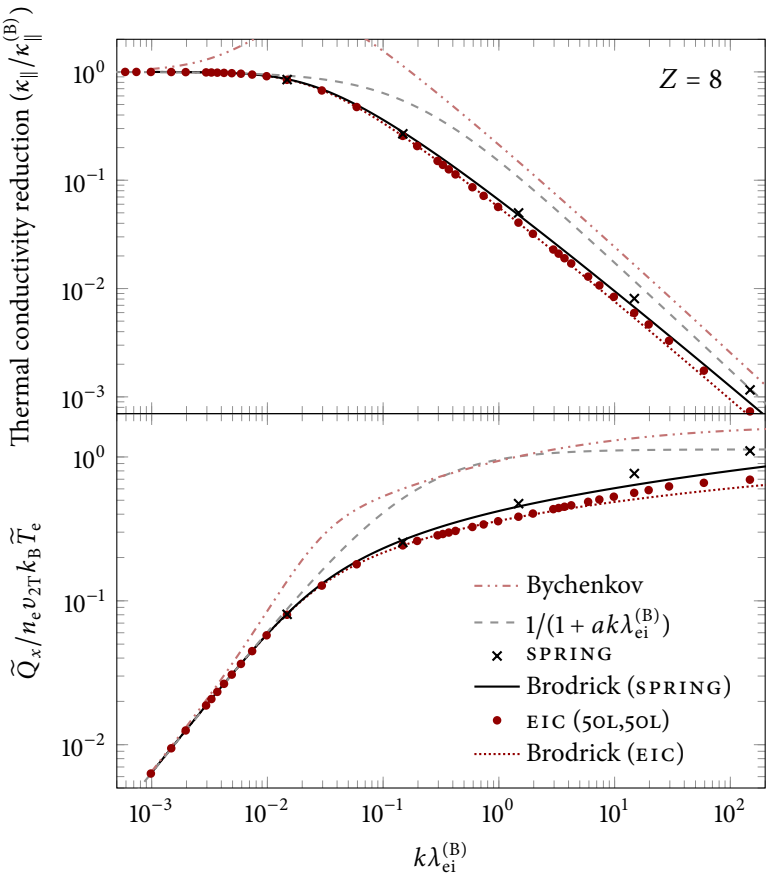

FIGURE 4.22: Comparison of the analytic fits given in eqs. (4.6.4), (4.6.6) and (4.6.10) to SPRING and EIC data for fully-ionised oxygen ($Z = 8$). The two versions of the new 'Brodrick' fit employ different coefficients (all given in table 4.7) to recover the trends arising from the assumptions of each code.

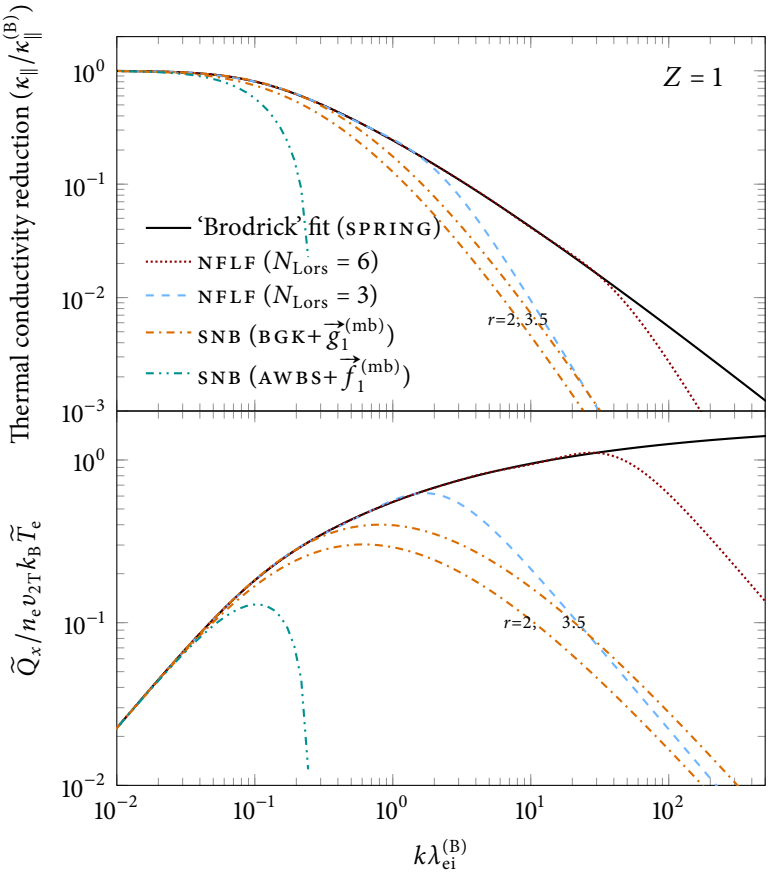

FIGURE 4.23: Comparison of the new analytic fits given in eq. (4.6.6) to the newly calibrated NFLF (using coefficients given in appendix A with p.e.$_{max}$ = 2.5%) and SNB models for hydrogen.

Coefficients were derived for hydrogen and oxygen using the constrained variable projection method described in section 3.4 and compared to the analytical fit in figs. 4.23 and 4.24 respectively. Choosing to optimise the range in which the NFLF model agrees with the new fit by p.e.$_{max}$ = 2.5%, such accuracy was achieved up to nonlocalities of $k\lambda_{ei}^{(B)} = 1.6$ for hydrogen and 0.3 for oxygen when using three Lorentzians, while with six Lorentzians this increased to $k\lambda_{ei}^{(B)} = 33$ and 5.9 respectively. A detailed table of optimal coefficients using any number of Lorentzians between 2 and 12 (inclusive) is provided in appendix A.

4.6.3 *Behaviour of the SNB model across all collisionalities*

So far we have only analysed the SNB model in the semicollisional and the collisionless regimes; but in fact the behaviour of the SNB model at all collisionalities

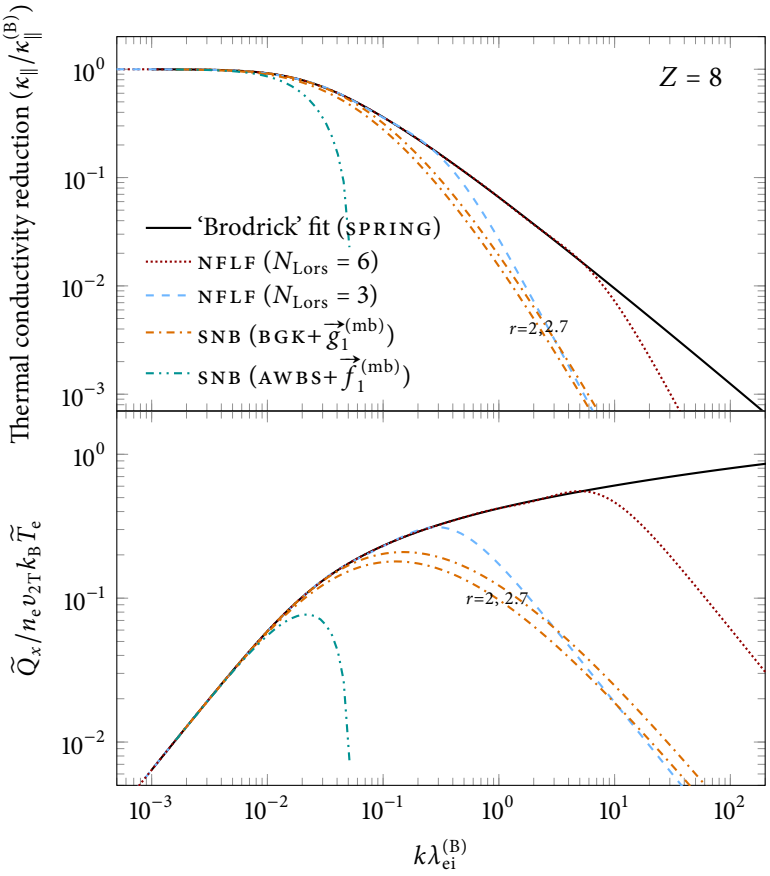

FIGURE 4.24: Comparison of the new analytic fits given in eq. (4.6.6) to the newly calibrated NFLF (using coefficients given in appendix A with p.e.$_{max}$ = 2.5%) and SNB models for oxygen.

in the low-amplitude limit can conveniently be obtained completely analytically. This is in part due to the fact that the electric field correction to the electron-ion mfp does not contribute when the amplitude of the temperature sinusoid is truly infinitesimal:

$$\frac{1}{\lambda_{ei}^{*(E)}} = \frac{1}{\lambda_{ei}^{*}} + \frac{(1+\beta_\parallel)|\vec{\nabla} k_B T_e|}{\tfrac{1}{2} m_e v^2} \tag{4.6.11}$$

$$\implies \lambda_{ei}^{*(E)} = \lambda_{ei}^{*}\left(1 - \frac{(1+\beta_\parallel)k|\sin(kx)|k_B \delta T_e}{\tfrac{1}{2} m_e v^2}\lambda_{ei}^{*}\right). \tag{4.6.12}$$

Thus the correction vanishes due to its proportionality to the temperature amplitude. For a more formal derivation of this claim see appendix B.9. Note that this noncontribution of the electric field correction was not considered by Schurtz

et al. (2000) due to their neglecting the amplitude-dependence of the electric field.

Once the electric field contribution has been ignored, derivation of the SNB model prediction for $\delta\widetilde{f}_0$ is fairly straightforward if a BGK approximation for the electron-electron collision operator is used. Starting from the continuum form of the SNB model and defining the velocity-dependent variable $X(v) = \xi Z k^2 \lambda_{\mathrm{ei}}(v)^2$,

$$\widetilde{H}^{(\mathrm{BGK})} = -\frac{\mathrm{i}Zk\lambda_{\mathrm{ei}}}{12r}\frac{V^9\{1, V^2-4\}}{1+X/3r}\mathrm{e}^{-V^2}\widetilde{Q}^{(\mathrm{B})}\,\mathrm{d}V. \tag{4.6.13}$$

The total heat flow is thus given by

$$\frac{\widetilde{Q}_x^{(\mathrm{BGK})}}{\widetilde{Q}_x^{(\mathrm{B})}} = \int_0^\infty \frac{V^9\{1, V^2-4\}\mathrm{e}^{-V^2}/12}{1+32X^{(\mathrm{B})}V^8/27\pi r}\,\mathrm{d}V, \tag{4.6.14}$$

where the velocity-independent parameter $X^{(\mathrm{B})} = \xi Z k^2 \lambda_{\mathrm{ei}}^{(\mathrm{B})2}$ has been defined. As in section 4.3.6, the curly brackets distinguish the original source term containing $\vec{f}_1^{(\mathrm{mb})} = -(V^2-4)\lambda_{\mathrm{ei}}^* f_{\mathrm{e}}^{(\mathrm{mb})}\vec{\nabla}T_{\mathrm{e}}/T_{\mathrm{e}}$ (right) from the modified source term with $\vec{g}_1^{(\mathrm{mb})} = -\lambda_{\mathrm{ei}}^* f_{\mathrm{e}}^{(\mathrm{mb})}\vec{\nabla}T_{\mathrm{e}}/T_{\mathrm{e}}$ (left) used by Schurtz et al. in the standard implementation of the model. While both integrals above can be expressed analytically in terms of the exponential integral Ei, doing so is not very enlightening.

A similar analysis can be performed for the AWBS collision operator, but an integrating factor method must be used to solve the first-order ODE in velocity-space

$$\widetilde{H}^{(\mathrm{AWBS})} = \frac{V^5}{12}\mathrm{e}^{X/24}\int_\infty^V \mathrm{e}^{-X'/24} iZk\lambda_{\mathrm{ei}}(V')V'^3\{1, V'^2-4\}\mathrm{e}^{-V'^2}\,\mathrm{d}V'\widetilde{Q}^{(\mathrm{B})}\,\mathrm{d}V. \tag{4.6.15}$$

The nonlocal correction to the heat flow can then be found using integration by parts

$$\frac{\delta\widetilde{Q}_x^{(\mathrm{AWBS})}}{\widetilde{Q}_x^{(\mathrm{B})}} = \int_0^\infty \frac{\gamma\left(\frac{5}{4}, \frac{-X}{24}\right)\mathrm{e}^{-X/24}V^9\{1, V^2-4\}\mathrm{e}^{-V^2}}{3(-4X/24)^{1/4}}\,\mathrm{d}V \tag{4.6.16}$$

$$\Longrightarrow \frac{\widetilde{Q}_x^{(\mathrm{AWBS})}}{\widetilde{Q}_x^{(\mathrm{B})}} = \int_0^\infty \frac{\gamma\left(\frac{1}{4}, \frac{-4X^{(\mathrm{B})}V^8}{27\pi}\right)\mathrm{e}^{-4X^{(\mathrm{B})}V^8/27\pi}V^9\{1, V^2-4\}\mathrm{e}^{-V^2}}{12(-4X^{(\mathrm{B})}V^8/27\pi)^{1/4}}\,\mathrm{d}V, \tag{4.6.17}$$

Don't worry, despite fractional roots of negative numbers all expressions evaluate to purely real numbers!

is the ratio of the nonlocal to the local heat flow, where γ is the incomplete gamma function.

Recall that the use of the modified source term $-\vec{\nabla}\cdot\vec{g}_1^{(\mathrm{mb})}$ (first term in the curly brackets) with the AWBS operator has already been ruled out in section 4.3.6 due to its underestimation of the initial nonlocal deviation of the heat flow in the semicollisional regime (parametrised by b_Q) by a factor of almost 5. However, computing the definite integral using the kinetic source term $-\vec{\nabla}\cdot\vec{f}_1$ (second term in curly brackets) numerically with Mathematica shows that the AWBS thermal conductivity can become negative for $X^{(\mathrm{B})} > 0.0154$, which corresponds to $k\lambda_{\mathrm{ei}}^{(\mathrm{B})} > 0.124/\sqrt{\xi Z}$. Such negative values of thermal conductivity should never occur in the linearised problem considered here (i.e. decay of a small-amplitude temperature perturbation) as it would result in instabilities at these wavelengths. But again, this does not mean in and of itself that the AWBS operator can never be a good approximation for electron-electron collisions in other models, such as the MN model which ensure positive definiteness in an alternative way as well as using a different treatment of the electric field and return current

There is less of an argument that the AWBS operator should be tuned by a multiplicative constant as it is based more directly on the actual form of $C_{\mathrm{ee}0}$ than the BGK operator.

The consequences of the choice of collision operator on the performance of the SNB model for ionisations of $Z = 1$ and 8 are illustrated in figs. 4.23 and 4.24 respectively. Specifically, the AWBS SNB model with the kinetic source term $-\vec{\nabla}\cdot\vec{f}_1$ is compared to the original SNB model using the modified source term $-\vec{\nabla}\cdot\vec{g}_1$ and the simple BGK collision operator but with the new tuning factor r set to two different values—one which would recover the correct nonlocal deviation in the semicollisional regime ($r = 3.5$ for hydrogen and 2.7 for oxygen) and another which will be suggested in the next chapter to be the optimal choice for all ionisations when relative temperature differences are large ($r = 2$). In both cases the BGK SNB is found to perform somewhat worse than the 3 Lorentzian NFLF model, reaching errors. of 30% as early as $k\lambda_{\mathrm{ei}}^{(\mathrm{B})} = 0.5$(hydrogen)/0.14(oxygen) with $r = 2$ and $k\lambda_{\mathrm{ei}}^{(\mathrm{B})}$1.1/0.2 when the fully tuned values of r are used. On the other hand, using the AWBS operator is clearly a bad choice due to the unphysical sign change at rather low degrees of nonlocality.

Remember that the rapid fall of the SNB heat flow to zero is intrinsic to the diffusive approximation rather than some of the model's more confusing assumptions.

4.7 CONCLUSIONS

In this chapter, the behaviour of the electron heat flow has been extensively studied under a range of different assumptions for a low-amplitude temperature sinusoid. Some conclusions have also been made about the effect of nonlocality on the electric field in the semicollisional and collisionless regimes. As a result, by fitting to VFP and EIC data we have suggested a new analytic Fourier space closure eq. (4.6.6) that reproduces the correct asymptotic behaviour and is significantly more accurate and robust than that previously given by Bychenkov et al. (1995).

Nevertheless, Ji and Held's (2014) closure (currently only calculated for $Z = 1$) is still found to be slightly more accurate than the new fit at high degrees of nonlocality while using the same number of free parameters; but its configuration space formulation may be less convenient for use in certain nonlocal approaches such as Fourier-based Landau fluid models (see section 2.3.6).

The new analytic fit was used to generate optimal coefficients for the NFLF model and to calibrate the SNB model in the semicollisional regime. Additionally, a new interpretation of the SNB function H was provided that recovered the correct high-velocity behaviour in the semicollisional regime. By comparing with VFP and analytic results, we can rank the models in terms of their overall performance for the problem of a low-amplitude temperature sinusoid as follows:

1. The NFLF model,
2. The EIC model,
3. The SNB model using the BGK collision operator, a modified source term containing $\vec{g}_1^{(\mathrm{mb})}$, and a tuning factor r between 2 and 3.5
4. The SNB model using the AWBS collision operator, the original kinetic source term containing $\vec{f}_1^{(\mathrm{mb})}$, and no tuning factor.

This is of course neglecting the fact that the NFLF model can surely not be considered predictive, as it is *designed* to reproduce the analytic results. It is only the EIC model that is able to provide reasonable results over a wide range of collisionalities *a priori*. In the next chapter we shall see whether or not this ranking holds true for the top three models (we shall here dispense with further study of the AWBS-SNB) in a case where the temperature differences are anything but infinitesimal.

5

TEST PROBLEMS WITH LARGE TEMPERATURE DIFFERENCES

Having thoroughly studied the performance of the EIC, NFLF and SNB models for a temperature sinusoid with a very small amplitude, it is now imperative to investigate more realistic and fusion-relevant scenarios with large relative temperature differences—such as might be observed between the core and the divertor or between the hohlraum gas fill and the hohlraum wall. A large variety of relevant problems are presented in this chapter including thermal ramp relaxation and laser heating under uniform ionisations and the relaxation of 1D profiles taken from a HYDRA simulation of a gadolinium hohlraum. However, the NFLF and EIC models will only be reviewed for the first problem—thermal ramp relaxation in hydrogen—after which point they will be discarded due to the finding that their performance is significantly worse than the SNB model in the presence of large relative temperature differences.

Unless stated otherwise the 'separated' version of the SNB model using distinct electron-ion and electron-electron mfp's will be employed throughout rather than the original 'averaged' version with a geometrically averaged mfp. Recall that the only difference this makes under uniform ionisation is the way the electric field correction affects the diffusion part of the SNB equation, which can be amended by use of a multiplier E_{mult}. The 'separated' version is explicitly shown to provide an improvement to the standard 'averaged' version in the presence of steep ionisation gradients in section 5.4 and shown to perform favourably.

The high precision of the value of the Coulomb logarithm here does not, of course, reflect the certainty to which this can be calculated, but is merely the value that allowed a nice conversion between dimensional and normalised units when beginning collaborative comparisons against IMPACT with the HYDRA team in LLNL.

5.1 THERMAL RAMP RELAXATION IN HYDROGEN

The first set of problems, presented in both this section and the next, concern the relaxation of simple temperature ramps that flatten out into surrounding hot and cold baths. This has the advantages of allowing simple reflective boundary conditions and not requiring any external heating/cooling mechanisms that would also need to be carefully calibrated between codes. Furthermore, the use of large temperature baths increase the time until boundary effects become important and avoid the possibility of the temperature differential dying out completely before a 'quasistationary' heat flux can be identified. In all cases the electron density and ionisation were homogeneous and fixed in time, with the

electron-ion and electron-electron Coulomb logarithm both assumed to equal $\log \Lambda = 7.09433$.

For the case of hydrogen (fully-ionised with $Z = 1$), quantities will be discussed in terms of reference quantities (T_0, n_0, etc.) encouraging the translation of the problem to both ICF- and MCF-relevant situations. The temperature profile, connecting hot and cold baths of temperatures of T_0 and $0.15T_0$ respectively, was a cubic ramp given by

$$T_e/T_0 = \begin{cases} 1 & n'_c \leqslant -75 \\ 0.575 - \dfrac{0.85}{300} n'_c \left(3 - \left(\dfrac{n'_c}{75}\right)^2\right) & n'_c \in [-75, 75] \\ 0.15 & n'_c \geqslant 75, \end{cases} \tag{5.1.1}$$

where $n'_c \in [-154, 100]$ is the cell number counting from the centre of the temperature ramp. Cell size in mfp's was uniform but varied between simulations to scan a range of collisionalities. The initial and final temperature profile is illustrated in the top panel fig. 5.1 for the smallest cell-size used ($\Delta x = 0.03\lambda_{ei}^{(B)}(T_0)$).

The VFP simulations performed with KIPP predicted a gradual reduction of the heat flow from the local (due to using the initialisation method detailed in section 4.1.2) to the nonlocal over an initial transient phase (over which the temperature ramp flattened somewhat). Completion of the transient phase was determined by the ratio of the KIPP heat flow to the expected local heat flow reaching a minimum. Upon completion, this ratio begins to slowly increase as the thermal conduction flattens the temperature ramp and the ratio of the scalelength to mfp increases (i.e. the thermal transport slowly becomes more local). This progression is illustrated for the steepest ramp in fig. 5.2, which shows the evolution of the peak KIPP heat flow compared to the corresponding peak local flux as a function of time. The transient is observed to last just under 2 collision times. Inclusion of the $r = 2$ SNB model (which was most successful at matching KIPP data) shows how the quasistationary assumption is only valid after the transient period, and the observed convergence of the peak KIPP flux to the SNB is somewhat reminiscent of the 'slowest damping mode' interpretation applied to the damping of a low-amplitude temperature sinusoid in the previous chapter (see section 4.1.2).

The KIPP temperature profile obtained at the end of the transient phase (for the $\Delta x = 0.03\lambda_{ei}^{(B)}(T_0)$ ramp) was fed into the various nonlocal models to calculate the associated heat flux for this profile. The Hermite-Laguerre basis was chosen for the EIC model as this proved to converge faster for this specific problem. Both

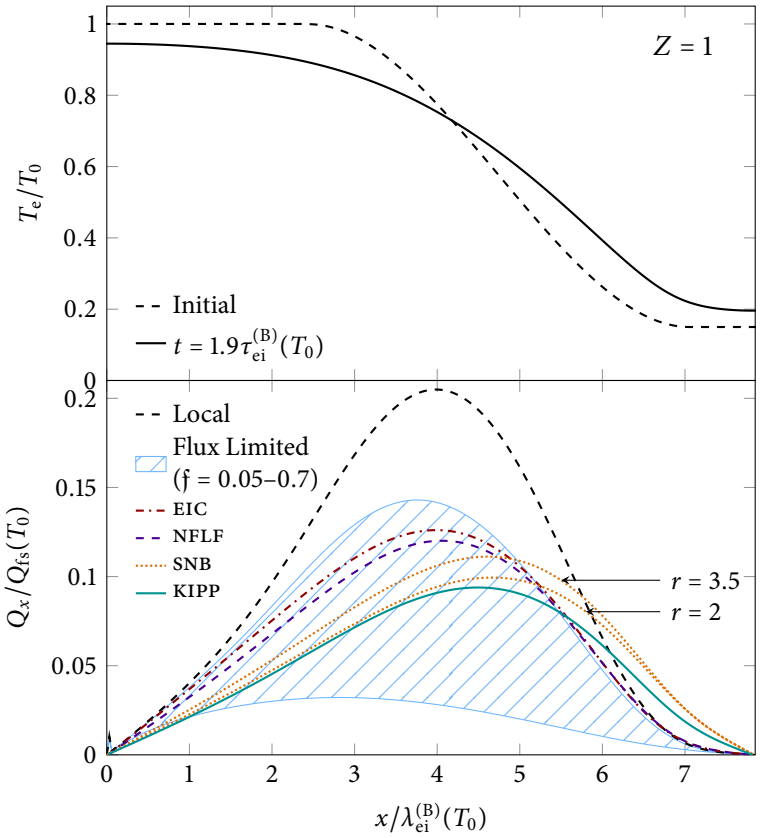

FIGURE 5.1: The initial and final temperature profile for the steepest hydrogen cubic ramp simulated with KIPP are depicted in the top panel, while the heat flow associated with the KIPP temperature profile at 1.9 collision times (just at the end of the initial transient period) as a ratio of the free-streaming limit $Q_{fs} = n_e k_B T_e v_{1T}$ (for electrons with energy $k_B T_0$) is depicted in the bottom panel. Three Lorentzians were used for the NFLF model, and the EIC employed 16,4 HL moments.

the EIC and NFLF models are seen to agree well with each other in fig. 5.1 (to within 10% almost everywhere for the snapshot shown). Nevertheless, agreement with KIPP is not nearly as good; the models overestimate the peak heat flux by 30–35% and do not predict the observed preheat into the cold region.

The SNB model, however, is shown to perform much better here and does indeed predict preheat features. Schurtz et al.'s implementation choices (confirmed optimal in the previous chapter) of a BGK model electron-electron collision operator with modified source term $-\vec{\nabla} \cdot \vec{g}_1$ were used. The full range of viable options for the BGK tuning factor r were investigated, with the observation that the lowest such value trialled ($r = 2$) best matched the peak heat flux, to within 6%, rather than the $r = 3.5$ previously identified as necessary to reproduce the

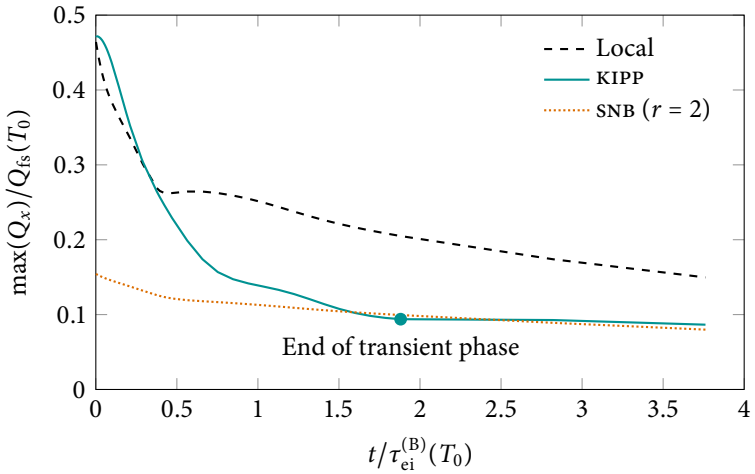

FIGURE 5.2: The evolution of the peak KIPP heat flow is compared to the peak local and SNB heat flows obtained by postprocessing instantaneous KIPP temperature profiles.

kinetic behaviour for a hydrogen temperature sinusoid in the semicollisional regime. This suggests that the latter value is not the universally optimal value for all problems, and later in this chapter a case will be made for the former value $r = 2$ to be preferable in a greater range of scenarios.

The wide range of heat flow profiles resulting from different flux-limiters between 0.05 and 0.7 are also shown in fig. 5.1. These were obtained using the formula $1/Q_{\mathrm{fl}} = 1/Q^{(\mathrm{B})} + 1/\mathfrak{f}Q_{\mathrm{fs}}$. A flux-limiter of ~0.25 best matched the peak kinetic heat flow, but in this case the peak is shifted towards the hot rather than the cold bath as observed in the KIPP simulation. Similar results are observed at all temperature ramp scalelengths investigated as illustrated in fig. 5.3, which depicts the reduction in the peak heat flow compared to the local prediction.

5.1.1 *Attempting to improve the* NFLF *model*

The capability of the NFLF model to closely match the results of the EIC for the case of homogeneous density and ionisation seems fairly impressive, considering that only 6 Lorentzians were needed for convergence compared to EIC's 64 moments. This implies that the NFLF is about 5 times faster (assuming the NFLF's second-order ODE's take approximately twice the time to solve as EIC's first-order). However, this result should not be too surprising as both models are based on some kind of linearisation procedure, causing them to fail in almost exactly the same way for a 'nonlinear' problem. For example, the lack of preheat or spatial shift in peak location predicted by the models are features also observed

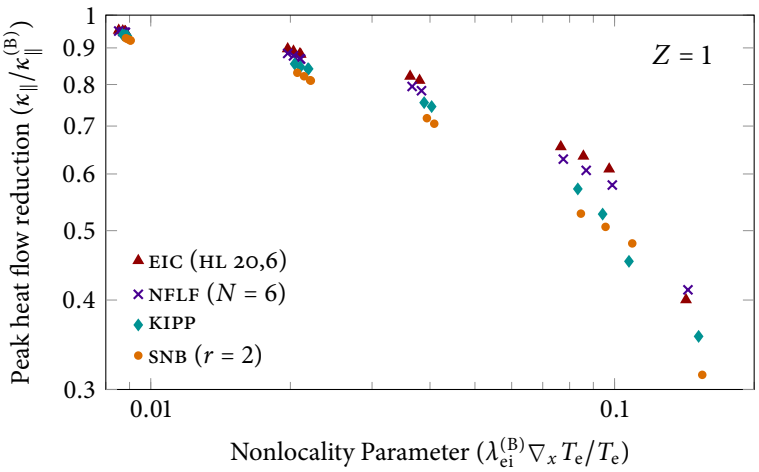

FIGURE 5.3: Ratio of peak heat flow to that predicted classically against inverse scalelength $\lambda_{ei}^{(B)}/L_T$ (calculated at the location of maximum heat flow predicted by each model) for snapshots from the hydrogen cubic ramp simulations using different initial gradients.

in the linear problem studied in the previous chapter. As for the SNB model, convergence was achieved with as few as 25 groups, corresponding to a very slightly faster computation time than the EIC model.

Improving performance of the NFLF and EIC models for large temperature variations require approaches that would not affect the performance in the linearised limit. For the EIC, a simple method is nonlinear iteration; i.e. updating the right-hand side of equation (2.3.43) by adding on nonlinear terms such as $\frac{eE_\parallel}{m_e}\frac{\partial \delta f_e}{\partial v_\parallel} - \sum_n w_n \frac{\partial g_n}{\partial s_\parallel}$ from the initial calculation and repeating until convergence. However, the computational time to apply the differential operators and separate into eigenvector components would probably increase the computational time by an undesirably large factor on the order of the number of moments used.

Conversely, a correct approach for improving the NFLF model is not immediately apparent, and probably requires deeper analysis of the link between the model and the VFP equation. Nevertheless, it is conceivable that this could be done without additional computational expense. One such possibility would be to multiply both sides of all modified Helmholtz equations by spatially-varying functions D, W and then commute them with the divergence/Laplacian operators. Such a procedure would lead to the NFLF heat flow contributions obeying the equation

$$\left[q_j^2 D + (a\lambda_{ei}^{(B)})^2 \vec{\nabla} \cdot D \vec{\nabla}\right] W \vec{Q}_j = p_j D W \vec{Q}^{(B)}. \tag{5.1.2}$$

Comparison with the analytical behaviour of the SNB model in the semicollisional regime suggested that $D = 1/n_e$, $W = {T_e}^4$ could be reasonable first guesses.

Encouragingly, application of this nonlinear correction, shown in fig. 5.4, greatly improves the accuracy of the NFLF model at high and intermediate collisionalities; in particular preheat is now properly predicted, making the NFLF comparable with the SNB model. However, at the lowest collisionalities the degree of preheat predicted by the new NFLF model is far greater than that obtained by KIPP or SNB; so much greater in fact that the peak heat flux is overestimated by over 30% with the NFLF model. This limitation of the simplistic nonlinear correction trialled here could probably be circumvented by more sophisticated forms of D and W, perhaps involving the temperature gradient scalelength itself. But a clear way forward is not apparent.

Coupled with its ability to accurately capture very fine scale effects, the new ability of the NFLF model to predict preheat (even if it can somewhat grossly overestimate it at very low collisionalities) could arguably make it a powerful tool for studying the potential effect of preheat in the SOL on the divertor temperature. However, the critical issue remains of the NFLF model being unable to accurately handle ionisation gradients (which may be important in studying detached divertors) in its current form.

5.2 THERMAL RAMP RELAXATION IN HELIUM AND ZIRCONIUM

Due to the failure of the EIC and improved NFLF models at accurately reproducing VFP results in the presence of large relative temperature gradients, from this point onwards only the SNB model will be investigated. While the SNB model performed fairly satisfactorily for the hydrogen ramp relaxation, it was important to ascertain whether this accuracy persisted at higher ionisations (values of Z). Similar ramp relaxation problems were therefore investigated in helium ($Z = 2$) and zirconium ($Z = 40$), ionisations indicative of those found in the hohlraum gas-fill and the highly ionised gold bubble .

Both due to higher ionisations being more relevant to hohlraum energetics, and to maintain consistency with the next chapter where comparisons will be made with other laser-plasma codes, dimensional units were used to reflect similarity with typical ICF scenarios. Specifically, the uniform electron density was taken to be 5×10^{20} cm^{-3} (characteristic of typical hohlraum gas fill) with a Coulomb

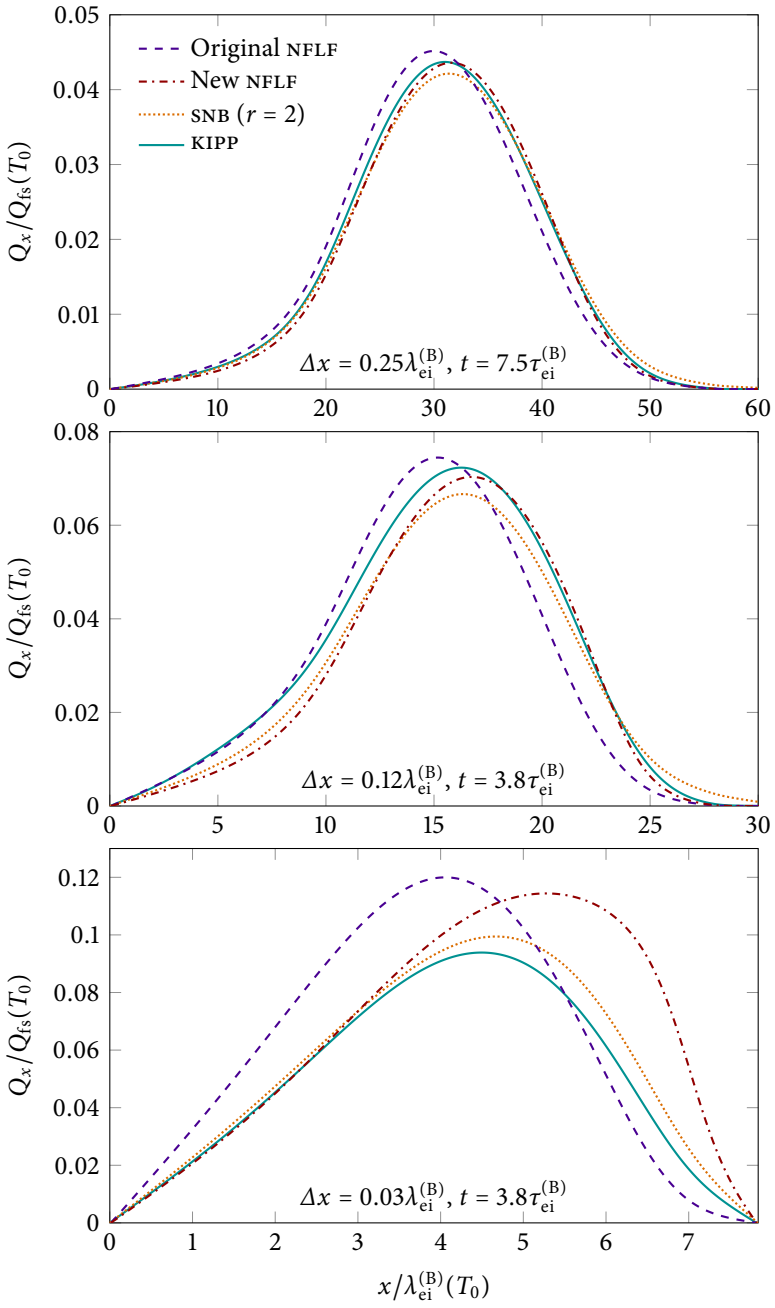

FIGURE 5.4: Comparing the new NFLF nonlinear correction $D = 1/n_e$, $W = {T_e}^4$, with the original $D = 1$, $W = 1$ for three different ramp widths. Six Lorentzians were used in all cases.

logarithm of $\log \Lambda = 7.09433$. The reference temperature is taken to be $T_0 = 1\,\mathrm{keV}$ and a tanh ramp is employed rather than the cubic ramp

$$T_\mathrm{e}/\mathrm{eV} = 575 - 425\tanh(x/L), \tag{5.2.1}$$

where L is the ramp half-width (corresponding to a straight line ramp with an equivalent gradient at $x = 0$), with $L \approx 50\,\mu\mathrm{m}$ suggested by M Marinak at LLNL as most relevant to indirect drive.

The reason for the different choice of ramp studied in the previous section is merely historical: Initially a straight line ramp was studied (see section 6.3) but the rapid change of gradient between the bath and the ramp led to unphysical features in the VFP simulations, particularly at low collisionalities. To avoid this the ramp was smoothed using the above tanh formula. When later trying to set up a similar problem with the KIPP code for hydrogen the number of spatial cells was limited by the number of processors per node available, 256; this meant that the bath size had to be reduced if resolution in the ramp was not to be compromised. It was therefore desirable to use a temperature profile that flattened out as quickly as possible, but still in a smooth manner (i.e. continuous second derivative); the cubic ramp meets this requirement.

Despite its artificial treatment of electron-electron collisions in the $\vec{f}_1$ equation, the IMPACT VFP code was used to perform these simulations as it was the only one available to the author at the time. Nevertheless, there were benefits in this approach; by eliminating the treatment of anisotropic electron-electron collisions as a possible source of discrepancy between the VFP code and SNB model, other assumptions could be focussed on. Furthermore, the same problem was later studied with the K2 code in the presence of magnetic fields (see section 7.2) using a more complete treatment of electron-electron collisions, and differences in thermal transport were observed to be not too significant. The simulations presented here included electron inertia, although this was only switched on after the first two timesteps for the helium simulations in order for the local form of $\vec{f}_1$ to be rapidly obtained. Additional simulations were also performed without any electron inertia but are not presented here. As always, reflective boundary conditions were used for scalar parameters such as electron density, temperature and ionisation (corresponding to zero flow conditions for the heat flux and electric field at the boundary) with the spatial grid extending from at least $-9L$ to $5L$, with cell size $\Delta x = L/50$. And the uniform velocity grid was parametrised by $\Delta v = 0.1 v_{2\mathrm{T}}(150\,\mathrm{eV})$, $v_\mathrm{max} = 25 v_{2\mathrm{T}}(150\,\mathrm{eV})$ corresponding to electrons with energy 93.75 keV. The timestep varied with L and Z, examples

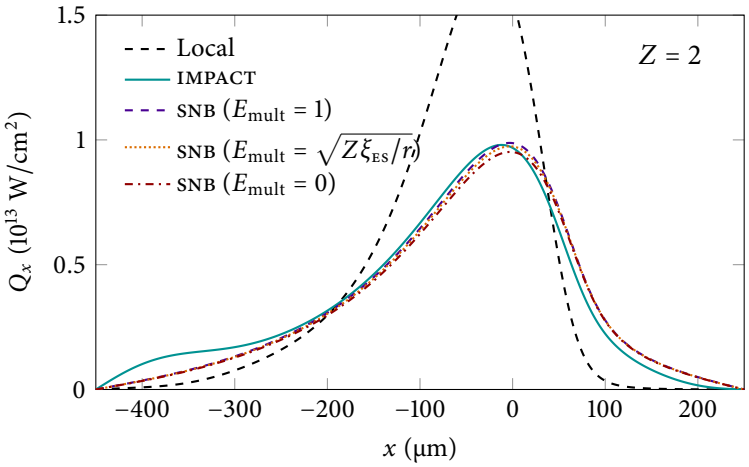

FIGURE 5.5: Helium thermal ramp heat flow profiles resulting from the IMPACT temperature profile after 12.1 ps relaxation.

being $\Delta t = 33.5$ fs for the $L = 50$ μm helium run and $\Delta t = 17$ fs for the $L = 17.3$ μm zirconium run.

5.2.1 *Effect of tuning the electric field correction*

One element of the SNB model that can not be obtained by a direct analysis of the VFP equations is the phenomenological limitation of the diffusive mfp by the electric field

$$\frac{1}{\lambda^{(E)}} = \frac{1}{\lambda} + \frac{|e\vec{E}|}{\tfrac{1}{2} m_e v^2} \tag{5.2.2}$$

As demonstrated in section 4.6.3, this is a purely nonlinear correction. In this chapter we now have the opportunity to explore the effect of the electric field on the heat flow for our test problems.

Recall that when first presenting the SNB model in section 2.3.3, there were two versions discussed: the original 'averaged' implementation using a geometrically averaged mfp λ_e and a newer 'separated' model first presented by Nicolaï et al. in 2006 using distinct electron-electron and electron-ion mfp's. In the 'separated' version it is the electron-ion mfp that appears in the diffusive part of the SNB equation (2.3.25) and is subject to the electric field correction. When converting from the 'averaged' to the 'separated' version, the original SNB equation (2.3.19) must be multiplied by a factor $\sqrt{\lambda_{ee}/\lambda_{ei}^{\star}} = \sqrt{Z\xi/r}$. Therefore, in order for the electric field correction to have an identical effect in the 'separated' and the

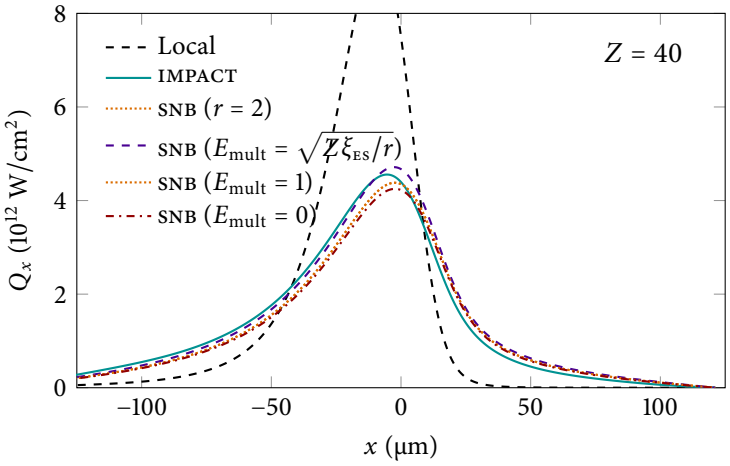

FIGURE 5.6: Zirconium thermal ramp heat flow profiles resulting from the IMPACT temperature profile after 3 ps relaxation.

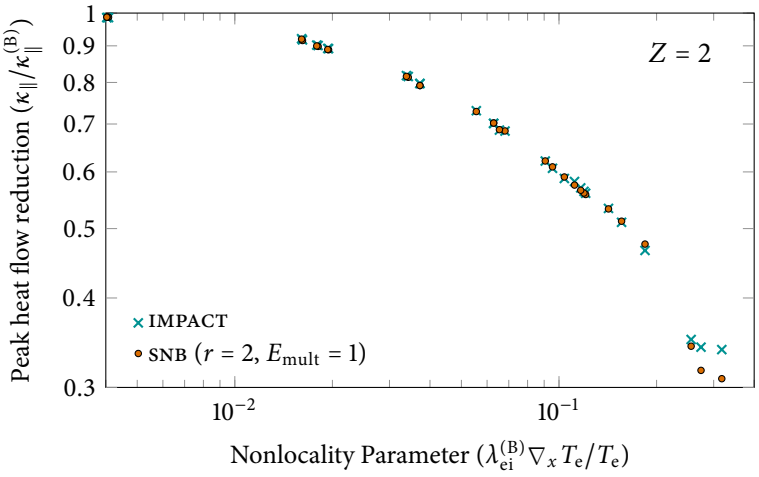

FIGURE 5.7: Ratio of peak heat flow to that predicted classically against inverse scalelength $\lambda_{\text{ei}}^{(\text{B})}/L_T$ (calculated at the location of maximum heat flow predicted by each model) for snapshots from the helium tanh ramp simulations using different initial gradients.

'averaged' models, the 'separated' electric field must be multiplied by this same factor (represented by the factor E_{mult}). Of course, there is no a priori reason why it should be the average mfp rather than just the electron-ion part is affected, and so both possibilities $E_{\text{mult}} = \sqrt{Z\xi/r}$ and $E_{\text{mult}} = 1$ as well as $E_{\text{mult}} = 0$ shall be trialled.

Comparing these three options for the $L = 50\,\mu\text{m}$ helium ramp by postprocessing the 12.1 ps IMPACT temperature profile in fig. 5.5 seems to suggest the electric field limitation does not have a large effect on the heat flux. Part of this finding is due to the fact that the multiplier for helium $\sqrt{2\xi_{\text{ES}}(2)/2} = 0.6$ is not too far from unity. Nevertheless, differences are just about discernible for the peak heat fluxes where both choices of nonzero multiplier show better agreement than using no electric field at all. Note that the increase in peak heat flux with E_{mult} is expected due to the relocalising effect of the electric field.

Looking instead at the zirconium ramp in fig. 5.6, variation with E_{mult} is found to be much more noticeable due to the $\sqrt{Z\xi/r}$ multiplier this time being greater than unity. It is clear that this multiplier now gives a better agreement with VFP especially for the cooling of the hot bath at $x \lessapprox -2020\,\mu\text{m}$ (although the peak heat flux is overestimated slightly). However, we must be careful not to leap to the conclusion that there is therefore anything inherently 'correct' or 'physical' in this particular approach to modifying the diffusive mfp and the success of the $\sqrt{Z\xi/r}$ multiplier could be pure coincidence. One particular issue with the general SNB approach to the electric field by reducing the mfp noted by Manheimer et al. (2012) is that it applies equally to electrons travelling in all directions, not taking into account the fact that electrons travelling antiparallel to the electric field should be accelerated and thus experience an *increased* mfp.

Comparisons of SNB and VFP peak heat flows were again extended to a range of collisionalities (or ramp widths), but only for the helium ramp. This is presented in fig. 5.7, confirming that the SNB overestimate of the peak heat flux did not exceed 10% for any nonlocality parameter $\lambda_{\text{ei}}^{(\text{B})} \nabla_x T_{\text{e}}/T_{\text{e}} \lessapprox 0.3$. Another general observation to be made from the entire heat flux profile comparisons in figs. 5.5 and 5.6 is that the SNB model persistently overestimates the amount of preheat compared to VFP, a finding in line with previous research (e.g. Marocchino et al. 2013).

Also worthy of comment is the 'bump' on the helium heat flow profile (fig. 5.5) in the region of $-450\,\mu\text{m} < x < -250\,\mu\text{m}$. This stems from the inclusion of electron inertia ($\frac{\partial \vec{f}_1}{\partial t}$) after the first two timesteps in the IMPACT simulations which introduces advective behaviour on top of the mainly diffusive nature of the VFP equations at high collisionalities. Electron inertia 'waves' are then seen to propag-

ate to the boundaries as transient effects evanesce, and once a 'quasistationary' state has been set up the bumps are no longer noticeable. Interestingly, it is only when using the IMPACT initialisation process of turning electron inertia off for the first two timesteps that such features are observable as illustrated in fig. 5.8. It was for this reason that electron inertia was chosen to be present from the very beginning of the zirconium simulation.

5.3 LASER HEATING

Thus far, only simplistic ramp relaxation problems have been investigated. As the shape of the ramp does not change much over the simulated timescales it is very difficult to critique any differences in temperature profile when evolving with the SNB model instead of IMPACT. It is therefore worthwhile extending our study to a greater variety of scenarios. One such possibility is the nitrogen laser heating experiment carried out by Froula et al. (Froula et al. 2007) and later simulated in 2D with IMPACT by Ridgers et al. (2008a; 2008) for a variety of magnetic fields. In this chapter, a simplified 1D version of this problem is studied making it easier to directly compare heat and temperature profiles resulting from the different approaches.

The 1D simulation consisted of a fully-ionised nitrogen plasma ($Z = 7$) with uniform electron density 1.5×10^{19} cm^{-3}, initial temperature 20 eV and an assumed constant Coulomb logarithm of 7.5 being heated by a continuous 6.3×10^{13} W/cm^2 laser (no time envelope was applied). The intensity profile of the laser was uniform in the y and z directions and Gaussian in the x-direction with a full width at half maximum of 150 μm. In order to avoid additional distortions to the EDF due to inverse bremsstrahlung effects, the Maxwellian heating operator described in section 2.2.3 was used. (The effect of inverse bremstrahlung on the EDF and heat flow was was previously explored in detail by C P Ridgers (2008)). Due to the high peak temperatures reached in the simulation in the presence of a much colder background, the velocity grid was resolved with a total of 250 cells extending up to $v_{\max} = 25 v_{2T}(20\,\text{eV})$, corresponding to electrons with an energy of 12.5 keV. The spatial domain, consisting of 400 cells, extended to 1000 μm from the centre of the pulse with reflective boundary conditions being used. A timestep of 60 fs was used.

The top panel of fig. 5.9 shows that after 120 ps IMPACT predicted that the nitrogen plasma heats up to just over 300 eV at the centre of the pulse. It should not be concerning that this is slightly warmer than that predicted after 440 ps in section 5.3 of C P Ridgers' thesis (2008) as the 1D geometry used here greatly

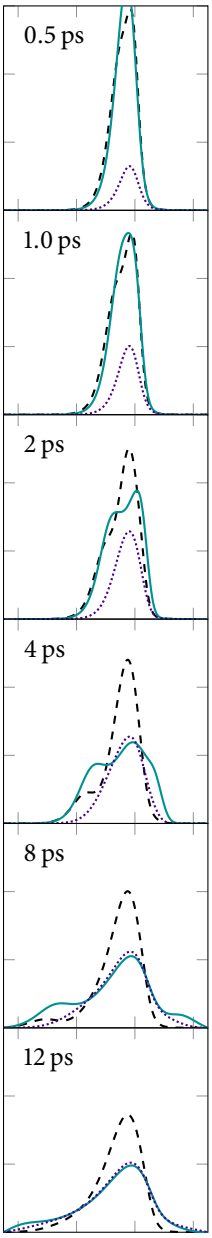

FIGURE 5.8: *Evolution of helium heat flow profiles. Solid green and purple dotted lines correspond to* VFP *simulations with and without electron inertia switched off for the first two timesteps, while the black dashed line is the local heat flow. Ticks on the y-axis represent intervals of* 10^{13} W/cm^2.

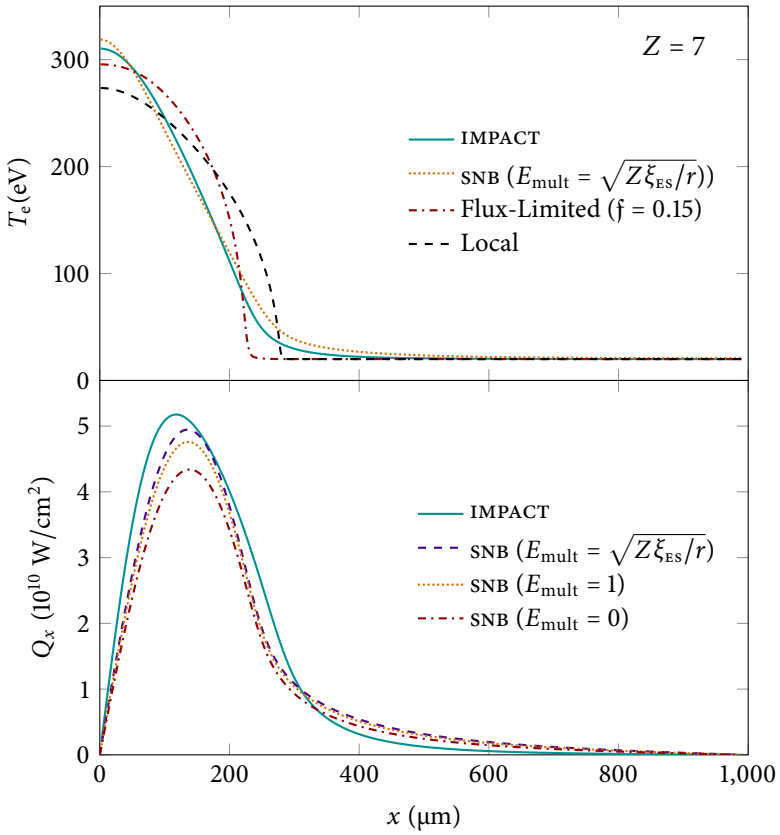

FIGURE 5.9: Comparison of temperature profiles (top) after 120 ps Maxwellian laser heating along with either IMPACT or a classical/flux-limited/SNB transport model. The IMPACT heat flow profile is shown in the bottom panel with SNB heat flow profiles obtained by postprocessing the IMPACT temperature profile above using various multipliers on the electric field. The local heat flow is not shown as it is about four times higher than the nonlocal.

restrict the avenues through which thermal energy can be conducted away. Results of postprocessing the IMPACT temperature profile with the SNB model are presented in the bottom panel, showing that again the multiplier $\sqrt{Z\xi_{ES}/r}$ is best at replicating the VFP heat flux. In this case, however, the discrepancy between the SNB and VFP heat flow is slightly more significant, especially towards the centre of the laser beam. This discrepancy could be due to the Maxwellian heating operator providing a constant source of thermal electrons at ever increasing temperatures to replenish those being conducted away. Due to its quasistationary presumption, the SNB model does not in any way take into account the effect of the heating operator on the EDF: all ways of achieving a given temperature profile are considered equal by the SNB model. Alternatively, the previous ramp

relaxation problems could have just been particular cases where the SNB model happens to work very well by coincidence.

Instead of just postprocessing the final IMPACT temperature profile, the effect of evolving from the initial uniform 20 eV was investigated. Additionally, the consequence of using simple local and flux-limited treatments (a flux-limiter of $f = 0.15$ was found to be optimal here) was explored in a similar way. An exceedingly simple forward Euler method was used to update the temperature according to the prescribed heating operator and thermal conduction model. It is seen in the top panel of fig. 5.9 that the agreement between the evolved SNB and IMPACT temperature profiles is impressively good, with the largest percentage difference being a 36% overestimate of the temperature at the foot of the hot spot. On the other hand, traditional local and flux-limited approaches predict completely different shapes for the temperature profile, mostly due to the absence of preheat. It turns out that the agreement between VFP and SNB heat fluxes after the same simulation time is better when co-evolving (not pictured) than when postprocessing. This is due to the heat flux being compensated by the developing temperature gradient; e.g. in the centre of the pulse, where the SNB underestimates the heat flow, higher temperatures are allowed to develop leading to a higher heat flux that happens to closely match the VFP heat flux.

5.4 GADOLINIUM HOHLRAUM

5.4.1 *Problem definition*

While a number of comparisons between the SNB model and VFP codes had previously been performed (Schurtz et al. 2000; Marocchino et al. 2013), none involved spatially-inhomogeneous ionisation. As inertial fusion experiments typically involve steep ionisation and density gradients (for example, at the interface between the helium gas-fill and the ablated gold plasma), it was critical that the SNB model be tested in such an environment. Variations in ionisation may also be important in the 'detached' divertor scenario where a moderate-Z gas is injected in front of the divertor to radiate excess heat.

Through collaboration with researchers at Livermore, a simple test problem, relevant to indirect drive ICF was designed; this involved the laser-heating of a gadolinium hohlraum containing a typical helium gas-fill. For simplicity, 1D spherical geometry was employed in the HYDRA simulation, including a leak source with an area equal to the laser entrance hole to achieve a realistic energy balance. The VFP code chosen to analyse this was IMPACT due to its ability

to simulate inhomogeneous ionisation profiles and the K2 and OSHUN codes not being available to the author when these simulations were first performed. (The correct treatment of electron-electron collisions offered by K2 and OSHUN but lacking in IMPACT could make it worthwhile to repeat these simulations in the future. However, the need for this is made somewhat less immediate by Sherlock et al.'s (2017) qualitatively similar findings when using K2 and SNB to analyse another problem.) Electron temperature, density and ionisation profiles at 20 ns (shown in the upper panel of fig. 5.10) were extracted and used as the initial conditions for the IMPACT simulation along with the standard assumption that the electron distribution function is initially Maxwellian everywhere. At this point very steep gradients in all three variables were set up with a change from $T_e = 2.5\,\mathrm{keV}$, $n_e = 5{\times}10^{20}\ \mathrm{cm}^{-3}$, $Z = 2$ to $T_e = 0.3\,\mathrm{keV}$, $n_e = 5{\times}10^{21}\ \mathrm{cm}^{-3}$, $Z = 39$ across approximately 100 μm at the helium-gadolinium interface.

The mesh refinement and spline interpolation procedures detailed in section 3.6 were used to increase the spatial resolution near the steep interface for the IMPACT simulations, helping both numerical stability and runtime due to needing a reduced number of nonlinear iterations. The IMPACT simulation transformed the problem onto a simple planar geometry with reflective boundary conditions. Electron inertia was neglected in the simulations presented here and a timestep of 1.334 fs was used with the n_e and Z profiles kept fixed. For simplicity, the Coulomb logarithm was treated as a constant $\log \Lambda_{ei} = \log \Lambda_{ee} = 2.1484$; note that in reality the plasma is only strongly coupled in the colder region of the gadolinium bubble beyond ~1.7 mm with higher values of $\log \Lambda_{ei} \approx 8$ being reached in the hotter corona corresponding to $x \lessapprox 1.6\,\mathrm{mm}$. While potentially affecting the physics and evolution of plasma profiles compared to reality this simplification of constant Coulomb logarithm should not affect the conclusions made on the most successful implementation of the SNB model as compared to IMPACT when both models are using identical treatments of $\log \Lambda_\alpha$.

5.4.2 *Results*

As with VFP simulations in the previous sections, an initial transient phase was observed where the IMPACT heat flux gradually reduces from the Braginskii prediction as the distribution function rapidly moves away from Maxwellian. Once again this transient phase is considered to be over when the ratio of the peak heat flow to the Braginskii prediction stops reducing. This ratio is not observed to change by more than 5% after the first 5 ps of the 15.7 ps IMPACT simulation. Therefore, it should be safe to treat the transient phase as complete after 5 ps, at

which point the temperature front has advanced by approximately 8 μm leading to a maximum temperature change of 41%.

In comparing the IMPACT and SNB heat flow profiles an important subtlety concerning the implementation of the model was highlighted. While more recent publications concerning the SNB model (Nicolaï et al. 2006; Del Sorbo et al. 2015) and the results already presented in this chapter use the formulation with separate electron-ion and electron-electron mfp's/collision frequencies, the original paper (Schurtz et al. 2000) used a geometrically averaged mfp $\lambda_e = \sqrt{\lambda_{ee}\lambda_{ei}^*} = \sqrt{Z\xi/r}\lambda_{ei}$. This averaging process, however, is only valid for the case of homogeneous ionisation, and the potential for significant errors when the ionisation varies is demonstrated by the overestimate of both the peak heat flux by a factor of almost two and the thermal conduction in the corona by a factor of almost three when using this approach (lower panel of fig. 5.10). Fortunately, using separate electron-ion and electron-electron mfp's provides a greatly improved prediction of the preheat into the hohlraum, the peak heat flow (to within 16% of the IMPACT simulation) and the thermal conduction in the gas-fill region. However, the latter is still too large by a factor of approximately two. This discrepancy could potentially lead to an overestimate of hohlraum temperatures, causing issues similar to those arising with using an overly restrictive flux limiter (Rosen et al. 2011).

Interestingly, completely neglecting the electric field correction to the electron-ion mfp further improves the accuracy of the separated SNB peak heat flux and coronal thermal conduction. However, it does not give quite as impressive an agreement with the preheat into the hohlraum wall. This is the first time in this chapter that using a multiplier of zero gives arguably the best agreement with VFP, but the electric field limitation also has a much larger influence here than elsewhere due to the extremely steep gradients present. Perhaps then it would be better to dispense with the electric field correction altogether due to its lack of first principles justification and the fact that its removal would only lead to minor losses of accuracy in certain problems. Additionally, this would avoid the overly strong amplitude dependence caused by the electric on temperature sinusoid damping, but sacrifices the purely numerical benefit of efficiently removing large high-frequency noise/grid effects alluded to by Schurtz et al. (2000).

It is worthwhile to also consider potential sources of inaccuracy in the IMPACT simulation itself. As the temperature gradient across the gadolinium bubble is so steep, the degree of nonlocality can get very high, potentially invalidating the P1 expansion made by IMPACT. Furthermore, the strong coupling present in the cooler part of hohlraum wall, represented by the low value of the Coulomb

logarithm, could render the effect of collisions in this region only accurate to $\mathcal{O}(1/\log \Lambda_\alpha) \approx$ ~50%. However, as the SNB model also uses a P1 expansion and an identical treatment of the Coulomb logarithm to IMPACT, these simplifications should not affect the conclusion that the separated SNB model predicts the same heat flow into the wall as IMPACT while overpredicting that in the corona. It has simply been demonstrated that reduced models can be an effective stepping stone between hydrodynamic and VFP approaches. Nevertheless. these considerations do act as a reminder that even a highly sophisticated VFP code could be faced with challenging inaccuracies in certain regions of the plasma (though it would surely still be an improvement to a purely hydrodynamic approach which would experience the same difficulties with strongly coupled plasmas); a potential method in overcoming this and incorporating large-angle collisions in a continuum code could be a Monte Carlo based approach (Turrell et al. 2015). Similar points can be made for other deficiencies, such as collisions with neutrals and Fermi degeneracy, although these are probably slightly easier to address and incorporate into models(Kolobov and Arslanbekov 2006; Brown and Haines 1997).

5.5 SUMMARY AND CONCLUSIONS

In this chapter, we have investigated a wide range of test problems with relative temperature differences that are relevant to many potential approaches to fusion energy. In the very first comparison for the hydrogen cubic ramp, the NFLF and EIC models were found to overestimate the peak heat flux by up to 35% as well as failing to predict preheat. And although a simple improvement to the NFLF model was found to noticeably reduce errors and recover preheat at moderate collisionalities, the degree of preheat became grossly overestimated at SOL-relevant collisionalities of $\lambda_{\mathrm{ei}}^{(\mathrm{B})}/L_T > 0.1$. Therefore these two models were therefore considered to be less desirable for fusion-relevant scenarios than the SNB model, which performed well for all test problems. As the degree of collisionalities investigated were all well below unity, even the SNB model can only be considered validated for the case of hohlraum transport and mean SOL profiles, whereas it could certainly break down at the shorter scalelengths relevant to transient events such as filaments, ELM's and disruptions. Furthermore, no sensible way of including sheath boundary conditions has yet been suggested for applying the SNB model to SOL transport.

From the problems studied here, it seems that the optimal implementation of the SNB model consists of the modified source term including $\nabla \cdot \vec{g}_1^{(\mathrm{mb})}$ suggested

by Schurtz et al. (2000) and the BGK model electron-electron collision operator but with a multiplier of $r = 2$. Separating the electron-electron and electron-ion collisionalities in this equation further improves agreement with VFP for the gadolinium hohlraum problem with spatially-varying ionisation. As for the treatment of electric fields through MFP limitation, it is not entirely conclusive whether it is more reasonable to include this phenomenological treatment or not. If retained, all tests point towards using a multiplier of $E_{\text{mult}} = \sqrt{Z\xi_{\text{ES}}/r}$ to ensure consistency with the original averaged model. However, neglecting the electric field correction completely results in much better agreement for the gadolinium hohlraum problem with respect to the peak and coronal heat fluxes.

One final limitation of this study is the focus on postprocessing VFP temperature profiles instead of co-evolving them with the SNB model. But if, aside from initial transient features, the SNB model is able to to consistently approximate VFP heat fluxes with an acceptable degree of accuracy on a snapshot-to-snapshot basis, then the temperature profile should evolve similarly with both models. This reasoning is confirmed by the one inline test that was done involving nitrogen laser heating, indicating that slight inaccuracies in the SNB heat flow self-correct rather than build up over time. Nevertheless, there is more substantial disagreement for the gadolinium hohlraum particularly in the low density gas fill, and the manner in which this could affect the physics or have knock-on effects on laser-plasma interactions can only be properly understood by simulating over a longer timescale. For further exploration of the time-integrated effect the reader is referred to work of Sherlock et al. (2017) to which the author of this thesis contributed.

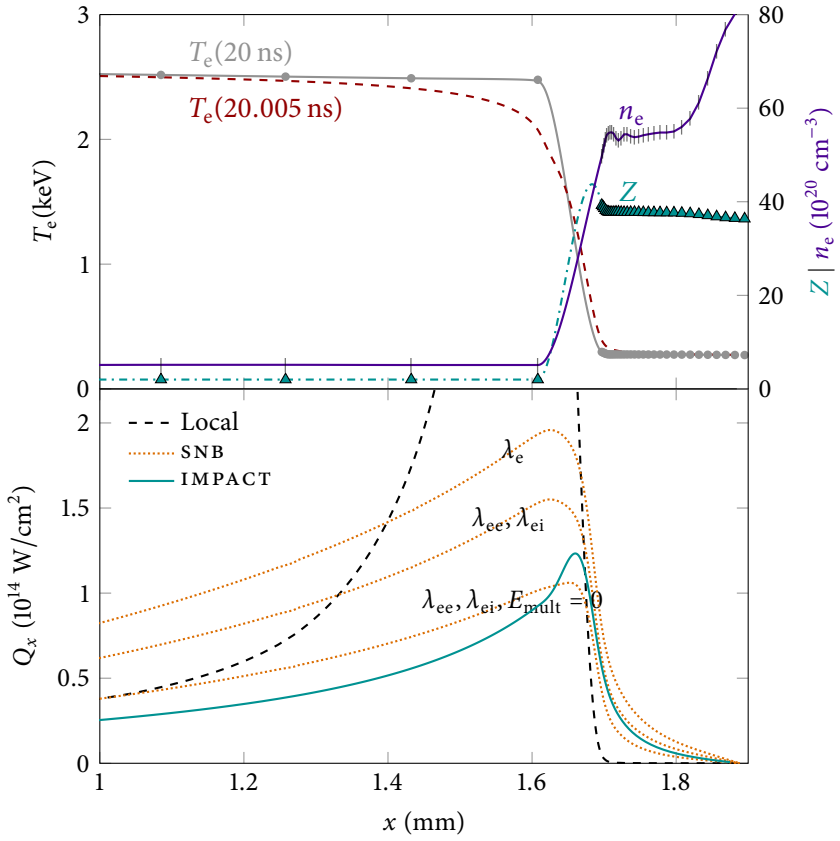

FIGURE 5.10: Temperature, density and ionisation profiles after 20 ns simulated laser heating with HYDRA (marks) are shown in the top panel along with interpolated profiles used to initialise IMPACT simulations (curves), as well as the temperature profile after a further 5 ps. Comparison of heat flow predictions with the $r = 2$ SNB model using geometrically averaged (denoted by λ_e) or separated mfp's (denoted by λ_{ee}, λ_{ei}) based on temperature profile after 5 ps IMPACT simulation are provided in the lower panel. The separated SNB is shown with electric field multiplier of both $E_{mult} = \sqrt{Z\xi_{ES}/r}$ and $E_{mult} = 0$ on the electric field. The maximum local heat flow is 2.2×10^{15} W/cm^2.

6

BENCHMARKING THE SNB MODEL IN RAD-HYDRO CODES

6.1 SOURCES OF CONFUSION IN THE ORIGINAL SNB PAPER

In what follows in this chapter we shall find that there are significant differences between the SNB model in the DUED/HYDRA codes and the 'optimal' implementation identified in the previous chapter. These discrepancies stem not merely from the new developments concerning the tuning of the Krook collision frequency, multipliers on the electric field or even the separation of the electron-electron and electron-ion mfp's, but from conflicting definitions of the thermal velocity v_T used when deriving the SNB model from the kinetic equations in sec. III F of (Schurtz et al. 2000). At first glance, the appearance of e^{-v^2/v_T^2} on p. 4245 suggests that the definition $v_T = v_{2T} = \sqrt{2k_B T_e/m_e}$ has been employed. However, looking closer, the definition of the electron-ion mfp given just after eq. (56)

$$\lambda_{ei} = \left(\frac{v}{v_T}\right)^4 \frac{4\pi\varepsilon_0{}^2 (k_B T_e)^2}{n_e e^4 \log\Lambda} \tag{6.1.1}$$

(converted from Gaussian to SI units) is only consistent with that used in P1 VFP codes (such as IMPACT) if the thermal velocity is instead defined as $v_T = v_{1T} = \sqrt{k_B T_e/m_e}$. Missing this conflict, and simply assuming that $v_T = v_{2T}$ throughout, results in all mfp's being over estimated by a factor of 4. Rescaling the SNB PDE so that all this is wrapped up into the electron-electron mfp, an identical approach would be achieved by multiplier of $r = 16$ (ignoring the phenomenological mfp modification due to the electric field).

6.2 THE SNB MODEL IN DUED

One of the most thorough comparisons previously presented between the SNB model and VFP codes was performed by Marocchino et al. (2013). However, a major finding of this work was that the accuracy of the SNB model, implemented in the University of Rome hydro code DUED, worsened as ionisation increased. This seemed rather peculiar as the SNB model was derived in the Lorentz limit (i.e. by neglecting electron-electron collision in the $\vec{f}_1$ equation). Upon inspection, though, it turned out that this unexpected trend can be explained by two specific implementation details: using a different definition of the thermal velocity in the

definition of the mfp's essentially equivalent to using a Krook multiplier of $r = 16$ (as explained above) and the absence of the collision fix ξ to approximate the effect of anisotropic electron-electron collisions. This combination of factors leads the DUED SNB to become closer to the $r = 2$, $\xi = \xi_{ES}$ implementation suggested in this thesis at low ionisations ($r = 2$); in fact for a linearised problem in hydrogen it performs even better as it is then equivalent to using an $r = 16\xi_{ES} = 3.8$, $\xi = \xi_{ES}$ implementation (we showed previously that in order to match kinetic behaviour in the semicollisional regime for sinusoid damping the correct factor should be $r = 3.5$).

Recall $\xi_{ES} = (Z + 0.24)/(Z + 4.2)$

This analysis was confirmed by reproducing Marocchino et al.'s results for a damping temperature sinusoid at ionisations of $Z = 1$, 2 and 4. It is found that implementing the supposed implementation of $r = 16$, $\xi = 1$ (pink dashed) matches the DUED results very well at high collisionalities but diverges slightly at shorter wavelengths. This disagreement could potentially be explained by convergence issues in the Marocchino et al. paper. On the other hand, the preferability of the generally optimal $r = 2$, $\xi = \xi_{ES}$ implementation (black dot-dashed) at matching VFP results demonstrably increases with ionisation. No attempt was made to revisit the ramp relaxation problem also presented by (Marocchino et al. 2013).

6.3 THE SNB MODEL IN HYDRA

In collaboration with Marty Marinak, Mehul Patel and Gary Kerbel at LLNL, the implementation of the SNB model in the Lagrangian rad-hydro code HYDRA was compared to both the in-house version used in this thesis and IMPACT. These studies found that the HYDRA SNB was implemented in a similar way to that in DUED (i.e. $r = 16$, $\xi = 1$). Two test problems were used to arrive at this conclusion: relaxation of a linear temperature ramp in helium and the nitrogen laser heating problem studied in section 5.3. The first of these was the test problem that later morphed into the tanh ramp relaxation explored in section 5.2 and used exactly the same plasma parameters except for the initial temperature profile (depicted in the top panel of fig. 6.2).

In order to be as careful as possible in the benchmarking process, agreement was first sought between local heat flows. This was done by first taking the local dimensional thermal conductivity provided directly from HYDRA to obtain the dimensionless thermal conductivity

$$\kappa_{\|c} = \frac{\sqrt{2m_e}}{12\pi^{3/2}} \frac{e^4 Z \log\Lambda_{ei}}{{\varepsilon_0}^2 {k_B}^{7/2} {T_e}^{5/2}} \kappa_{\|} \tag{6.3.1}$$

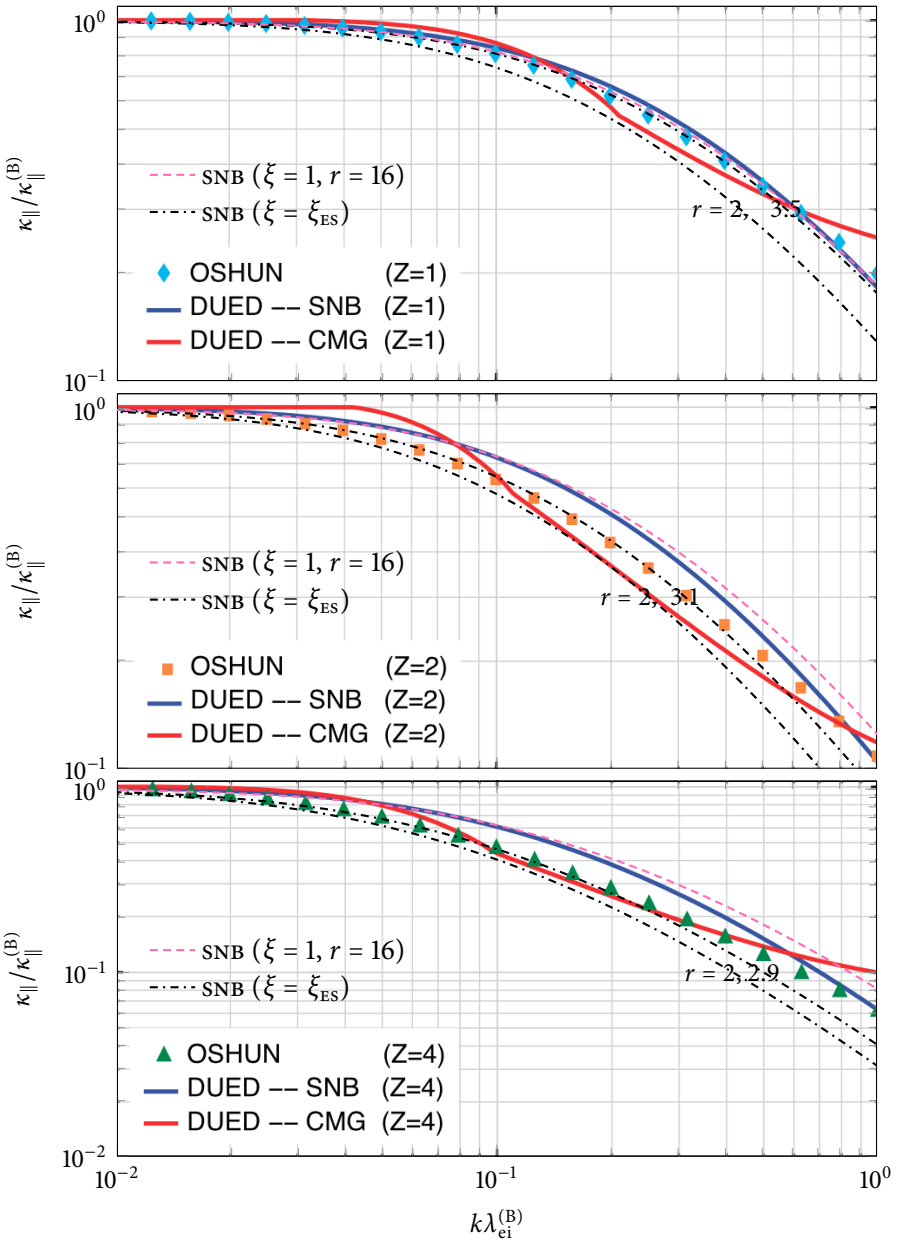

FIGURE 6.1: Thermal conductivity reduction as a function of nonlocality parameter for a low-amplitude temperature sinusoid with ionisations $Z = 1$, 2 and 4. Figures are reproduced from (Marocchino et al. 2013) with different implementation choices of the in-house SNB model overlaid.

where the temperature was interpolated from cell centres to boundaries using a simple arithmetic average. The value of $\kappa_{\|c}^{(\mathrm{B})}$ inferred from the HYDRA simulation was found to be 7–8% higher than that predicted by Epperlein and Haines (1986, γ_0 in Tab. IV). Much more surprising was the variation of $\kappa_{\|c}^{(\mathrm{B})}$ in space; HYDRA predicted it to increase at the lower temperatures found on the right-hand side (illustrated for helium in the middle panel of fig. 6.2). After eliminating differences in numerical differencing and the Coulomb logarithm as a potential source of disagreement, the only explanation remaining for this spatial variation is intrinsic differences in the HYDRA Lee-More conductivity model compared to the Epperlein-Haines model.

To avoid discrepancies in local heat flows propagating through to the nonlocal, the HYDRA local heat flow was fed into the source term of the in-house SNB model. The version of the SNB model with the geometrically averaged mfp $\lambda_\mathrm{e} = \sqrt{\lambda_\mathrm{ei}\lambda_\mathrm{ee}}$ was used, in alignment with the implementation of HYDRA at the time. Comparing the supposed $r = 2$, ξ_ES and the suggested $r = 2$, $\xi = \xi_\mathrm{ES}$ for the helium and nitrogen problems in figs. 6.2 and 6.3 respectively confirms that changing the implementation of the HYDRA SNB accordingly should significantly improve agreement with kinetic results, reducing the overestimation of peak heat flow for the nitrogen heating from 55% to 1.3%. Two possible sources of differences between the HYDRA SNB and the in-house $r = 16$, $\xi = 1$ implementation are treatment of the electric field mfp limitation and a special added feature in the HYDRA SNB model to approximate the slowing down of fast electron due to the electric field; the latter is implemented by including the veloicity derivative of the EDF in the SNB PDE, thus linking all the groups together and requiring the equation set to be solved in a cascade from highest to lowest energy group.

While the disagreement between the HYDRA SNB and IMPACT does not seem overly concerning for these benchmark problems, the error increases at higher ionisations. Such conditions are often present in the highly-ionised gold bubble where ionisations reach up to $Z \approx 40$–50. The potential of the previous implementation of the HYDRA SNB to significantly overpredict the nonlocal heat flow by a factor of 2–3 in hohlraum relevant is revealed by applying the $r = 16$, $\xi = 1$ model to the gadolinium hohlraum problem studied in section 5.4.

In response to the observed issues in the HYDRA SNB, LLNL implemented the suggested changes of modifying the multiplier on the electron-electron mfp and incorporating the Epperlein-Short collision fix ξ and made this available to the HYDRA design team through the boolean switch `nletc_brodrick_cf`. Furthermore, the ability to separate mfp's to improve performance in steep ionisation gradient was provided by the switch `nletc_separate_lgs`. The first of

these switches has been confirmed to agree with the calibrated version of the SNB model ($r = 2$, $\xi = \xi_{ES}$) for the helium thermal ramp relaxation and the nitrogen laser heating problems as well as a number of low-amplitude sinusoid problems. However, validation of the mfp separation is still underway

6.4 THE SNB MODEL IN CHIC

The last benchmarking comparison was performed on the SNB model in CHIC, originally implemented by the developers of the model: Schurtz et al. Since its creation the model has gone through a number of evolutions, and, by careful calibration with the in-house SNB model and collaboration with researchers at CELIA (particularly Philippe Nicolaï and Jean-Luc Feugeas), the CHIC SNB was found to well replicated by the separated SNB's with a multiplier on the electron-electron MFP of $r = 2\sqrt{2}$ but with the collision fix neglected (i.e. $\xi = 1$). This perhaps surprising choice of multiplier can be explained in two steps: Firstly, the original SNB model incorporated a factor of ½ into the geometrically average MFP λ_e in order to obtain agreement with the LMV kernel (Luciani et al. 1983) (see first eq. on p. 4242 of Schurtz et al. 2000); if the mfp's are then separated and all correction factors rolled solely on to the electron-electron mfp then this is equivalent to using a factor of $r = 4$. Secondly, the electron-electron collision frequency is reduced by a factor of $\sqrt{2}$ due to a suggestion of Decoster et al. (Decoster et al. 1998), giving $r = 2\sqrt{2}$.

The two benchmark problems shown here to support the given interpretation of the CHIC SNB are the helium tanh thermal ramp relaxation problem (presented in section 5.2) and, once again, the gadolinium hohlraum problem. The heat flow comparisons presented in figs. 6.5 and 6.6 do not appear too conclusive as to which implementation is the most accurate. This should not be too surprising as the CHIC SNB is only a factor of $2^{1/4}$ more local in the Lorentz limit and just under 1.4 times more *nonlocal* when $Z = 2$ (as the estimated degree of nonlocality is affected by the factor $\sqrt{\xi/r}$ contained in the geometrically averaged mfp λ_e). If we had extended our benchmarking to a hydrogen test case, the differences would have surely increased. Furthermore, it is clearly not desirable to neglect the collision fix as is done in CHIC because this would fail to recover the ionisation dependence of the nonlocal deviation in the semicollisional regime predicted by the EIC model in section 4.3.5.

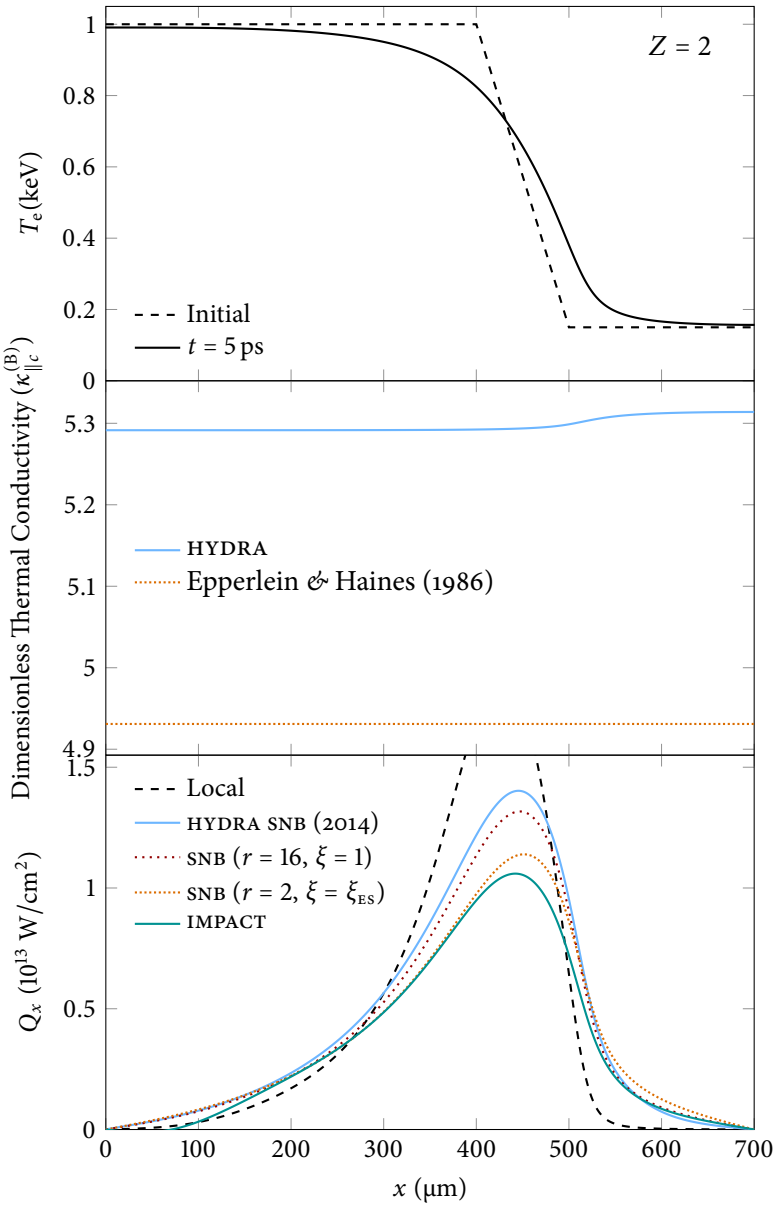

FIGURE 6.2: Initial and final IMPACT temperature profiles (top panel) for the helium linear ramp relaxation problem used to benchmark the HYDRA SNB model, followed by a comparison of the dimensionless thermal conductivity corresponding to the *local* HYDRA heat flow with that of Epperlein and Haines (1986). The nonlocal HYDRA SNB heat flows at 15 ps are compared to IMPACT and two possible implementations of the in-house SNB model (here using the geometrically averaged mfp λ_e and using the local HYDRA heat flow in the source term).

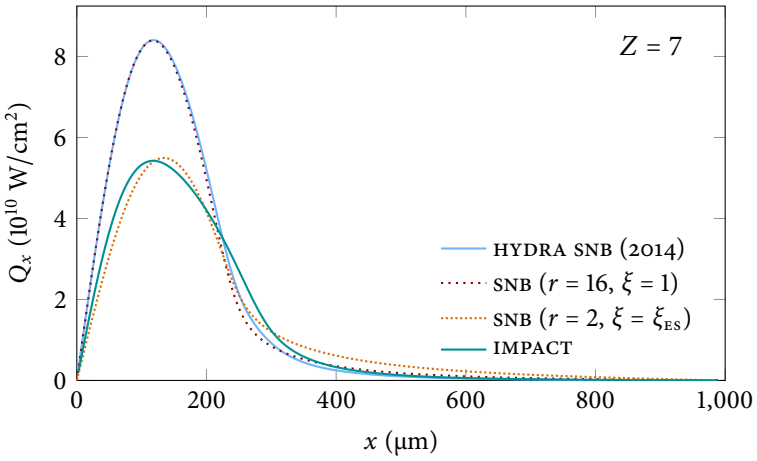

FIGURE 6.3: Heat flow profiles after 15 ps relaxation of helium thermal ramp with IMPACT. Local profile is not shown as peak is about 4 times higher than IMPACT.

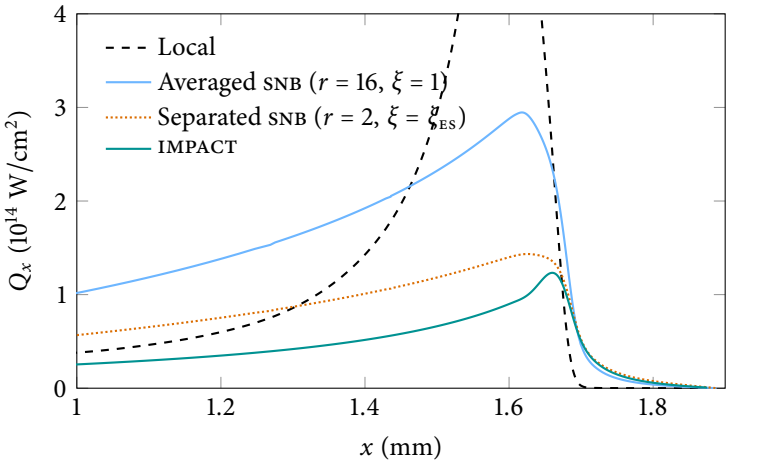

FIGURE 6.4: Comparison of postprocessed heat flow predictions for the gadolinium hohlraum problem at 20.005 ns using the current HYDRA implementation with the averaged mfp λ_e and $r = 16$, $\xi = 1$ with the suggested $r = 2$, $\xi = \xi_{ES}$ SNB model using separated electron-ion and electron-electron mfp's. The maximum local heat flow is 2.2×10^{15} W/cm^2.

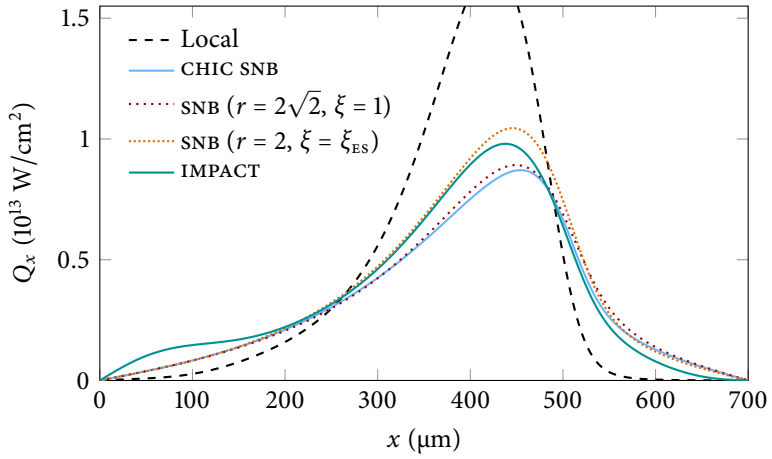

FIGURE 6.5: Comparison of the CHIC SNB with the in-house SNB model and IMPACT for the helium tanh ramp relaxation problem presented in section 5.2 at 12.1 ps.

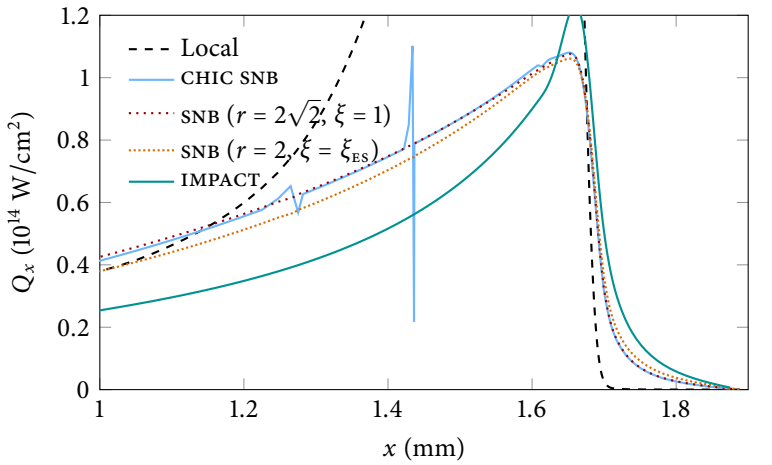

FIGURE 6.6: Comparison of postprocessed heat flow predictions for the gadolinium hohlraum problem at 20.005 ns between CHIC and the in-house SNB with $r = 2$, $\xi = \xi_{ES}$ SNB model. Both models here have removed the electric field correction the mfp (i.e. $E_{mult} = 0$). The kinks in the CHIC heat flow are probably due to the specific differencing methodology used by CHIC struggling to handle the very specific profile supplied to it on a non-uniform grid.

7

NONLOCAL NERNST ADVECTION

In this chapter, the existing research on the nonlocal Nernst effect is consolidated by comparing VFP and flux-limited transport approaches at high and low ionisations. A theoretical overview will first be presented in section 7.1 to discuss the dominant terms governing the evolution of temperature and magnetic field profiles in the following simulations. A wide range of one-dimensional test problems are considered here including relaxation of a temperature ramp with an initially uniform imposed magnetic field in section 7.2, laser heating of nitrogen in section 7.3 and a lineout from an indirect-drive HYDRA simulation in section 7.4. The main observation is that while both thermal conduction and Nernst advection can be strongly affected by nonlocality, their ratio is not. This allows for a simple method of extending nonlocal thermal transport models, such as the SNB, to approximate the Nernst velocity.

7.1 MAGNETISED TRANSPORT IN ONE DIMENSION

For simplicity, the problems considered here will be limited to spatial variation in one direction (x) only. In particular, this avoids the possibility of self-generated fields due to the Biermann battery or other anisotropic effects. For a magnetic field pointing solely in the z-direction, the evolution of the magnetic field and temperature profile are determined by

$$\frac{\partial B_z}{\partial t} = -\frac{\partial E_y}{\partial x}, \quad \frac{\partial T_e}{\partial t} = -\frac{2}{3n_e}\left(\frac{\partial Q_x}{\partial x} + \frac{E_y}{\mu_0}\frac{\partial B_z}{\partial x}\right), \tag{7.1.1}$$

where E_y is the electric field in the y-direction and Q_x is the heat flow parallel to the temperature gradient. The final term is the Joule heating term, $\vec{E} \cdot \vec{j}$, where the electric current $\vec{j}$ has been substituted with $\vec{\nabla} \times \vec{B}/\mu_0$ using Ampere's law with the displacement current neglected. In the VFP simulations presented in this chapter the magnetic field gradients are not very steep, meaning that this term is not as important as the heat flow divergence in determining the plasma temperature.

Both temperature and magnetic field gradients contribute to their own and each other's evolution. Only four transport effects exist in this 1D geometry under the assumption of cold ion:

$$Q_x = \underbrace{-\kappa_\perp \frac{\partial k_\mathrm{B} T_\mathrm{e}}{\partial x}}_{\textit{Thermal Conduction}} + \underbrace{\frac{\beta_\wedge k_\mathrm{B} T_\mathrm{e}}{e\mu_0}\frac{\partial B_z}{\partial x}}_{\textit{Ettingshausen Effect}}, \tag{7.1.2}$$

$$E_y = \underbrace{-\frac{\beta_\wedge}{e}\frac{\partial k_\mathrm{B} T_\mathrm{e}}{\partial x}}_{\textit{Nernst Advection}} - \underbrace{\frac{\alpha_\perp}{e^2 n_\mathrm{e}\mu_0}\frac{\partial B_z}{\partial x}}_{\textit{Resistive Diffusion}}. \tag{7.1.3}$$

Again, the weak magnetic field gradients present mean that the Ettingshausen effect and resistive diffusion are small corrections to the Nernst and thermal conduction terms, and are therefore not discussed in too much detail here. Additionally, the heat flow perpendicular to both the magnetic field and temperature profile, is given by

$$Q_y = \underbrace{-\kappa_\wedge \frac{\partial k_\mathrm{B} T_\mathrm{e}}{\partial x}}_{\textit{Righi-Leduc Heat Flow}} + \underbrace{\frac{\beta_\perp k_\mathrm{B} T_\mathrm{e}}{e\mu_0}\frac{\partial B_z}{\partial x}}_{\textit{Peltier Effect}}. \tag{7.1.4}$$

Once again, only the first term is usually dominant in the cases studied here.

7.2 TEMPERATURE RAMP RELAXATION

7.2.1 *Methodology*

The temperature tanh ramp relaxation problems presented in section 5.2 were repeated for helium ($Z = 2$) and zirconium ($Z = 40$) but with the addition of an initially uniform magnetic field. As a reminder, a fixed and uniform electron density of 5×10^{20} cm^{-3}. and constant Coulomb logarithm of 7.09433 were used in both cases. The initial temperature profile connecting the two regions of 1 keV and 150 eV was given by

$$T_\mathrm{e}/\mathrm{eV} = 575 - 425\tanh(x/L), \tag{7.2.1}$$

where the initial scalelength L was 50 μm for the helium simulations and 17.3 μm for the zirconium in order to impose a similar degree of nonlocality. The simulation domains extended to $\pm 7L$, and reflective boundary conditions were used,

restricting heat flow and electric field values to be zero at the boundaries. A range of initial magnetic fields were considered. For convenience, a formula to calculate the magnetisation in the hottest and coldest regions of the plasma is provided here:

$$\chi^{(1\text{ keV})} = 0.54 \times (B_z/\text{tesla})/Z, \tag{7.2.2}$$

$$\chi^{(150\text{ eV})} = 0.031 \times (B_z/\text{tesla})/Z. \tag{7.2.3}$$

The helium simulations were performed using the K2 and OSHUN VFP codes due to their use of the full anisotropic electron-electron collision operator, which was necessary to achieve acceptable values of $\beta_\wedge$ at low ionisations (recall the errors arising from instead using the collision fix noted in fig. 2.2). Typically, the K2 simulations used spherical harmonics up to order 1, and the OSHUN simulations up to order 2. The codes showed reasonable agreement with each other and slight discrepancies were attributable to the number of harmonics used and exact implementation of boundary conditions, but only K2 simulations are presented here. An artificial multiplier of 100 on the permittivity ε_0 was used in the Ampere-Maxwell law with K2, allowing for manageable timesteps of 0.5 fs. The simulation domain extended from −350 μm to 350 μm over 100 cells (7 μm in width) and the uniform velocity grid consisted of 240 cells peaking at 9.4×10^6 m/s (25 keV).

For the zirconium simulations, IMPACT was used instead, as the percentage error on the Nernst coefficient $\beta_\wedge$ due to neglecting the effect of electron-electron collisions on the anisotropic part of the EDF is below 10% at such high ionisations. The reason for using the collision fix here was the absence of local transport coefficients for $Z = 40$ in the literature to compare with the classical transport simulations (although these could be derived). The electron inertia term ($\frac{\partial f_1}{\partial t}$) was retained. The simulation parameters used were a spatial domain extending from $-9L$ to $7L$ over 800 cells (each with a width of 3.46 μm), a uniform velocity grid extending up to 1.8×10^7 m/s (94 keV) and a timestep of 3.35 fs.

The distribution functions for all VFP simulations were initialised as isotropic Maxwellians, with the anisotropic part (and thereby the heat flow) and electric field initially growing from zero. Initial transient effects damped within 12 ps in the helium and 2 ps in the zirconium simulations (equivalent to about 4 corrected collision times, $\xi\tau_{\text{ei}}^{(\text{B})}$, of suprathermal 3–4 keV electrons); this was determined by both Q_x and E_y reaching a maximum. It is observed that the electric field takes longer to reach its peak than the heat flow, most likely due to the Nernst coefficient $\beta_\wedge$ depending on higher moments of the EDF than $\kappa_\perp$ (see section 2.2.1), making

it more sensitive to the dynamics of less collisional high-energy electrons. The magnetic field and temperature profiles at this point of the simulations (12 ps for helium, 2 ps for zirconium) were then used to initialise classical transport simulations with various combinations of Nernst and thermal flux-limiters.

The Classical Transport Code (CTC) (see section 3.2) was used to provide local and flux-limited Braginskii comparisons to the kinetic simulations. For the zirconium simulation the Lorentz limit transport coefficients were used but multiplied the average collision time $\tau_{ei}^{(B)}$ by the Epperlein-Short collision fix ξ_{ES}. Neither hydrodynamics nor super-Gaussian transport coefficients were included in the simulation. Independent values of Nernst and thermal flux-limiters, implemented as described in section 2.3.1, were investigated.

7.2.2 *Results*

Instantaneous snapshots of perpendicular heat flow (Q_x), Righi-Leduc heat flow (Q_y) and the Nernst-relevant out-of-plane electric field (E_y) at the end of the initial transient periods are respectively presented in the top, middle and bottom panels of figs. 7.1 to 7.4 for selected simulations: Low and high magnetisation helium runs are presented in figs. 7.1 and 7.2 corresponding to initial magnetic fields of 0.1 tesla and 2 tesla respectively, while zirconium profiles resulting from initial magnetic fields of 1 tesla and 10 tesla respectively are provided in figs. 7.3 and 7.4. As results from the various simulations are qualitatively similar we shall discuss them all simultaneously. These profiles will first be compared to the local Epperlein and Haines transport theory before considering the instantaneous and time-integrated effects of using flux-limiters. Finally, section 7.2.3 will feature an exploration of a simple method of adapting existing reduced nonlocal thermal transport models such as the SNB.

With respect to the local predictions it is clear that there are both flux-reduction and preheat effects in the Q_x and Q_y heat flow profiles, but these nonlocal effects are much more pronounced for the Righi-Leduc heat flow due to its dependence on higher moments of the distribution function (see section 2.2.1). On the other hand, the transverse electric field E_y mainly experiences a shift in the peak toward the cooler region of the plasma with little reduction in its actual value and in fact an *increase* of the value of the electric field in the colder region of the plasma where the temperature gradient is relatively flat, which shall be referred to as 'pre-Nernst.' These observations are qualitatively similar to those previously seen by both Kho and Haines (1985, 1986) and Hill and Kingham (2017).

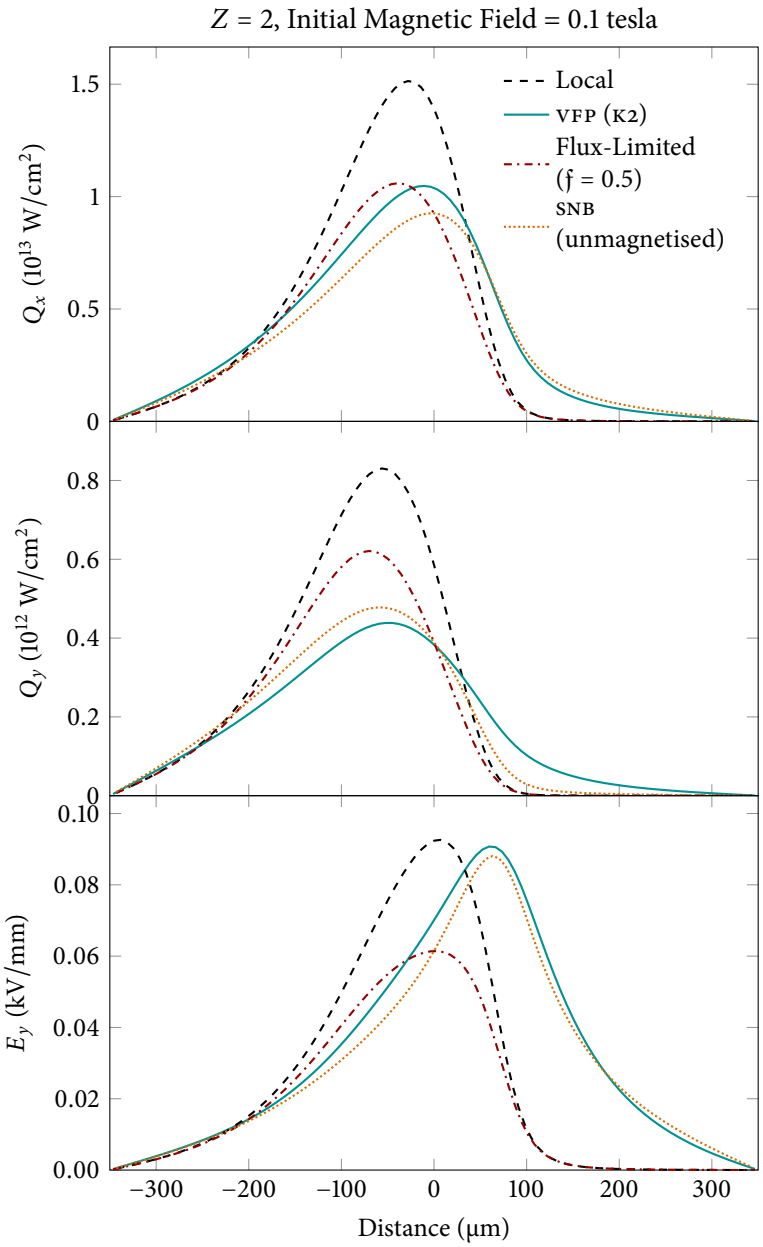

FIGURE 7.1: Perpendicular and Righi-Leduc heat flows Q_x (top), Q_y (middle) and the Nernst-dominated out-of-plane electric field E_y (bottom) after 15 ps K2 VFP helium simulation with an initial magnetic field of 0.1 tesla. Local, flux-limited and SNB profiles were postprocessed using the K2 temperature and magnetisation profiles. SNB E_y and Q_y are calculated by multiplying the (unmagnetised) SNB Q_x profile by the corresponding ratio in the local limit (E_y/Q_x, Q_y/Q_x).

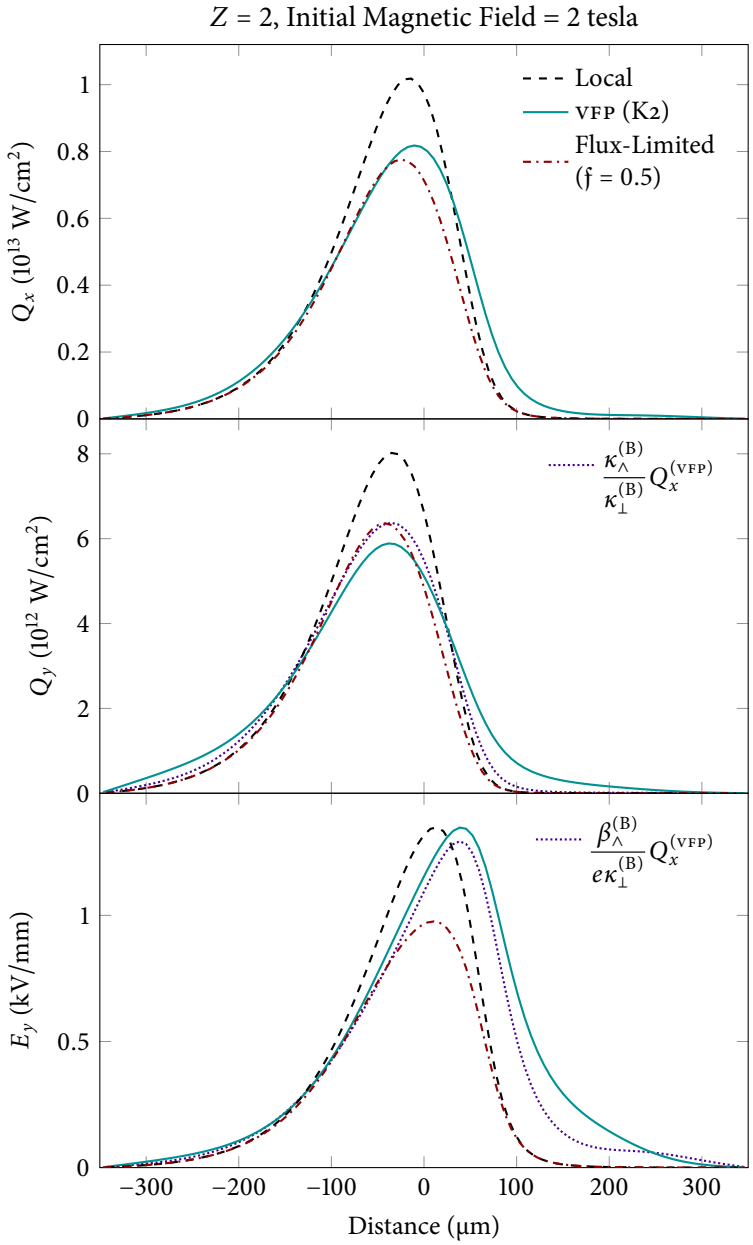

FIGURE 7.2: Perpendicular heat flow Q_x (top), Q_y (middle) and the Nernst-dominated out-of-plane electric field E_y (bottom) after 12 ps K2 VFP helium simulation with an initial magnetic field of 2 tesla. Local and flux-limited profiles were postprocessed using the K2 temperature and magnetisation profiles.

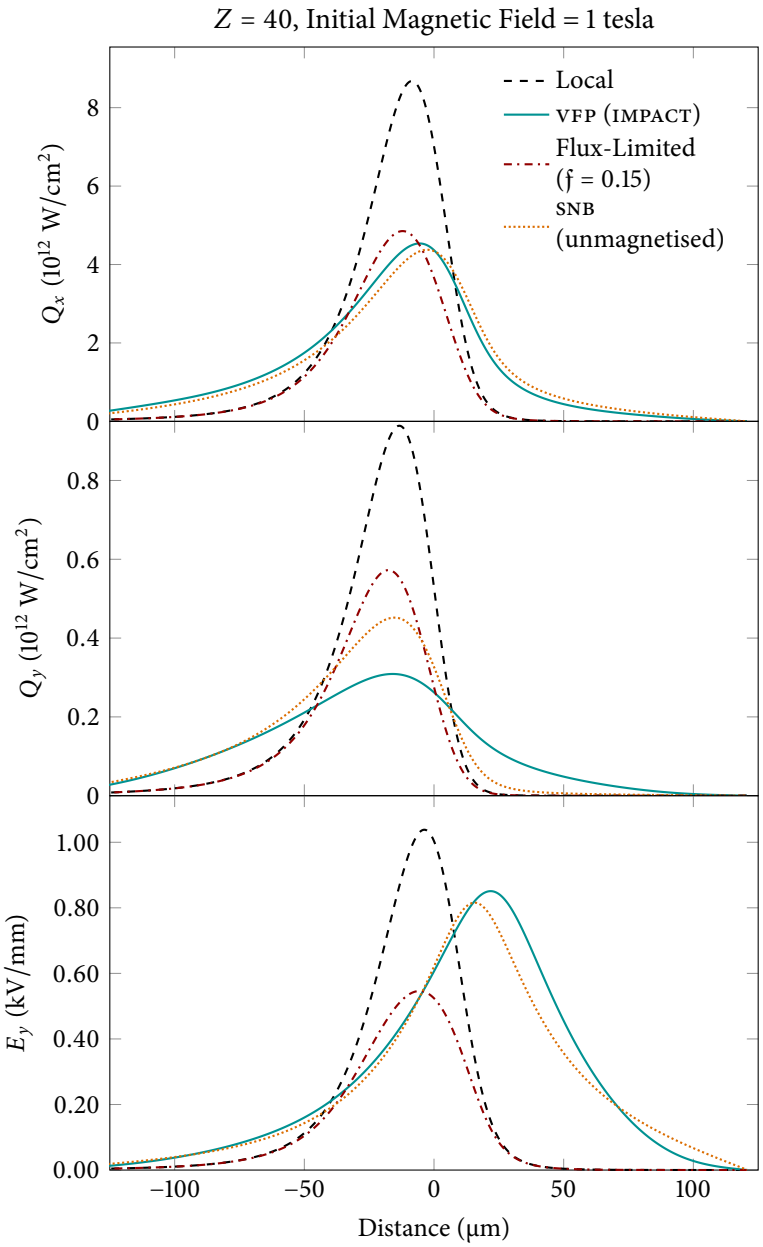

FIGURE 7.3: Perpendicular and Righi-Leduc heat flows Q_x (top), Q_y (middle) and the Nernst-dominated out-of-plane electric field E_y (bottom) after 4 ps IMPACT VFP zirconium simulation with an initial magnetic field of 1 tesla. Local, flux-limited and SNB profiles were postprocessed using the IMPACT temperature and magnetisation profiles. SNB E_y and Q_y are calculated by multiplying the (unmagnetised) SNB Q_x profile by the corresponding ratio in the local limit (E_y/Q_x, Q_y/Q_x).

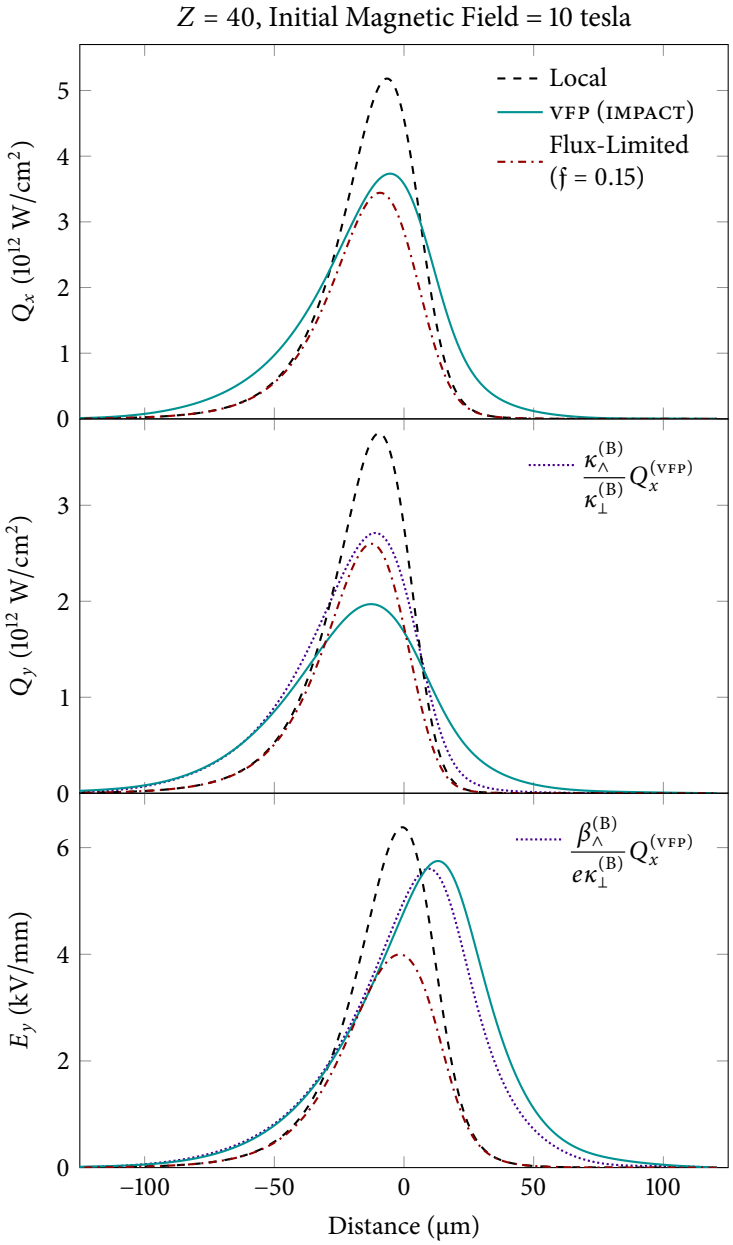

FIGURE 7.4: Perpendicular and Righi-Leduc heat flows Q_x (top), Q_y (middle) and the Nernst-dominated out-of-plane electric field E_y (bottom) after 4 ps IMPACT VFP zirconium simulation with an initial magnetic field of 10 tesla. Local and flux-limited profiles were postprocessed using the IMPACT temperature and magnetisation profiles.

It may seem surprising that, despite the similar degrees of nonlocality and relative flux-limitation of the helium and zirconium simulations, the actual values of flux-limiters deemed optimal which best matched the kinetic heat flow profiles turn out to be quite different (0.5 for helium and 0.15 for zirconium). However, this is simply due to differences in the Z-dependence of the perpendicular thermal conductivity $\kappa_\perp \propto \xi/Z$ and the nonlocality parameter $\sqrt{\xi Z}\lambda_{\mathrm{ei}}^{(\mathrm{B})}|\nabla T_\mathrm{e}|/T_\mathrm{e} \propto \sqrt{\xi/Z}$. The maximum nonlocality parameter in both the helium and zirconium simulations was arranged to be approximately equal to 0.1 by using different length scales $L \propto \sqrt{\xi/Z}$. Therefore, in order to obtain equivalent flux-limiting factors $\theta_Q = Q_x^{(\mathrm{FL})}/Q_x^{(\mathrm{Local})}$ (see eq. (2.3.5)), the thermal flux-limiters f_Q need to make up a further factor $\sqrt{\xi/Z}$ to fully compensate the ionisation-scaling of the thermal conductivity. This explains the discrepancy in their optimal values: $\sqrt{40/\xi(40)}0.15 \approx \sqrt{2/\xi(2)}0.5$. If different values for L had not been used, the values of the thermal flux-limiters would have indeed been similar to each other, but the resulting flux-limitation factors θ_Q would be closer to unity for zirconium than helium. These observations suggest that it is worth carefully considering whether the value of flux-limiter used in laser-plasma codes should be made material dependent, perhaps through an inline calculation of the nonlocality parameter at each point in space.

The appearance of the multiplier $\sqrt{Z}$ in the nonlocality parameter dates back at least as far as seminal work by Luciani, Mora and Virmont (1983), and the later incorporation of the collision fix can be traced back to Epperlein and Short (1991). To further understand this consider the dependence of the heat flow on $\xi Z k^2 \lambda_{\mathrm{ei}}^{(\mathrm{B})2}$ in the semicollisional regime given in eq. (4.3.1).

As magnetic fields should in theory relocalise the transport it may seem surprising that the optimal flux-limiter value does not appear to depend greatly on magnetisation. Nevertheless, the heat flow does indeed approach its local value as higher magnetisations are reached. This is possible because of the reduction of the *local* heat flow in the presence of strong magnetic fields to well below the free-streaming limit.

Looking at the E_y profiles which determine the evolution of the magnetic field due to Nernst advection, we see that using the same flux-limiter as for Q_x gets the profile about right in the hot region of the plasma. However, doing so grossly underestimates the *peak* electric field and the flux-limiter approach inherently fails to capture any of the prominent pre-Nernst observed. The former observation in particular suggests that perhaps it would be desirable to use a larger Nernst flux-limiter in order to match the peak. Contrastingly, it is clear that a *lower* flux-limiter is necessary on the Righi-Leduc heat flow to capture its higher degree of flux suppression due to nonlocality.

The results shown in figs. 7.1 to 7.4 are sufficiently early in the simulations that the magnetic field profile has not evolved significantly. The top panel of fig. 7.5 shows the magnetic field profiles predicted by K2 and CTC with varying combinations of flux-limiters at 200 ps for a helium simulation with an initial

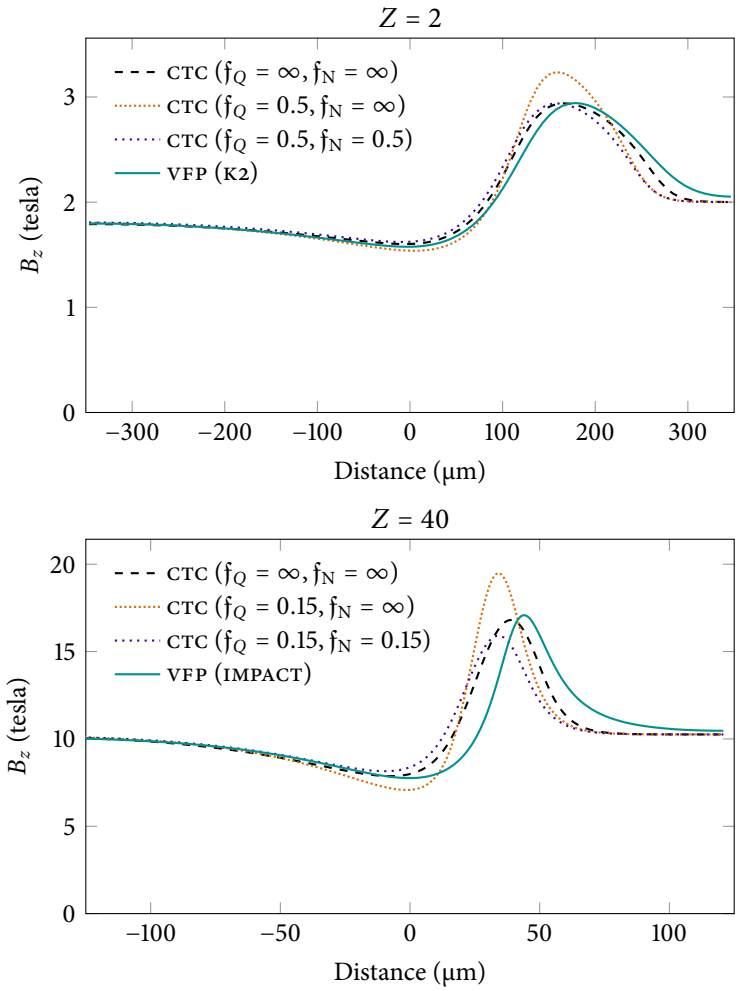

FIGURE 7.5: Comparison of magnetic field profiles predicted by the Classical Transport Code CTC with different combinations of thermal and Nernst flux-limiters f_Q, f_N respectively. Helium profiles (top) were evolved independently for a further 188 ps starting from the K2 T_e and B_z profiles at 12 ps, while the zirconium profiles (bottom) were simulated independently for a further 48 ps from the IMPACT profiles at 2 ps.

magnetic field of 2 T (recall that the classical transport simulation was started 12 ps in) and a similar comparison between IMPACT and CTC for the 10 T zirconium at 50 ps (with CTC starting at 2 ps) in the bottom panel. It is observed that when using only a thermal flux-limiter (orange dash-dotted), as is traditional , the relative amplification of the magnetic field is overestimated, by over 30% for the case of the zirconium simulation. Additionally, the degree of magnetic cavitation is also slightly overestimated by the traditional approach. Incorporating a Nernst limiter noticeably improves agreement with VFP but does not account for the smearing and shifting of the peak beyond the foot of the temperature gradient. Despite these noticeable differences in the final magnetic field profiles these were not sufficient to cause distinguishable modifications on the final temperature profiles.

Although Nernst advection in the zirconium simulation might be considered slightly over-constrained by a limiter of 0.15, it still seems that the most sensible method of limiting Nernst advection is to always use $f_N = f_Q$ as other choices are ad hoc and cannot be justified physically. This also conveniently prevents the undesirable introduction of an additional tunable parameter. Also note that when instead dispensing with flux-limiters completely in these simulations (i.e. $f_N = f_Q = \infty$) the best agreement with the VFP magnetic field profiles is achieved as the cold plasma is allowed to heat up quicker, thereby enhancing the spread of magnetic field. However, it would indeed be preferable to go beyond flux-limiters to a more predictive approach, such as a reduced nonlocal model, that could account for the prominent smearing and delocalisation effects of pre-Nernst observed.

7.2.3 *Potential of the SNB Model*

Previous chapters have demonstrated that the SNB model is able to fairly accurately capture both flux reduction and preheat effects for a wide range of fusion-relevant problems; however, the model traditionally gives no prescription for nonlocal modifications to Nernst advection. Of course, if a relation between the energy group contribution H_g and the nonlocal perturbation to the isotropic part of the EDF δf_0 were proven to be reliable and accurate, this would provide a simple method of calculating corrections to the Nernst coefficient $\beta_\wedge$ by taking moments of the EDF (see, for example, eq. (2.2.20)). But we have seen in both chapter 4 and (Sherlock et al. 2017) that the original method of reconstructing the EDF given by Schurtz et al. (2000), $H_g = 2\pi m_e v_g^5 \delta f_0 \, \mathrm{d}v_g$, does not agree well with VFP predictions. And while the alternative link identified in section 4.3.6

does accurately capture the high-velocity behaviour of δf_0 for a long-wavelength temperature sinusoid, it may be less accurate for other problems. Therefore, it would be desirable to come up with a more reliable method of using the SNB model to account for nonlocal Nernst advection.

One such approach of extending the SNB model is to use the observation that the ratio between the Nernst and heat flow velocities does not depend greatly on nonlocality (Haines 1986a; Kho and Haines 1985, 1986). Specifically, if a good approximation for the nonlocal heat flow can be obtained (such as from the SNB model) then we should be able to estimate the nonlocal electric field by simply multiplying the former by the ratio expected in the local limit: $\beta_\wedge^{(\mathrm{B})}/e\kappa_\perp^{(\mathrm{B})} \equiv B\Psi^{(\mathrm{B})}/P_\mathrm{e}$. That is, $E_y^{(\mathrm{Nonlocal})} \approx (B\Psi^{(\mathrm{B})}/P_\mathrm{e})Q_x^{(\mathrm{Nonlocal})}$. The wide range of problems investigated here provide a perfect opportunity to thoroughly test whether this approximation is indeed accurate and reliable.

Although a magnetised extension of the SNB model has been developed and is implemented in the CHIC code (Nicolaï et al. 2006), this has not yet been extensively tested against VFP simulations. Therefore, the *unmagnetised* model is simply applied to simulations with low magnetisations ($\chi < 0.03$) in which the heat flow and degree of nonlocality are not strongly affected by the presence of a magnetic field. The specific SNB implementation used here corresponds with the optimal one identified in the previous chapter, consisting of (1) imposing a scaling factor on the Krook electron-electron collision frequency of $r = 2$, (2) separating the electron-electron and electron-ion mfp's, and (3) multiplying the electron-ion mfp by the collision fix ξ.

The bottom panels of figs. 7.1 and 7.3 include the results of using this approximation for the helium 0.1 tesla and zirconium 1 tesla simulations. Temperature and magnetic field profiles at 15 ps and 4 ps respectively were used to calculate the SNB heat flow before converting this to an estimate for E_y. It is observed that this method for obtaining the SNB electric field exhibits remarkable agreement with VFP, closely matching both the degree of flux reduction and the preheat at very little additional computational cost.

At higher magnetisations, the claim that nonlocality does not affect the link between thermal conduction and Nernst advection was instead tested by multiplying the VFP heat flow by the ratio $B\Psi^{(\mathrm{Local})}/P_\mathrm{e}$. This is depicted for the 2 tesla helium and the 10 tesla zirconium runs in the bottom panels of figs. 7.2 and 7.4 respectively. Again, the ratio method provides a good approximation for E_y, with the main discrepancy being a slight underestimate of the pre-Nernst on the right-hand side. This discrepancy arises due to the dependence of $\beta_\wedge$

on higher-velocity moments of the EDF than $\kappa_\perp$ (see eqs. (2.2.18) and (2.2.20)), making it more sensitive to nonlocal effects.

All findings are summarised in fig. 7.6 which presents the nonlocal VFP prediction for the dimensionless ratio $\Psi^{(\mathrm{VFP})} = P_\mathrm{e} E_y^{(\mathrm{VFP})}/BQ_x^{(\mathrm{VFP})}$ as a function of magnetisation for both helium and zirconium temperature ramp relaxation simulations. Profiles were extracted at 25 ps for the helium simulation and 5 ps for the zirconium. It is shown that Ψ approximately follows the local prediction indicated by the dashed lines, clearly exhibiting a strong ionisation dependence that would not be captured by the constant ratio approximations suggested by other authors (Haines 1986a; Davies et al. 2015; Lancia et al. 2014). The prominent flick-ups seen at the low magnetisation end (left-hand side) of this figure correspond to the increased reach of pre-Nernst as compared to pre-heat arising from the dependence of $\beta_\wedge$ on higher-velocity moments of the EDF.

The effectiveness of using a similar process to estimate the Righi-Leduc heat flow as $Q_y^{(\mathrm{Nonlocal})} \approx (Q_x^{(\mathrm{B})}/Q_y^{(\mathrm{B})})Q_x^{(\mathrm{Nonlocal})}$ was also investigated in the middle panel of figs. 7.1 to 7.4. However, this approach underestimates the degree of flux-limitation and does not capture the high degree of preheat arising from the higher velocity moments used in calculating the Righi-Leduc heat flow. Nevertheless, it is still a definite improvement on both the local Braginskii and flux-limiter approaches at lower magnetisations.

7.3 LASER SPOT HEATING

As the degree of nonlocality for the temperature ramp relaxation problem at high magnetisations was not sufficient to cause observable differences in the final temperature profiles, even after tens of collision times, a laser-heating problem where the degree of nonlocality continually increases with time was also studied. This included a fully-ionised nitrogen plasma ($Z = 7$) of uniform electron density 1.5×10^{19} cm^{-3} and an assumed constant Coulomb logarithm of 7.5 being heated by a continuous 6.3×10^{13} W/cm^2 laser (no time envelope was applied here). The intensity profile was essentially uniform in the y and z directions and Gaussian in the x-direction with a full width at half maximum of 150 μm. Again ion motion was neglected. This setup is based on an experiment performed by Froula et al. (2007) that has previously been simulated with IMPACT by Ridgers et al. (2008a). This time round the K2 code was used to correctly account for the effect of electron-electron collisions on the anisotropic part of the distribution function and a simplified one-dimensional geometry employed for the sake of keeping runtimes short. (Thus, the beam profile is planar rather than cylindrical.)

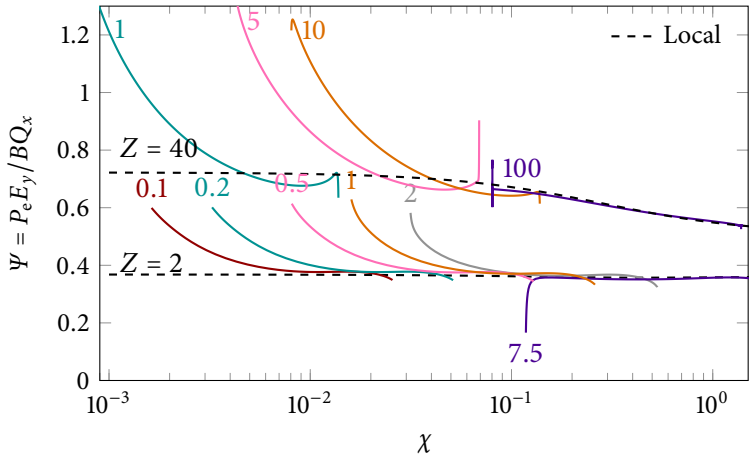

FIGURE 7.6: Solid coloured lines show the variation of $\Psi = P_e E_y / BQ_x$ (proportional to the ratio of nonlocal Nernst and heat flow velocities) with magnetisation χ after 25 ps VFP simulation for the helium runs (bottom) and 5 ps for the zirconium (top). Colors differentiate between values of the initial magnetic field, which are labelled in units of tesla. Dashed lines show the prediction for Ψ in the local limit. The proximity of the centre of the colored lines to the dashed shows that the ratio between the peak magnetic and electric field is not strongly affected by nonlocality (and is in fact more affected by ionisation). The 50% overestimate of the local prediction at low magnetisations shows that the pre-Nernst advecting magnetic field beyond the temperature gradient is more pronounced than preheat. At higher magnetisations, nonlocality is unimportant at such early times and the observed dip in the value of Ψ for the 7.5 T run at low temperatures is simply a numerical feature due to the small values of E_y and Q_x in these regions.

Furthermore, the plasma had an initially uniform temperature of 50 eV which was slightly higher than the 20 eV previously simulated by Ridgers et al. to reduce the number of velocity cells required. A total of 250 velocity cells were used extending up to $v_{max} = 25 v_{1T}(50\,\text{eV})$, corresponding to electrons with an energy of 15.6 keV. The spatial domain, consisting of 100 cells, extended to 500 μm from the centre of the pulse and again reflective boundary conditions were used, with a timestep of 2 fs. The initial magnetic field was simply a uniform 4 tesla.

Due to the initially uniform temperature profile, nonlocality did not begin to emerge until at least 50 ps. This meant that the CTC simulations could also be started from $t = 0$. Despite nonlocality continually increasing, a flux-limiter of 0.15 was found be a good match for the heat flow profile throughout most of the simulation. However, even at the end of the 600 ps simulation the nonlocal reduction of the heat flow down the temperature gradient was only about 10%. as shown in the top panel fig. 7.7 While the electric field in the bottom panel

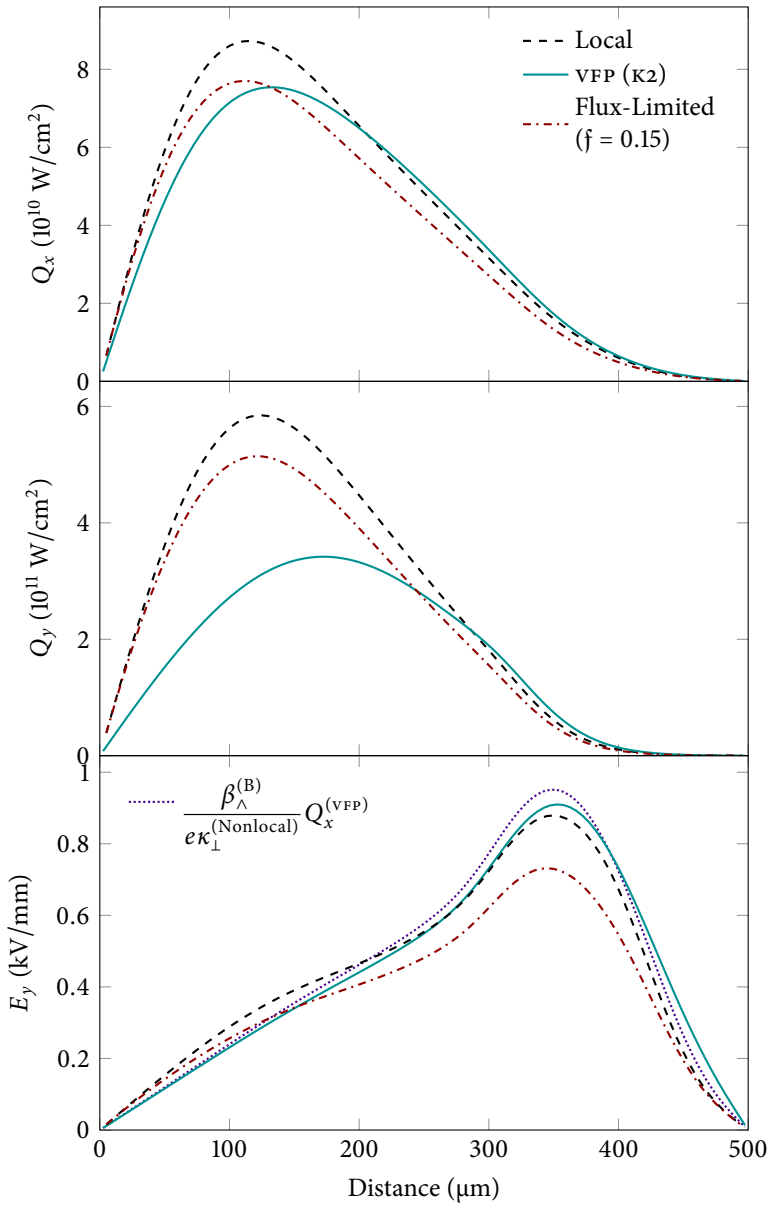

FIGURE 7.7: Perpendicular and Righi-Leduc heat flows Q_x (top), Q_y (middle) and the Nernst-dominated out-of-plane electric field E_y (bottom) after 600 ps K2 VFP simulation for the Froula-type heating problem with an initial magnetic field of 4 tesla. Local and flux-limited profiles were postprocessed using the K2 temperature and magnetisation profiles.

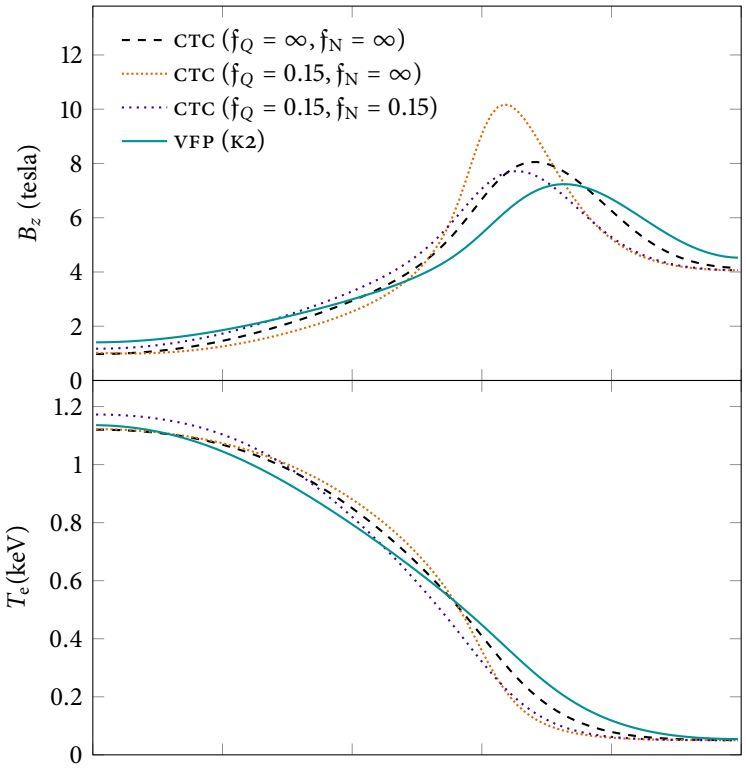

FIGURE 7.8: Comparison of magnetic field and temperature profiles for the nitrogen heating problem predicted by K2 and CTC with different combinations of thermal and Nernst flux-limiters f_Q, f_N respectively. All profiles were evolved independently from an initial temperature of 50 eV and magnetic field of 4 T for 600 ps.

experiences a similar reduction near the position of maximum heat flow, its peak is actually increased. This may seem surprising but is explained by its occurrence in a region where preheat naturally occurs (near the foot of the temperature gradient at 400 μm), thus enhancing the Nernst velocity due to a surplus of suprathermal electrons coming from the centre of the hot spot.

Comparing to the CTC simulations we again observe that applying only a thermal flux-limiter leads to an overamplification of the peak magnetic field (fig. 7.8 top panel) at the end of the simulation by over 3 tesla (nearly 50%). In contrast, including a Nernst limiter reduces this error to less than 10%. However, there is still a nearly 50 μm discrepancy in the location of the magnetic field crest due to the inability of the flux-limiter approach to incorporate the effect of pre-Nernst. For this problem, there is a small but observable difference between the effect of the different approaches in the final temperature profiles shown in the bottom panel of fig. 7.8; while inclusion of a Nernst limiter slightly increases

the peak temperature it noticeably improves the prediction at 200–250 μm. Again the Righi-Leduc heat flow was found to experience a much more severe flux-limitation (the peak flux was reduced by a factor of ~50%).

7.4 LINEOUT FROM HYDRA SIMULATION WITH SELF-GENERATED FIELDS

The effectiveness of linking Nernst advection to thermal conduction in a more realistic scenario was confirmed by analysing a recent NIF viewfactor shot (MacLaren et al. 2014) that employed a Mn/Co microdot (Barrios et al. 2016) on the capsule surface for diagnostic purposes. Radial lineouts were taken from a 5 ns HYDRA simulation that used a thermal flux-limiter of $f_Q = 0.15$ (Farmer et al. 2018, see fig 3 and the bottom panel of fig 9 in); this employed the newly implemented MHD suite (including Nernst) outlined in (Farmer et al. 2017). These lineouts were located 3 mm from the centre of the capsule, starting in the low-density gas-fill at $r = 0$ and ending just inside the partially heated hohlraum wall at $r = 2.7$ mm, and used to initialise a 100 ps VFP relaxation simulation using 1D planar geometry. Again, only temperature and magnetic profiles were allowed to evolve while the density profile was fixed by neglecting ion hydrodynamics and using the zero current constraint. In order to maintain consistency with the rest of this chapter and to reinforce the fact that planar geometry was used, Cartesian coordinates x, y, z will be used in place of their cylindrical counterparts $r, z, (-)\phi$. The initial and final ionisation, electron density, temperature and magnetic field profiles are illustrated in fig. 7.9.

For this problem IMPACT was used to simplify treatment of the spatially-varying ionisation profile. When calculating the local/flux-limited heat flow and Nernst profiles this enabled us to use the Lorentz limit ($Z = \infty$) transport coefficients with a multiplier of ξ on all appearances of the collision time $\tau_{ei}^{(B)}$ instead of trying to interpolate between transport coefficients at other ionisations. Note that there is a loss of accuracy incurred by making this simplification, particularly at low ionisations; this error is worst around $x = 1$ mm where the ionisation is low and the magnetisation is not too high leading to an underestimate of the Nernst velocity by a factor of approximately two (see fig. 2.2). The simulation setup included a spatial cell width of 13.8 μm and a geometric velocity grid where the width in velocity-space of the highest energy cell (located at 225 keV) was 30 times larger than the lowest energy cell. A timestep of 25 fs was used the Coulomb logarithm taken to be constant at 4.1.

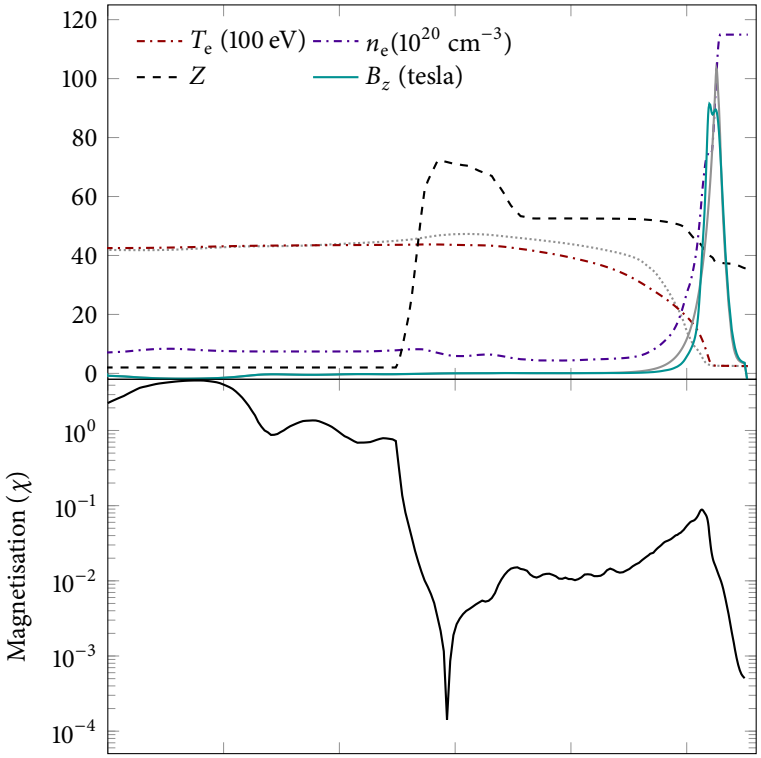

FIGURE 7.9: Spatial profiles of plasma temperature, electron density, ionisation, magnetic field, (top) and magnetisation (bottom) profiles based on a lineout after from a 5 ns HYDRA + 100 ps IMPACT simulation. The initial temperature and magnetic field profile input to IMPACT are shown in grey.

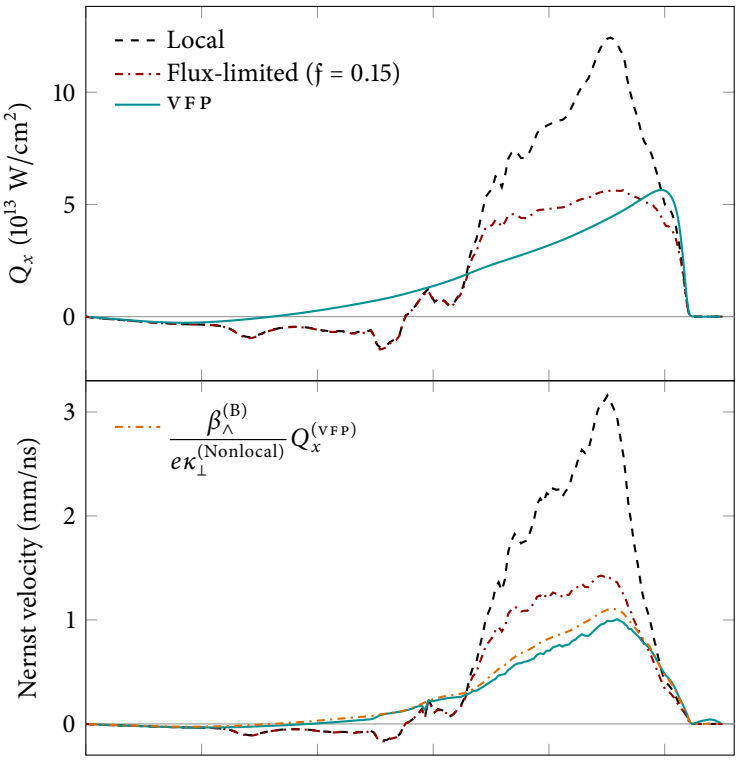

FIGURE 7.10: The heat flow (top) and Nernst velocity (bottom) for the HYDRA lineout after 100 ps IMPACT simulation.

The magnitude of the magnetisation is illustrated in the bottom panel of fig. 7.9, but note that this conceals the reversal of the magnetic field at about 1.45 mm. It is shown that, despite the magnetic field reaching megagauss levels in the hohlraum wall, the degree of magnetisation is actually quite low due to the very high collisionality in this region. Conversely, the highest levels of magnetisation (exceeding unity) are reached near the centre ($x = 0$) of the lineout, deep in the hot gas-fill. Therefore, instead of plotting the axial electric field E_y, which increases almost linearly with magnetic field and would be largest in the hohlraum wall where magnetisation effects are unimportant, the Nernst velocity $v_N = E_y/B$ itself is featured in the bottom panel of fig. 7.10. Note that the magnetisation profile does not change noticeably over the 100 ps simulation as it is highest in a region of relatively homogeneous temperature.

Reduction of the Nernst velocity relative to the local prediction between $x = 1.6$ mm and 2.5 mm shows that magnetic field is advected into the hohlraum wall at a slower rate than expected, reducing the amplification of the magnetic field in a similar manner to the previous test problems. Relocalisation due to

the high magnetic field means that there is a very low degree of preheat into the hohlraum beyond $x = 2.5$ mm. Closer to the centre we see a reversal of the Nernst velocity compared to the local prediction, meaning that the magnetic field is allowed to climb up the temperature gradient. This is again another effect that could not be captured by a flux-limiter (red dotted). Here a Nernst flux-limiter of 0.15 (as calculated by postprocessing the 100 ps profiles with CTC) seems slightly conservative, and a lower value would be necessary to capture the high degree of flux reduction between 1.5 mm and 2 mm, but is nevertheless an improvement on the pure Braginskii approach. Using the new method of multiplying the local Nernst term by the ratio between the nonlocal VFP and local Braginskii heat flows is highly accurate within a radius of approximately 2.61 mm, at which point resistive diffusion becomes more important. For the case of the heat flow shown in the *top* panel of fig. 7.10 a flux-limiter of 0.15 gets the peak about right, but again misses the nonlocal flux reversal observed and overestimates the heat flow near to $x = 2$ mm.

7.5 DISCUSSION

The findings in this chapter confirm, generalise and extend a number of previous observations (Lancia et al. 2014; Haines 1986b; Haines 1986a; Joglekar et al. 2016; Read et al. 2016; Davies et al. 2015) about the effect of nonlocality on Nernst advection. Nonlocal limitation of the Nernst velocity reduces both the rate at which the magnetic field cavitates from hot regions of the plasma and the associated convective amplification of the magnetic field at the foot of the temperature gradient. It is the latter effect that is especially affected by nonlocality due to the additional effect of suprathermal electrons allowing the magnetic field to spread out further than would be expected from a local prediction; a phenomenon that could never be replicated by a flux-limiter approach.

By studying a wide range of problems and ionisations, the claim made by Haines (1986a) that the relationship between thermal conduction and Nernst advection should not be greatly affected by nonlocality is fully confirmed. This allows for a simple method of using the prediction from a nonlocal heat flow model (such as the SNB) to calculate the Nernst velocity $v_\mathrm{N} \approx \Psi^{(\mathrm{B})} Q_x / P_\mathrm{e}$, where $\Psi^{(\mathrm{B})} = P_\mathrm{e}\beta_\wedge^{(\mathrm{B})}/eB\kappa_\perp^{(\mathrm{B})}$ is calculated using the Epperlein and Haines (1986) coefficients. Crucially, this differs from previous suggestions that treat Ψ as a constant (either $\frac{2}{5}$ (Davies et al. 2015; Joglekar et al. 2016; Ridgers et al. 2008a; Haines 1986a) or $\frac{2}{3}$ (Lancia et al. 2014)) potentially resulting in errors of up to 80% (see fig. 2.2).

Our analysis on the effects of using different combinations of flux-limiters, suggests that if a more sophisticated approach is not available then the recommended conservative approach is to use identical flux-limiters on heat flow and Nernst advection rather the introducing an additional tunable parameter and the possibility of overfitting. Specifically, this should be applied in such a way that relative reductions in Q_x and E_y are equivalent.

While it may seem comforting that nonlocal modifications to the Nernst velocity do not seem to have significant knock-on effects (such as on the evolution of temperature profiles) in the problems studied, this may not be universally true. Firstly, the keV-scale reductions in plasma temperature associated with including Nernst advection in indirect-drive HYDRA simulations observed by Farmer et al. (2017) suggest that limiting Nernst should increase the final temperature by a non-negligible amount if applied throughout the entire simulation (as opposed to the rather limited 100 ps considered in section 7.4). These increases in the plasma temperature due to Nernst limitation could reduce the absorption of laser energy due to inverse bremsstrahlung; if such temperature rises were concentrated in the gold bubble the resulting ability of the inner beams to deposit their energy nearer the hohlraum midplane could lead to a more prolate implosion. However, the MHD simulations performed by Farmer et al. (2017) with the Nernst term disabled essentially put a bound on the degree to which Nernst limitation could affect the x-ray drive, meaning that nonlocal effects are unlikely to fully explain the drive deficit. Nevertheless, nonlocality of Nernst advection could be more important for experiments involving externally imposed fields, as was the case for the direct-drive shot studied by Davies et al. (2015) where modifying the Nernst limiter led to discernible differences in the neutron yield and ion temperature. Finally, the reversal of Nernst advection observed in section 7.4 may have unexpected effects such as pinning the magnetic field to the hohlraum wall, and somewhat reducing the thermal insulation in the interior of the corona.

One omission that was made in all VFP simulations presented in this paper was the neglection of ion hydrodynamics. This was to simplify the analysis by focussing only on heat and magnetic field transport. Such an assumption is unlikely to greatly affect the resulting physics over the timescales studied here. For example, rerunning the flux-limited CTC simulations with ion motion included for the helium temperature ramp relaxation problem revealed that the resulting change in the electron density over 300 ps would not exceed 5%. While this has slight knock-on effects for the evolution of the magnetic field, decreasing the degree of amplification and cavitation by up to 5%, the consequence for the temperature profile is negligible.

It is worth pausing to consider the potential importance of nonlocal effects on other transport phenomena in the magnetised regime. Perhaps the strongest candidate for further investigation is the Righi-Leduc heat flow due to its dependence on very high velocity moments of the EDF (e.g. $\langle V^{12} \rangle$, as elucidated in eq. (2.2.19)). Severe flux-limitation of the Righi-Leduc heat flow, as observed here, could potentially alleviate some of the hot spot cooling recently observed in simulations by Walsh et al. (2017) in the stagnation phase of indirect-drive implosions (although the degree of nonlocality in their simulations may not have been sufficiently high enough for a significant alleviation). Also, the field compressing magneto-thermal instability involves the coupling of Righi-Leduc heat flow with Nernst advection (Bissell et al. 2010) and the work here could help achieve a better understanding of how it behaves under non-local conditions without performing expensive VFP calculations. However, the absence of an obvious link with the perpendicular heat flux means that there is no simple way of accounting for nonlocal effects on the Righi-Leduc heat flow without having to resort to the addition of a new *independent* flux-limiter or a more sophisticated reduced nonlocal model capable with stronger links to the EDF itself (such as as the MN model (Del Sorbo et al. 2015, 2016) including B-fields; whose accuracy has yet to be fully established).

Less affected by nonlocality is the usually negligible effect of resistive diffusion which relaxes steep magnetic field gradients. This is due to the relevant transport coefficient $\alpha_\perp$ only depending on the fifth velocity moment $\langle V^5 \rangle$ of the distribution function (Epperlein 1994).

One phenomena not investigated here is the the self-generation of magnetic fields by the Biermann battery effect that occurs in presence of transverse density and temperature gradients. And Kingham and Bell (2002) have shown that nonlocality can lead to analogous magnetic field generation even in the complete absence of density gradients. Further work is therefore required to consider the importance of and develop models for these nonlocally generated fields.

7.6 CONCLUSIONS

In this chapter we have seen that the advection of magnetic fields down steep temperature gradients due to the Nernst effect experiences both a nonlocal flux reduction as well as a significant degree of 'pre-Nernst', which transports magnetic field beyond the temperature gradient. Our simulations show both these effects working together to reduce the build-up of magnetic field and smearing it out into colder regions. If these effects are not taken into account it is possible that

overamplification of the magnetic field could lead to unphysical thermal transport barriers. A simple but effective method of obtaining a reliable nonlocal prediction for the Nernst thermoelectric coefficient from a nonlocal heat flow model, one that does not require developing a new highly sophisticated model capable of accurately approximating the entire EDF, is $\beta_{\wedge}^{(\text{Nonlocal})} = \kappa_{\perp}^{(\text{Nonlocal})} \beta_{\wedge}^{(\text{B})} / \kappa_{\perp}^{(\text{B})}$.

8

CONCLUSIONS

So finally we come to the end of our nonlocal adventure. We have assessed the accuracy of the SNB, NFLF and EIC models in a wide range of scenarios, some especially pertinent to inertial fusion. All in all, it is the practical and highly versatile SNB multi-group difusion model that has proven the most robust at approximating kinetic heat flows across all test problems. The success of the SNB model over the NFLF and EIC should be regarded as a testament to the conceptually physics-based approach taken by the authors Schurtz et al. that is able to take into account the inherently nonlinear effects so prevalent in inertial fusion especially, such as steep spatial gradients in electron density and ionisation profiles in a manner far simpler than that would be possible when starting with the initial linearised formulation employed by the NFLF and EIC models. Despite the numerous questionable assumptions made by the SNB model when presenting a derivation from the kinetic equations (Schurtz et al. 2000) the exhibited link to the VFP formulation ensures that the most important physical effects are retained and provides a powerful angle from which to understand the model. Nevertheless, the aforementioned assumptions obscures the link between the SNB function H and the actual electron distribution function limiting the ease to which the model can be refined or extended to include further complexities such as the presence of magnetic fields.

Furthermore, it is important to appreciate the computational costs and benefits of the SNB model; as the SNB model typically exhibits reasonable convergence with as few as 25 groups, the local heat flow calculation is only slowed down by a factor of approximately 25, reflecting the diffusion of each group which can be solved for independently in parallel or serial . However, as the heat flow calculation is not the (only) bottleneck in these codes, inclusion of the SNB model more typically slows the code down by a factor of approximately only two (personal communication with Mehul Patel). If instead a two-dimensional radiation-hydrodynamics code were to be fully replaced by a VFP code in a similar vein to IMPACT, K2 or OSHUN (which would be far from a trivial task considering all the complex multi-physics effects that need to be taken into account such as equation of state, ray-tracing and radiation absorption) the relative computational cost would be much more significant. At the very least 60 velocity cells are typically needed for sensible behaviour of a VFP code, but this

is usually more on the order of 100 to ensure accurate computation of the heat flow moment. Added to this either an intensive matrix solve when employing an implicit solve , or a timestep on the order of the plasma frequency (at least 100 times smaller than typical ALE code timsteps) as well as the memory requirements for retaining information on the distribution function at every timestep and a transition to VFP codes could foreseeably lead to a slow down by approximately 10^4.

The specific implementation of the SNB model deemed optimal from these studies uses the standard modified source term $\vec{g}_1^{(\mathrm{mb})}$ on the right-hand side, but with distinct separate electron-ion and electron-electron mfp's rather than the original geometrically averaged one. Furthermore, the electron-ion mfp is found to require an ionisation-dependent multiplier, such as the Epperlein-Short collision fix ξ_{ES} (Epperlein and Short 1991), to account for the increasing importance of electron-electron collisions on the anisotropic part of the EDF at low ionisations. Finally, an additional multiplier was added to the electron-electron mfp corresponding to $r = 2$ in the notation introduced in section 2.3.3.

The value of the multiplier r was arrived at by first quantifying the nonlocal deviation of the heat flow in the long-wavelength limit for the linearised problem ('semicollisional' regime, see section 4.3.5) from the local limit at various ionisations. In fact this initially indicated a value of $r \approx 2.4$ in the Lorentz limit, increasing to $r \approx 3$ when $Z = 1$; however, further benchmarking presented in chapter 5 indicated that an ionisation independent value of $r = 2$ was better at reproducing VFP heat flow profiles for thermal relaxation and laser heating test problems when relative temperature differences were large. A convenient benefit of this particular multiplier is that it supports the new interpretation of the SNB model H arising from a link to the high-velocity limit of the electron-electron collision operator identified in section 4.3.6, $H \approx 2\pi k_{\mathrm{B}} T_{\mathrm{e}} v^4 \frac{\partial \delta f_0 / f_{\mathrm{e}}^{(\mathrm{mb})}}{\partial v} f_{\mathrm{e}}^{(\mathrm{mb})} \, \mathrm{d}v$, in terms of the the deviation of the isotropic part of the EDF from a Maxwellian $\delta f_0 = f_0 - f_{\mathrm{e}}^{(\mathrm{mb})}$. Nevertheless, higher values of r have not been completely ruled out and if strong arguments for values of r between 2 and 4 were to be presented in the future these should always be carefully considered.

Despite these implementation adjustments, some inaccuracies of the SNB model concerning overprediction of preheat and coronal heat flow, particularly in the presence of steep ionisation gradients still remain. Modifications to the SNB electric field treatment can make some further progress towards reducing such discrepancies. Comparisons presented in chapter 5 suggest either using a multiplier of $E_{\mathrm{mult}} = \sqrt{Z\xi_{\mathrm{ES}}/r}$ on the electric field, in line with the original model before the separation of mfp's, or eliminating the electric field entirely. No

other promising improvements to the SNB model have been investigated in detail here but one potential route is to build on the new interpretation of the function H by attempting to rederive the SNB model with a collision operator closer to the linearised electron-electron collision operator and retain terms that the original models neglects. Another use for the relation between H and δf_0 would be to assess nonlocal modifications to the damping rates of parametric instabilities, this could be particularly reliable for instabilities with high phase velocities such as SRS or Langmuir waves due to the accuracy of the identified relationship in the tails of the EDF, but probably not so much for other instabilities with lower phase velocities such as the return current instability where accuracy worsens.

In order to allow for an in-depth understanding and reduce simulation times, the test problems presented in this thesis have been exclusively limited to 1D. And while some 2D tests have been performed in other works (Schurtz et al. 2000; Del Sorbo et al. 2015), these have neither been extensively benchmarked against VFP nor use the new calibrated version of the SNB model. While the natural multi-dimensional formulation of the SNB model suggests that a lot of the core 1D behaviour (fairly accurate prediction of peak heat flow, sizeable overestimate of preheat) should follow through to 2D and 3D, the success of the SNB model to accurately estimate inherently anisotropic features such as the flux rotation caused by imbalanced temperature gradients should be validated more rigorously.

Furthermore, while the potential of a reduced model to capture nonlocal effects on Nernst advection by simply multiplying the *nonlocal* heat flow by the *local* ratio between the Nernst and heat flow velocities was confirmed in chapter 7, the magnetised SNB model itself has not been fully validated. It is imperative in moving towards a reliable and trustworthy model for the increasingly important magnetised regime that the risks and inaccuracies associated with the magnetised SNB be fully evaluated and understood. Another important topic of predictively modelling fusion plasma heat flows that can be answered using VFP codes is the additional modifications of the EDF towards a Dum-Langdon-Matte type super-Gaussian (Dum 1978b,a; Langdon 1980; Matte et al. 1988) due to inverse bremsstrahlung absorption of laser energy could provide further alterations to transport processes (Ridgers et al. 2008b). Perhaps there is a simple modification to the SNB model that could be identified to incorporate this, but current kinetic simulations suggest that this IB effect is not too important for indirect drive experiments (personal communication with Mark Sherlock).

Less critical to our findings are the inaccuracies experienced by VFP codes in strongly coupled plasmas. While this could play a role in the cooler part of the hohlraum wall, such as in the gadolinium hohlraum test in section 5.4, where the

Coulomb logarithm drops to ~2 (theoretically rendering the effect of collisions in this region only accurate to $\mathcal{O}(1/\log\Lambda_\alpha)$~50%) it does not affect the conclusion made that the separated SNB model predicts a similar heat flow into the wall as IMPACT while overpredicting that in the corona as both use the same treatment of $\log\Lambda$. Instead, the results in this thesis have simply shown quantitatively that reduced models can be an effective stepping stone between hydrodynamic and VFP approaches. However. this does act as a reminder that even a highly sophisticated VFP code could be faced with challenging inaccuracies in certain regions of the plasma (though it would surely still be an improvement to a purely hydrodynamic approach which would experience the same difficulties with strongly coupled plasmas); a potential method in overcoming this and incorporating large-angle collisions in a continuum code could be a Monte Carlo based approach (Turrell et al. 2015). Similar points can be made for other deficiencies, such as collisions with neutrals and Fermi degeneracy, although these are probably slightly easier to address and incorporate into models (Kolobov and Arslanbekov 2006; Brown and Haines 1997), with one such approach is suggested by Sijoy et al. (2017)

In addition to identifying SNB as the nonlocal model of choice for inertial fusion simulations and some scrape-off layer studies a number of other valuable results have been advanced by the studies in this thesis. Characterisation of the limiting long- and short-wavelength behaviour of the electron heat flow for the case of small perturbations in chapter 4 led to the derivation of a new analytic approximation to the dependence of the thermal conductivity reduction on the nonlocality parameter $k\lambda_{\mathrm{ei}}^{(\mathrm{B})}$ (eq. (4.6.6)),

$$\frac{\kappa_\parallel}{\kappa_\parallel^{(\mathrm{B})}} = \left(1 + \left(\frac{1}{b_Q Z k^2 \lambda_{\mathrm{ei}}^{(\mathrm{B})2}} + \frac{1}{a k\lambda_{\mathrm{ei}}^{(\mathrm{B})}(1 + c_1(k\lambda_{\mathrm{ei}}^{(\mathrm{B})})^{-\eta})}\right)^{-1}\right)^{-1},$$

(see section 4.6.1 for more details). This fit was a significant improvement to those of Hammett and Perkins (1990) and Bychenkov et al. (1994 eq. 14, 1995 eq. 57) and almost as accurate as Ji's configuration space closure. It was this fit that was used to obtain the fitting coefficients given in appendix A for the non-Fourier Landau-fluid model, enabling an accuracy within 2.5% for $k\lambda_{\mathrm{ei}}^{(\mathrm{B})} < 1.6$ for $Z = 1$ and $k\lambda_{\mathrm{ei}}^{(\mathrm{B})} < 0.29$ for $Z = 8$.

When moving on to more fusion relevant scenarios with large relative temperature differences, both the EIC and NFLF models failed to capture the marked preheat or peak relocation that was observed. While a nonlinear Picard iteration scheme in a similar vein to IMPACT could perhaps help the EIC model at the cost of computational time, it was instead a simple improvement to the NFLF

model that was investigated in section 5.1.1. This involved modifying the core equations in such a way that its predictions would only be altered when relative temperature perturbations could not be considered small. Inspired by the success of the SNB model these modifications render the NFLF equations as

$$\left[\frac{q_j^2}{n_\mathrm{e}} + (a\lambda_\mathrm{ei}^{(\mathrm{B})})^2\vec{\nabla}\cdot\frac{1}{n_\mathrm{e}}\vec{\nabla}\right]T_\mathrm{e}{}^4\vec{Q}_j = \frac{T_\mathrm{e}{}^4}{n_\mathrm{e}}p_j\vec{Q}^{(\mathrm{B})}.$$

The impact of this was to improve the behaviour of the model in the presence of mild nonlocalities, now predicting preheat and peak translation, but greatly overpredicting the preheat when temperature gradients become overly steep ($\lambda_\mathrm{ei}^{(\mathrm{B})}|\vec{\nabla}T_\mathrm{e}|/T_\mathrm{e} \gtrapprox 0.1$).

Finally, in chapter 6, we observed that the implementation of the popular SNB model in various inertial fusion codes (HYDRA, CHIC and DUED) can differ greatly. Collaboration with researchers at LLNL have resulted in an option (now set as default) to incorporate the calibrations suggested in this thesis. These model adjustments have the potential to play a role in shot design, particularly in improving implosion symmetry. And sensitivity analysis is being performed to assess the impact of this. It is hoped that similar amendments might be made to the SNB model in CHIC, and other codes where necessary.

In conclusion, the significant improvements to the SNB model identified in this thesis should have real consequences that could potentially qualitatively affect the predictions of rad-hydro simulations (particularly with regards to symmetry predictions). The thorough analysis presented in this thesis provides a high degree of confidence in continued use of the model. Additionally, the key current issue for the SNB has been identified as its overprediction of preheat at high degrees of nonlocality, especially in the low density corona. The possible implications of this overprediction should be carefully considered by designers when analysing simulations, although of course it would be ideal if further refinements to the model were found. Unfortunately, no validation has here been performed of the magnetised SNB model and completion of this is vital if the role of magnetic fields in inertial fusion is to be fully understood. If the magnetised SNB were found to be acceptably accurate the findings of chapter 7 would provide nonlocal corrections to Nernst advection free of charge. For the case of scrape-off layer transport, using the unmagnetised SNB parallel to field lines again seems to be the strongest candidate due to the large relative temperature differences involved, but the greatest challenge concerns the application of sheath-like boundary conditions at the plasma exhaust which could have a large impact when mean profiles evolve so slowly.

A

NFLF FITTING COEFFICIENTS

TABLE A.1: Coefficients for the NFLF model guaranteeing a percentage error less than 2.5% compared to the analytical approximation (eq. (4.6.6)) of $\kappa_\parallel(k\lambda_{ei}^{(B)})/\kappa_\parallel^{(B)}$ for $Z = 1$ and $k\lambda_{ei}^{(B)} < k_{max}\lambda_{ei}^{(B)}$.

$N = 2$		$N = 3$		$N = 4$		$N = 5$	
$k_{max}\lambda_{ei}^{(B)} = 0.4$		$k_{max}\lambda_{ei}^{(B)} = 1.6$		$k_{max}\lambda_{ei}^{(B)} = 5.0$		$k_{max}\lambda_{ei}^{(B)} = 13.8$	
p_j	q_j	p_j	q_j	p_j	q_j	p_j	q_j
4.859e−3	1.208e−1	2.176e−3	1.020e−1	8.623e−4	8.493e−2	3.102e−4	7.002e−2
2.986e−1	6.690e−1	6.316e−2	3.513e−1	3.159e−2	2.549e−1	1.804e−2	2.025e−1
		1.682	2.455	3.248e−1	1.088	1.422e−1	6.866e−1
				6.311	7.256	1.195	2.901
						1.923e1	1.901e1

$N = 6$		$N = 8$		$N = 10$		$N = 12$	
$k_{max}\lambda_{ei}^{(B)} = 33.2$		$k_{max}\lambda_{ei}^{(B)} = 151.7$		$k_{max}\lambda_{ei}^{(B)} = 363.9$		$k_{max}\lambda_{ei}^{(B)} = 914.2$	
p_j	q_j	p_j	q_j	p_j	q_j	p_j	q_j
1.036e−4	5.719e−2	1.179e−5	3.841e−2	1.169e−6	2.509e−2	1.604e−7	1.734e−2
1.062e−2	1.686e−1	3.457e−3	1.251e−1	6.924e−4	9.009e−2	1.184e−4	6.518e−2
7.381e−2	4.785e−1	2.741e−2	2.814e−1	1.096e−2	1.859e−1	4.290e−3	1.390e−1
4.851e−1	1.669	1.318e−1	7.722e−1	4.488e−2	4.174e−1	2.067e−2	2.711e−1
3.447	6.867	6.487e−1	2.307	1.774e−1	1.035	6.950e−2	5.952e−1
4.970e1	4.445e1	3.280	7.700	6.942e−1	2.704	2.384e−1	1.366
		1.959e1	3.098e1	2.730	7.610	7.985e−1	3.265
		2.500e2	1.972e2	1.159e1	2.389e1	2.675	8.257
				5.910e1	8.877e1	9.383	2.254e1
				6.606e2	5.094e2	3.630e1	6.832e1
						1.690e2	2.429e2
						1.773e3	1.321e3

TABLE A.2: Coefficients for the NFLF model guaranteeing a percentage error less than 1.0% compared to the analytical approximation (eq. (4.6.6)) of $\kappa_\parallel(k\lambda_{ei}^{(B)})/\kappa_\parallel^{(B)}$ for $Z = 1$ and $k'\lambda_{ei}^{(B)} < k_{max}\lambda_{ei}^{(B)}$.

$N = 2$		$N = 3$		$N = 4$		$N = 5$	
$k_{max}\lambda_{ei}^{(B)} = 0.2$		$k_{max}\lambda_{ei}^{(B)} = 0.9$		$k_{max}\lambda_{ei}^{(B)} = 2.6$		$k_{max}\lambda_{ei}^{(B)} = 4.8$	
p_j	q_j	p_j	q_j	p_j	q_j	p_j	q_j
2.663e−3	1.058e−1	1.123e−3	8.936e−2	4.429e−4	7.483e−2	9.954e−5	5.678e−2
1.893e−1	4.984e−1	3.872e−2	2.773e−1	2.170e−2	2.175e−1	1.043e−2	1.676e−1
		9.644e−1	1.647	1.898e−1	7.989e−1	7.259e−2	4.736e−1
				3.511	4.616	4.959e−1	1.665
						7.385	8.783

$N = 6$		$N = 8$		$N = 10$		$N = 12$	
$k_{max}\lambda_{ei}^{(B)} = 15.2$		$k_{max}\lambda_{ei}^{(B)} = 66.2$		$k_{max}\lambda_{ei}^{(B)} = 251.8$		$k_{max}\lambda_{ei}^{(B)} = 240.5$	
p_j	q_j	p_j	q_j	p_j	q_j	p_j	q_j
5.343e−5	5.066e−2	6.471e−6	3.440e−2	9.483e−7	2.413e−2	2.717e−7	1.913e−2
7.716e−3	1.533e−1	2.396e−3	1.154e−1	5.834e−4	8.723e−2	1.941e−4	7.128e−2
5.291e−2	3.991e−1	2.160e−2	2.497e−1	1.004e−2	1.799e−1	5.658e−3	1.497e−1
3.125e−1	1.280	9.736e−2	6.489e−1	4.114e−2	3.974e−1	2.516e−2	3.017e−1
1.960	4.680	4.501e−1	1.832	1.597e−1	9.722e−1	8.800e−2	6.833e−1
2.603e1	2.602e1	2.091	5.650	6.153e−1	2.499	3.118e−1	1.616
		1.096e1	2.023e1	2.368	6.887	1.080	4.007
		1.273e2	1.105e2	9.726	2.100e1	3.796	1.061e1
				4.733e1	7.486e1	1.426e1	3.079e1
				5.130e2	4.077e2	6.099e1	1.016e2
						3.469e2	4.110e2
						3.212e3	2.673e3

TABLE A.3: Coefficients for the NFLF model guaranteeing a percentage error less than 2.5% compared to the analytical approximation (eq. (4.6.6)) of $\kappa_\parallel(k\lambda_{\text{ei}}^{(\text{B})})/\kappa_\parallel^{(\text{B})}$ for $Z = 8$ and $k'\lambda_{\text{ei}}^{(\text{B})} < k_{\max}\lambda_{\text{ei}}^{(\text{B})}$.

$N = 2$		$N = 3$		$N = 4$		$N = 5$	
$k_{\max}\lambda_{\text{ei}}^{(\text{B})} = 0.07$		$k_{\max}\lambda_{\text{ei}}^{(\text{B})} = 0.29$		$k_{\max}\lambda_{\text{ei}}^{(\text{B})} = 0.89$		$k_{\max}\lambda_{\text{ei}}^{(\text{B})} = 2.4$	
p_j	q_j	p_j	q_j	p_j	q_j	p_j	q_j
1.097e−3	6.066e−2	4.384e−4	4.997e−2	1.568e−4	4.064e−2	5.206e−5	3.281e−2
7.561e−2	3.282e−1	1.723e−2	1.783e−1	8.535e−3	1.310e−1	4.647e−3	1.040e−1
		4.053e−1	1.198	8.235e−2	5.336e−1	3.694e−2	3.367e−1
				1.523	3.590	2.849e−1	1.408
						4.681	9.417

$N = 6$		$N = 7$		$N = 8$		$N = 10$	
$k_{\max}\lambda_{\text{ei}}^{(\text{B})} = 5.9$		$k_{\max}\lambda_{\text{ei}}^{(\text{B})} = 12.9$		$k_{\max}\lambda_{\text{ei}}^{(\text{B})} = 27.0$		$k_{\max}\lambda_{\text{ei}}^{(\text{B})} = 109.9$	
p_j	q_j	p_j	q_j	p_j	q_j	p_j	q_j
1.720e−5	2.656e−2	5.751e−6	2.158e−2	1.992e−6	1.765e−2	2.835e−7	1.219e−2
2.597e−3	8.644e−2	1.413e−3	7.330e−2	7.298e−4	6.267e−2	1.694e−4	4.625e−2
1.990e−2	2.379e−1	1.182e−2	1.797e−1	7.454e−3	1.427e−1	3.184e−3	1.001e−1
1.201e−1	8.170e−1	6.103e−2	5.372e−1	3.473e−2	3.819e−1	1.421e−2	2.261e−1
8.256e−1	3.392	3.278e−1	1.830	1.604e−1	1.140	5.437e−2	5.686e−1
1.279e1	2.265e1	2.110	7.555	7.979e−1	3.852	2.092e−1	1.534
		3.147e1	5.023e1	4.939	1.583e1	8.504e−1	4.538
				7.150e1	1.045e2	3.955	1.527e1
						2.367e1	6.267e1
						3.293e2	4.137e2

TABLE A.4: Coefficients for the NFLF model guaranteeing a percentage error less than 1.0% compared to the analytical approximation (eq. (4.6.6)) of $\kappa_\parallel(k\lambda_{\mathrm{ei}}^{(\mathrm{B})})/\kappa_\parallel^{(\mathrm{B})}$ for $Z = 8$ and $k'\lambda_{\mathrm{ei}}^{(\mathrm{B})} < k_{\max}\lambda_{\mathrm{ei}}^{(\mathrm{B})}$.

$N = 2$		$N = 3$		$N = 4$		$N = 5$	
$k_{\max}\lambda_{\mathrm{ei}}^{(\mathrm{B})} = 0.04$		$k_{\max}\lambda_{\mathrm{ei}}^{(\mathrm{B})} = 0.15$		$k_{\max}\lambda_{\mathrm{ei}}^{(\mathrm{B})} = 0.45$		$k_{\max}\lambda_{\mathrm{ei}}^{(\mathrm{B})} = 1.2$	
p_j	q_j	p_j	q_j	p_j	q_j	p_j	q_j
5.624e−4	5.235e−2	2.102e−4	4.305e−2	7.530e−5	3.523e−2	2.548e−5	2.863e−2
4.982e−2	2.504e−1	1.057e−2	1.423e−1	5.669e−3	1.116e−1	3.198e−3	9.203e−2
		2.346e−1	8.021e−1	4.855e−2	3.900e−1	2.451e−2	2.669e−1
				8.275e−1	2.238	1.637e−1	9.827e−1
						2.438	5.598

$N = 6$		$N = 7$		$N = 8$		$N = 10$	
$k_{\max}\lambda_{\mathrm{ei}}^{(\mathrm{B})} = 2.7$		$k_{\max}\lambda_{\mathrm{ei}}^{(\mathrm{B})} = 5.9$		$k_{\max}\lambda_{\mathrm{ei}}^{(\mathrm{B})} = 12.3$		$k_{\max}\lambda_{\mathrm{ei}}^{(\mathrm{B})} = 46.9$	
p_j	q_j	p_j	q_j	p_j	q_j	p_j	q_j
8.621e−6	2.330e−2	2.999e−6	1.908e−2	1.093e−6	1.575e−2	1.653e−7	1.100e−2
1.781e−3	7.783e−2	9.512e−4	6.660e−2	4.822e−4	5.725e−2	1.071e−4	4.229e−2
1.423e−2	1.982e−1	8.881e−3	1.553e−1	5.773e−3	1.269e−1	2.462e−3	9.177e−2
7.749e−2	6.217e−1	4.282e−2	4.331e−1	2.594e−2	3.211e−1	1.135e−2	1.990e−1
4.614e−1	2.275	2.088e−1	1.355	1.121e−1	9.027e−1	4.171e−2	4.816e−1
6.394	1.291e1	1.159	4.938	5.065e−1	2.810	1.530e−1	1.242
		1.540e1	2.794e1	2.706	1.023e1	5.806e−1	3.463
				3.496e1	5.776e1	2.438	1.074e1
						1.255e1	3.907e1
						1.557e2	2.201e2

B

DERIVATIONS & PROOFS

B.1 EXPLICIT FORM OF THE LINEARISED ELECTRON-ELECTRON COLLISION OPERATOR

The linearised form of the electron-electron collision operator appearing on the right-hand of the equation for f_0, the isotropic part of the distribution function in a Cartesian tensor expansion, (eq. 2.1.11) is obtained by ignoring terms proportional to ${\delta f_0}^2$:

$$C_{\mathrm{ee0}}^{(\mathrm{L})}(\delta f_0) = \frac{\Gamma_{\mathrm{ee}}}{v^2}\frac{\partial}{\partial v}\Big(I_0(\delta f_0) f_{\mathrm{e}}^{(\mathrm{mb})} + I_0(f_{\mathrm{e}}^{(\mathrm{mb})})\delta f_0 + D(\delta f_0)\frac{\partial f_{\mathrm{e}}^{(\mathrm{mb})}}{\partial v} + D(f_{\mathrm{e}}^{(\mathrm{mb})})\frac{\partial \delta f_0}{\partial v}\Big) \tag{B.1.1}$$

$$= \frac{4\pi\Gamma_{\mathrm{ee}}}{v^2}\frac{\partial}{\partial v}\Bigg(\int_0^v \psi f_{\mathrm{e}}^{(\mathrm{mb})} u^2\,\mathrm{d}u\; f_{\mathrm{e}}^{(\mathrm{mb})} + \int_0^v f_{\mathrm{e}}^{(\mathrm{mb})} u^2\,\mathrm{d}u\;\psi f_{\mathrm{e}}^{(\mathrm{mb})} - \frac{m_{\mathrm{e}}}{k_{\mathrm{B}}T_{\mathrm{e}}}\int_0^v u^2\int_u^\infty \psi f_{\mathrm{e}}^{(\mathrm{mb})} w\,\mathrm{d}w\,\mathrm{d}u\; f_{\mathrm{e}}^{(\mathrm{mb})} + \frac{1}{v}\int_0^v u^2\int_u^\infty f_{\mathrm{e}}^{(\mathrm{mb})} w\,\mathrm{d}w\,\mathrm{d}u\,\Big(\frac{\partial\psi}{\partial v} - \frac{m_{\mathrm{e}}v}{k_{\mathrm{B}}T_{\mathrm{e}}}\psi\Big) f_{\mathrm{e}}^{(\mathrm{mb})},\Bigg) \tag{B.1.2}$$

where δf_0 has been replaced with $\psi f_{\mathrm{e}}^{(\mathrm{mb})}$. Evaluating some of the integrals directly or by parts gives

$$C_{\mathrm{ee0}}^{(\mathrm{L})}(\delta f_0) = \frac{4\pi\Gamma_{\mathrm{ee}}}{v^2}\frac{\partial}{\partial v}\Bigg(\cancelto{0}{\int_0^v \psi f_{\mathrm{e}}^{(\mathrm{mb})} u^2\,\mathrm{d}u\; f_{\mathrm{e}}^{(\mathrm{mb})}} + \cancelto{0}{\int_0^v f_{\mathrm{e}}^{(\mathrm{mb})} u^2\,\mathrm{d}u\;\psi f_{\mathrm{e}}^{(\mathrm{mb})}} - \int_0^v u^2\Big(\cancelto{0}{\psi f_{\mathrm{e}}^{(\mathrm{mb})}} + \int_u^\infty \frac{\partial\psi}{\partial v} f_{\mathrm{e}}^{(\mathrm{mb})}\Big)\,\mathrm{d}w\,\mathrm{d}u\; f_{\mathrm{e}}^{(\mathrm{mb})} + \int_0^v u^2 f_{\mathrm{e}}^{(\mathrm{mb})}\,\mathrm{d}u\,\Big(\frac{k_{\mathrm{B}}T_{\mathrm{e}}}{m_{\mathrm{e}}v}\frac{\partial\psi}{\partial v} - \cancelto{0}{\psi}\Big) f_{\mathrm{e}}^{(\mathrm{mb})}\Bigg) \tag{B.1.3}$$

$$= \frac{n_{\mathrm{e}}\Gamma_{\mathrm{ee}}}{v^2}\frac{\partial}{\partial v}\Big(\frac{f_{\mathrm{e}}^{(\mathrm{mb})}}{2}\hat{L}\Big[\frac{\partial\psi}{\partial v}\Big]\Big) \tag{B.1.4}$$

where $\hat{L}\Big[\dfrac{\partial\psi}{\partial v}\Big] := \dfrac{2k_{\mathrm{B}}T_{\mathrm{e}}}{m_{\mathrm{e}}v}\dfrac{I_0\big(f_{\mathrm{e}}^{(\mathrm{mb})}\big)}{n_{\mathrm{e}}}\dfrac{\partial\psi}{\partial v} - 8\pi\displaystyle\int_0^v u^2\int_u^\infty \frac{f_{\mathrm{e}}^{(\mathrm{mb})}}{n_{\mathrm{e}}}\frac{\partial\psi}{\partial w}\,\mathrm{d}w\,\mathrm{d}u.$ (B.1.5)

Substituting $V = v/\sqrt{m_e/2k_B T_e}$ produces

$$\hat{L}\left[\frac{\partial\psi}{\partial V}\right] = \frac{2}{\sqrt{\pi}}\frac{\gamma(3/2, V^2)}{V}\frac{\partial\psi}{\partial V} - \frac{8}{\sqrt{\pi}}\int_0^V U^2 \int_U^\infty \mathrm{e}^{-W^2}\frac{\partial\psi}{\partial W}\,\mathrm{d}W\,\mathrm{d}U, \qquad \text{(B.1.6)}$$

where $\gamma(n, x) = \int_0^x x^{n-1}\mathrm{e}^{-x}\,\mathrm{d}x$ is the lower incomplete gamma function.

B.2 APPLICATION OF ENERGY CONSERVATION

For a plasma with a given density and temperature profile the non-Maxwellian part of the distribution function δf_0 can not contribute to the local density and temperature as this is already completely provided by the Maxwellian part $f_e^{(\mathrm{mb})}$, therefore

$$4\pi\int_0^\infty v^2\delta f_0\,\mathrm{d}v = 0 \text{ and } 4\pi\int_0^\infty \frac{1}{2}m_e v^4\delta f_0\,\mathrm{d}v = 0. \qquad \text{(B.2.1)}$$

These can be combined to calculate the implication on the derivative of ψ as

$$\int_0^\infty \left(V^4 - \frac{3}{2}V^2\right)\psi e^{-V^2}\,\mathrm{d}V = 0 \qquad \text{(B.2.2)}$$

$$\implies \left[-\frac{V^3}{2}\psi e^{-V^2}\right]_0^\infty + \int_0^\infty \frac{V^3}{2}\frac{\partial\psi}{\partial V}e^{-V^2}\,\mathrm{d}V = 0 \qquad \text{(B.2.3)}$$

$$\implies \int_0^\infty V^3\frac{\partial\psi}{\partial V}e^{-V^2}\,\mathrm{d}V = 0, \qquad \text{(B.2.4)}$$

assuming that $\psi(v = 0)$ is finite.

B.3 HIGH-VELOCITY LIMIT OF THE LINEARISED ELECTRON-ELECTRON COLLISION OPERATOR

The behaviour of the $\hat{L}$ operator in the limit of high-velocity can be evaluated by integrating the second term by parts:

$$\lim_{V\to\infty}\hat{L}\left[\frac{\partial\psi}{\partial V}\right] = \frac{1}{V}\frac{\partial\psi}{\partial V} - \frac{4}{\sqrt{\pi}}\left\{\begin{array}{l}\left[\dfrac{U^3}{3}\displaystyle\int_U^\infty \mathrm{e}^{-W^2}\frac{\partial\psi}{\partial W}\,\mathrm{d}W\right]_0^V \\ + \displaystyle\int_0^V \frac{V^3}{3}\mathrm{e}^{-U^2}\frac{\partial\psi}{\partial U}\,\mathrm{d}U\end{array}\right\} \qquad \text{(B.3.1)}$$

$$= \frac{1}{V}\frac{\partial\psi}{\partial V} \qquad , \qquad \text{(B.3.2)}$$

where both terms in the curly brackets can be neglected as they approach zero exponentially fast. Note how the second term in the curly brackets vanishes at infinity due to the energy conservation discussed in the previous section.

B.4 INVERSE OF THE ELECTRON-ELECTRON COLLISION OPERATOR

In section 4.3.1 a form for the inverse of the operator $\hat{L}$ was provided without proof:

$$\hat{L}_*^{-1}[S(V)] = \frac{\sqrt{\pi}}{2}\frac{VS(V)}{\gamma(3/2, V^2)} - 2\sqrt{\pi}V\int_*^V \frac{Y^2\int_0^Y S(T)Te^{-T^2}\,dT}{\gamma(3/2, Y^2)^2}\,dY, \tag{B.4.1}$$

which is an inverse for any nonnegative value of $*$, but this should be chosen so as to conserve energy. This can be shown by applying $\hat{L}$ to both sides of the equation and integrating by parts multiple times. Substituting $G(V) = S(V)Ve^{-V^2}$ for compactness we find

$$\hat{L}\left[\hat{L}_*^{-1}[S(V)]\right]$$

$$= S - 4\gamma(3/2, V^2)\int_*^V \frac{Y^2\int_0^Y G\,dT}{\gamma(3/2, V^2)^2}\,dY \tag{B.4.2}$$

$$- 4\int_0^V U^2\int_U^\infty \frac{G(W)}{\gamma(3/2, W^2)} - 4We^{-W^2}\int_*^W \frac{Y^2\int_0^Y G\,dT}{\gamma(3/2, Y^2)^2}\,dY\,dW\,dU$$

$$= S - 4\Bigg\{\gamma(3/2, V^2)\int_*^V \frac{Y^2\int_0^Y G\,dT}{\gamma(3/2, Y^2)^2}\,dY + \int_0^V U^2\int_U^\infty \frac{G(W)}{\gamma(3/2, W^2)}\,dW \tag{B.4.3}$$

$$- U^2\int_U^\infty \frac{2W^2e^{-W^2}\int_0^W G\,dT}{\gamma(3/2, W^2)^2}\,dW - 2U^2e^{-U^2}\int_*^U \frac{Y^2\int_0^Y G\,dT}{\gamma(3/2, Y^2)^2}\,dY\,dU\Bigg\}$$

$$= S - 4\Bigg\{\gamma(3/2, V^2)\int_*^V \frac{Y^2\int_0^Y G\,dT}{\gamma(3/2, Y^2)^2}\,dY + \int_0^V U^2\int_U^\infty \frac{G(W)}{\gamma(3/2, W^2)}\,dW \tag{B.4.4}$$

$$- U^2\int_U^\infty \frac{G(W)}{\gamma(3/2, W^2)}\,dW + U^2\left[\frac{\int_0^Y G\,dT}{\gamma(3/2, W^2)}\right]_U^\infty$$

$$+ \frac{U^2\int_0^U G\,dT}{\gamma(3/2, U^2)}\,dU - \gamma(3/2, V^2)\int_*^V \frac{Y^2\int_0^Y G\,dT}{\gamma(3/2, Y^2)^2}\,dY\Bigg\}$$

$$= S - 4\int_0^V \frac{U^2\int_0^\infty G\,dT}{\Gamma(3/2)}\,dU, \tag{B.4.5}$$

When integrating eqs. (B.4.2) and (B.4.3) by parts terms in red are integrated, while terms in blue are differentiated. In eq. (B.4.4) color-coding is merely used to indicate which terms cancel.

where $\Gamma(3/2) = \sqrt{\pi}/2$. Therefore, $\hat{L}_*^{-1}$ successfully inverts $\hat{L}$ as long as the integral of G vanishes. This is guaranteed to be the case as it is equivalent to requiring that the v^4 moment of the (left-hand side of the) f_0 equation is zero due to energy conservation.

B.5 NONCONTRIBUTION OF NONSTATIONARITY IN PERTURBING THE DISTRIBUTION FUNCTION

The time-derivative of f_0 which appears in the source is proportional to V^3

$$\hat{L}_*^{-1}[V^3] = \frac{\sqrt{\pi}}{2}\frac{V^4}{\gamma(3/2, V^2)} - 2\sqrt{\pi}V\int_*^V \frac{Y^2\int_0^Y T^4 e^{-T^2}\,dT}{\gamma(3/2, Y^2)^2}\,dY \tag{B.5.1}$$

$$= \frac{\sqrt{\pi}}{2}\frac{V^4}{\gamma(3/2, V^2)} - \sqrt{\pi}V\int_*^V \frac{3}{2}\frac{Y^2}{\gamma(3/2, Y^2)} - \frac{Y^5 e^{-Y^2}}{\gamma(3/2, Y^2)^2}\,dY \tag{B.5.2}$$

$$= \frac{\sqrt{\pi}}{2}\frac{V^4}{\gamma(3/2, V^2)} - \frac{\sqrt{\pi}}{2}V\left[\frac{Y^3}{\gamma(3/2, Y^2)}\right]_*^V \tag{B.5.3}$$

$$= 0 \tag{B.5.4}$$

B.6 CONVERGENCE OF ITERATIVE FORM OF INVERSE COLLISION OPERATOR

In section 4.3.1 we provided an iterative approximation to calculate the second term in the inverse of the collision operator

$$\int_0^V \frac{Y^2\int_0^Y S\,T e^{-T^2}\,dT}{\gamma(3/2, Y^2)^2}\,dY \approx \sum_{n=1}^N \frac{n! I^n\left[e^{V^2}\int_0^V S\,T e^{-T^2}\,dT\right]}{\gamma(3/2, V^2)^{n+1}}, \tag{B.6.1}$$

where $I[F(V)] = \int_0^V 2U^2 e^{-U^2} F(U)\,dU$ and $\hat{L}_0^{-1}[S(V)]^{\langle 0\rangle} = 0$. It can be shown that this approximation converge by proving that the error term

$$\Delta_N[S] = \left|\int_0^V \frac{Y^2\int_0^Y S\,T e^{-T^2}\,dT}{\gamma(3/2, Y^2)^2}\,dY - \sum_{n=1}^N \frac{n! I^n\left[e^{V^2}\int_0^V S\,T e^{-T^2}\,dT\right]}{\gamma(3/2, V^2)^{N+1}}\right| \tag{B.6.2}$$

$$= \left|2(n+1)!\int_0^V \frac{Y^2 e^{-Y^2} I^N\left[e^{Y^2}\int_0^V S\,T e^{-T^2}\,dT\right]}{\gamma(3/2, Y^2)^{N+2}}\,dY\right| \tag{B.6.3}$$

goes to zero as N increases. In order to do this, we first need to ascertain a number of properties of the lower incomplete gamma function.

Lemma B.6.1 Absolute bounds on the incomplete gamma function
An upper bound of the gamma function

$$\gamma(n,x) = \int_0^x x^{n-1}\mathrm{e}^{-x}\,\mathrm{d}x \leqslant \frac{x^n}{n}, \tag{B.6.4}$$

is obtained using the fact that $\mathrm{e}^{-x} \leqslant 1$, $\forall x \geqslant 0$. Alternatively, integrating by parts and noting that the lower incomplete gamma function is strictly increasing with respect to it's second argument yields a useful lower bound:

$$\gamma(n,x) = \frac{x^n}{n}\mathrm{e}^{-x} + \frac{\gamma(n+1,x)}{n} \geqslant \min\left(\frac{x^n}{n}\mathrm{e}^{-x}, n^{n-1}\mathrm{e}^{-n}\right). \tag{B.6.5}$$

Lemma B.6.2 Relative bounds on the incomplete gamma function
It is useful to show that for $m \geqslant n+1$

$$\gamma(m,x) = x^{m-n}\gamma(n,x) - (m-n)\int_0^x x^{m-n-1}\gamma(n,x)\,\mathrm{d}x \tag{B.6.6}$$

$$\leqslant x^{m-n}\gamma(n,x), \tag{B.6.7}$$

which can be improved upon by using the usual recurrence relation

$$m\gamma(m,x) = x^m\mathrm{e}^{-x} + \gamma(m+1,x) \tag{B.6.8}$$

$$\leqslant x^m\mathrm{e}^{-x} + x^{m-n}\gamma(n+1,x) \tag{B.6.9}$$

$$\leqslant nx^{m-n}\gamma(n,x). \tag{B.6.10}$$

While this inequality will be useful in the low-velocity limit, the following lemma will be applied in the high-velocity limit.

Lemma B.6.3 The lower regularised gamma function is strictly decreasing with respect to its first argument
The regularised gamma function is defined as $P(n,x) = \gamma(n,x)/\Gamma(n)$, where $\Gamma(n) = \gamma(n,\infty)$. For any $m > n$,

$$P(m,x) - P(n,x) = \int_0^x \left(\frac{x^{m-n}}{\Gamma(m)} - \frac{1}{\Gamma(n)}\right) x^{n-1}\mathrm{e}^{-x}\,\mathrm{d}x \tag{B.6.11}$$

can be shown to be nonpositive. This is trivial for $x \leqslant (\,\Gamma(m)/\Gamma(n)\,)^{1/(m-n)}$; in order to demonstrate that the integral does not exceed zero at higher velocities it can be rewritten as:

$$P(m,x) - P(n,x) = \int_\infty^x \left(\frac{1}{\Gamma(n)} - \frac{x^{m-n}}{\Gamma(m)}\right) x^{n-1}\mathrm{e}^{-x}\,\mathrm{d}x, \tag{B.6.12}$$

which has a negative integrand for all $x \geqslant (\,\Gamma(m)/\Gamma(n)\,)^{1/(m-n)}$. Thus $\frac{\partial P(n,x)}{\partial n} \leqslant 0$, $\forall x \geqslant 0$.

Lemma B.6.4 Upper bound of iterated integral for a monomial S
Assuming that $S(V) = V^j$ where $j > 2$, then the iterated integral has the following upper bound

$$I^n\left[\mathrm{e}^{V^2}\int_0^V S\,T\mathrm{e}^{-T^2}\,\mathrm{d}T\right] \leqslant \frac{V^{j+2}}{3}\frac{\left(\,V^{1-j}\gamma(\tfrac{j+2}{2},V^2)\,\right)^n}{n!} \tag{B.6.13}$$

for all $n \geqslant 1$.
Proof for n = 1.

$$I^1\left[\mathrm{e}^{V^2}\int_0^V S\,T\mathrm{e}^{-T^2}\,\mathrm{d}T\right] = \int_0^V 2U^2\int_0^V T^{j+1}\mathrm{e}^{-T^2}\,\mathrm{d}U \leqslant \frac{V^3}{3}\gamma(\tfrac{j+2}{2},V^2) \tag{B.6.14}$$

Proof by induction. Assume

$$I^n\left[\mathrm{e}^{V^2}\int_0^V S\,T\mathrm{e}^{-T^2}\,\mathrm{d}T\right] \leqslant \frac{V^{j+2}}{3}\frac{\left(\,V^{1-j}\gamma(\tfrac{j+2}{2},V^2)\,\right)^n}{n!} \tag{B.6.15}$$

$$\implies I^{n+1}\left[\mathrm{e}^{V^2}\int_0^V S\,T\mathrm{e}^{-T^2}\,\mathrm{d}T\right] \leqslant \int_0^V \frac{2U^{4+j}\mathrm{e}^{-U^2}}{3}\frac{\left(\,U^{1-j}\gamma(\tfrac{j+2}{2},U^2)\,\right)^n}{n!}\,\mathrm{d}U \tag{B.6.16}$$

$$\leqslant \frac{V^{2+j}}{3}\frac{\left(\,V^{1-j}\gamma(\tfrac{j+2}{2},V^2)\,\right)^{n+1}}{(n+1)!} \tag{B.6.17}$$

using integration by parts. □

Theorem B.6.5 For all $\epsilon > 0$, $\exists N$ such that $\Delta_M[V^j] < \epsilon$ for all $M > N$
Proof. Choose

$$N = \max\left[C_j + 1, -\frac{W_{-1}\big(-3\log(\Xi)\epsilon\Xi^{-Z}/A_j\big)}{\log(\Xi)} - Z\right], \tag{B.6.18}$$

where $W_{-1}(f)$ is the lower branch of the Lambert W function, which provides an inverse of the function $f(z) = z\mathrm{e}^z$ for $z \leqslant -1$ and

$$C_j = \frac{j+2}{j-1}, \Xi = \frac{j+2}{3}, Z = 1 + \frac{B_j}{A_j}(C_j + 2) \tag{B.6.19}$$

has been defined in terms of upper bounds corresponding to theorems B.6.2 and B.6.3. These are given by

$$A_j = \frac{9}{4}\mathrm{e}^{-i\pi(j-1)/2}\gamma\left(\tfrac{j-1}{2}, -\tfrac{3}{2}\right) + \left[V^* - \sqrt{\tfrac{3}{2}}\right]\frac{2\left(\frac{j+4}{2\mathrm{e}}\right)^{(j+4)/2}}{\gamma(3/2, 3/2)^2} \tag{B.6.20}$$

$$= \int_0^{\sqrt{\frac{3}{2}}} \frac{U^{j+4}\mathrm{e}^{-U^2}}{\left(\frac{2}{3}U^3\mathrm{e}^{-U^2}\right)^2}\,\mathrm{d}U + \int_{\sqrt{\frac{3}{2}}}^{V^*} \frac{2\left(\frac{j+4}{2\mathrm{e}}\right)^{(j+4)/2}}{\gamma(3/2, 3/2)^2}\,\mathrm{d}U \tag{B.6.21}$$

$$> \int_0^{V^*} \frac{2U^{j+4}\mathrm{e}^{-U^2}}{\gamma(3/2, U^2)^2}\,\mathrm{d}U \tag{B.6.22}$$

$$B_j = \frac{3V^{*\,j+2}}{\gamma(3/2, V^{*2})(j-1)} \tag{B.6.23}$$

$$= V^{*\,N(j-1)}(N - C_j)\int_{V^*}^{\infty} \frac{2U^{j+4-N(j-1)}\mathrm{e}^{-U^2}}{\frac{2}{3}U^3\mathrm{e}^{-U^2}\gamma(3/2, V^{*2})}\,\mathrm{d}U \tag{B.6.24}$$

$$> (N - C_j)\int_{V^*}^{\infty} \frac{2U^{j+4}\mathrm{e}^{-U^2}}{\gamma(3/2, U^2)^2}\left(\frac{V^*}{U}\right)^{N(j-1)}\mathrm{d}U \tag{B.6.25}$$

V^* is the velocity at which the two upper bounds presented in theorems B.6.2 and B.6.3 for the function $\gamma(\frac{j+2}{2}, V^2)$ are equal to each other:

$$V^{*\,j-1} = \frac{\Gamma\left(\frac{j+2}{2}\right)}{\Gamma\left(\frac{3}{2}\right)}\Xi \tag{B.6.26}$$

Thus, for all $M > N$

$$\epsilon > A_j(M+Z)\mathrm{e}^{-\log(\Xi)(M+Z)}\Xi^Z/3 \tag{B.6.27}$$

$$> \left(A_j(M+1) + B_j(C_j+2)\right)\Xi^{-M}/3 \tag{B.6.28}$$

$$> \frac{(M+1)}{3}\left(\int_0^{V^*} \frac{2U^{j+4}\mathrm{e}^{-U^2}}{\gamma(3/2, U^2)^2}\,\mathrm{d}U + \frac{B_j}{N - C_j}\right)\Xi^{-M} \tag{B.6.29}$$

$$> \frac{(M+1)}{3}\int_0^{\infty} \frac{2U^{j+4}\mathrm{e}^{-U^2}}{\gamma(3/2, U^2)^2}\min\left(\frac{3}{j+2}, \frac{\Gamma\left(\frac{j+2}{2}\right)}{\Gamma(3/2), U^{j-1}}\right)^M\mathrm{d}U \tag{B.6.30}$$

$$> \frac{(M+1)}{3}\int_0^{\infty} \frac{2U^{j+4}\mathrm{e}^{-U^2}}{\gamma(3/2, U^2)^{2+N}}\left(\,U^{1-j}\gamma\left(\tfrac{j+2}{2}, U^2\right)\right)^M\mathrm{d}U \tag{B.6.31}$$

$$> 2(M+1)!\int_0^{\infty} \frac{U^2\mathrm{e}^{-U^2}}{\gamma(3/2, U^2)^{N+2}}I^M\left[\mathrm{e}^{U^2}\int_0^U T^{j+1}\mathrm{e}^{-T^2}\,\mathrm{d}T\right]\mathrm{d}U \tag{B.6.32}$$

$$> \Delta_N\left[V^{j+1}\right] \qquad \square$$

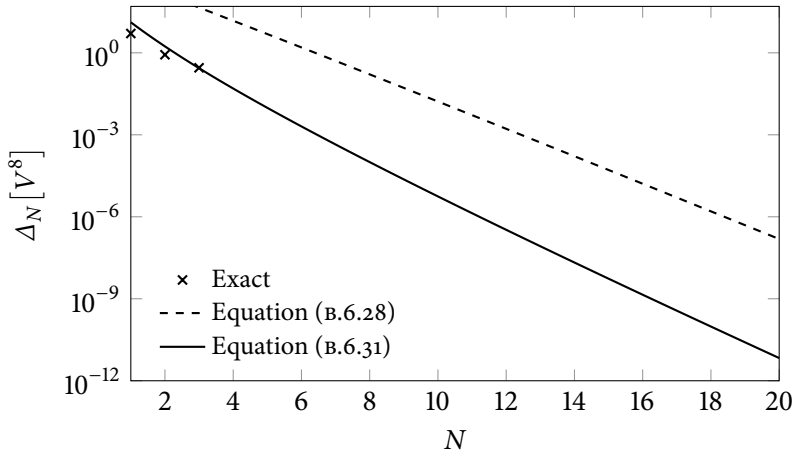

FIGURE B.1: Reduction of the maximum error of the integral in eq. (B.6.1) after N iterations for the monomial source V^8 resulting from a linearised temperature sinusoid (see eq. 4.3.13): (the nonstationary V^3 term does not contribute to pertubrations of the distribution function). Dashed lines depict the large overestimate of the error resulting from eq. (B.6.28), while the solid line result provides uses the improved approximation in eq. (B.6.31) for the exact error Δ_N evaluated at $V = \infty$, which has been calculated numerically for up to three iterations and marked by crosses. (Zero iterations leads to an error that diverges with increasing velocity).

By this theorem and the linearity of the iterated integral on S its convergence is guaranteed for any source $S(V)$ bounded above by a polynomial that does not include a constant, linear or quadratic term (i.e. $S \leqslant \sum_{j=2}^{\infty} c_j V^j$ for any combination of $c_j \in \mathbb{R}$). Note that the minimum number of iterations N required for a maximum error less than ϵ turns out to be much less than suggested by equation eq. (B.6.18).

B.7 ASYMPTOTIC EXPANSION FOR COLLISIONLESS DIFFUSION APPROXIMATION

Consider the integral

$$F_j(u) = \frac{4}{\sqrt{\pi}} \int_0^{\infty} V^{(2+j)} \mathrm{e}^{-V^5 u - V^2} \, \mathrm{d}V \tag{B.7.1}$$

appearing in the expression for the electric potential in the collisionless limit under the diffusive approximation eq. (4.4.48). Its asymptotic expansion as

$u \to \infty$ can be obtained by changing variables to $x = V^5$ and applying the general form of Watson's lemma (Watson 1916) presented by Oberhetting (1959);

$$F_j(u) = \frac{4}{5\sqrt{\pi}} \int_0^\infty x^{(j-2)/5} \mathrm{e}^{-xu-x^{2/5}} \,\mathrm{d}x \tag{B.7.2}$$

$$\implies F_j \sim \frac{4}{5\sqrt{\pi}} \frac{1}{u^{(j+3)/5}} \sum_{m=0}^{\infty} \frac{(-1)^m}{m!} \Gamma\left[\frac{3+j+2m}{5}\right] \frac{1}{u^{2m/5}} \text{as } u \to \infty. \tag{B.7.3}$$

B.8 ASYMPTOTIC EXPANSION FOR REGIME OF COLLISIONLESS SUPRATHERMALS

The integrals appearing in the expression for the heat flow in the collisionless suprathermals (eq. 4.5.11) obtained by using a low-velocity approximation for the electron-electron collision integral take the form

$$J_n(V_*) = \int_0^\infty \frac{w^n \mathrm{e}^{-w^2 V_*^2}}{1 + c_\psi w^5} \,\mathrm{d}w. \tag{B.8.1}$$

We are interested in the asymptotic expansion of J_n in the short-wavelength limit corresponding to $V_* \to 0$. Applying the Mellin transform finds that

For derivation of eq. (B.8.3) *see example 2.3 of (Oosthuizen 2011)*

$$\mathcal{M}[J_n](s) = \frac{\Gamma(s/2)}{2} \int_0^\infty \frac{w^{n-s}}{1 + c_\psi w^5} \,\mathrm{d}w \tag{B.8.2}$$

$$= \frac{\pi}{10 c_\psi^{(n+1)/5}} \Gamma(s/2) \operatorname{cosec}(\pi(1+n-s)/5), \tag{B.8.3}$$

which is analytic on the strip given by $\max(0, n-4) < \mathrm{Re}(s) < n+1$ as long as $n > -1$. The singular expansion of eq. (B.8.2) is given by

$$\mathcal{M}[J_n](s) \asymp \frac{1}{c_\psi^{(n+1)/5}} \sum_{k=0}^{\infty} \frac{(-1)^k}{k!} \frac{1}{s+2k} \sum_{m=-\infty}^{\infty} \frac{1}{s-(n+1-5m)}, \tag{B.8.4}$$

where all poles corresponding to $\mathrm{Re}(s) \leqslant \max(0, n-4)$ contribute to the asymptotic series of $J_n(V_*)$ at $V_* \to 0^+$. This can be found by applying Oosthuizen's (2011) converse mapping theorem. Due to the varying occurence of double poles with different values of n this can not be done generally and must be carried out on a case-by-case basis. We shall provide an example for a particularly tricky case of $n = 4$.

Example B.8.1

To obtain the first two terms for the asymptotic series of $J_4(V_*)$ as $V_* \to 0$ we

need to separate the double and single poles contributing to the singular element of $J_4(V_*)$ at $s = V_*$ (using Oosthuizen's notation)

$$\Big[\mathcal{M}[J_4](s)\Big]_{s=0} = \frac{1}{c_\psi}\left(\frac{1}{s^2} + \frac{1}{s}\left(\sum_{k=1}^{\infty}\frac{(-1)^k}{k!}\frac{1}{s+2k} + \sum_{m\neq 1}\frac{1}{s+5(m-1)}\right)\right), \tag{B.8.5}$$

while the second sum evaluates to zero due to cancellation, the first sum is more complicated but equating it to $\Gamma(s/2)/2 - 1/s$ allows the limit $-\gamma_\mathrm{E}/2$ at $u = 0$ to be computed (where γ_E is the Euler-Mascheroni constant).

$$\therefore \Big[\mathcal{M}[J_4](s)\Big]_{s=0} = \frac{1}{c_\psi}\left(\frac{1}{s^2} - \frac{\gamma_\mathrm{E}}{2s}\right) \tag{B.8.6}$$

$$\implies \qquad J_4(V_*) = \frac{1}{c_\psi}\big(-\log(V_*) - \gamma_\mathrm{E}/2\big) + \mathcal{O}(V_*^2) \tag{B.8.7}$$

by the converse mapping theorem.

B.9 NONCONTRIBUTION OF THE SNB ELECTRIC FIELD CORRECTION FOR A LOW-AMPLITUDE TEMPERATURE SINUSOID

Lemma B.9.1
$\forall \epsilon, Y > 0 \exists \delta T_\mathrm{e}/T_0 > 0 \mid \forall (k, v) \in \{\mathbb{R}^2 | k\lambda_\mathrm{ei}^{(0)} v^2/v_\mathrm{2T}^2 < Y\} | \frac{\lambda_\mathrm{ei}^{*(E)}}{\lambda_\mathrm{ei}^*} - 1| < 1$, In other words, a small enough amplitude can always be chosen such that electric fields can be ignored up to any given product of k and v^2.
Proof. Choose $\delta T_\mathrm{e}/T_0 = \epsilon/(1+\beta_\parallel)\xi Y$, then from eq. (4.6.11) we find that

$$\left|\frac{\lambda_\mathrm{ei}^{*(E)}}{\lambda_\mathrm{ei}^*} - 1\right| = \frac{(1+\beta_\parallel)k|\sin(kx)|\delta k_\mathrm{B} T_\mathrm{e}}{\frac{1}{2} m_\mathrm{e} v^2}\lambda_\mathrm{ei}^* \leq \epsilon \quad \square \tag{B.9.1}$$

B.10 ASYMPTOTIC BEHAVIOUR OF JI-HELD CLOSURE

Here we derive the asymptotic short-wavelength behaviour of the Ji-Held closure (Ji and Held 2014) for the thermal conductivity of a fully-ionised hydrogen temperature sinusoid

$$\kappa_{\parallel c} = 2\int_0^\infty K_{hh}(s')\cos(\sqrt{2}k\lambda_\mathrm{ei}^{(\mathrm{B})}s')\,\mathrm{d}s', \tag{B.10.1}$$

where $K_{hh}(s) = -(d + a\exp(-b|s|^c)\log(1 - \alpha\exp(-\beta|s|^\gamma))$,

In order to calculate the dominant terms as $k\lambda_{\mathrm{ei}}^{(\mathrm{B})} \to \infty$ we can apply the method of Wong and Lin (1978)/ Dai and Naylor (1992), which requires expressing the above cosine transform as a complex Fourier transform,

$$\kappa_{\parallel c} = \mathrm{Re}\left[2\int_0^\infty K_{hh}(s')\exp(\sqrt{2}ik\lambda_{\mathrm{ei}}^{(\mathrm{B})}s')\,\mathrm{d}s'\right], \tag{B.10.2}$$

and then change variable to $t = -is'$

$$\implies \kappa_{\parallel c} = \mathrm{Re}\left[2i\int_0^\infty K_{hh}(it)\exp(-\sqrt{2}k\lambda_{\mathrm{ei}}^{(\mathrm{B})}t)\,\mathrm{d}t\right]. \tag{B.10.3}$$

The asymptotic behaviour of $\kappa_{\parallel c}$ at $k\lambda_{\mathrm{ei}}^{(\mathrm{B})} \to \infty$ is then determined by that of K_{hh} at $t \to 0$;

$$\begin{aligned}\implies \kappa_{\parallel c} = -2(d+a)\,\mathrm{Re}\Big[\int_0^\infty i\Big(&\log(\beta) + \gamma\log(it) \\ &- \frac{\beta(it)^\gamma}{2} + \mathcal{O}(t^c\log(t))\Big)\mathrm{e}^{-\sqrt{2}k\lambda_{\mathrm{ei}}^{(\mathrm{B})}t}\,\mathrm{d}t\Big]\end{aligned} \tag{B.10.4}$$

assuming $c > \gamma > 0$ as is the case for the parameters given by Ji and Held. Carrying out the integration yields

$$\begin{aligned}\kappa_{\parallel c} = &-\frac{\sqrt{2}(d+a)}{k\lambda_{\mathrm{ei}}^{(\mathrm{B})}}\,\mathrm{Re}\Big[i\Big(\log(\beta) + \gamma(i\pi/2 - \gamma_{\mathrm{E}} - \log(\sqrt{2}k\lambda_{\mathrm{ei}}^{(\mathrm{B})})) \\ &- \frac{\beta i^\gamma\Gamma(1+\gamma)}{2(\sqrt{2}k\lambda_{\mathrm{ei}}^{(\mathrm{B})})^\gamma} + \mathcal{O}\Big(\frac{\log(k\lambda_{\mathrm{ei}}^{(\mathrm{B})})}{(k\lambda_{\mathrm{ei}}^{(\mathrm{B})})^c}\Big)\Big)\Big]\end{aligned} \tag{B.10.5}$$

$$= \frac{\pi(d+a)\gamma}{\sqrt{2}k\lambda_{\mathrm{ei}}^{(\mathrm{B})}}\Big(1 - \frac{\beta\sin(\pi\gamma/2)\Gamma(\gamma)}{2^{\gamma/2}\pi} + \mathcal{O}\Big(\frac{\log(k\lambda_{\mathrm{ei}}^{(\mathrm{B})})}{(k\lambda_{\mathrm{ei}}^{(\mathrm{B})})^c}\Big)\Big). \tag{B.10.6}$$

This allows us to associate the Ji-Held fitting parameters with the coefficients defined in eq. (4.5.1) that parametrise the damping behaviour of temperature sinusoids as the collisionless limit is approached: $\chi_1 = \pi(d+a)\gamma/3$, $\eta = \gamma$ and $c_1 = \beta\sin(\pi\gamma/2)\Gamma(\gamma)/2^{\gamma/2}\pi$.

SPARK A VFP code by Epperlein *et al.* (1988a,b; 1991) which employs the ADI method in one velocity and up to two spatial dimensions to solve the VFP equations in the diffusion approximation and incorporates the effect of electron-electron collisions on $\vec{f}_1$ by modifying ν_{ei} (see 3.1.2).

ADI (Alternate Direction Implicit) Numerical method used to solve multi-dimensional partial differential equations by treating in turn only one dimension implicitly and the others explicitly.

ALE Describes a particular spatial discretisation scheme used in hydrodynamics codes designed for simulating implosions.

AWBS (Albritton-Williams-Bernstein-Swartz) Refers usually to an approximation of the electron-electron collision operator that only retains the slowing down term, see section 2.3.2.

BGK (Bhatnagar-Gross-Krook) collision operator

BOUT++ Collaborative code used to simulate boundary turbulence in complex tokamak geometry.

CELIA (Centre Lasers Intenses et Applications.) Laboratory based in Bourdeaux, France. Home to the CHIC code and birthplace of the SNB model.

CFL (Courant-Friedrichs-Lewy condition) Provides an upper bound for the timestep Δt corresponding to a given cell size Δx in hyperbolic PDE's.

CHIC Radiation-hydrodynamics code with ALE capabilities used at CELIA.

CTC (Classical Transport Code) A 2D finite element code developed by Bissell et al. (2010) able to simulate flux-limited Braginskii transport including appropriate corrections for inverse bremmstrahlung due to laser absorption along with simple hydrodynamics used as a comparison to VFP simulations.

DILL (Diffusive Implicit Linearised Lorentz) A code for solving the VFP code under the Diffusive approximation using a fully-Implicit formulation adapted for Linearised (small amplitude) problems in the Lorentz (high-Z) limit. Details can be found in section 3.1.4.

DKE (Drift Kinetic Equation) A 1D2V PDE derived from the gyro-averaged VFP equation under the assumption that the departure of the distribution function from Maxwellian is small and does not vary too fast. It is often applied in tokamak studies and is introduced in eq. (2.1.5).

DRACO Rad-hydro code used by LLE, Rochester.

DUED The University of Rome hydro code, see Atzeni 1986; Atzeni et al. 2005.

EDF (Electron Distribution Function) The probability density of finding an electron in a particular location in the six-dimensional position/velocity phase-space.

EIC (Eigenvector-Integral Closure) Nonlocal model based on Ji, Held and Sovinec's moment description of the distribution function Ji et al. 2009. Further developed by Omotani et al. (2013; 2015).

ELM (Edge Localised Mode) Large energy-releasing disruption in tokamaks that manifests as filaments escaping the SOL.

HYDRA The LLNL rad-hydro code.

ICF (Inertial Confinement Fusion) refers to any approach to fusion energy where the primary method is to obtain very high fuel densities for short periods of time.

IMPACT (Implicit Magnetised Plasma and Collisional Transport) fully-implicit VFP code by Kingham and Bell (2004) which retains only the first two terms in a Cartesian tensor expansion and approximates the effect of electron-electron collisions on $\vec{f}_1$ by modifying ν_{ei} (see 3.1.2).

ITER The world's largest tokamak, currently under construction in Cadarache, France.

JET The largest *operational* tokamak in the world, situated at the Culham Centre for Fusion Energy.

K2 A VFP code in the KALOS formulation developed by Mark Sherlock at LLNL, very similar to OSHUN.

KALOS (Kinetic Laser-plasma Simulation) Used to denote the spherical harmonic formulation presented by Bell et al. (2006) used in the code with the same name

KIPP (Kinetic Code for the Plasma Periphery) A 1D2V VFP code developed by Chankin et al. (2012) at IPP Garching.

LASNEX An 2D radiation-hydrodynamics code for simulating inertial fusion experiment using a finite element method.

LILAC Another University of Rochester rad-hydro code (Holstein et al. 1986).

LLE at the University of Rochester, home to the Omega Laser Facility

LLNL (Lawrence Livermore National Laboratory) in California, location of National Ignition Facility.

LMV (Luciani, Mora and Virmont) Usually used to refer to a convolution kernel suggested in Luciani et al. 1983 (see section 2.3.2).

*Mag*LIF (Magnetised Liner Confinement Fusion) is a novel hybrid approach to achieving fusion gain by sending short electric pulse through thin hohlraums containing fusion fuel.

MCF (Magnetic Confinement Fusion) refers to various approaches to realising fusion energy by containing the fuel with magnetic fields, including tokamaks and stellarators.

mfp refers to a representative distance that a particle (electron/ion) can travel in a plasma without being overly affected by collisions. More precisely, this is often calculated as the ratio between a (thermal) velocity and collision frequency, for example the Braginskii electron-ion mfp is given by $\lambda_{\mathrm{ei}}^{(\mathrm{B})} = v_{\mathrm{IT}}\tau_{\mathrm{ei}}^{(\mathrm{B})}$.

MHD (Magnetohydrodynamics) A term used to encompass encompass a cohort of related effects involving the evolution of magnetic fields and electric currents in conductive fluids.

MUMPS (MUlti-frontal Massively Parallel sparse direct Solver) The matrix solver used in the KIPP code to calculate the Rosenbluth potentials and evaluate the effect of the Fokker-Planck collisions.

NFLF (Non-Fourier Landau-Fluid) The nonlocal model invented by Dimits, Joseph and Umansky (2013, 2014 see also Umansky et al. 2015) based on fitting a sum of modified Helmholtz equations to behaviour of a low-amplitude temperature sinusoid.

NIF (National Ignition Facility) World's first megajoule-scale inertial fusion experiment.

ODE (Ordinary Differential Equation)

OECD (Organisation for Economic Co-operation and Development)

OSHUN A VFP code using the spherical harmonics formulation developed by Tzoufras et al. (2011). Most time-differencing is performed explicitly but some implicit features are available using operator splitting.

PDE (Partial Differential Equation)

PIC (Particle-in-Cell) An approach to modelling kinetic effects in plasma by simulating typically 10^4 – -10^6 charged particles on each cell making up a larger grid, electromagnetic fields at each cell are then calculated based on the resulting charge and current densities on the grid.

SNB (Schurtz, Nicolaï, Busquet) The multigroup diffusion model, sometimes referred to solely as the Schurtz model presented in section 3.3.

SOL (Scrape-Off Layer) Region just outside the last closed flux surface in a tokamak that transports heat and particles from the core to the divertor.

SOLPS (Scrape-Off Layer Plasma Simulation) Fluid code for 2D modeling SOL transport coupled to Monte Carlo neutral code B2-EIRENE.

SPRING is a rather ancient Fourier-space VFP code developed by Epperlein and Short (1994) that is able to include arbitrary harmonics.

SRS (Stimulated Raman Scattering)

UEDGE A fully-implicit 2D code developed at LLNL for modelling the tokamak edge.

VARPRO (Variable Projection) A Fortran implementation of the separable nonlinear least squares algorithm.

VFP (Vlasov-Fokker-Planck) A continuum approach to a fully kinetic description of a plasma. This can be fully represented where the full collision operator C_e typically neglects large-angle scattering and truncates an expansion to first in the inverse Coulomb logarithm $1/\log \Lambda_\alpha$ in its derivation.

a is a coefficient appearing in the NFLF model used to parametrise the damping behaviour of a low-amplitude temperature sinusoid in the collisionless limit with $\widetilde{Q} \to \widetilde{Q}^{(\mathrm{B})}/ak\lambda_{\mathrm{ei}}^{(\mathrm{B})}$. This can be related to the dimensionless thermal conductivity $\kappa_{\|c}^{(\mathrm{B})}$ Hammett and Perkins coefficient χ_1 by $a = \kappa_{\|c}^{(\mathrm{B})}/(3\!/\!_2\sqrt{2}\chi_1) \approx \sqrt{\pi}\kappa_{\|}^{(\mathrm{B})}/3\sqrt{2}$.

$\vec{B}$ is the magnetic field.

b_E determines the lowest order deviation of the electric field from the local limit for a low-amplitude temperature sinusoid in the semicollisional regime as $\vec{E} \to 1 - b_E k^2 \lambda_{\mathrm{ei}}^{(\mathrm{B})2}$.

b_Q determines the lowest order deviation of the heat flow from the local limit for a low-amplitude temperature sinusoid in the semicollisional regime as $\vec{Q} \to 1 - b + Qk^2\lambda_{\mathrm{ei}}^{(\mathrm{B})2}$.

c is the speed of light.

c_∞ appears in the expression introduced in section 4.5 $\mathrm{Im}[\widetilde{Q}_x] = -3\!/\!_2\chi_1(1 - c_\infty/(k\lambda_{\mathrm{ei}}^{(\mathrm{B})})^\eta)n_{\mathrm{e}}v_{2\mathrm{T}}k_{\mathrm{B}}\widetilde{T}_{\mathrm{e}}$ which approximates the imaginary part of the heat flow arising from a damping low amplitude temperature sinusoid at high degrees of nonlocality where the suprathermal electrons can be considered collisionless.

c_1 is used to replace c_∞ to achieve a better fit to simulations across a wide range of collisionalities.

$C_\alpha(f_\alpha) = \sum_\beta C_{\alpha\beta}(f_\alpha, f_\beta)$ represents the full Fokker-Planck collision operator for collisions of species α between all species, including itself. In this work only electron-electron and electron-ion species are considered.

$C_{\mathrm{ee}0}(f_0) = \frac{\Gamma_{\mathrm{ee}}}{v^2}\frac{\partial}{\partial v}\left(I_0(f_0)f_0 + D(f_0)\frac{\partial f_0}{\partial v}\right)$ represents the action of the nonlinear Fokker-Planck electron-electron collision operator on the isotropic part of the distribution function f_0.

$C_{\mathrm{ee}}^{(\mathrm{L})}0(\delta f_0) = C_{\mathrm{ee}}\left(\delta f_0, f_{\mathrm{e}}^{(\mathrm{mb})}\right) + C_{\mathrm{ee}}\left(f_{\mathrm{e}}^{(\mathrm{mb})}, \delta f_0\right)$ is the linearised collision operator, valid when the deviation from Maxwellian is small, for collisions of electrons with themselves introduced at the beginning of chapter 4.

$D(f) = 4\pi\int_0^v u^2\int_u^\infty f_0 w\,\mathrm{d}w\,\mathrm{d}u/v$ is an integral operator appearing in the electron-electron collision operator for the isotropic part of the distribution function $C_{\mathrm{ee}0}$.

e is Euler's number.

e is the magnitude of the electron charge.

$_{\mathrm{e}}$ denotes an electron species.

$\vec{E}$ is the electric field.

$\vec{E}^{(\mathrm{B})}$ is the local electric field according Braginskii (1965) or Spitzer-Härm theory typically using the more accurate coefficients obtained by Epperlein and Haines (1986).

E_{mult} allows for a multiplier on the local electric field used in the SNB model.

f_α is the distribution function for species α.

$\mathfrak{f}_{\mathrm{N}}$ is the Nernst flux-limiter.

$\mathfrak{f}_Q$ is the thermal flux-limiter.

$\mathfrak{f}_{\mathrm{RL}}$ is the flux-limiter for the Righi-Leduc heat flow.

$f_{\mathrm{e}}^{(\mathrm{mb})} = n_{\mathrm{e}} \exp(-v^2/v_{2\mathrm{T}}^2)/(\sqrt{\pi} v_{2\mathrm{T}})^3$ is the Maxwell-Boltzmann electron distribution function.

$f_0 = \int f_{\mathrm{e}} \, \mathrm{d}^2\Omega/4\pi$is the isotropic part of the distribution function in either a spherical harmonic or Cartesian tensor expansion.

$\delta f_0 = f_0 - f_{\mathrm{e}}^{(\mathrm{mb})}$is the isotropic perturbation to the distribution function.

$\delta f_{\mathrm{e}} = f_\alpha - f_{\mathrm{e}}^{(\mathrm{mb})}$ is the total deviation of the electron distribution function from a Maxwellian.

$\vec{f}_1$ represents the first-order anisotropy in the distribution function in either a spherical harmonic or Cartesian tensor expansion.

$\mathrm{He}_n\,(x) = (-1)^n \mathrm{e}^{x^2} \frac{\mathrm{d}^n}{\mathrm{d}x^n} \mathrm{e}^{-x^2}$ are the Hermite polynomials.

H_g is the term that is solved for in the SNB model from which the nonlocal heat flow can be obtained. Schurtz *et al.* (2000) suggest that this can be related to the isotropic perturbation of the distribution function δf_0.

$I_N(f) = 4\pi \int_0^v f u^{N+2} \, \mathrm{d}u \, / v^N$

i is the imaginary unit

$I_N^{(\mathrm{B})}$ is the modified Bessel function of the first kind.

$_{\mathrm{i}}$ denotes an electron species.

$\vec{j}$ is the electric current.

k typically represents the wave number representing the temperature gradient unless otherwise specified.

k_{B} is Boltzmann's constant

$K_N^{(\mathrm{B})}$ is the modified Bessel function of the second kind.

$\mathrm{Kn} = \lambda_{\mathrm{ei}}^{(\mathrm{B})}/L_T$ is the nonlocality parameter or Knudsen number assumed to be small in the Chapman-Enskog expansion.

$\mathrm{L}_n^{(\alpha)}\,(x) = \frac{x^{-\alpha}\mathrm{e}^x}{n!} \frac{\mathrm{d}^n}{\mathrm{d}x^n}(\mathrm{e}^{-x} x^{n+\alpha})$ are the generalised Laguerre polynomials of order α.

L_T is the temperature scalelength, which is usually calculated by $L_T = |T_\mathrm{e}/\vec{\nabla} T_\mathrm{e}|$ unless specified otherwise. For the temperature sinusoid damping studied chapter 4 this is instead taken to be $1/k$.

m_α is the mass of species α.

n_α is the number density of species α.

$\mathrm{P}_n\,(x) = \frac{1}{2^n n!}\frac{\mathrm{d}^n}{\mathrm{d}x^n}(x^2-1)^n$ are the Legendre polynomials.

p_j are the linear coefficients in NFLF

$P_\mathrm{e} = n_\mathrm{e} k_\mathrm{B} T_\mathrm{e}$ is the electron pressure.

$\mathrm{P}_l^m\,(x) = (-1)^m(1-x^2)^{m/2}\frac{\mathrm{d}^m}{\mathrm{d}x^m}P_l(x)$ are the associated Legendre polynomials.

$\vec{Q}$ is the electron heat flow.

q_j are the linear coefficients in NFLF

$Q_\mathrm{fs} = n_\mathrm{e} k_\mathrm{B} T_\mathrm{e} v_\mathrm{1T}$ is the free-streaming heat flux.

$\vec{Q}^{(\mathrm{B})}$ is the local heat flow as given by Braginskii (1965) or Spitzer-Härm theory using the more accurate coefficients obtained by Epperlein and Haines (1986).

R is the normalised response function defined by Hammet and Perkins (1990) appearing in the linear analysis of a collisionless plasma.

r is a numerical factor used to correct the velocity-dependent Krook frequency ν_ee in the SNB model.

T_α is the temperature of species α.

v typically denotes the velocity of a particular energy group.

$v_\mathrm{1T} = \sqrt{k_\mathrm{B} T_\mathrm{e}/m_\mathrm{e}}$ is a commonly used definition of the electron thermal velocity.

$v_\mathrm{2T} = \sqrt{2k_\mathrm{B} T_\mathrm{e}/m_\mathrm{e}}$ is a another definition of the electron thermal velocity corresponding to the velocity of electrons with kinetic energy $k_\mathrm{B} T_\mathrm{e}$.

$v_\mathrm{N} = -\beta_\wedge \nabla_\perp T_\mathrm{e}/eB$ is the Nernst velocity at which magnetic fields are advected down temperature gradients.

$w_g = \int_{\beta_{g-½}}^{\beta_{g+½}} \beta^4 \mathrm{e}^{-\beta}/24\,\mathrm{d}\beta$ is the weighting function used in the SNB model.

Z is the average ionisation.

$\alpha_\perp$ is the perpendicular resistivity represent the dependence of the electric field on any current travelling parallel to it.

$\beta_g = \epsilon_g/k_\mathrm{B} T_\mathrm{e}$ is the relative energy of a group of electrons compared to the thermal energy at that point.

$\beta_\parallel$ is the parallel thermoelectric coefficient which determines the dependence of the parallel electric field on the parallel temperature gradient as well as the dependence of the parallel heat flow on any current travelling parallel to the magnetic field.

$\beta_\perp$ is the thermoelectric coefficient which determines the dependence of the electric field perpendicular to the magnetic field and temperature gradi-

ent on the temperature gradient itself as well as the dependence of the parallel heat flow on any currents travelling in an opposite direction.

$\beta_\wedge$ is the thermoelectric coefficient which determines the dependence of the electric field perpendicular to the magnetic field and temperature gradient on the parallel temperature gradient itself as well as the dependence of the heat flow on any currents travelling in a perpendicular direction.

$\epsilon = \frac{1}{2} m_e v^2$ is the energy corresponding to a particular group g of electrons with velocity v.

ε_0 is the permitivitty of free space.

$\Gamma_{\alpha\beta} = 4\pi(Z_\alpha Z_\beta e^2/4\pi m_\alpha \varepsilon_0)^2 \log \Lambda_{\alpha\beta}$ is a velocity-independent terms that appears in the collision operator $C_{\alpha\beta}$ between species $\alpha$and β. Here Z_α is the average charge of species α relative to the magnitude of the electron charge e.

$\gamma(n, x) = \int_0^x x^{n-1} \mathrm{e}^{-x}\, \mathrm{d}x$ is the lower incomplete gamma function.

γ_D represents the damping rate of a temperature sinusoid.

$\gamma_\mathrm{E} = 0.5772\ldots$ is the Euler-Mascheroni constant.

$\Gamma(n) = \int_0^\infty x^{n-1} \mathrm{e}^{-x}\, \mathrm{d}x$ is the complete gamma function.

η appears in the expression introduced in section 4.5 $\widetilde{Q}_x = -\frac{3}{2}\chi_1(1-c_\infty/(k\lambda_{\mathrm{ei}}^{(\mathrm{B})})^\eta) n_\mathrm{e} v_{2\mathrm{T}} k_\mathrm{B} \widetilde{T}_\mathrm{e}$ which approximates the imaginary part of the heat flow arising from a damping low amplitude temperature sinusoid at high degrees of nonlocality where the suprathermal electrons can be considered collisionless.

$\theta\,(t)$ is the Heaviside step function which takes the value 1 if $t > 0$ and 0 otherwise.

$\kappa_\parallel$ is the dimensional thermal conductivity in the absence of or parallel to an applied magnetic field.

$\kappa_\parallel^{(\mathrm{B})}$ is the parallel dimensional thermal conductivity in the local limit. This was originally calculated by Braginskii (1965), but more accurate calculations have been performed by Epperlein and Haines (1986).

$\kappa_\perp$ is the dimensional thermal conductivity perpendicular to an applied magnetic field but parallel to the temperature gradient.

$\kappa_\wedge$ is the dimensional thermal conductivity perpendicular to both the temperature and applied magnetic field.

$\log \Lambda_{\alpha\beta}$ is the Coulomb logarithm based on collisions between species α and β. While there are a number of different expressions for this in the literature, both electron-electron and electron-ion forms are typically assumed to take equivalent and constant values in this work.

$\lambda_\mathrm{D} = v_{1\mathrm{T}}/\omega_{\mathrm{pe}}$ is the Debye length for a plasma with cold ions.

$\lambda_{\mathrm{ee}} = v/\nu_{\mathrm{ee}}$ is the velocity-dependent Krook electron-electron mean free path used in the SNB model.

$\lambda_{ei} = v/\nu_{ei}$ is the velocity-dependent electron-ion mean free path

$\lambda_{ei}^{(0)} = \lambda_{ei}(v_{2T})$ is the electron-ion mean free path of an electron with energy $k_B T_e$

$\lambda_{ei}^{(B)} = 3\sqrt{\pi}\lambda_{ei}^{(0)}/4\sqrt{2}$ is the electron-ion mean free path as defined by Braginskii (1965).

$\lambda_{ei}^{*} = \xi v/\nu_{ei}$ is the velocity-dependent electron-ion mean free path.

$\lambda_{ei}^{(T)} = \lambda_{ei}(v_{1T}) = \lambda_{ei}^{(0)}/4$ is the Trubnikov (1965) electron-ion mean free path.

$\lambda_e^{*} = \sqrt{\lambda_{ei}^{*}\lambda_{ee}}$ is the velocity-dependent geometrically averaged mean free path appearing in the original SNB model (Schurtz et al. 2000) (note that this depends on the value chosen for r).

$\lambda_s^{(0)} = k_B T_e/e|\vec{E}|$ is the stopping distance of a thermal electron with energy $\epsilon = k_B T_e$ travelling antiparallel to an electric field.

μ_0 is the permeability of free space.

$\vec{\nabla}$ is the vector gradient operator.

$\nu_{ee} = r\nu_{ei}/Z$ is the velocity-dependent 'Krook' electron-electron frequency used in the SNB model.

$\nu_{ei} = n_i \Gamma_{ei}/v^3$ is the velocity-dependent electron-ion collision frequency that appears in the equation for $\vec{f}_1$.

$\nu_{ei}^{(0)} = \nu_{ei}(v_{2T})$ is the rate at which a first-order anisotropy of the distribution occuring at $k_B T_e$ is damped due to electron-ion collisions.

$\nu_{ei}^{*} = \nu_{ei}/\xi$ is the corrected velocity-dependent electron-ion collision frequency that appears in the equation for $\vec{f}_1$.

ϕ is the electric potential.

$\rho = e(n_i - n_e)$ is the charge density.

$\tau_{ei}^{(0)} = 1/\nu_{ei}^{(0)}$ is the collision time for an electron with energy $k_B T_e$ against a cold ion background.

$\tau_{ei}^{(B)} = 3\sqrt{\pi}\tau_{ei}^{(0)}/4$ is the mean collision time defined by Braginskii (1965).

$\tau_{ei}^{(T)} = 1/\nu_{ei}(v_{1T}) = \tau_{ei}^{(0)}/4$ is the Trubnikov electron-ion collision time (1965).

ξ is the electron-ion collision fix reducing the electron-ion mean free path λ_{ei} to approximate the effect of electron-electron collisions on the anisotropic part of the distribution function $\vec{f}_1$. The form most commonly used in this is that Epperlein and Short (1991): $\xi = (Z + 0.24)/(Z + 4.2)$.

$\xi_{ES} = (Z + 0.24)/(Z + 4.2)$ allows an explicit shorthand to specify that it is the Epperlein Short collision fix that is being used rather than another one.

$\chi\ \omega_{ce}\tau_{ei}^{(B)}$ is the Hall parameter representing the importance of magnetic fields over collisionality.

χ_1 is a coefficient appearing in the NFLF model used to parametrise the damping behaviour of a low-amplitude temperature sinusoid in the collisionless limit with.

Ψ is the dimensionless ratio between the Nernst and heat flux coefficients $P_e\beta_\wedge/eB\kappa_\perp$.

$\psi = \delta f_0/f_e^{(mb)}$ is the relative nonlocal perturbation on the isotropic part of the distribution function.

$\omega_{ce} = eB/m_e$ is the electron cyclotron frequency.

$\omega_{pe} = \sqrt{n_e e^2/m_e\varepsilon_0}$ is the electron plasma frequency.

MN An alternative (and essentially equivalent) method to closing the VFP equation when expanding in spherical harmonics or Cartesian tensors by maximising 'angular entropy.' This approach conveniently ensures positive-definiteness of the the distribution function by re-expressing the EDF in terms of Lagrange multipliers as $f = \exp(\alpha_0(v) + \vec{v} \cdot \overrightarrow{alpha}_1(v)/v + \dots)$

PN The most common closure used in VFP codes that expand the distribution function according to anisotropy (i.e. with spherical harmonics or Cartesian tensors). This corresponds to performing a truncation by enforcing $f_{N+1} = 0$.

REGIME OF COLLISIONLESS SUPRATHERMALS Describes the approach to the collisionless regime where the collisions of electron that have speeds exceeding the thermal velocity can be neglected.

BRAGINSKII Corresponds to the local theory of magnetised plasmas presented by Braginskii (1965), although more exact transport coefficients were later calculated by Epperlein et al. (1986).

CARTESIAN TENSOR EXPANSION A method for expressing a multi-dimensional scalar function, such as a distribution function, as series of terms with increasing anisotropy: $f = f_0(v) + \frac{v_i}{v} f_{1i}(v) + \frac{v_i v_j}{v^2} f_{2ij}(v) + \dots$

CHAPMAN-ENSKOG EXPANSION An approach to understanding transport theory by expanding the distribution in increasing order of nonlocality represent by the Knudsen number Kn

COLLISIONLESS REGIME The behaviour of a plasma when collisions are completely neglected on the timescale of the problem, in this case collestive effects such as plasma oscillations and Landau damping are unavoidably important.

HYDRODYNAMIC REGIME Corresponds to the conditions where the local theory holds

SEMICOLLISIONAL REGIME Plasma conditions such that the mean free path is still much smaller than the temperature scalelength but the lowest (second) order perturbations on the heat flow begin to be noticeable.

SEPARABLE NONLINEAR LEAST SQUARES An algorithm used to optimise fits that consist of a series of weighted nonlinear problem

BIBLIOGRAPHY

Albritton, J R, E A Williams, I B Bernstein and K P Swartz (1986) 'Nonlocal electron heat transport by not quite Maxwell-Boltzmann distributions' *Phys. Rev. Lett.* **57**, p. 1887.

Atzeni, S, A Schiavi, F Califano, F Cattani, F Cornolti, D D Sarto, T Liseykina, A Macchi and F Pegoraro (2005) 'Fluid and kinetic simulation of inertial confinement fusion plasmas' *Comp. Phys, Comm.* **169** (1) Proceedings of the Europhysics Conference on Computational Physics 2004, pp. 153–159.

Atzeni, S (1986) '2-D lagrangian studies of symmetry and stability of laser fusion targets' *Comp. Phys. Comm.* **43** (1), pp. 107–124.

Barrios, M A et al. (2016) 'Electron temperature measurements inside the ablating plasma of gas-filled hohlraums at the national ignition facility' *Physics of Plasmas* **23** (5), p. 056307.

Batishchev, O V et al. (1997) 'Kinetic effects in tokamak scrape-off layer plasmas' *Phys. Plasmas* **4**, pp. 1672–1680.

Bell, A R, A P L Robinson, M Sherlock, R J Kingham and W Rozmus (2006) 'Fast electron transport in laser-produced plasmas and the KALOS code for solution of the Vlasov-Fokker-Planck equation' *Plasma Phys. Control. Fusion* **48** (3), R37.

Bissell, J J (2011) 'Magnetised Transport and Instability in Laser Produced Plasmas' PhD thesis Imperial College London.

Bissell, J (2012) *Flux-Limited Heat-flow and Magnetic-Field Transport in Laser-Plasmas* tech. rep. Central Laser Facility Annual Report, pp. 1–4.

Bissell, J J, C P Ridgers and R J Kingham (2010) 'Field compressing magneto-thermal instability in laser plasmas' *Phys. Rev. Lett.* **105** (17), p. 175001.

Björk, A (2007) 'Commentary' in: *Milestones in Matrix Computation: The Selected Works of Gene H Golub with Commentaries* ed. by R H Chan, C Greif and D P O'Leary Oxford Science Publications, pp. 129–147.

Bolstad, J (2007) *VARPRO computer program* see `leda.univ-lyon1.fr/pleinpot/vpnonlinf1.html` and `www.netlib.org/opt/varpro`.

Book, D, J Boris and K Hain (1975) 'Flux-corrected transport II: generalizations of the method' *J. Comp. Phys.* **18** (3), pp. 248–283.

Boyd, T and J Sanderson (2003) *The Physics of Plasmas* Cambridge University Press.

Brackbill, J U and S R Goldman (1983) 'Magnetohydrodynamics in laser fusion: fluid modeling of energy transport in laser targets' *Communications on Pure and Applied Mathematics* **36** (4), pp. 415–436.

Braginskii, S I (1965) 'Transport processes in a plasma' in: *Reviews of Plasma Physics* ed. by A M Leontovich vol. 1 New York: Consultants Bureau, p. 251.

Brantov, A V, V Yu Bychenkov, V T Tikhonchuk and W Rozmus (1996) *JETP* **42** (4), p. 716.

Breil, J and P-H Maire (2007) 'A cell-centered diffusion scheme on two-dimensional unstructured meshes' *J. Comput. Phys.* **224** (2), pp. 785–823.

Brodrick, J P et al. (2018) 'Incorporating kinetic effects on nernst advection in inertial fusion simulations' *Plasma Phys. Control. Fusion* **60** (8), p. 084009.

Brodrick, J P et al. (2017) 'Testing nonlocal models of electron thermal conduction for magnetic and inertial confinement fusion applications' *Phys. Plasmas* **24** (9), p. 092309.

Brown, L S, D L Preston and R L Singleton Jr. (2005) 'Charged particle motion in a highly ionized plasma' *Phys. Rep.* **410** (4), pp. 237–333.

Brown, M (2018) 'What will be the true impact of electric vehicles?' *Power Engineering Inernational.*

Brown, S R and M G Haines (1997) 'Transport in partially degenerate, magnetized plasmas. Part 1. collision operators' *Journal of Plasma Physics* **58** (4), pp. 577–600.

Bychenkov, V Yu, J Myatt, W Rozmus and V T Tikhonchuk (1994) 'Ion acoustic waves in plasmas with collisional electrons' *Phys. Rev. E* **50** (6), p. 5134.

Bychenkov, V Yu, J Myatt, W Rozmus and V T Tikhonchuk (1995) 'Kinetic theory of ion acoustic waves in a plasma with collisional electrons' *Phys. Rev. E* **52** (6), p. 6759.

Callahan, D A et al. (2018) 'Exploring the limits of case-to-capsule ratio, pulse length, and picket energy for symmetric hohlraum drive on the National Ignition Facility Laser' *Phys.Plasmas* **25** (5), p. 056305.

Cao, D, G Moses and J Delettrez (2015) 'Improved non-local electron thermal transport model for two-dimensional radiation hydrodynamics simulations' *Phys. Plasmas* **22** (8), p. 082308.

Chang, P Y, G Fiksel, M Hohenberger, J P Knauer, R Betti, F J Marshall, D D Meyerhofer, F H Séguin and R D Petrasso (2011) 'Fusion yield enhancement in magnetized laser-driven implosions' *Phys. Rev. Lett.* **107** (3), p. 035006.

Chang, Z and J D Callen (1992) 'Unified fluid/kinetic description of plasma microinstabilities. Part I: basic equations in a sheared slab geometry' *Phys. Fluids B* **4**, pp. 1167–1181.

Chankin, A V and D P Coster (2009) 'Comparison of 2D models for the plasma edge with experimental measurements and assessment of deficiencies' *J. Nucl. Mater.* **390–391** Proceedings of the 18th International Conference on Plasma-Surface Interactions in Controlled Fusion Devices, pp. 319–324.

Chankin, A V, D P Coster and G Meisl (2012) 'Development and benchmarking of a new kinetic code for plasma periphery (KIPP)' *Contrib. Plasma Phys.* **52** (5–6), pp. 500–504.

Chapman, S, T G Cowling and D Burnett (1953) *The Mathematical Theory of Non-uniform Gases* Cambridge University Press.

Chodura, R (1990) 'Non-local heat conduction along a scrape-off layer with strong recycling' *Contrib. Plasma Phys.* **30** (1), pp. 153–156.

Chrisafis, A and A Vaughan (2017) 'France to ban sales of petrol and diesel cars by 2040' *The Guardian* (7th July 2017).

Churchill, R M, J M Canik, C S Chang, R Hager, A W Leonard, R Maingi, R Nazikian and D P Stotler (2016) 'Kinetic simulations of scrape-off layer physics in the DIII-D tokamak' *Nuclear Materials and Energy*.

Colombant, D and W Manheimer (2008) 'The development of a krook model for nonlocal transport in laser produced plasmas. ii. application of the theory and comparisons with other models' *Physics of Plasmas* **15** (8), p. 083104.

Conte, S D and C de Boor (1972) *Elementary Numerical Analysis: an Algorithmic Approach* McGraw-Hill.

Cooper, G E and P T Herman (1973) 'Effect of velocity dependence of Coulomb logarithm on the solution of the Fokker-Planck equation' *Phys. Fluids* **16** (1), pp. 118–121.

Coren, M (2017) 'Solar and wind are now the cheapest energy around—unless you need to store it' *Quartz*.

Cox, P M, C Huntingford and M S Williamson (2018) 'Emergent constraint on equilibrium climate sensitivity from global temperature variability' *Nature* **553** (Jan. 2018), pp. 319–322.

Dai, H H and D Naylor (1992) 'On an asymptotic expansion of Fourier integrals' *Proceedings: Mathematical and Physical Sciences* **436** (1896), pp. 109–120.

Davies, J R, R Betti, P-Y Chang and G Fiksel (2015) 'The importance of electrothermal terms in ohm's law for magnetized spherical implosions' *Phys. Plasmas* **22** (11), p. 112703.

Decoster, A, P A Markowich and B Perthame (1998) *Modeling of colisions* ed. by P A Raviart Gauthier-Villars.

Del Sorbo, D, J-L Feugeas, Ph Nicolaï, M Olazabal-Loumé, B Dubroca, S Guisset, M Touati and V Tikhonchuk (2015) 'Reduced entropic model for studies of

multidimensional nonlocal transport in high-energy-density plasmas' *Phys. Plasmas* **22**, p. 082706.

Del Sorbo, D, J-L Feugeas, r Nicolaï, M Olazabal-Loumé, B Dubroca and V Tikhonchuk (2016) 'Extension of a reduced entropic model of electron transport to magnetized nonlocal regimes of high-energy-density plasmas' *Laser and Particle Beams* **34** (3), pp. 412–425.

Del Sorbo, D (2015) 'An entropic approach to magnetized nonlocal transport and other kinetic phenomena in high-energy-density plasmas' Theses Université de Bordeaux, Dec. 2015.

Dimits, A M, I Joseph and M V Umansky (2013) *Bull. American Phys. Soc.* **58**, p. 281.

Dimits, A M, I Joseph and M V Umansky (2014) 'A fast non-Fourier method for Landau-fluid operators' *Phys. Plasmas* **21**, p. 055907.

Drax (2017) *How electric vehicles will impact global power demand* tech. rep.

Dubroca, B, J Feugeas and M Frank (2010) 'Angular moment model for the Fokker-Planck equation' *Eur. Phys. J. D* **60** (2), pp. 301–307.

Dum, C T (1978a) 'Anomalous electron transport equations for ion sound and related turbulent spectra' *Phys. Fluids* **21** (6), pp. 956–969.

Dum, C T (1978b) 'Anomalous heating by ion sound turbulence' *Phys. Fluids* **21** (6), pp. 945–955.

Ďuran, I, K Ješko, V Fuchs, M Groth, C Guillemaut, J Gunn, J Horacek, R Pitts, D Tskhakaya and J-E Contributors (2015) 'Assessment of the effect of parallel temperature gradients in the jet sol on te measured by divertor target langmuir probes' *J. Nucl. Mater.* **463**, pp. 432–435.

Energy Information Administration (2017) *International Energy Outlook* tech. rep.

Epperlein, E M (1984) 'The accuracy of braginskii's transport coefficients for a lorentz plasma' *J. Phys. D: Appl. Phys.* **17** (9), p. 1823.

Epperlein, E M (1994) 'Effect of electron collisions on ion-acoustic waves and heat flow' *Phys. Plasmas* **1** (1), pp. 109–115.

Epperlein, E M and M G Haines (1986) 'Plasma transport coefficients in a magnetic field by direct numerical solution of the Fokker-Planck equation' *Phys. Fluids* **29**, p. 1029.

Epperlein, E M, G J Rickard and A R Bell (1988a) 'A code for the solution of the Vlasov-Fokker-Planck equation in 1-D or 2-D' *Comp. Phys.Communications* **52** (1), pp. 7–13.

Epperlein, E M, G J Rickard and A R Bell (1988b) 'Two-dimensional nonlocal electron transport in laser-produced plasmas' *Phys. Rev. Lett.* **61** (21), pp. 2453–2456.

Epperlein, E M and R W Short (1991) 'A practical nonlocal model for electron heat transport in laser plasmas' *Phys. Fluids B* **3** (11), p. 3092.

Epperlein, E M and R W Short (1994) 'Generalized electron fluid equations in the presence of laser irradiation' *Physics of Plasmas* **1** (9), pp. 3003–3007.

Farmer, W A, J M Koning, D J Strozzi, D E Hinkel, L F B Hopkins, O S Jones and M D Rosen (2017) 'Simulation of self-generated magnetic fields in an inertial fusion hohlraum environment' *Phys. Plasmas* **24** (5), p. 052703.

Farmer, W A et al. (2018) 'Heat transport modeling of the dot spectroscopy platform on nif' *Plasma Phys. Control. Fusion* **60** (4), p. 044009.

Froula, D H et al. (2007) 'Quenching of the nonlocal electron heat transport by large external magnetic fields in a laser-produced plasma measured with imaging thomson scattering' *Phys. Rev. Lett.* **98** (13), p. 135001.

Fuchs, J (2017) Private communication.

Fundamenski, W (2005) *Plasma Phys. Control. Fusion* **47**, R163.

García-Rubio, F and J Sanz (2018) 'Magnetic pressure effects in a plasma-liner interface' *Phys. Plasmas* **25** (4), p. 042114.

Gericke, D O, M S Murillo and M Schlanges (2002) 'Dense plasma temperature equilibration in the binary collision approximation' *Phys. Rev. E* **65** (3 2002), p. 036418.

Golub, G H and V Pereyra (1973) 'The differentiation of pseudo-inverses and nonlinear least squares problems whose variables separate' *SIAM Journal on Numerical Analysis* **10** (2), pp. 413–432.

Golub, G and V Pereyra (1972) *The Differentiation of pseudoinverses and nonlinear least squares problems whose variables separate* tech. rep. STAN-B-72-261 Computer Science Department, School of Humanities and Sciences Stanford University.

Golub, G and V Pereyra (2003) 'Separable nonlinear least squares: the variable projection method and its applications' *Inverse Problems* **19** (2), R1.

Gomez, M R et al. (2014) 'Experimental demonstration of fusion-relevant conditions in magnetized liner inertial fusion' *Phys. Rev. Lett.* **113** (15), p. 155003.

Gotchev, O V, N W Jang, J P Knauer, M D Barbero, R Betti, C K Li and R D Petrasso (2008) 'Magneto-inertial approach to direct-drive laser fusion' *Journal of Fusion Energy* **27** (1), pp. 25–31.

Haines, M G (1986a) 'Heat flux effects in ohm's law' *Plasma Phys. Control. Fusion* **28** (11), p. 1705.

Haines, M G (1986b) 'Magnetic-field generation in laser fusion and hot-electron transport' *Can. J. Phys.* **64** (8), pp. 912–919.

Hammett, G W and F W Perkins (1990) 'Fluid moment models for Landau damping with application to the ion-temperature-gradient instability' *Phys. Rev. Lett.* **64**, p. 3019.

Hill, D W and R J Kingham (2017) 'Enhancement of Pressure Perturbations in Ablation due to Kinetic Magnetised Transport Effects under Direct-Drive ICF relevant conditions' *ArXiv e-prints* arXiv: 1712.02663 [physics.plasm-ph].

Hohenberger, M, P-Y Chang, G Fiksel, J P Knauer, R Betti, F J Marshall, D D Meyerhofer, F H Séguin and R D Petrasso (2012) 'Inertial confinement fusion implosions with imposed magnetic field compression using the omega laser' *Phys. Plasmas* **19** (5), p. 056306.

Holstein, P A, J Delettrez, S Skupsky and J P Matte (1986) 'Modeling nonlocal heat flow in laser-produced plasmas' *J. Applied Phys.* **60** (7), pp. 2296–2300.

Horacek, J, R Pitts, P Stangeby, O Batishchev and A Loarte (2003) 'Predicted effects of parallel temperature gradients on the overestimation of tcv divertor target langmuir probe t e measurements' *J Nucl. Mater.* **313**, pp. 931–935.

Hornberger, G M (n.d.) 'New manuscript guidelines for the reporting of stable hydrogen, carbon, and oxygen isotope ratio data' *Water Resources Research* **31** (12), pp. 2895–2895.

Hsu, S C et al. (2017) 'Experiment to form and characterize a section of a spherically imploding plasma liner' *IEEE Trans Plasma Sci.* **PP** (99), pp. 1–11.

Huba, J D (2016) *NRL Plasma Formulary* tech. rep.

Igumenshchev, I V, A B Zylstra, C K Li, P M Nilson, V N Goncharov and R D Petrasso (2014) 'Self-generated magnetic fields in direct-drive implosion experiments' *Phys. Plasmas* **21** (6), p. 062707.

Izacard, O (2016) 'Kinetic corrections from analytic non-Maxwellian distribution functions in magnetized plasmas' *Phys. Plasmas* **23** (8), p. 082504.

J T Omotani, B D Dudson, E Havlíčková and M Umansky (2015) 'Non-local parallel transport in BOUT++' *J. Nucl. Mater.* **463**, pp. 769–772.

Jaworski, M A et al. (2012) 'Modification of the electron energy distribution function during lithium experiments on the national spherical torus experiment' *Fusion Eng. and Design* **87** (10) The 2nd International Symposium of Lithium Application for Fusion Devices, pp. 1711–1718.

Jaworski, M A et al. (2013) 'Observation of non-Maxwellian electron distributions in the NSTX divertor' *J. Nucl. Mater.* **438** Proceedings of the 20th International Conference on Plasma-Surface Interactions in Controlled Fusion Devices, S384–S387.

Ji, J Y and E D Held (2014) 'Electron parallel closures for arbitrary collisionality' *Phys. Plasmas* **21**, p. 122116.

Ji, J Y, E D Held and C R Sovinec (2009) *Phys. Plasmas* **16** (2), p. 022312.

Joglekar, A S, C P Ridgers, R J Kingham and A G R Thomas (2016) 'Kinetic modeling of nernst effect in magnetized hohlraums' *Phys. Rev. E* **93** (4), p. 043206.

Joglekar, A S, B J Winjum, A Tableman, H Wen, M Tzoufras and W B Mori (2018) 'Validation of OSHUN against collisionless and collisional plasma physics' *Plasma Phys. Control. Fusion* **60** (6), p. 064010.

Johnston, T W (1960) 'Cartesian tensor scalar product and spherical harmonic expansions in boltzmann's equation' *Phys. Rev.* **120** (4 1960), pp. 1103–1111.

Jones, O S, C A Thomas, P A Amendt, G N Hall, N Izumi, M A Barrios Garcia, L F B Hopkins, H Chen, E L Dewald, D E Hinkel et al. (2016) 'Towards a more universal understanding of radiation drive in gas-filled hohlraums' *J. Phys.: Conf. Series* **717** (1), p. 012026.

Kaufman, L (1975) 'A variable projection method for solving separable nonlinear least squares problems' *BIT Numer. Math.* **15** (1), pp. 49–57.

Kho, T H and M G Haines (1985) 'Nonlinear kinetic transport of electrons and magnetic field in laser-produced plasmas' *Phys. Rev. Lett.* **55** (8), pp. 825–828.

Kho, T H and M G Haines (1986) 'Nonlinear electron transport in magnetized laser plasmas' *Phys. Fluids* **29** (8), p. 2665.

Kingham, R J and A R Bell (2002) 'Nonlocal magnetic-field generation in plasmas without density gradients' *Phys. Rev. Lett.* **88** (4 2002), p. 045004.

Kingham, R J and A R Bell (2004) 'An implicit Vlasov-Fokker-Planck code to model non-local electron transport in 2-D with magnetic fields' *J. Comput. Phys.* **194**, pp. 1–34.

Knapp, C E and R C Kirkpatrick (2014) 'Possible energy gain for a plasma-liner-driven magneto-inertial fusion concept' *Phys. Plasmas* **21** (7), p. 070701.

Kodanova, S K, T S Ramazanov, M K Issanova, G N Nigmetova and Z A Moldabekov (2014) 'Investigation of coulomb logarithm and relaxation processes in dense plasma on the basis of effective potentials' *Contrib. Plasma Phys.* **55** (2–3), pp. 271–276.

Kolobov, V and R Arslanbekov (2006) 'Simulation of electron kinetics in gas discharges' *IEEE Transactions on Plasma Sci.* **34** (3), pp. 895–909.

Kruger, C J C (2002) 'Constrained cubic spline interpolation for chemical engineering applications' *Korf Technology* `korf.co.uk/util_2.html`.

Lancia, L et al. (2013) 'Simultaneous measurement of self-generated magnetic fields and electron heat transport in dense plasma' *Laser and Particle Beams* **31** (4), pp. 653–661.

Lancia, L et al. (2014) 'Topology of megagauss magnetic fields and of heat-carrying electrons produced in a high-power laser-solid interaction' *Phys. Rev. Lett.* **113** (23), p. 235001.

Langdon, A B (1980) 'Nonlinear inverse bremsstrahlung and heated-electron distributions' *Phys. Rev. Lett.* **44** (9), pp. 575–579.

Lawton, W H and E A Sylvestre (1971) 'Elimination of linear parameters in nonlinear regression' *Technometrics* **13** (3), pp. 461–467.

LeVeque, R J (2004) 'High-resolution methods' in: *Finite-Volume Methods for Hyperbolic Problems* Cambridge University Press, pp. 106–115.

Li, C K et al. (2009) 'Observations of electromagnetic fields and plasma flow in hohlraums with proton radiography' *Phys. Rev. Lett.* **102** (20), p. 205001.

Lipschultz, B, J Coenen, H Barnard, N Howard, M Reinke, D Whyte and G Wright (2012) 'Divertor tungsten tile melting and its effect on core plasma performance' *Nucl. Fusion* **52** (12), p. 123002.

Luciani, J F, P Mora and A Bendib (1985) 'Magnetic field and nonlocal transport in laser-created plasmas' *Phys. Rev. Lett.* **55** (22), pp. 2421–2424.

Luciani, J F, P Mora and J Virmont (1983) 'Nonlocal heat transport due to steep temperature gradients' *Phys. Rev. Lett.* **51**, p. 1664.

Ma, Q, J Dai, D Kang, Z Zhao, J Yuan and X Zhao (2014) 'Molecular dynamics simulation of electron-ion temperature relaxation in dense hydrogen: a scheme of truncated coulomb potential' *High Energy Density Physics* **13**, pp. 34–39.

MacLaren, S A et al. (2014) 'Novel characterization of capsule x-ray drive at the national ignition facility' *Phys. Rev. Lett.* **112** (10), p. 105003.

Maksimov, A and V Silin (1993) 'Theory of the filamentary instability in a collisional plasmas' *JETP* **76** (1), pp. 39–47.

Maksimov, A and V Silin (1994) 'Nonstationary electron density perturbation in a weakly collisional plasma' *JETP* **78** (5), pp. 669–676.

Manheimer, W, D Colombant and V Goncharov (2008) 'The development of a krook model for nonlocal transport in laser produced plasmas. i. basic theory' *Phys. Plasmas* **15**, p. 083103.

Manheimer, W, D Colombant and A J Schmitt (2012) 'Calculations of nonlocal electron energy transport in laser produced plasmas in one and two dimensions using the velocity dependent krook model' *Physics of Plasmas* **19** (5), p. 056317.

Marocchino, A, M Tzoufras, S Atzeni, A Schiavi, Ph D Nicolaï, J Mallet, V Tikhonchuk and J-L Feugeas (2013) 'Comparison for non-local hydrodynamic thermal conduction models' *Phys. Plasmas* **20**, p. 022702.

Matte, J P, M Lamoureux, C Moller, R Y Yin, J Delettrez, J Virmont and T W Johnston (1988) 'Non-Maxwellian electron distributions and continuum X-ray emission in inverse bremsstrahlung heated plasmas' *Plasma Phys. Control. Fusion* **30** (12), p. 1665.

Miller, A J (2004) *A collection of Mathematical and Statistical routines in Fortran 90* archive available at http://jblevins.org/mirror/amiller/.

Montgomery, D S et al. (2015) 'Use of external magnetic fields in hohlraum plasmas to improve laser-coupling' *Phys. Plasmas* **22** (1), 010703, p. 010703.

Mulser, P, G Alber and M Murakami (2014) 'Revision of the coulomb logarithm in the ideal plasma' *Physics of Plasmas* **21** (4), p. 042103.

Nicolaï, Ph D, J-L A Feugeas and G P Schurtz (2006) *Phys. Plasmas* **13**, p. 032701.

Nishiguchi, A, T Yabe, M G Haines, M Psimopoulos and H Takewaki (1984) 'Convective amplification of magnetic fields in laser-produced plasmas by the nernst effect' *Phys. Rev. Lett.* **53** (3), pp. 262–265.

Oberhetting, F (1959) 'On a modification of Watson's lemma' *J. Res. Natl. Bur. Stand.* **63B** (1), pp. 15–17.

O'Leary, D P and B W Rust (2013) 'Variable projection for nonlinear least squares problems' *Computational Optimization and Applications* **54** (3), pp. 579–593.

Omotani, J T and B D Dudson (2013) 'Non-local approach to kinetic effects on parallel transport in fluid models of the scrape-off layer' *Plasma Phys. Control. Fusion* **55** (5), p. 055009.

Ongena, J and G V Oost (2012) 'Energy for future centuries: prospects for fusion power as a future energy source' *Fusion Sci. Tech.* **61** (2T), pp. 3–16.

Onsager, L (1931) 'Reciprocal relations in irreversible processes. i.' *Phys. Rev.* **37** (4 Feb. 1931), pp. 405–426.

Oosthuizen, J (2011) *The Mellin Transform* tech. rep. Department of Mathematical Sciences, Stellenbosch University.

Osborne, M R (1972) 'Some aspects of non-linear least squares calculations' in: *Numerical Methods for Non-linear Optimization* ed. by F A Lootsma Academic Press, London.

Osborne, M R (2007) 'Separable least squares, variable projection, and the Gauss-Newton algorithm' *Electronic Transactions on Numerical Analysis* **28** (2), pp. 1–15.

Perkins, L J, D D-M Ho, B G Logan, G B Zimmerman, M A Rhodes, D J Strozzi, D T Blackfield and S A Hawkins (2017) 'The potential of imposed magnetic

fields for enhancing ignition probability and fusion energy yield in indirect-drive inertial confinement fusion' *Physics of Plasmas* **24** (6), p. 062708.

Read, M, R Kingham and J Bissell (2016) 'The influence of magnetised electron transport on thermal self-focusing and channelling of nanosecond laser beams' *Journal of Physics: Conference Series* **717** (1), p. 012111.

Reiter, D (1992) 'Progress in two-dimensional plasma edge modelling' *J. Nucl. Mater.* **196–198**, p. 80.

Ridgers, C P (2008) 'Magnetic Fields and Non-Local Transport in Laser Plasmas' PhD thesis Imperial College London.

Ridgers, C P, R J Kingham and A G R Thomas (2008a) 'Magnetic cavitation and the reemergence of nonlocal transport in laser plasmas' *Phys. Rev. Lett.* **100** (7), p. 075003.

Ridgers, C P, A G R Thomas, R J Kingham and A P L Robinson (2008b) 'Transport in the presence of inverse bremsstrahlung heating and magnetic fields' *Phys. Plasmas* **100** (9), 092311, p. 075003.

Riquier, R (2016) 'Magnetic field in laser plasmas: non-local electron transport and reconnection' PhD thesis École polytechnique, Paris Saclay.

Rognlien, T, P Brown, R Campbell, T Kaiser, D Knoll, P McHugh, G D Porter, M Rensink and G Smith (1994) '2-D fluid transport simulations of gaseous/radiative divertors' *Contrib. Plasma Phys.* **34** (2–3), pp. 362–367.

Rosen, M D, H Scott, D E Hinkel, E Williams, D Callahan, R Town, L Divol, P Michel, W Kruer, L Suter et al. (2011) 'The role of a detailed configuration accounting (DCA) atomic physics package in explaining the energy balance in ignition-scale hohlraums' *High Energy Density Physics* **7**, p. 180.

Rosenbluth, M N, W M MacDonald and D L Judd (1957) 'Fokker-Planck equation for an inverse-square force' *Phys. Rev.* **107** (1), pp. 1–6.

Ryzhkov, S V (2014) 'Current state, problems, and prospects of thermonuclear facilities based on the magneto-inertial confinement of hot plasma' *Bull. Russ. Acad. Sci.: Phys.* **78** (5), pp. 456–461.

Schneider, R, D Reiter, H P Zehrfeld, B Braams, M Baelmans, J Geiger, H Kastelewicz, J Neuhauser and R Wunderlich (1992) 'B2-eirene simulation of asdex and asdex-upgrade scrape-off layer plasmas' *J. Nucl. Mater.* **196–198**, pp. 810–815.

Schurtz, G P, Ph D Nicolaï and M Busquet (2000) 'A nonlocal electron conduction model for multidimensional radiation hydrodynamics codes' *Phys. Plasmas* **7**, p. 4238.

Sefkow, A B, S A Slutz, J M Koning, M M Marinak, K J Peterson, D B Sinars and R A Vesey (2014) 'Design of magnetized liner inertial fusion experiments using the z facility' *Phys. Plasmas* **21** (7), p. 072711.

Séguin, F H et al. (2012) 'Time evolution of filamentation and self-generated fields in the coronae of directly driven inertial-confinement fusion capsules' *Phys. Plasmas* **19** (1), p. 012701.

Sherlock, M, J P Brodrick and C P Ridgers (2017) 'A comparison of non-local electron transport models for laser-plasmas relevant to inertial confinement fusion' *Phys. Plasmas* **24** (8), p. 082706.

Shoucri, M M and R R J Gagne (1978) 'Splitting schemes for the numerical solution of a two-dimensional Vlasov equation' *J. Comput. Phys.* **27**, pp. 315–322.

Sijoy, C, V Mishra and S Chaurasia (2017) 'An improved and fully implicit multi-group non-local electron transport model and its validations' *High Energy Density Physics* **24**, pp. 56–63.

Slutz, S A, M C Herrmann, R A Vesey, A B Sefkow, D B Sinars, D C Rovang, K J Peterson and M E Cuneo (2010) 'Pulsed-power-driven cylindrical liner implosions of laser preheated fuel magnetized with an axial field' *Phys. Plasmas* **17** (5), p. 056303.

Slutz, S A and R A Vesey (2012) 'High-gain magnetized inertial fusion' *Phys. Rev. Lett.* **108** (2), p. 025003.

Spitzer, L and R Härm (1953) 'Transport phenomena in a completely ionized gas' *Phys. Rev.* **89** (5), pp. 977–981.

Stamper, J A (1991) 'Review on spontaneous magnetic fields in laser-produced plasmas: phenomena and measurements' *Laser and Particle Beams* **9** (4), pp. 841–862.

Strozzi, D J, L Perkins, M Marinak, D Larson, J Koning and B G Logan (2015) 'Imposed magnetic field and hot electron propagation in inertial fusion hohlraums' *J. Plasma Phys.* **81** (6).

Takizuka, T and H Abe (1977) 'A binary collision model for plasma simulation with a particle code' *J. Comp. Phys.* **25** (3), pp. 205–219.

The International Energy Administration (2002) *Environmental and health impacts of electricity generation* tech. rep.

Thomas, A G R, M Tzoufras, A P L Robinson, R J Kingham, C P Ridgers, M Sherlock and A R Bell (2012) 'A review of Vlasov-Fokker-Planck numerical modeling of inertial confinement fusion plasma' *J. Comp. Phys.* **231** (3) Special Issue: Computational Plasma Physics, pp. 1051–1079.

Touati, M, J-L Feugeas, P Nicolaï, J J Santos, L Gremillet and V T Tikhonchuk (2014) 'A reduced model for relativistic electron beam transport in solids and dense plasmas' *New Journal of Physics* **16** (7), p. 073014.

Trubnikov, B A (1965) 'Particle interactions in a fully ionized plasma' in: *Review of Plasma Physics* ed. by A M Leontovich vol. 1 New York: Consultants Bureau, pp. 105–204.

Turnyanskiy, M, R Neu, R Albanese, R Ambrosino, C Bachmann, S Brezinsek, T Donne, T Eich, G Falchetto, G Federici et al. (2015) 'European roadmap to the realization of fusion energy: mission for solution on heat-exhaust systems' *Fusion Eng. and Design* **96–97** Proceedings of the 28th Symposium On Fusion Technology (SOFT-28), p. 361.

Turrell, A, M Sherlock and S Rose (2015) 'Self-consistent inclusion of classical large-angle coulomb collisions in plasma monte carlo simulations' *J. Comput. Phys.* **299**, pp. 144–155.

Tzoufras, M, A R Bell, P A Norreys and F S Tsung (2011) *J. Comput. Phys* **230** (17), pp. 6475–6494.

Tzoufras, M, A Tableman, F S Tsung, W B Mori and A R Bell (2013) 'A multi-dimensional Vlasov-Fokker-Planck code for arbitrarily anisotropic high-energy-density plasmas' *Phys. Plasmas* **20** (5), p. 056303.

Umansky, M V, A M Dimits, I Joseph, J T Omotani and T D Rognlien (2015) 'Modeling of tokamak divertor plasma for weakly collisional parallel electron transport' *J. Nucl. Mater.* **463** Proceedings of the 21st International Conference on Plasma-Surface Interactions in Controlled Fusion Devices, p. 506.

Van Kampen, N (1955) 'On the theory of stationary waves in plasmas' *Physica* **21** (6), pp. 949–963.

Walsh, C A, J P Chittenden, K McGlinchey, N P L Niasse and B D Appelbe (2017) 'Self-generated magnetic fields in the stagnation phase of indirect-drive implosions on the national ignition facility' *Phys. Rev. Lett.* **118** (15), p. 155001.

Watson, G N (1916) 'The harmonic functions associated with the parabolic cylinder' *Proceedings of the London Mathematical Society* **s2-17** (1), pp. 116–148.

Willingale, L et al. (2010) 'Fast advection of magnetic fields by hot electrons' *Phys. Rev. Lett.* **105** (9), p. 095001.

Wong, R and J Lin (1978) 'Asymptotic expansions of Fourier transforms of functions with logarithmic singularities' *Journal of Mathematical Analysis and Applications* **64** (1), pp. 173–180.

Xiong, Z, R H Cohen, T D Rognlien and X Q Xu (2008) 'A high-order finite-volume algorithm for Fokker-Planck collisions in magnetized plasmas' *J. Comp. Phys.* **227** (15), pp. 7192–7205.

Zhao, Y (2017) 'Investigation of effective impact parameters in electron-ion temperature relaxation via particle-particle coulombic molecular dynamics' *Phys. Lett. A* **381** (35), pp. 2944–2948.